LCH Laboratoire de Constructions Hydrauliques
Laboratory of Hydraulic Constructions

ÉCOLE POLYTECHNIQUE
FÉDÉRALE DE LAUSANNE

Communication 57

Hydrodynamics of turbulent flows within arrays of circular cylinders

Ana Margarida da Costa Ricardo

Editeur : Prof. Dr A. Schleiss

Lausanne, 2014

Communications du Laboratoire de Constructions Hydrauliques ISSN 1661-1179
Ecole Polytechnique Fédérale de Lausanne
Editeur: Prof. Dr A. Schleiss

N° 30 2007 P. Heller
Méthodologie pour la conception et la gestion des aménagements hydrauliques à buts multiples

N° 31 2007 P. Heller
Analyse qualitative des systèmes complexes à l'aide de la méthode de Gomez & Probst

N° 32 2007 J. García Hernández, F. Jordan, J. Dubois, J.-L. Boillat
Routing System II - Modélisation d'écoulements dans des systèmes hydrauliques

N° 33 2007 Symposium - Flussbauliche Massnahmen im Dienste des Hochwasserschutzes, der Umwelt, Gesellschaft und Wirtschaft / Mesures d'aménagement des cours d'eau pour la protection contre les crues, l'environnement, la société et l'économie

N° 34 2007 B. Rosier
Interaction of side weir overflow with bed-load transport and bed morphology in a channel

N° 35 2007 A. Amini
Contractile floating barriers for confinement and recuperation of oil slicks

N° 36 2008 T. Meile
Influence of macro-roughness of walls on steady and unsteady flow in a channel

N° 37 2008 S. A. Kantoush
Experimental study on the influence of the geometry of shallow reservoirs on flow patterns and sedimentation by suspended sediments

N° 38 2008 F. Jordan, J. García Hernández, J. Dubois, J.-L. Boillat
Minerve - Modélisation des intempéries de nature extrême du Rhône valaisan et de leurs effets

N° 39 2009 A. Duarte
An experimental study on main flow, secondary flow and turbulence in open-channel bends with emphasis on their interaction with the outer-bank geometry

N° 40 2009 11. JUWI
Treffen junger Wissenschafterinnen und Wissenschafter an Wasserbauinstituten

N° 41 2010 Master of Advanced Studies (MAS) in Water Resources Management and Engineering, édition 2005-2007 - Collection des articles des travaux de diplôme

N° 42 2010 M. Studer
Analyse von Fliessgeschwindigkeiten und Wassertiefen auf verschiedenen Typen von Blockrampen

Preface

In rivers riparian vegetation can have not only strong interaction with the flow but also with the ecological services of the aquatic system. In wetlands and along riverbanks often tree-like vegetation with quite stiff trunks can be found. The study of the flow in the space between plant stems is highly relevant since it influences the deposition of suspended sediment and the transport of pollutants or nutrients. With her comprehensive experimental research study Mrs Dr. Ana Margarida da Costa Ricardo carried out a novel detailed spatial characterization, at the inter-stem scale, of the turbulent flow within arrays of emergent, rigid and cylindrical stems, randomly placed with constant and varying density in a flume.

Mrs Dr. da Costa Ricardo performed detailed measurement of instantaneous velocities with a 2D Particle Image Velocimetry (PIV) and a 3D Laser Doppler Anemometry (LDA). Part of the data was treated with Double-Averaging Methodology (DAM), used as an up-scaling technique to deal with heterogeneous flows.

Mrs Dr. da Costa Ricardo could reveal that the drag force per submerged stem length is not correlated directly with the stem areal number density and the stem Reynolds number. The drag force depends on the longitudinal variation of the stem areal number-density. It could be observed that the decrease of the latter is associated to larger flow resistance and that the drag coefficient increases with the relative roughness, revealing an influence of the bed on the definition of the flow structure. The importance of vortex shedding and unsteady separation of the flow on the stems could be highlighted.

Finally Mrs Dr. da Costa Ricardo gives a new insight in the dissipation rate of turbulent kinetic energy (TKE). She could contribute significantly to a better understanding of the complex flow within random arrays of rigid and emergent stems, at the inter-stem scale regarding flow resistance, budget of TKE and computation of dissipation rate of TKE.

We would like to thank the members of the jury Prof. António Luís Moreira, Instituto Superior Técnico, Lisbon, Portugal and Prof. Jochen Aberle, NTNU, Trondheim, Norway, as well as Prof. Fernando Porté-Agel, EPFL, Lausanne, Switzerland, for their helpful suggestions. Finally we also thank gratefully the Portuguese Foundation for Science and Technology (FTC) for their financial support under project PTDC/ECM/099752/2008 and the research grant SFRH/BD 33668/2009.

Prof. Dr. Anton Schleiss

Prof. Dr. Rui Ferreira

Abstract

In the context of environmental sciences, emergent circular cylinders function as an ersatz for wetland vegetation. The study of the flow in the space among plant stems is highly relevant as its hydrodynamics determine fluxes of suspended sediment, pollutants and nutrients, thus constituting the physical stratum upon which biological and ecological strata are formed.

The present research project aims at a detailed spatial characterization, at the inter-stem scale, of the turbulent flow within arrays of emergent, rigid and cylindrical stems, randomly placed with constant and varying density.

The main goals of this work include a detailed characterization and quantification of the flow in the space among plant stems, herein termed inter-stem space; the quantification of the forces acting on the stems and the respective drag coefficient; an integrated analysis of the spatial distribution of turbulent kinetic energy (TKE) conservation equation; the derivation of an equation to estimate of the rate of dissipation of TKE, exploiting the space-averaging of two-point correlations and statistics as a means to salvage the formalism of homogeneous and isotropic turbulence as well as the characterization and quantification of the rate of dissipation of TKE in the inter-stem space.

The work is mainly experimental, employing measurement of instantaneous velocities with a 2D Particle Image Velocimetry (PIV) and a 3D Laser Doppler Anemometry (LDA). Part of the data treatment is carried out following the framework of Double-Averaging Methodology (DAM), an upscaling technique to deal with heterogeneous flows. On the topic of drag forces, a dimensional analysis is performed to identify the relevant parameters on the characterization of flows within arrays of rigid and emergent stems. Theoretical work is performed to devise a formulation to compute the dissipation rate of energy for heterogeneous flow.

This work accounts with three innovations: i) a detailed spatial description of the budget of TKE and of the terms of the double-averaged momentum conservation equation; ii) an experimental procedure and associated data treatment, relying mostly on spatial measurements and thus avoiding the use of the frozen turbulence approximation; and iii) the theoretical framework for dealing with non-homogeneous flows, employing time and space-averaging as a means to apply

the formalism of homogeneous and isotropic turbulence (HIT).

Momentum conservation equations were upscaled with a sound mathematical framework, the Double-Averaging Methodology, and integrated vertically to obtain a model, without major simplifications, to compute the drag forces associated with the vertical elements. It was concluded that, locally at the patch scale, longitudinal gradient of stem areal number-density impacts the magnitude of the drag force. However, at the scale of the wavelength of the stem's distribution, if the variability of stem areal number-density is cyclic, there might be no appreciable effect of patchiness on the average momentum balance.

The spatial distribution of the terms of TKE budget, in the inter-stem space, is presented and discussed. It is verified that the main source of TKE is vortex shedding from individual stems and that the rates of production and dissipation are not in equilibrium, revealing important interactions of turbulence with mean flow, pressure field and turbulent transport of TKE. Regions with negative production, a previously unreported feature, were identified and discussed.

Exploring the space-averaging of two-point correlations and statistics of the turbulent flow as means to apply the formalism of homogeneous and isotropic turbulence, an equation to estimate the dissipation rate of turbulent kinetic energy was derived assuming valid local isotropy conditions. Obviously some caution is needed and it must be underlined that it is not the validity of the local isotropy for each instantaneous velocity series that is being claimed, instead it was proved that averages of sufficient long time series of the structures functions and energy spectra lead to the conclusions of the well known isotropic turbulence theory.

Advances on the understanding of the complex flow within random arrays of rigid and emergent stems, at the inter-stem scale, were attained in three relevant topics: flow resistance, budget of TKE and computation of dissipation rate of TKE.

The immediate progresses and methodologies of this program pertain to fluid mechanics domain, however it should be emphasized that the results will eventually mature into bioengineering design approaches, what will positively impact river engineering practices.

Keywords: Vegetated flows, inter-stem scale, PIV, LDA, Double-Averaging Methodology, turbulence, spatial analysis, TKE budget, momentum equations, drag coefficient, heterogeneity, dissipation rate of TKE

Resumo

No contexto das ciências ambientais, os cilindros circulares emergentes são muitas vezes usados para simular vegetação rígida de zonas húmidas. O estudo do escoamento no espaço entre hastes das plantas é de grande relevância na medida em que a sua hidrodinâmica determina fluxos de sedimentos suspensos, poluentes e nutrientes, constituindo assim o estrato físico no qual os estratos biológicos e ecológicos são formados.

O presente projecto de investigação visa a caracterização espacial detalhada, à escala do espaçamento médio entre hastes, de escoamentos turbulentos com uma distribuição de vegetação rígida emersa e de hastes cilíndricas, dispostas aleatoriamente com densidade constante e variável.

Os principais objectivos deste trabalho incluem a caracterização e quantificação do escoamento no espaço entre hastes; a quantificação das forças de arrastamento actuantes nas hastes e respectivo coeficiente de arrastamento; uma análise integrada da distribuição espacial dos termos da equação de conservação da energia cinética turbulenta (TKE); o desenvolvimento de uma equação para estimar a taxa de dissipação da TKE, explorando a média espacial das correlações a dois pontos e outras funções estatísticas, como forma de manter o formalismo da turbulência homogénea e isotrópica; caracterização e quantificação da taxa de dissipação da TKE.

O trabalho é essencialmente experimental, com medições de velocidades instantâneas com recurso aos sistemas 2D *Particle Image Velocimetry* (PIV) e 3D *Laser Doppler Anemometry* (LDA). Parte do tratamento de dados é realizado através da metodologia de dupla média espácio-temporal (DAM), que permite caracterizar escoamentos não homogéneos. No âmbito do estudo das forças de arrastamento, é realizada uma análise dimensional para identificar os parâmetros relevantes na caracterização de escoamentos no interior de zonas com hastes rígidas emergentes. O trabalho teórico consiste em desenvolver uma formulação para o cálculo da taxa de dissipação da energia cinética turbulenta em escoamentos heterogéneos.

O presente trabalho apresenta três inovações importantes: i) uma descrição espacial detalhada dos termos da equação de conservação da TKE da quantidade de movimento; ii) um procedimento experimental e respectivo tratamento de dados baseado fundamentalmente em medições espaciais, evitando por isso a utilização da hipótese de Taylor para converter escalas temporais em

escalas espaciais; e iii) o enquadramento teórico para lidar com escoamentos não homogéneos, aplicando médias temporais e espaciais como forma de salvaguardar o formalismo da turbulência homogénea e isotrópica.

As equações de conservação da quantidade de movimento foram foram re-escritas com uma formulação matemática adequada, de acordo com a metodologia DAM, e integradas na vertical para obter para calcular, sem demasiadas simplificações, a força de arrastamento nas hastes. Conclui-se localmente, num determinado troço com densidade de hastes constante, o gradiente longitudinal da densidade de hastes tem impacte na magnitude das forças de arrastamento. No entanto, à escala do comprimento de onda da distribuição de hastes, se a variabilidade espacial apresentada pela densidade de hastes for cíclica, o arranjo em troços com diferentes densidades de hastes não influência o balanço global da quantidade de movimento, uma vez que os efeitos de aumento e diminuição da densidade de hastes se cancelam.

A distribuição espacial da magnitude dos termos da equação de conservação da TKE, no espaço entre hastes, foi apresentado e discutido. Verificou-se que a principal fonte de TKE é a ejecção de vórtices devido à separação instável do escoamento em torno de cada haste. Verificou-se também que as taxas de produção e dissipação da TKE não estão em equilíbrio, revelando importantes interacções entre os movimentos turbulentos e o escoamento médio e importante transporte turbulento de TKE. Foram, ainda, identificadas regiões com taxas de produção de TKE negativas, geralmente, uma característica rara nos escoamentos.

Foi obtida uma equação para estimar a taxa de dissipação da energia cinética turbulenta através da média espacial da correlação de dois pontos e das estatísticas do escoamento turbulento, assumindo como válida a condição de isotropia local. Obviamente é necessária alguma precaução salientando que não é a validade da isotropia local para cada série de velocidades instantâneas que está a ser considerada. Em vez disso, foi provado que as médias de séries temporais suficientemente longas de funções de estrutura e espectros de energia apresentam a forma típica dessas funções em condições de turbulência homogénea e isotrópica.

Os avanços na compreensão dos complexos escoamento em zonas com distribuições aleatórias de hastes rígidas e emergentes, à escala do espaçamento médio entre hastes, foram obtidos na resistência do escoamento, balanço da TKE e cálculo da taxa de dissipação da TKE.

Os progressos e metodologias deste programa pertencem ao domínio da mecânica dos fluidos, no entanto os resultados poderão vir ser desenvolvidos para aplicação no domínio da bioengenharia, resultando num impacto positivo nas práticas de engenharia fluvial.

Palavras chave: escoamentos com vegetação, escala do espaçamento entre hastes, PIV, LDA, DAM, turbulência, análise espacial, balanço da TKE, equações da quantidade de movimento, coeficiente de arrastamento, heterogeneidade, taxa de dissipação da TKE.

Résumé

Dans le contexte des sciences environnementales, les cylindres circulaires émergés fonctionnent comme un ersatz de la végétation rigide des milieux humides. L'étude de l'écoulement parmi des tiges est très importante car son hydrodynamique détermine les flux de sédiments en suspension, de polluants et de nutriments, qui constituent ainsi la strate physique sur laquelle les strates biologiques et écologiques se forment.

Ce projet de recherche vise à obtenir une caractérisation spatiale détaillée, à l'échelle inter-tiges, de l'écoulement turbulent dans un réseau de tiges émergées, rigides et cylindriques, placées aléatoirement avec une densité constante et variable.

Les objectifs principaux de ce travail sont la caractérisation et la quantification détaillées de l'écoulement dans la zone entre les tiges; la quantification des forces de frottement sur les tiges et de leurs coefficients de frottement respectifs; l'analyse intégrée de la distribution spatiale de l'équation de conservation de l'énergie cinétique du mouvement d'agitation (TKE); la dérivation d'une équation permettant d'évaluer le taux de dissipation de TKE : celle-ci exploite la moyenne spatiale de la corrélation de deux points et les statistiques afin de récupérer le formalisme de la turbulence homogène et isotrope ; l'application de cette nouvelle équation à la caractérisation et à la quantification du taux de dissipation de TKE dans l'espace inter-tiges.

Ce travail est principalement expérimental et utilise la mesure de vitesses instantanées par PIV 2D (Particle Image Velocimetry – Mesure de vitesses par images de particules) et par LDA 3D (Laser Doppler Anemometry – Anémométrie Laser Doppler). Une partie du traitement de données est effectuée par la méthode des doubles moyennes (DAM – Double-Averaging Methodology) dans le domaine temporel et spatial, une technique d'amélioration du traitement des écoulements hétérogènes. En ce qui concerne les frottements, une analyse dimensionnelle est réalisée afin d'identifier les paramètres importants pour la caractérisation des écoulements dans un réseau de tiges rigides et émergées. Un travail théorique est également effectué pour concevoir une méthode de calcul du taux de dissipation de TKE dans un écoulement hétérogène.

Trois innovations sont apportées par ce travail : i) l'objectif principal du travail qui vise une description spatiale détaillée du bilan de TKE ainsi que des termes de l'équation moyenne de

conservation de la quantité de mouvement; ii) le procédé expérimental qui repose principalement sur des mesures spatiales, évitant ainsi l'utilisation de l'approximation de la turbulence figée; et iii) l'approche théorique de traitement des écoulements non-homogènes, en utilisant les moyennes temporelles et spatiales pour récupérer le formalisme de la turbulence homogène et isotrope.

Les équations de conservation de la quantité de mouvement ont été agrégées dans un cadre mathématique robuste, la méthodologie DAM, et intégrées verticalement pour obtenir un modèle, sans simplifications majeures, pour calculer les forces de frottement associées aux éléments verticaux. Il a été montré que localement, à l'échelle ponctuelle, le gradient longitudinal de la densité spatiale des tiges affecte la valeur de la force de frottement. Cependant, à plus grande échelle, celle de la longueur d'onde de la distribution des tiges,, si la variabilité de la densité spatiale des tiges est cyclique, il se peut qu'il n'y ait aucun effet notable de la répartition des tiges sur le bilan moyen de la quantité de mouvement, car les influences locales opposées s'annulent.

La distribution spatiale de la valeur des termes du bilan de TKE, dans l'espace inter-tiges a été présentée et discutée. Il a été vérifié que la source principale de TKE est la séparation des vortex par les tiges individuelles et que les taux de production et de dissipation ne sont pas en équilibre, révélant d'importantes intéractions de la turbulence avec l'écoulement moyen, le champ de pression et le transport turbulent de TKE. Des zones de production négative, jamais décrites jusqu'à présent, ont été identifiées.

En exploitant la moyenne spatiale de la corrélation entre deux points et les statistiques de l'écoulement turbulent de manière à récupérer le formalisme de la turbulence homogène et isotrope, une équation permettant d'estimer le taux de dissipation d'énergie cinétique turbulente a été dérivée, en considérant que la condition d'isotropie locale est valide. Évidemment, une certaine précaution est nécessaire et il doit être souligné que ce n'est pas la validité de l'isotropie locale pour chaque série de vitesses instantanées qui est réclamée. Au lieu de cela, il a été démontré que les moyennes de séries à suffisamment long terme des fonctions de structures et des spectres d'énergies mènent aux conclusions bien connues de la turbulence isotropique.

Des améliorations de la compréhension de l'écoulement complexe à travers des rangées aléatoires de tiges rigides et émergentes, à l'échelle inter-tiges, ont été obtenues sur la résistance de l'écoulement, le bilan de TKE et le calcul du taux de dissipation de TKE.

Les progrès immédiats et les méthodologies de ce projet portent sur le domaine de la mécanique des fluides. Cependant, les résultats pourraient évoluer vers des approches de conception de bio-ingénierie et influencer positivement les pratiques de l'ingénierie fluviale.

Mots-clés: Ecoulement en zones de végétation, échelle inter-tiges, PIV, LDA, DAM, turbulence, analyse spatiale, bilan de TKE, équation de la quantité de mouvement, coefficient de frottement, hétérogénéité, taux de dissipation de TKE

Acknowledgments

This research work was conducted at the CEHIDRO at Instituto Superior Técnico (IST) and at the Laboratory of Hydraulic Constructions (LCH) at Ecole Polytechnique Fédérale de Lausanne (EPFL), under the supervision of Professor Rui Ferreira and Professor Anton Schleiss, within the IST-EPFL Joint Doctoral Initiative. The financial support was granted by the Portuguese Foundation for Science and Technology (FCT) and by the LCH. FCT supported this PhD program with the research grant SFRH/BD 33668/2009 and the research project PTDC/ECM/099752/2008, and by the European Fund for Economic and Regional Development (FEDER) through the Program Operational Factor of Competitiveness (COMPETE) FCOMP 01 0124 FEDER 009735.

During the four years of my PhD work I was fortunate enough to received help, assistance, guidance and support from a large number of people. It is not possible to directly address everybody herein, but I am thankful to all those who, in some way, helped me to achieve this milestone.

My most heartfelt thanks are due to my supervisor, Prof. Rui Ferreira, for his endless support, commitment, enthusiasm, patience and friendship. His vast scientific knowledge and availability were of vital importance for the success of this work.

I would also like to thank Prof. Anton Schleiss to the opportunity to integrate his team at LCH. This opportunity, undoubtedly, enriched not only my professional experience but it was also an enriching personal experience.

I wish to express my gratitude to the members of the jury of my PhD defence, Prof. Jochen Aberle (NUST - Trondheim), Prof. Fernando Porté-Agel (EPFL), Prof. António Luis Moreira (IST) and Prof. Eugen Brühwiler (president of the jury, EPFL) for reading my thesis, for the comments given and for having promoted a very interesting discussion.

My gratitude goes also to Mário Franca for having contributed with fruitful collaboration and friendship. I also acknowledge his willingness to discuss my work and to review part of this thesis.

I had the chance to do part of the experimental work at the Laboratory of Leichtweiß Institute for Hydraulic Engineering at Technische Universität Braunschweig (LWI) in Germany. For

that opportunity, I am thankful to Prof. Dr. Andreas Dittrich, the responsible of the Wasserbau department, who kindly allowed the access to the laboratory facilities. I would also like to thank Mr. Uwe Ecklebe, LWI's laboratory technician for his invaluable contribution on the success of the experiments. To Katinka Koll I am grateful for her constant support.

I am grateful to all my colleagues and Professors at CEHIDRO for good working environment, it is a great pleasure to be part of this research unit. I special thank to my officemates, Ricardo Canelas and Patricia Lourenço, who never complained of my talkativeness and were always willing to help me, specially during the thesis writing. To João Pedro Caetano, IST's laboratory technician I am thankful for his collaboration during the two year I spent on the laboratory work at IST. I would also like to thank João Lory, Margarida Martinho and Pedro Sanches for helping with the experiments. To Dulce Fernandes, CEHIDRO's secretary, I am grateful not only for all the administrative issues but also for her care during all theses years.

I also want to express my gratitude to my friends and colleagues from LCH not only for the good working environment, but also for the fellowship I could feel since my first days in Lausanne. It was a great pleasure to be part of such a great team. I experience many enjoyable moments with these friends who also played the role of my family during my periods in Lausanne.

I am lucky and very happy to have many adorable friends, who gave the necessary personal equilibrium which was imperative in my professional life. A special thanks to Martin Bieri for having been an excellent work colleague, a great flatmate and an wonderful friend. To Fabio Daolio I remain grateful for having been my "older brother" since my first stay in Lausanne. It was a pleasure to live with him and share many enjoyable moments during my periods in Lausanne. To Ana Bejinha I am grateful for our long friendship. To Helena Nogueira and Maria João Teles I am thankful for the strong friendship and constant support, I will never forget the crucial encouragement, enthusiasm and help they always provide me. To Nuno Mota, Marion Huchet and Violaine Dugué I am grateful for having helped on the review of part of the thesis. A big thanks goes to Tamara Ghilardi for printing out my thesis for me.

There are no word to express my gratitude to my mother and my brother for their unconditional support, encouragement and love. My last, but definitely not the least, thanks goes to André who gave me extra support, motivation and love to face the last part of my PhD.

Contents

List of Figures **xv**

List of Tables **xxv**

List of Symbols **xxvii**

List of Acronyms **xxxi**

1 Chapter 1. Introduction **1**

1.1 Framework 1

1.2 Objectives 4

1.3 Methodology 5

1.4 Thesis structure 5

2 Chapter 2. State-of-art **7**

2.1 Introduction 7

2.2 Conceptual model 8

2.2.1 Navier-Stokes equations 8

2.2.2 Reynolds-Averaged Navier-Stokes equations (RANS) 9

2.2.3 Turbulent kinetic energy conservation equation 11

2.2.4 Double-Averaging Methodology 11

2.2.5 Double-Averaged Navier-Stokes equations (DANS) 13

2.2.6 Space-averaged turbulent kinetic energy equation (SATKE) 17

2.3 Turbulence 18
2.3.1 Nature of turbulence 18
2.3.2 Homogeneous and isotropic turbulence 20

3 Chapter 3. Experimental work 25

3.1 Introduction 25
3.2 Laboratory facilities 26
3.2.1 The flumes 26
3.2.2 Instrumentation 29
3.3 PIV: Particle Image Velocimetry 32
3.3.1 Historical notes and basic principals of PIV 32
3.3.2 Components of PIV 33
3.3.3 Seeding particles 37
3.3.4 The measuring principle 40
3.3.5 Control parameters of PIV 43
3.4 LDA: Laser Doppler Anemometry 44
3.4.1 Basic principles 44
3.4.2 Quality of measurements 50
3.5 Experimental tests 53
3.5.1 Test S1 53
3.5.2 Test S2 54
3.5.3 Test S3 58
3.6 Data treatment 59
3.6.1 Bed topography 59
3.6.2 Free-surface 60
3.6.3 Volumetric fluid fraction 60
3.6.4 PIV velocity maps 65

4 Chapter 4. Drag coefficient of flows within random arrays of rigid emergent stems 73

4.1 Introduction . . . 74
4.2 Governing equations . . . 76
4.2.1 Double-Averaged Navier Stokes Equations . . . 76
4.2.2 Mean pressure distribution . . . 77
4.2.3 Mean drag force . . . 77
4.3 Experimental tests . . . 78
4.4 Results . . . 83
4.4.1 Dimensional analysis . . . 83
4.4.2 Characterization of time- and space-averaged flow . . . 84
4.4.3 Quantification of drag forces and coefficients . . . 88
4.4.4 The use of F_D^* as a proxy for F_D . . . 89
4.4.5 The drag force per unit stem length, F_D . . . 90
4.4.6 Variation of C_D . . . 92
4.5 Conclusions . . . 95

5 Chapter 5. TKE budget within vegetation 97

5.1 Introduction . . . 98
5.2 Laboratory facilities and instrumentation . . . 100
5.3 Methodology for calculations of the terms of TKE equation . . . 102
5.3.1 Compatibility of PIV and LDA databases . . . 102
5.3.2 Methodology for the calculation of the rate of dissipation of TKE . . . 105
5.3.3 Methodology for the calculation of convective, productive and turbulent diffusion terms . . . 108
5.4 Quantification of the terms of the equation of conservation of TKE . . . 110
5.4.1 Computed terms . . . 110
5.4.2 Rate of production of TKE . . . 110
5.4.3 Convective transport of TKE . . . 112
5.4.4 Diffusion of TKE . . . 113
5.4.5 Rate of dissipation and overall budget of TKE . . . 113

5.5 Discussion 117
5.6 Conclusions 120

6 Chapter 6. Adaptation of HIT results 123

6.1 Introduction 123
6.2 Spatial version of Kolmogorov's equation 123
6.3 Order of the application of the average operators 130

7 Chapter 7. Dissipation of TKE in flows within arrays of rigid emergent stems 133

7.1 Introduction 133
7.2 Experimental facilities 136
7.3 Adaptation of HIT results 141
7.4 Dissipation rate 149
7.5 Conclusion 152

8 Chapter 8. Conclusions 155

8.1 Summary 155
8.2 Main results 156
8.3 Recommendations for future work 159

References 161

A Optimizing the location of sampling points for double-averaged turbulent quantities in flows within arrays of rigid emergent stems 171

B Spectral analysis 181

C Additional figures for the characterization of TKE budget within arrays of cylinders 191

List of Figures

2.1 Extract of a longitudinal instantaneous velocity time series acquired with a Laser Doppler Anemometry system. The dashed line represents the time-averaged velocity $\bar{u}$. 10

2.2 Representation of an eddy of wavenumber k and wavelength $2\pi/k$ (from Tennekes & Lumley, 1972, p. 259). 19

2.3 a) Autocorrelation function and corresponding integral scale, l_0 and Taylor's micro scale, λ (adapted from Chassaing, 2000, p. 55). b) Sketch of the correlation functions B_{LL} and B_{NN}. 21

3.1 Schematic view of the recirculating tilting flume at IST. 26

3.2 a) View from downstream of the vegetated reach and b) lateral view of the coarse weir, at IST flume. 27

3.3 a) Upstream part and b) the vegetated reach of the flume at LWI. 27

3.4 Traverse system used at LWI for positioning the LDA probes. 28

3.5 a) Scheme of the longitudinal profile of the flumes during the experiments; b) detail of the stem mounting; c) picture of stems and bed during the tests; and d) an view of IST's flume from upstream. 29

3.6 Apparatus for the introduction of seeding particles in the flow a) at IST and b) at LWI. 30

3.7 a) PIV laser head; b) digital thermometer; c) laser displacement sensor; d) ruler used to measure free-surface levels with video images; e) uEye camera used to measure free-surface levels and f) probes during LDA velocity measurements. . 31

3.8 Schematic representation of PIV components. 34

3.9 Photos of PIV components: a) laser head; b) laser beam generator; c) CCD camera; d) timer box and e) DynamicStudio software. 35

3.10 a) Scheme of a double cavity laser head (from Raffel *et al.*, 2007, p. 40); b) Picture of the double cavity laser head o the PIV system used in this work. . . . 36

3.11 Ratio r_p as function of the frequency f_c for the solid targets used in the present experimental work. 39

3.12 The polar distribution of the scattered light intensity for glass particles of diameter a) $d_p = 1\ \mu$m, b) $d_p = 10\ \mu$m and c) $d_p = 30\ \mu$m with incident light of wavelength $\lambda = 532$ nm, according to Mie's theory (from Raffel *et al.*, 2007, p. 20). 40

3.13 a) Division into interrogation areas (IA) of an image acquired with PIV; b) Illustration of the displacement of particles inside of an interrogation area, where the open circles correspond to the position of the filled circles Δt s later. 41

3.14 Examples of an IA in both frames and the respective correlation map. a) Case with a clear correlation peak corresponding to the particle's displacement; b) case with out-of-plane loss-of-pairs problem, where it is not possible to distinguish the peak of particle's displacement from the noise peaks. 42

3.15 Time-averaged longitudinal velocity profiles of a lateral position acquired with time between pulses of a)1250 μs, b)1500 μs and c) 1750 μs. 45

3.16 Time-averaged Reynolds shear stress profiles of a lateral position acquired with time between pulses of a)1250 μs, b)1500 μs and c) 1750 μs. 45

3.17 General layout of a backscatter LDA system (source: `http://www.dantecdynamics.com/measurement-principles-of-lda`). 47

3.18 Scheme of a LDA system in a) forward scatter mode and b) back scatter mode. 48

3.19 a) The laser generator, b) the probes and the acrylic case and c) the laser light beams during the experiments at LWI. 49

3.20 Fringe model (Source: Ferreira, 2011). 49

3.21 Crossing of laser beams: a) correct crossing with parallel fringe pattern; b) incorrect crossing due to lens aberration (Source: Ferreira, 2011). 51

3.22 Plan view of test S1. The solid lines aligned with flow direction indicate the location of the vertical plans measured with PIV. The rectangles point out the regions where horizontal velocity maps were acquired. The blue arrow indicates the flow direction. 53

3.23 Pictures of the flume during test S1: a) lateral view and b) plan view. 53

3.24 Plan view of test S2. The solid lines aligned with flow direction indicate the location of the vertical plans measured with PIV. The rectangles point out the regions where horizontal velocity maps were acquired. The blue arrow indicates the flow direction. The points along lines perpendicular to the flow direction represent the location of LDA measurements (P3 to P8). 55

3.25 Pictures of the flume during test S2 at IST: a) lateral view and b) plan view. . . 56

3.26 Plan view of test S3. The solid lines aligned with flow direction indicate the location of the vertical plans measured with PIV. The rectangles point out the regions where horizontal velocity maps were acquired. The blue arrow indicates the flow direction. 58

3.27 Pictures of the flume during test S3: a) lateral view and b) perspective 58

3.28 Longitudinal profiles of bed elevation of test S1 at a) $y = 0.100$ m, b) $y = 0.204$ m and c) $y = 0.333$ m. The red lines represent the averaged value of each series. . 61

3.29 Longitudinal profiles of bed elevation of test S2 at a) $y = 0.164$ m, b) $y = 0.204$ m and c) $y = 0.244$ m. The red lines represent the averaged value of each series. . 62

3.30 Oscillations of the free-surface at points a) $x = 7.25$ m and $y = 0.275$ m, and b) $x = 8.30$ m and $y = 0.204$ m, in test S1. 63

3.31 Oscillations of the free-surface at the point $x = 7.446$ m and $y = 0.204$ m in the measuring gap P7 of test S2. 63

3.32 Oscillations of the free-surface at the point $x = 7.192$ m and $y = 0.214$ m in the measuring gap P5 of test S2. 64

3.33 Oscillations of the free-surface at points a) $x = 7.90$ m and $y = 0.302$ m, and b) $x = 8.90$ m and $y = 0.217$ m, in test S3. 64

3.34 Longitudinal profiles of free-surface and bed elevation of tests a) S1, b) S2 and c) S3. 65

3.35 Vertical distribution of the volumetric fluid fractions for a) test S1, b) measuring gaps on the first wavelength of the stem distribution of test S2, c) measuring gaps on the second wavelength of the stem distribution of test S2 and d) test S3. . . . 66

3.36 PVC sheet used to calculate the calibration factor to convert velocity maps in image units (px/s) into metric units (m/s). 66

3.37 Instantaneous longitudinal velocity, u, maps at measuring gap P7 of test S2 at a) $y = 0.214$ m, b) $y = 0.224$ m and c) $y = 0.234$ m. Units of velocity colormaps are m/s. 67

3.38 Instantaneous vertical velocity, w, maps at measuring gap P7 of test S2 at a) $y = 0.214$ m, b) $y = 0.224$ m and c) $y = 0.234$ m. Units of velocity colormaps are m/s. 67

3.39 Time-averaged velocity maps at measuring gap P7 of test S2 at a) $y = 0.214$ m, b) $y = 0.224$ m and c) $y = 0.234$ m. The colormap represents the velocity magnitude, $\left(\bar{u}^2 + \bar{w}^2\right)^{1/2}$. Units of velocity colormaps are m/s. The arrow at the graphs bottom is the scale of the vector plot and it corresponds to 0.2 m/s. . . . 68

3.40 Time-averaged Reynolds shear stress $\left(-\rho\overline{u'w'}\right)$ maps at measuring gap P7 of test S2 at a) $y = 0.214$ m, b) $y = 0.224$ m and c) $y = 0.234$ m. Units of stress colormaps are Pa. 68

3.41 Longitudinal turbulent intensity $\left(\overline{u'u'}^{1/2}\right)$ maps at measuring gap P7 of test S2 at a) $y = 0.214$ m, b) $y = 0.224$ m and c) $y = 0.234$ m. Units of colormaps are m/s. 69

3.42 Vertical turbulent intensity $\left(\overline{w'w'}^{1/2}\right)$ maps at measuring gap P7 of test S2 at a) $y = 0.214$ m, b) $y = 0.224$ m and c) $y = 0.234$ m. Units of colormaps are m/s. . 69

3.43 Time-averaged velocity maps at the measuring gaps of test S2. Units of colormaps are m/s. 71

3.44 Time-averaged vorticity maps at the measuring gaps of test S2. Units of colormaps are s^{-1}. 72

4.1 Plan view of the stem covered reach where the measurements were carried out for each test: a) test S1; b) test S2 and c) test S3. The solid lines aligned with flow direction indicate the location of the vertical plans measured with PIV. . . 80

4.2 a) Double-averaged profiles of normal longitudinal form-induced stresses for identification of the flow layer controlled by the stems. The data presented correspond to test S2. b) Vertical profiles of void function, $\psi(x,z)$. The vertical axis is normalized by the flow depth, h. 83

4.3 a) Double-averaged longitudinal velocity profiles. b) Double-averaged vertical velocity profiles. 86

4.4 Double-averaged shear stresses: a) Reynolds; b) form-induced. 87

4.5 Double-averaged normal longitudinal stresses: a) Reynolds; b) form-induced. . 87

4.6 Double-averaged normal vertical stresses: a) Reynolds; b) form-induced. . . . 88

4.7 a) Drag force F_D calculated by Eq. (4.11) against the simplification F_D^* expressed by Eq. (4.13); b) the ratio F_D/F_D^* as a function of m. 90

4.8 Drag force per unit of length of submerged stem, F_D against the stem areal number-density, m. 91

4.9 Drag coefficient as function of stem Reynolds number $Re_p = Ud\rho/\mu$. 92

4.10 Drag coefficient as function of s/d. 93

4.11 C_D against Re_p. The solid curves are the results presented by Tanino and Nepf (2008) for $\phi = 0.091, 0.15, 0.20, 0.27$ and 0.35, the dashed line represents the variation of C_D with Re_p for a smooth isolated cylinder. The markers correspond to the results of the present study from tests S1 and S3. The solid markers represent the C_D computed with F_D calculated by Eq. (4.11) while the open markers with F_D^* expressed by Eq. (4.13). 94

4.12 Drag coefficient as function of h/d. 94

5.1 Plan view of the stem covered reach where the measurements were carried out. Dashed rectangles point out the regions where horizontal velocity maps (PIV) were acquired for each longitudinal position, P1 to P8. The solid lines aligned with flow direction indicate the location of the vertical plans measured with PIV. The points along lines perpendicular to the flow direction represent the location of LDA measurements (P3 to P8). 101

5.2 Comparison of $-\overline{u'v'}\partial\overline{u}/\partial y$ component of the turbulent production of TKE, computed from PIV and LDA databases for a) P7 and b) P5. Vertical dotted lines identify the y-coordinate of centres of stems close to the upstream limit of the measuring gap (see Appendix C for extra figures). 104

5.3 Comparison of $-\overline{v'v'}\partial\overline{v}/\partial y$ component of the turbulent production of TKE, computed from PIV and LDA databases for a) P6 and b) P8. Vertical dotted lines identify the y-coordinate of centres of stems close to the upstream limit of the measuring gap (see Appendix C for extra figures). 104

5.4 Correlation-coefficient spectra at a) $y = 0.215$ m for P5 and b) $y = 0.195$ m for P7. Computed from the LDA database. 106

5.5 a) Third-order structure function $S_{LL}^{(3)}$ and b) second-order structure function $S_{LL}^{(2)}$, for two longitudinal positions, P3 (at $y = 0.180$ m) and P8 (at $y = 0.165$ m). . . 107

5.6 Examples of $S_{LL}^{(3)} - 6\nu\partial S_{LL}^{(2)}(r)/\partial r$ for a point in P3 ($y = 0.180$ m) and a point in P8 ($y = 0.165$ m). Dotted lines highlight the linear reach with slope $-4/5\bar{\varepsilon}$. . . 107

5.7 Contributions of the a) convective term, b) turbulent production and c) turbulent diffusion of TKE equation for P8 at $y = 24.4$ cm. Open markers represent terms from horizontal database while filled markers are computed with the vertical database. Asterisks represent the sum of the 7 contributions. 109

5.8 a) Reynolds shear stresses $-\rho\overline{u'v'}$ and $-\rho\overline{v'w'}$ for P8. b) Lateral gradients of time averaged velocity components for P5. Both results are computed from LDA database. Vertical dotted lines identify the y-coordinate of centres of stems close to the upstream limit of the measuring gap. 110

5.9 Two-dimensional maps of turbulent production, $-\overline{u_i'u_j'}\partial\bar{u}_i/\partial x_j$, $\left(\mathrm{m^2s^{-3}}\right)$ for positions a) P7 and b) P8. Dots aligned horizontally identify the position of LDA measurements. The arrow indicates the flow direction (see Appendix C for extra figures). 111

5.10 Two-dimensional maps of the convective term, $1/2\bar{u}_j\partial\overline{u_i'u_i'}/\partial x_j$, $\left(\mathrm{m^2s^{-3}}\right)$ for positions a) P7 and b) P8. Dots aligned horizontally identify the position of LDA measurements. The arrow indicates the flow direction (see Appendix C for extra figures). 112

5.11 Two-dimensional maps of turbulent diffusion, $1/2\partial\overline{u_i'u_i'u_j'}/\partial x_j$, $\left(\mathrm{m^2s^{-3}}\right)$ for positions a) P7 and b) P8. Dots aligned horizontally identify the position of LDA measurements. The arrow indicates the flow direction (see Appendix C for extra figures). 114

5.12 Lateral profiles of the terms of TKE budget equation for longitudinal positions a) P3 and b) P7. Vertical dotted lines identify the y-coordinate of centres of stems close to the upstream limit of the measuring reach (see Appendix C for extra figures). 115

5.13 Lateral profiles of the terms of TKE budget equation for longitudinal positions a) P5 and b) P8. Vertical dotted lines identify the y-coordinate of centres of stems close to the upstream limit of the measuring reach (see Appendix C for extra figures). 116

5.14 Term IV, $\frac{1}{\rho}\frac{\partial\overline{p'u_j'}}{\partial x_j}$, of TKE equation for two longitudinal positions, P7 and P8. Vertical solid and dotted lines identify the y-coordinate of centres of stems close to the downstream limit of the measuring gap of P7 and P8, respectively. 117

5.15 Two-dimensional maps of $1/2\left(\overline{u'u'}+\overline{v'v'}\right)$ overlapped by a vector plot of the flux of TKE, for positions a) P7 and b) P8. The colorbar units are $\mathrm{m^2s^{-2}}$. The arrow on the left upper corner indicates the flow direction while the arrow on the bottom indicates the scale of the vector plot (see Appendix C for extra figures). 119

7.1 Plan view of part of the stem covered reach. Dashed rectangles depict the regions where the horizontal maps of velocity were measured for each patch, from P1 to P8. For each measuring gap a local referential is considered. 137

7.2 a) Example of an instantaneous velocity map at P5. b) Instantaneous and spatial longitudinal velocity series. 139

7.3 Time-averaged velocity maps (left) and time-averaged vorticity maps (right) at $z^{(a)}$ for each longitudinal position (P1 to P8, from the top to the bottom). 140

7.4 Longitudinal autocorrelation function for a) P3 and b) P5, at 4 different cross sections for a lateral position at height $z^{(a)}$. 142

7.5 Transverse autocorrelation function for a) P3 and b) P5, at 4 different cross sections for a lateral position at height $z^{(a)}$. 142

7.6 a) Double-averaged transverse autocorrelation function for a lateral position at height $z^{(a)}$. b) Mean macro-scale for each longitudinal and vertical positions. . 143

7.7 Dimensionless third order longitudinal structure function, $\langle S_3 \rangle$, for a lateral position at height $z^{(a)}$ for a) P7 and b) P5. 146

7.8 Dimensionless second order longitudinal structure function,$\langle S_{2L} \rangle$, for a lateral position at height $z^{(a)}$ for a) P3 and b) P5. The black dotted line with $+$-marker represents the relation given by (7.10a) for the upstream cross section. 147

7.9 Dimensionless spatial transverse spectra for a lateral position at height $z^{(b)}$ for patches a) P3 and b) P1. 148

7.10 Correlation-coefficient spectra a lateral position at height $z^{(a)}$ for a) P7 and b) P5. 149

7.11 Dissipation rate of kinetic energy along streamwise direction for several datasets: a) P3 for $y = 0.29 - 0.41$ cm at $z^{(b)}$, b) P5 for $y = 0.10 - 0.22$ cm at $z^{(b)}$, c) P6 for $y = 0.0.09 - 0.21$ cm at $z^{(a)}$ and d) P8 for $y = 0.23 - 0.35$ cm at $z^{(a)}$. The dashed rectangles indicate the measurement reach while the circles represent the cylinders. It should be noticed that plan views represented in these graphs preserve the geometrical scale indicated by the x-axis. 150

7.12 a) Measured and estimated mean dissipation rate, $\langle \overline{\varepsilon} \rangle_l$, for each longitudinal position. The dashed line at the bottom stand for relative stem density; b) Mean dissipation rate, $\langle \overline{\varepsilon} \rangle_l$, against the Taylor's micro scale based Reynolds number, $Re_{\lambda N}$. 151

7.13 a) Mean dissipation rate $\langle\overline{\varepsilon}\rangle_x$ against the macro scale based Reynolds number, Re_Λ, for each lateral position. b) Mean dissipation rate $\langle\overline{\varepsilon}\rangle_l$ against the macro scale based Reynolds number, Re_Λ, average of all lateral position for each longitudinal and vertical positions. The numbers indicate the corresponding longitudinal position. 152

A.1 Schematic view of the flume. 173

A.2 Plan view of working reach. The measuring region is the dot-dashed rectangle in horizontal plane and dashed lines in vertical plane). Point 1 and 2 are sample points that will be refereed latter for spectral analysis. 173

A.3 Maps of time-average velocity fluctuations (cm/s) measured in the horizontal planes at level: a) $z = 0.95$ cm and b) $z = 1.95$ cm. Circles stand for placement of the sample points of optimal solution and triangles of the uniform solution (section 5). 174

A.4 Mean vorticity fields (s^{-1}). (Remaining caption as in Figure A.3) 175

A.5 Instantaneous fluctuation velocity quiver and streamlines in a a) event of upward velocity and b) event of downward velocity. 175

A.6 Log-log plot of the power spectra of the flow at 1.95 cm above the bed in a) point 1 and b) point 2 (see Figure A.2). The continuous line is a moving average of the periodogram (dot-dashed line). 176

A.7 Plot of part of the objective function. 177

A.8 Frequency distribution of the a) velocity map at level $z = 1.95$ cm b) and its best fit with only 8 points. 177

A.9 a) Double-average longitudinal velocity profiles resulting of a DAM with the best set of 8 points (circles), a DAM presented in Ricardo (2008) (diamonds) and the integration on horizontal planes (asterisks). b) Velocity profile resulting of a uniform placement of the sample points (circles) compared with optimal solution (diamonds). 178

A.10 a) Longitudinal velocity map (cm/s) and placement of the sample points of the simpler solution (squares). b) Velocity profile resulting of a placement of the sample points with a simpler criterion (circles) compared with the best solution of placement algorithm (diamonds). 178

B.1 Dimensionless spatial transverse spectra for the lateral position between $y = 0.10$ m and $y = 0.22$ m at height $z^{(b)}$, for the measuring gaps P1 to P4 of test S2. Vertical lines indicate scales of interest: dotted – average macro scale of P3 and P7; solid – average macro scale of P2 and P6, and P4 and P8; dashed – average macro scale of P1 and P5; thicker dot-dashed – $k\Lambda_i = 1$; thinner dot-dashed – stem diameter. 182

B.2 Dimensionless spatial transverse spectra for the lateral position between $y = 0.10$ m and $y = 0.22$ m at height $z^{(b)}$, for the measuring gaps P5 to P8 of test S2 (*cf.* Fig. B.1 for meaning of vertical lines). 183

B.3 Dimensionless spatial transverse spectra for the lateral position between $y = 0.18$ m and $y = 0.30$ m at height $z^{(b)}$, for the measuring gaps P1 and P4 of test S2 (*cf.* Fig. B.1 for meaning of vertical lines). 184

B.4 Dimensionless spatial transverse spectra for the lateral position between $y = 0.18$ m and $y = 0.30$ m at height $z^{(b)}$, for the measuring gaps P5 to P8 of test S2 (*cf.* Fig. B.1 for meaning of vertical lines). 185

B.5 Dimensionless spatial longitudinal spectra for the lateral position between $y =$ 0.10 m and $y = 0.22$ m at height $z^{(b)}$, for the measuring gaps P1 to P4 of test S2 (*cf.* Fig. B.1 for meaning of vertical lines). 186

B.6 Dimensionless spatial longitudinal spectra for the lateral position between $y =$ 0.10 m and $y = 0.22$ m at height $z^{(b)}$, for the measuring gaps P5 to P8 of test S2 (*cf.* Fig. B.1 for meaning of vertical lines). 187

B.7 Dimensionless spatial longitudinal spectra for the lateral position between $y =$ 0.18 m and $y = 0.30$ m at height $z^{(b)}$, for the measuring gaps P1 to P4 of test S2 (*cf.* Fig. B.1 for meaning of vertical lines). 188

B.8 Dimensionless spatial longitudinal spectra for the lateral position between $y =$ 0.18 m and $y = 0.30$ m at height $z^{(b)}$, for the measuring gaps P5 to P8 of test S2 (*cf.* Fig. B.1 for meaning of vertical lines). 189

C.1 Comparison of $-\overline{u'v'}\partial\overline{u}/\partial y$ component of the turbulent production of TKE, computed from PIV and LDA databases for measuring gaps P3 to P8. Vertical dotted lines identify the y-coordinate of centres of stems close to the upstream limit of the measuring gap. 192

C.2 Comparison of $-\overline{v'v'}\partial\overline{v}/\partial y$ component of the turbulent production of TKE, computed from PIV and LDA databases for measuring gaps P3 to P8. 193

C.3 Two-dimensional maps of turbulent production, $-\overline{u_i'u_j'}\partial\bar{u}_i/\partial x_j$, $\left(\mathrm{m^2s^{-3}}\right)$ for measuring gaps P1 to P4. Dots aligned horizontally identify the position of LDA measurements. 194

C.4 Two-dimensional maps of turbulent production, $-\overline{u_i'u_j'}\partial\bar{u}_i/\partial x_j$, $\left(\mathrm{m^2s^{-3}}\right)$ for measuring gaps P5 to P8. Dots aligned horizontally identify the position of LDA measurements. 195

C.5 Two-dimensional maps of the convective term, $1/2\bar{u}_j\partial\overline{u_i'u_i'}/\partial x_j$, $\left(\mathrm{m^2s^{-3}}\right)$ for measuring gaps P1 to P4. Dots aligned horizontally identify the position of LDA measurements. 196

C.6 Two-dimensional maps of the convective term, $1/2\bar{u}_j\partial\overline{u_i'u_i'}/\partial x_j$, $\left(\mathrm{m^2s^{-3}}\right)$ for measuring gaps P5 to P8. Dots aligned horizontally identify the position of LDA measurements. 197

C.7 Two-dimensional maps of turbulent diffusion, $1/2\partial\overline{u_i'u_i'u_j'}/\partial x_j$, $\left(\mathrm{m^2s^{-3}}\right)$ for measuring gaps P1 to P4. Dots aligned horizontally identify the position of LDA measurements. 198

C.8 Two-dimensional maps of turbulent diffusion, $1/2\partial\overline{u_i'u_i'u_j'}/\partial x_j$, $\left(\mathrm{m^2s^{-3}}\right)$ for measuring gaps P5 to P8. Dots aligned horizontally identify the position of LDA measurements. 199

C.9 Lateral profiles of the terms of TKE budget equation for measuring gaps P3 to P5. 200

C.10 Lateral profiles of the terms of TKE budget equation for measuring gaps P6 to P8. 201

C.11 Two-dimensional maps of $1/2\left(\overline{u'u'}+\overline{v'v'}\right)$ overlapped by a vector plot of the flux of TKE, for measuring gaps P1 to P4. The colorbar units are $\mathrm{m^2s^{-2}}$. . . . 202

C.12 Two-dimensional maps of $1/2\left(\overline{u'u'}+\overline{v'v'}\right)$ overlapped by a vector plot of the flux of TKE, for measuring gaps P1 to P4. The colorbar units are $\mathrm{m^2s^{-2}}$. . . . 203

C.13 Two-dimensional maps of $1/2\left(\overline{u'u'}+\overline{v'v'}\right)$ overlapped by a vector plot of the flux of TKE, for measuring gaps P5 to P8. The colorbar units are $\mathrm{m^2s^{-2}}$. . . . 204

C.14 Two-dimensional maps of $1/2\left(\overline{u'u'}+\overline{v'v'}\right)$ overlapped by a vector plot of the flux of TKE, for measuring gaps P5 to P8. The colorbar units are $\mathrm{m^2s^{-2}}$. . . . 205

List of Tables

3.1 Features of the experimental measurements and flow properties for test S1. . . . 54

3.2 Features of the experimental measurements and flow properties for test S2 at IST. 57

3.3 Features of the experimental measurements and flow properties for test S2 at LWI. 57

3.4 Features of the experimental measurements and flow properties for test S3. . . . 59

4.1 Features of the experimental measurements and flow properties for each test. . 81

4.2 Values of F_D, C_D and F_D^* for each patch. 89

5.1 Features of the experimental measurements and flow properties for each longitudinal position. 103

7.1 Features of the experimental tests and flow properties for each longitudinal position. 138

7.2 Taylor's micro scales and Reynolds numbers based on the micro and macro scales of the flow. 144

List of Symbols

Symbol	Description	Dimension
A_f	Area occupied by fluid	$[\mathrm{L}^2]$
A_T	Total area	$[\mathrm{L}^2]$
B_{LL}	Longitudinal autocorrelation function	$[\mathrm{L}^2\mathrm{T}^{-2}]$
B_{NN}	Transverse autocorrelation function	[-]
C_D	Drag coefficient of the array of stems	[-]
C_{LN}	Correlation-coefficient spectra	[-]
d	Stem diameter	[L]
d_p	Seeding particles diameter	[L]
d_s	Median diameter of the gravel bed	[L]
E_L	Longitudinal one-dimensional energy spectrum	$[\mathrm{L}^3\mathrm{T}^{-2}]$
E_N	Transverse one-dimensional energy spectrum	$[\mathrm{L}^3\mathrm{T}^{-2}]$
Fr	Froude number	[-]
$\left\langle \bar{f}_x^{(s)} \right\rangle$	Force exerted on the stems per unit of plan area	$[\mathrm{ML}^{-1}\mathrm{T}^{-2}]$
F_D	Drag force per unit of submerged stem length	$[\mathrm{MT}^{-2}]$
F_D^*	Simplification of the drag force per unit of submerged stem length	$[\mathrm{MT}^{-2}]$
f	Frequency	$[\mathrm{T}^{-1}]$
f_c	Cut off frequency	$[\mathrm{T}^{-1}]$
g	Gravitational acceleration	$[\mathrm{LT}^{-2}]$
g_i	i^{it} component of gravitational acceleration	$[\mathrm{LT}^{-2}]$
h	Mean flow depth	[L]
$\langle \bar{h} \rangle$	Mean flow depth	[L]
H	Depth of the water column where the flow is controlled by the stems	[L]
k	Wavenumber	$[\mathrm{L}^{-1}]$
k_d	Roughness of the stems	[L]
l	Length scale	[L]
l_0	Integral length scale	[L]

Symbol	Description	Dimension
m	Stem areal number-density	$\left[\mathrm{L}^{-2}\right]$
n_i	i^{it} component of the unit normal vector directed from the solid into the fluid	[-]
p	Local pressure	$\left[\mathrm{ML}^{-1}\mathrm{T}^{-2}\right]$
$\langle\bar{p}\rangle$	Double-averaged pressure	$\left[\mathrm{ML}^{-1}\mathrm{T}^{-2}\right]$
p'	Time fluctuation of the pressure field	$\left[\mathrm{ML}^{-1}\mathrm{T}^{-2}\right]$
$\bar{p}$	Time-averaged pressure	$\left[\mathrm{ML}^{-1}\mathrm{T}^{-2}\right]$
$\tilde{p} \equiv \overline{\tilde{p}}$	Space fluctuation of the time-averaged pressure field	$\left[\mathrm{ML}^{-1}\mathrm{T}^{-2}\right]$
Q	Discharge	$\left[\mathrm{L}^{3}\mathrm{T}^{-1}\right]$
R_L	Longitudinal autocorrelation function	[-]
R_N	Transverse autocorrelation function	[-]
Re	Reynolds number	[-]
Re_p	Stem Reynolds number	[-]
Re_Λ	Reynolds number based on the macro scale	[-]
Re_λ	Reynolds number based on the Taylo's micro scale	[-]
r_p	Ratio to evaluate the ability of a given seeding to follow a given flow	[-]
r	Space lag	[L]
S_{int}	Solid-fluid interface surface	$\left[\mathrm{L}^{2}\right]$
S_{2L}	Longitudinal second-order structure function	$\left[\mathrm{L}^{2}\mathrm{T}^{-2}\right]$
$S_{LL}^{(2)}$	Longitudinal second-order structure function	$\left[\mathrm{L}^{2}\mathrm{T}^{-2}\right]$
S_{2N}	Transverse second-order structure function	$\left[\mathrm{L}^{2}\mathrm{T}^{-2}\right]$
S_{3L}	Longitudinal third-order structure function	$\left[\mathrm{L}^{2}\mathrm{T}^{-2}\right]$
$S_{LL}^{(3)}$	Longitudinal third-order structure function	$\left[\mathrm{L}^{2}\mathrm{T}^{-2}\right]$
S_t	Strouhal number	[-]
s	Mean inter-stem distance	[L]
$s^{(p)}$	Seeding particles density	[-]
$s^{(w)}$	Water density	[-]
s_{ij}	Symmetric part of turbulent strain tensor	$\left[\mathrm{T}^{-1}\right]$
t	Time	[T]
T	Temperature	
u	Longitudinal velocity component	$\left[\mathrm{LT}^{-1}\right]$
u_i	i^{it} component of the velocity field	$\left[\mathrm{LT}^{-1}\right]$
$u_i^{(I)}$	i^{it} component of the velocity vector of the solid-fluid interface	$\left[\mathrm{LT}^{-1}\right]$
$\bar{u}$	Time-averaged longitudinal velocity	$\left[\mathrm{LT}^{-1}\right]$
u'	Turbulent fluctuations of longitudinal velocity	$\left[\mathrm{LT}^{-1}\right]$

Symbol	Description	Dimension
$\tilde{u}$	Space fluctuation of longitudinal velocity	$[LT^{-1}]$
$\langle\bar{u}\rangle$	Double-averaged longitudinal velocity	$[LT^{-1}]$
u_L	Projection of the velocity vector on the direction of r	$[LT^{-1}]$
u_N	Projection of the velocity vector on any perpendicular direction of r	$[LT^{-1}]$
U	Depth averaged of the double-averaged longitudinal velocity profile	$[LT^{-1}]$
V_p	Modulus of seeding terminal fall velocity	$[LT^{-1}]$
V	Modulus of flow velocity	$[LT^{-1}]$
v	Spanwise velocity component	$[LT^{-1}]$
$\bar{v}$	Time-averaged spanwise velocity	$[LT^{-1}]$
v'	Turbulent fluctuations of spanwise velocity	$[LT^{-1}]$
$\tilde{v}$	Space fluctuation of spanwise velocity	$[LT^{-1}]$
$\langle\bar{v}\rangle$	Double-averaged spanwise velocity	$[LT^{-1}]$
w	Vertical velocity component	$[LT^{-1}]$
$\bar{w}$	Time-averaged vertical velocity	$[LT^{-1}]$
w'	Turbulent fluctuations of vertical velocity	$[LT^{-1}]$
$\tilde{w}$	Space fluctuation of vertical velocity	$[LT^{-1}]$
$\langle\bar{w}\rangle$	Double-averaged vertical velocity	$[LT^{-1}]$
x	Streamwise coordinate	[L]
y	Spanwise coordinate	[L]
z	Vertical coordinate	[L]
z_{fs}	Free surface elevation	[L]
z_{bed}	Bed elevation	[L]
$\forall_f$	Volume occupied by fluid in the control volume	$[L^3]$
$\forall_T$	Total control volume	$[L^3]$
$\varkappa(x,z)$	Deviation to the hydrostatic pressure distribution	$[L^2T^{-2}]$
β	Flume's slope	[-]
Δt	Time between pulses	[T]
δ	Distance between fringes	[L]
δ_{ij}	Kronecker's delta	[-]
$\bar{\varepsilon}$	Time-averaged dissipation rate of TKE	$[L^2T^{-3}]$
$\langle\varepsilon\rangle$	Mean dissipation rate of TKE	$[L^2T^{-3}]$
η	Kolmogorov's length scale	[L]
θ	Angle between beans	[-]
λ	Light wavelength	[L]

Symbol	Description	Dimension
λ_L	Longitudinal Taylo's micro scale	[L]
λ_N	Transverse Taylo's micro scale	[L]
μ	Dynamic viscosity	$\left[\mathrm{ML^{-2}T^{-1}}\right]$
ν	Kinematic viscosity	$\left[\mathrm{L^{2}T^{-1}}\right]$
ρ	Fluid volumetric mass density	$\left[\mathrm{ML^{-3}}\right]$
$-\rho\tilde{u}\tilde{w}$	Form-induced shear stress	$\left[\mathrm{ML^{-1}T^{-2}}\right]$
$-\rho\overline{u'w'}$	Reynolds shear stress	$\left[\mathrm{ML^{-1}T^{-2}}\right]$
σ_{ij}	Stress tensor	$\left[\mathrm{ML^{-1}T^{-2}}\right]$
ψ	Volumetric fluid fraction	[-]
ϕ	Volumetric solid fraction	[-]
Ω	Measuring domain	$[-]$

List of Acronyms

Acronym	Description
AI	Interrogation area
CCD	Charge-couple device
CMOS	Complementary metal oxide semi-conductor
CRIV	Recirculating tilting flume
DAM	Double-Averaging Methodology
DA	Double-Averaged
DANS	Double-Average Navier Stokes equations
EPFL	Ecole Polytechnique Fédérale de Lausanne
FCT	Portuguese Foundation for Science and Technology
HIT	Homogeneous and isotropic turbulence
IST	Instituto Superior Técnico
LCH	Laboratory of Hydraulic Constructions
LDA	Laser Doppler Anemometry
LWI	Leichtweiß Institute for Hydraulic Engineering
PIV	Particle image velocimetry
PVC	Polyvinyl chloride
RANS	Reynolds-Averaged Navier-Stokes equations
SATKE	Space-averaged urbulent kinetic energy equation
TKE	Turbulent kinetic energy
YAG	Yittrium Aluminium Garnet

Chapter 1

Introduction

1.1 Framework

Emergent vegetation, featuring a wide range of different species and with different ecological roles, plays an ubiquitous role in coastal and riverine systems. Such systems, herein designated wetlands, are characterized by a profound interaction of physical, biological and ecological processes, and by relevant transport processes (Ferreira *et al.*, 2010; Ghisalberti & Nepf, 2004; Tanino & Nepf, 2008). Vegetation influences geomorphologic processes, affects the fluxes of sediment, nutrients and contaminants, promotes water quality, maintains biodiversity and improves landscape integrity. On the other hand, the existence of vegetation in a stream is associated to a higher flow resistance, and hence greater flood risk (Kadlec, 1990).

The characterization of flows within wetlands is thus a relevant topic for river engineering, but the difficulties arising, mostly associated to fluid-stem interaction, are, simultaneously, highly challenging fluid mechanics problems. The present research is motivated by the former but its methods and language pertains essentially to fluid mechanics. To avoid a conflict between applications and methods that could unfocus this work, they should be clearly stated.

Ultimately, the realm of the application of the present research is fluvial and estuarine management, as its results are relevant to increase the knowledge of the physics of water bodies populated with aquatic vegetation. Within the framework of the EU water directive, this physical knowledge is fundamental to devise strategies to improve and maintain the quality of water bodies in its biological, ecological and societal dimensions.

The research methods pertain to fluid mechanics in two fundamental aspects regarding the compromise between physical verisimilitude and experimental feasibility and the scale of work. In the first case, the option favoured in this thesis was to perform laboratory work in idealised controlled conditions procuring unambiguous data interpretation. Hence, emergent

rigid cylindrical stems are employed as a proxy for natural stems. The stems are slightly rough and are randomly placed as an effort to increase verisimilitude.

Concerning the length scales that characterize the flow within vegetation, one can generally consider four main scales:

i. the stem scale, defined by the stem's diameter;
ii. the inter-stem scale, an intermediate scale corresponding to the mean distance between the axis of neighbouring plant stems;
iii. the patch scale, the distance representative of a domain where stem properties and stem areal distributions are homogeneous;
iv. the reach scale, encompassing several vegetation patches, for instance a river reach or a laboratory channel with non-homogeneous stem distribution.

In this thesis, the emphasis is placed on the characterization and quantification of flows at the intermediate inter-stem (ii) and patch (iii) scales.

A great amount of research has been developed at these intermediate scales. Some of the key works during the last decades included laboratory experiments with arrays of flexible (Dittrich *et al.*, 2012; Fathi-Maghadam & Kouwen, 1997; James *et al.*, 2008; Järvelä, 2002; Nepf & Vivoni, 1999) or rigid stems (Ferreira *et al.*, 2009b; Li & Shen, 1973; Nepf, 1999; Stone & Shen, 2002; Tanino & Nepf, 2008; White & Nepf, 2008). Theoretical works can also be found in the literature (Cheng, 2013; Lee *et al.*, 2004; Maheshwari, 1992; Yen, 2002) where models and respective application domains are presented, as well as, in the computational realm, there is an increasing number of numerical databases for flows within vegetation reaches (Coceal *et al.*, 2007; Defina & Bixio, 2005; Kim & Stoesser, 2011; López & García, 1998, 2001; Stoesser *et al.*, 2010).

The characterization of drag forces on vegetation elements has important applications in civil engineering, namely in the estimation of hydraulic resistance for design of fluvial channels or flood forecasting (Kadlec, 1990; López & García, 1998). The vegetation drag coefficient, C_D, empirically derived and a function of the fluid, flow and vegetation properties, is thus of great importance to river engineers who seek for practical models to evaluate the flow resistance and as an input to numerical hydrodynamic models. However, most of existing criteria for channels protected with vegetation and simulation models employ resistance formulas such as Manning's and Chezy's, necessarily calibrated *ad hoc*.

Moving towards physically-based design criteria, progresses have been made in the characterization of 3D flows over irregular boundaries and over canopies, mainly due to the application of the Double-Averaging Methodology (DAM), which is a particular form of upscaling in the spatial and temporal sense (Finnigan, 2000; Gimenez-Curto & Corniero Lera, 1996; Nikora *et al.*, 2001, 2007a; Raupach *et al.*, 1986). Such methods are especially pertinent for the characterization of the flow within and in the near vicinity of plant canopies, due to the spatial heterogeneity that characterizes this type of flow.

The flow in the inter-stem space is turbulent provided that the areal distribution of stems is not too dense (quantitative criteria in Sumner *et al.*, 2005). Vortex shedding from individual stems is the main source of turbulent kinetic energy (TKE). The spatial distribution of flow variables is complex. The velocity field is nonhomogeneous, being mostly determined by the interaction of vortexes shed by individual stems (Sumner *et al.*, 2005). The spatial characterization and quantification of the terms of TKE conservation equation may allow progresses on the understanding of the nature of turbulence generated in these conditions. In particular, the turbulence at the inter-stem space has to be known in detail in order to attempt closures for time- or double-averaged (in time and space) conservation equations (Raupach & Thom, 1981).

The characterization and quantification of the rate of dissipation of TKE in flows within arrays of stems is also a major research need, since it is a fundamental variable for the parametrization of the unclosed terms. To this date, there is no general formulation relating the amount of energy loss to the areal number-density of plant stems and the global Reynolds number. The existing methods of calculation of the mean (time- and space-averaged) rate of dissipation of TKE may be unreliable since they incorporate major simplifications (Finnigan, 2000). The point-wise time-averaged rate of dissipation of TKE can be easily calculated for homogeneous and isotropic turbulence (HIT), within Kolmogorov's theoretical framework, requiring only a spectral description of the fluctuating motion or the computation of structure functions. If turbulence is not homogeneous, as is the case of the flow in the inter-stem space, there are several competing theories expressing the dissipation tensor (e.g. Moser, 1994; Nazarenko *et al.*, 1999; Oberlack, 1997; Perot & Natu, 2004) but which are not analytically tractable.

A thorough review of previous work focusing on the aforementioned intermediate scales, inter-stem and patch scales, led to the identification of the following research needs, which were considered in the establishment of the objectives of this research study and are enunciated in the next sub-section:

i. a characterization of the terms of the momentum conservation equation at patch-scale as a physically based mean to compute drag forces due to the presence of vegetation;
ii. an evaluation of the budget of turbulent kinetic energy (TKE) at the inter-stem scale;
iii. an adequate analysis of the small-scale turbulence aiming at the estimation of the dissipation rate of TKE at the inter-stem scale in non-homogeneous flows.

The developments contained in the present thesis were guided by the following fundamental premises:

- large-scale hydrodynamic effects must be integrated from smaller scale phenomena;
- before the derivation of closures to time- or double-averaged conservation equations are attempted, a detailed knowledge of the turbulent flow in the inter-stem space is needed;
- upscaling operations must be performed within a well-defined mathematical framework;
- quantification of TKE budget allows for a deep understanding of the nature of the turbulence

and opens possibilities for turbulent modelling;
- the rate of dissipation of turbulent kinetic energy is a fundamental variable for the parametrization of the terms, that require turbulent modelling.

1.2 Objectives

The present research project aims at a detailed spatial characterization, at the inter-stem scale, of the turbulent flow within arrays of emergent, rigid and cylindrical stems, randomly placed with constant and varying areal number-density, defined as the number of stems per unit of plan area and expressed in stems$/\mathrm{m}^2$. It includes experimental work, employing measurements of instantaneous velocities with Particle Image Velocimetry (PIV) and Laser Doppler Anemometry (LDA), and theoretical work on the basic conservation equations of the flow.

The goals of this work, bearing in mind the research needs stated earlier in the text, can be organized in three main blocks:

i. characterization of the terms of the upscaled momentum conservation equation, in which the particular objectives are:
   - a detailed characterization and quantification of the flow within vegetated areas susceptible to be simulated by dense arrays of vertical emergent stems;
   - the quantification of the drag forces acting on the stems and a discussion on the dependence of the drag coefficient on the non-dimensional parameters that characterize these flows.

ii. characterization and quantification of the spatial distribution of the terms of the TKE conservation equation in the inter-stem space;

iii. study of small-scale turbulence, in which the specific goals are:
   - the derivation of an equation akin to Kolmogorov's equation to estimate the rate of dissipation of TKE, exploiting the space-averaging of two-point correlations and statistics as a means to use the formalism of homogeneous and isotropic turbulence;
   - the characterization and quantification of the rate of dissipation of TKE in the inter-stem space.

The originality of this PhD research study introduces three innovations:

i. a detailed spatial description of the budget of TKE and of the terms of the double-averaged momentum conservation equation;

ii. an experimental procedure and associated data treatment, relying mostly on spatial measurements and thus avoiding the use of the frozen turbulence approximation;

iii. the theoretical framework for dealing with non-homogeneous flows, employing time and space-averaging as a means to apply the formalism of homogeneous and isotropic turbulence (HIT);

The immediate progresses and methodologies of this research program pertain to the fluid mechanics domain, however it will eventually mature into bioengineering design approaches and water quality monitoring strategies, that will positively impact river engineering and management practices.

1.3 Methodology

To support the proposed objectives, three experimental tests were performed in two laboratory facilities, employing two different techniques to acquire instantaneous velocity fields. At Laboratory of Hydraulics and Environment of Instituto Superior Técnico (IST) in Lisbon, Portugal, 2D velocity maps were acquired with Particle Image Velocimetry (PIV) system and at the Laboratory of Leichtweiß Institute for Hydraulic Engineering at Technische Universität Braunschweig (LWI) in Germany 3D point-wise velocity series were acquired with Laser Doppler Anemometry (LDA) Two of the tests simulate emergent vegetation conditions with constant stem areal number-density. These two tests were reproduced only in one facility, where the PIV measurements took place. Since actual wetlands exhibit patchiness and spatial variability in stem density, one of the tests featured a periodic distribution of the stem areal number-density, alternating dense and sparse patches. This test was reproduced, with the very same conditions, in both facilities.

The experimental tests were designed to allow for detailed measurements of the instantaneous flow velocity, and these data were used to compute the relevant turbulent quantities. The characterization of the flow includes time-averaged velocity and vorticity maps, autocorrelation functions, second- and third-order structures functions and power spectral density functions.

Part of the data treatment is carried out following the framework of Double-Averaging Methodology (DAM), to account for the great heterogeneity that characterizes the flows within rigid stems at the inter-stem scale. On the topic of drag forces, a dimensional analysis is performed to identify the relevant parameters for the characterization of flows within arrays of rigid and emergent stems. Theoretical work is performed to devise an adequate formulation to compute the dissipation rate of energy for heterogeneous flows, from the performed velocity measurements. It consists in following the procedures of homogeneous and isotropic turbulence, exploiting the space-averaging of two-point correlations and statistics.

1.4 Thesis structure

The present thesis is organized in eight chapters. After the present introductory chapter, a brief literature review is exposed, introducing the fundamental conservation equations and some of the results of the classic homogeneous and isotropic turbulence. The main principles of

Double-Averaging Methodology (DAM) are explained in this chapter.

Chapter 3 presents details of the experimental work. The important role of the experimental work in this PhD program justifies the extension of this chapter, where a complete description of the laboratory facilities, instrumentation and experimental procedure is given.

Chapter 4 is written as a journal paper. This chapter aims at the quantification of the drag coefficient of emergent rigid stems, and at the identification of the parameters to which drag is most sensitive. Data treatment involved Double-Averaging methods and a dimensional analysis identifying the relevant non-dimensional parameters for these flows.

Chapter 5 corresponds also to a journal paper. In this chapter, the quantification and discussion of the relative magnitude of key terms of the equation of conservation of turbulent kinetic energy (TKE) is discussed, at the inter-stem space of a flow within arrays of vertical cylinders simulating plant stems of emergent and rigid vegetation. The calculation of these terms is based on new databases consisting of three-component LDA velocity series and two-dimensional PIV velocity maps, obtained in controlled laboratory conditions.

Chapter 6 presents the mathematical formalism of the theoretical framework for dealing with non-homogeneous flows, employing time and space-averaging as a means to apply the formalism of homogeneous and isotropic turbulence. This chapter was included as appendix for the publication corresponding to chapter 7. However, since it demonstrates a very important result applied in the following chapter, it was here included as a separate chapter.

Chapter 7 includes the main body of a article to be submitted to a fluid mechanics journal, which includes as appendix the mathematical formalism presented in chapter 6. The objective of this chapter is the characterization and quantification of the rate of dissipation of turbulent kinetic energy (TKE) in flows within arrays of emergent, rigid and cylindrical stems, at scales of the order of magnitude of the mean inter-stem characteristic length.

Although presented with the thesis layout, Chapters 4 to 7 include three articles submitted to peer-reviewed journals, therefore some repetition of information may be found.

The last chapter summarizes the main conclusions drawn in the previous chapters and provides recommendations for future works.

Chapter 2

State-of-art

2.1 Introduction

Vegetation has a key role in the fluvial environment, providing depuration of contaminated waters and protection against scour, among other relevant features. However, there is a knowledge gap concerning channels protected vegetation. For instance, most of the existing design criteria for wetlands employ resistance formulas such as Manning's or Chezy's, calibrated *ad hoc* (Rahmeyer *et al.* 1995). Introducing the physics of vegetated channels requires tackling the complex fluid dynamics problem that involves a hydrodynamic characterization of boundary, plant stems and foliage and turbulent flow.

Double-Averaging Methodology (DAM), a particular form of upscaling, in both time and space, allowed progress in the characterization of the 3D flow over irregular boundaries. Such methods are especially pertinent for the characterization of the flows within and in the near vicinity of plant canopies which are spatially heterogeneous. However, the detailed knowledge of turbulent processes at smaller scales remains of paramount importance in the characterization of flows within vegetated reaches.

This chapter is organized in two main sections. The first part introduces the fundamental conservation equations, introducing the Double-Averaging Methodology (DAM) and the resulting equations. The second part is a revision of some of the results of the classic homogeneous and isotropic turbulence, which are the base for some of methods applied in the present thesis.

2.2 Conceptual model

2.2.1 Navier-Stokes equations

The well-known Navier-Stokes equations are non-linear differential equations that describe the flow of Newtonian fluids, expressing the balance of mass, surface and inertial forces. The Navier-Stokes equations are obtained from the momentum conservation equation and the constitutive equation which relates the strain rate and stress of the flow.

The momentum conservation equation for an incompressible fluid is defined, in tensor notation, by (Currie, 1993, p. 17)

$$\rho \frac{\partial u_j}{\partial t} + \rho \frac{\partial u_j u_i}{\partial x_i} = \rho g_j + \frac{\partial \sigma_{ij}}{\partial x_i}. \tag{2.1}$$

In this equation, as in all the equations hereinafter, a Cartesian coordinate system is adopted where x, y and z are the streamwise, spanwise and vertical coordinates, respectively, and u, v and w are the corresponding instantaneous velocity components. Tensor notation is applied according to $\{x_1, x_2, x_3\} \equiv \{x, y, z\}$ and $\{u_1, u_2, u_3\} \equiv \{u, v, w\}$, and Einstein notation is applied to simply the writing of sums in equations. In equation (2.1), ρ stands for the fluid volumetric mass density, g_i is i^{th} component of the gravitational acceleration, σ_{ij} is the stress tensor and $i = 1,2,3$ and $j = 1,2,3$ correspond to each of the space directions, x, y and z, respectively.

The constitutive equation for an incompressible Newtonian fluid is expressed by

$$\sigma_{ij} = -p\delta_{ij} + \mu \left(\frac{\partial u_i}{\partial x_j} + \frac{\partial u_j}{\partial x_i} \right) \tag{2.2}$$

where p is the local pressure and μ is the fluid dynamic viscosity (Currie 1993, p. 28; Pope 2000, pp. 16-17). The term $p\delta_{ij}$ expresses the isotropic pressure acting on the fluid, while $\mu \left(\frac{\partial u_i}{\partial x_j} + \frac{\partial u_j}{\partial x_i} \right)$ is the stress tensor of a Newtonian fluid.

Considering the fluid incompressibility and assuming that μ is constant, the derivation of equation (2.2) results

$$\frac{\partial \sigma_{ij}}{\partial x_i} = -\frac{\partial p}{\partial x_j} + \mu \frac{\partial^2 u_j}{\partial x_i \partial x_i}. \tag{2.3}$$

Substituting this result in equation (2.1), dividing all terms by ρ and considering the mass conservation equation for incompressible fluids $\left(\frac{\partial u_i}{\partial x_i} = 0 \right)$, one obtains the Navier-Stokes equations for incompressible fluids (Schlichting 1968, p. 62; Monin & Yaglom 1971, p. 30; Currie 1993, p.

31):

$$\frac{\partial u_j}{\partial t} + \frac{\partial u_j u_i}{\partial x_i} = g_j - \frac{1}{\rho}\frac{\partial p}{\partial x_j} + \nu \frac{\partial^2 u_j}{\partial x_i \partial x_i} \tag{2.4}$$

where $\nu = \mu/\rho$ is the fluid kinematic viscosity. This equation expresses the second's Newton law, where momentum variations in the left hand side, expressed as a force per mass unit, is balanced by the external forces in the right hand side, where g_j represents the mass force, $\frac{\partial p}{\partial x_j}$ the pressure surface force and $\nu \frac{\partial^2 u_j}{\partial x_i \partial x_i}$ the viscous surface force.

2.2.2 Reynolds-Averaged Navier-Stokes equations (RANS)

Most of the flows in nature are turbulent. Turbulent flows are random, unsteady, three-dimensional and contain many eddies with different lengths and time scales. Typically, in a free surface flow, largest eddy scales have the size of the flow depth. The smallest eddy scales one can find in a turbulent flow are characterized by sizes of the order of magnitude of the fluid molecules. Due to its complexity, turbulent flows are very difficult to predict. The Navier-Stokes equations are able to describe all the details of the turbulent velocity fields of a flow, from the largest to the smallest scale. However, when recurring to numerical solvers, such detail leads to extremely expensive computational time to solve those equations even for simple cases. Therefore, Navier-Stokes equations are considered, practically, impossible to apply to solve any engineering problem (Pope, 2000, p.8).

The development of the so-called Reynolds-Averaged Navier-Stokes equations (RANS) was motivated by the impossibility to solve actual problems with Navier-Stokes equations and it is based in the application of a time-average operator over a time period larger than the largest characteristic period of the flow motion. To obtain the RANS, it is necessary to introduce first the Reynolds decomposition in the Navier-Stokes equations before the application of the time-average operator. Reynolds decomposition consists in the decomposition of the instantaneous flow variables into mean and fluctuating components, as exemplified in Figure 2.1. Hence, an instantaneous generic variable θ can be written as

$$\theta(x,y,z,t) = \overline{\theta}(x,y,z) + \theta'(x,y,z,t) \qquad \text{with } \overline{\theta'} = 0 \tag{2.5}$$

where overbars identify the time-averaged component and primes the fluctuations to the time-average. Introducing Reynolds decomposition and time-averaging each term of equation (2.4), as follows

$$\overline{\frac{\partial\left(\bar{u}_j + u'_j\right)}{\partial t}} + \overline{\frac{\partial\left(\bar{u}_j + u'_j\right)\left(\bar{u}_i + u'_i\right)}{\partial x_i}} = \bar{g}_j - \frac{1}{\rho}\overline{\frac{\partial\left(\bar{p} + p'\right)}{\partial x_j}} + \nu \overline{\frac{\partial^2\left(\bar{u}_j + u'_j\right)}{\partial x_i \partial x_i}} \tag{2.6}$$

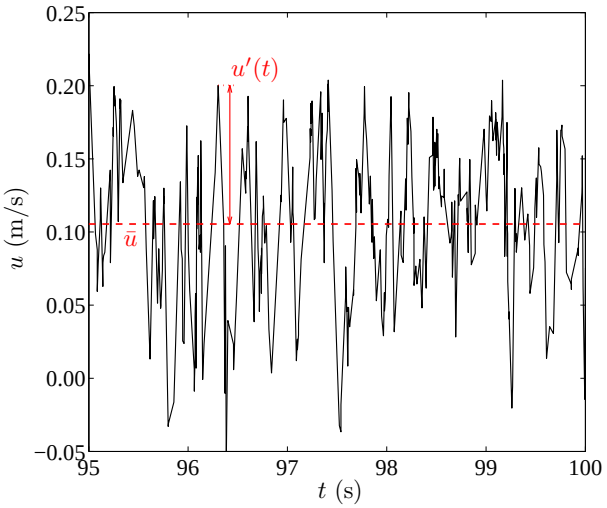

Figure 2.1: Extract of a longitudinal instantaneous velocity time series acquired with a Laser Doppler Anemometry system. The dashed line represents the time-averaged velocity $\bar{u}$.

and considering the following rules of the time-average operator (Hinze 1975, pp. 6-7, Monin & Yaglom 1971, p. 207)

$$\bar{\bar{\theta}} = \bar{\theta} \qquad \overline{\theta + \xi} = \bar{\theta} + \bar{\xi}$$

$$\overline{\bar{\theta}\xi} = \bar{\theta}\bar{\xi} \qquad \overline{\frac{\partial \theta}{\partial s}} = \frac{\partial \bar{\theta}}{\partial s}$$

$$\overline{\theta\xi} \neq \bar{\theta}\bar{\xi}$$

(where θ and ξ stand for any generic flow variable) one obtains the RANS for a flow of an incompressible Newtonian fluid (Schlichting, 1968, p. 529):

$$\frac{\partial \bar{u}_j}{\partial t} + \bar{u}_i \frac{\partial \bar{u}_j}{\partial x_i} = g_j - \frac{1}{\rho}\frac{\partial \bar{p}}{\partial x_j} - \frac{\partial \overline{u'_j u'_i}}{\partial x_i} + \nu \frac{\partial^2 \bar{u}_j}{\partial x_i \partial x_i} \tag{2.7}$$

Most of the terms in the Navier-Stokes equations were simply replaced by their time-averaged counterparts in the RANS, but a new term has arisen due to the non-linearity of the convective acceleration term. This term, the third term on the right hand side of equation (2.7), is known as the Reynold stress term and it represents, to the mean flow, the transport of momentum associated to velocity fluctuations by the turbulent component of the flow.

The Reynolds stress tensor, also named turbulent stress tensor, is defined by $-\rho\overline{u'_j u'_i}$, and it is an additional stress tensor which is caused by turbulent fluctuations (Monin & Yaglom, 1971, p. 261) being often modelled as a turbulent diffusion of momentum (Schlichting, 1968, p. 546). Several closure models for the Reynolds stress term have been proposed in order to find numerical

solutions for the RANS (Patel *et al.*, 1985).

The RANS have been used as a tool for both modelling and interpreting numerical and experimental results. However, when the time-averaged flow is highly spatially heterogeneous, RANS are not convenient. Therefore, to conceptually solve this issue, time-averaged equations should be supplemented by space averaging (Nikora *et al.*, 2007a).

2.2.3 Turbulent kinetic energy conservation equation

Particularly relevant within the scope of turbulent flows is the equation of balance of turbulent energy, which describes the variation of the density of kinetic energy of the fluctuating motion (Monin & Yaglom, 1971, p. 374). Hereinafter, the term turbulent kinetic energy (TKE) refers to the mean kinetic energy of the turbulent motion per unit mass of the fluid, defined as $E_t = 1/2\overline{u_i' u_i'}$.

The TKE balance equation results from the subtraction of the kinetic energy equation for the mean flow from the total kinetic energy equation. The former is obtained by multiplying the RANS by the mean velocity $\bar{u}_j$, while the total kinetic energy equation is obtained by the multiplication of the Navier-Stokes equations by the instantaneous velocity u_j followed by the time-average of all terms (Tennekes & Lumley 1972, pp. 59-63, Hinze 1975, pp. 68-72).

For steady flows, the equation of conservation of TKE is written as

$$\underbrace{\frac{1}{2}\overline{u_j}\frac{\partial \overline{u_i' u_i'}}{\partial x_j}}_{\text{I}} + \underbrace{\overline{u_i' u_j'}\frac{\partial \overline{u_i}}{\partial x_j}}_{\text{II}} + \underbrace{\frac{1}{2}\frac{\partial \overline{u_i' u_i' u_j'}}{\partial x_j}}_{\text{III}} = \underbrace{-\frac{1}{\rho}\frac{\partial \overline{p' u_j'}}{\partial x_j}}_{\text{IV}} + \underbrace{2\nu\frac{\partial \overline{s_{ij} u_i'}}{\partial x_j}}_{\text{V}} - \underbrace{\bar{\varepsilon}}_{\text{VI}}, \tag{2.8}$$

where s_{ij} is the symmetric part of turbulent strain tensor $\frac{\partial u_i'}{\partial x_j}$ and $\bar{\varepsilon}$ is the time-averaged dissipation rate of TKE.

Equation (2.8) shows that the density of turbulent energy at a given point of the flow may vary due to the interaction with the mean flow (term I, convective term), the transformation of part of the energy of the mean motion into turbulent energy (term II, turbulent production), the transport of turbulent energy by the fluctuating motion (term III, turbulent diffusion), the transport of turbulence by pressure fluctuations (term IV, pressure diffusion), the action of internal friction (term V, viscous term) and the transformation of kinetic energy into heat by viscous dissipation (term VI, TKE dissipation rate) (Monin & Yaglom, 1971, pp. 373-382).

2.2.4 Double-Averaging Methodology

Double-averaging (DA) methods are a particular form of upscaling, both in time and space. The conservation equations of turbulent flows are expressed for time-averaged quantities which,

in case of unsteady flow, are defined in a time-window smaller than the fundamental unsteady flow time-scale, and for space-averaged quantities, defined in space windows larger than the characteristic wavelength of the boundary irregularities (Franca & Czernuszenko, 2006). The Double-Averaging Methodology (DAM) allowed progress in the characterization of the 3D flow over irregular boundaries and as a result of these studies, the most consolidate advances concern upscaling the RANS equations. The conservation of momentum ceases to be applicable at a continuum of points in space to be applied at a mesh of bounded sets of finite measures, mapping the continuum space. DAM is far more than a simple statistical procedure since it produces mathematically significant physical terms that have been added *ad hoc* to the RANS during many years, namely form-induced stresses and form and viscous drag.

The first double-averaging methods appeared in the field of multi-phase and ground-water flow hydrodynamics (Gray & Lee, 1977; Whitaker, 1967). In free-surface hydraulics, the idea of double-averaging was first introduced by Smith & McLean (1977) for characterizing a flow over large dunes. However, the formal apparatus of the DAM theory has been built in atmospheric boundary layer studies to describe turbulent flows within and above terrestrial canopies (Finnigan, 2000; Finnigan & Shaw, 2008; Poggi *et al.*, 2004a,b; Raupach *et al.*, 1991, 1986; Raupach & Shaw, 1982; Wilson & Shaw, 1977, among others).

Concerning hydraulic flows, among the first published works it should be highlighted the work of Gimenez-Curto & Corniero Lera (1996) who introduced the term "form-induced stress" to describe the spatial disturbances in the time-averaged flow over rough surfaces. Later, López & García (1998) used insights from the DAM to model the suspended sediment transport in a flow through simulated vegetation. However, most of the development of the DAM in water flows has been carried out during the last 12 years, mainly applied to flows over rough gravel beds (Campbell, 2005; Ferreira *et al.*, 2010, 2008; Franca *et al.*, 2008; Manes *et al.*, 2007; Mignot *et al.*, 2009a; Nikora *et al.*, 2013; Nikora *et al.*, 2001, 2004, 2007a; Pokrajac *et al.*, 2008).

Nikora *et al.* (2001) suggested that the double-averaged momentum equations should be used as a natural basis for hydraulics of rough-bed open-channel flows, especially with small relative submergence of the roughness. According to the authors the main advantages of the DAM are: the consistent link between spatially averaged roughness parameters and double-averaged flow variables; the explicit appearance of a form drag term and form-induced stresses in the momentum equations; the possibility for scaling considerations and parametrizations based on double-averaged variables; and the possibility for the consistent scale partitioning of the roughness parameters and flow properties.

Nikora *et al.* (2004) presented several models for the vertical distribution of the double-averaged longitudinal velocity in flows over rough boundaries, suggesting constant, exponential or linear profiles depending on roughness geometry and flow conditions.

Nikora *et al.* (2007a), Nikora *et al.* (2007b) and Nikora *et al.* (2013) present a review of the progresses achieved so far in the DAM theory as well as several applications of this theory in hydraulics, highlighting its advantages and strengths. Ferreira *et al.* (2008) show the application of the DAM in the characterization and quantification of the flow resistance in free surface flows over rough, porous and mobile beds. Ferreira *et al.* (2010) applied DAM to evaluate the impacts of sand transport on flow hydrodynamics and on vertical dissolved oxygen distribution in gravel-bed rivers. This study concluded that neglecting the form-induced vertical fluxes of mass leads to underestimating the concentrations of dissolved oxygen in the pythmenic layer.

In what concerns vegetated boundaries, DAM has been successfully employed to calculate the drag exerted on arrays of identical stems (Poggi *et al.*, 2004a) or the drag on plants with dense foliage (Righetti & Armanini, 2002). The upscaled momentum equations are especially pertinent, at the adequate scales, to calculate the drag partition (Raupach *et al.*, 1991) and the bulk flow resistance of a stem array (Ferreira *et al.*, 2009a).

2.2.5 Double-Averaged Navier-Stokes equations (DANS)

Similarly to the process of obtaining the RANS from de Navier-Stokes equations, a set of equations, named Double-Averaged Navier-Stokes equations (DANS) are derived from the RANS introducing a spatial decomposition and applying the space-average operator. It should be noticed that, herein, the space-averaging is introduced after the time-averaging. However, the inverse order of the average operators would render the same results in what concerns the momentum conservation equation (Nikora *et al.*, 2007a; Pokrajac *et al.*, 2008).

The spatial decomposition of a generic time-averaged flow variable $\bar{\theta}$ is expressed by

$$\bar{\theta}(x,y,z) = \left\langle \bar{\theta} \right\rangle (z) + \tilde{\bar{\theta}}(x,y,z) \tag{2.9}$$

where angle brackets represent the space-averaging and tildes the spatial fluctuation of the time-averaged variables regarding its space-averaged value. To simplify the notation, $\tilde{\theta} \equiv \tilde{\bar{\theta}}$ will be used hereinafter.

It should be noticed that the space-averaging here is considered over a thin layer parallel to the mean channel bed, therefore $\left\langle \bar{\theta} \right\rangle$ depends only on the vertical coordinate z. The dimensions of the averaging domain in the plane parallel to the mean bed should be larger than the dominant turbulence scales, but much smaller than the large-scale features.

The space-average operator is subjected to the following rules (Finnigan & Shaw, 2008)

$$\langle \langle \theta \rangle \rangle = \langle \theta \rangle \qquad \langle \theta + \xi \rangle = \langle \theta \rangle + \langle \xi \rangle$$
$$\langle \langle \theta \rangle \xi \rangle = \langle \theta \rangle \langle \xi \rangle \qquad \langle \theta \xi \rangle \neq \langle \theta \rangle \langle \xi \rangle$$

where θ and ξ stand for any generic flow variables, as for example, the velocity, u_i, or the pressure, p. Moreover, it should be underlined that space-average operator does not always commute with time and spatial differential operators (Raupach & Shaw, 1982; Wilson & Shaw, 1977). Actually,

$$\left\langle \frac{\partial \theta}{\partial x_j} \right\rangle = \frac{\partial \langle \theta \rangle}{\partial x_j}$$

is only true when the control volume is constituted only by fluid. When the control volume has both a liquid and a solid fraction

$$\left\langle \frac{\partial \theta}{\partial x_j} \right\rangle \neq \frac{\partial \langle \theta \rangle}{\partial x_j} ,$$

thus, to apply the spatial-average to differential terms two theorems should be invoked (details can be found in Campbell, 2005; Finnigan, 2000; Gray & Lee, 1977; Nikora *et al.*, 2007a; Raupach *et al.*, 1986).

These theorems are the spatial-averaging theorem

$$\left\langle \frac{\partial \theta}{\partial x_j} \right\rangle = \frac{1}{\psi} \frac{\partial \psi \langle \theta \rangle}{\partial x_j} - \frac{1}{\forall_f} \int_{S_{int}} \theta n_j \mathrm{d}S, \tag{2.10}$$

and the general transport equation

$$\left\langle \frac{\partial \theta}{\partial t} \right\rangle = \frac{1}{\psi} \frac{\partial \psi \langle \theta \rangle}{\partial t} + \frac{1}{\forall_f} \int_{S_{int}} \theta u_i^{(I)} n_i \mathrm{d}S, \tag{2.11}$$

where θ is some tensorial quantity, vector or scalar, defined only in the fluid; S_{int} is the solid-fluid interface surface; $\psi = \frac{\forall_f}{\forall_T}$ expresses the fluid fraction, *i.e.*, the percentage of volume occupied by fluid, $\forall_f$, within the total control volume, $\forall_T$; n_i is the i^{th} component of the unit normal vector, directed from the solid into the fluid; $u_i^{(I)}$ is the i^{th} component of the velocity vector of the solid-fluid interface. When the boundary is rigid, no-slip and non-porous $u_i^{(I)} = 0$, thus the last term of the general transport equation vanishes. Hereinafter the superscript I is omitted in non-ambiguous cases.

The double-averaged continuity equation follows straightforwardly by the application of theorem (2.10) to the time-averaged version of this equation $\left(\frac{\partial \bar{u}_i}{\partial x_i} = 0\right)$:

$$\left\langle \frac{\partial \bar{u}_i}{\partial x_i} \right\rangle = \frac{1}{\psi} \frac{\partial \psi \langle \bar{u}_i \rangle}{\partial x_i} - \frac{1}{\forall_f} \int_{S_{int}} \bar{u}_i n_i \mathrm{d}S = 0$$

$$\frac{1}{\psi}\frac{\partial \psi \langle \bar{u}_i \rangle}{\partial x_i} = \frac{1}{\forall_f}\int_{S_{int}} \bar{u}_i n_i \mathrm{d}S \tag{2.12}$$

which becomes, for rigid, no-slip and non-porous boundaries

$$\frac{\partial \psi \langle \bar{u}_i \rangle}{\partial x_i} = 0 \tag{2.13}$$

Considering the presented rules, theorems and the double-averaged continuity equation, the double-averaged momentum conservation equations, DANS, for incompressible fluids are given by

$$\begin{aligned}\frac{\partial \langle \bar{u}_j \rangle}{\partial t} + \langle \bar{u}_i \rangle \frac{\partial \langle \bar{u}_j \rangle}{\partial x_i} &= g_j - \frac{1}{\psi\rho}\frac{\partial \psi \langle \bar{p} \rangle}{\partial x_j} - \frac{1}{\psi}\frac{\partial \psi \left\langle \overline{u'_j u'_i} \right\rangle}{\partial x_i} - \frac{1}{\psi}\frac{\partial \psi \langle \tilde{u}_j \tilde{u}_i \rangle}{\partial x_i} \\ &+ \frac{1}{\psi}\frac{\partial}{\partial x_i}\left(\psi \left\langle \nu \frac{\partial \bar{u}_j}{\partial x_i} \right\rangle\right) + \frac{1}{\rho \forall_f}\int_{S_{int}} \bar{p} n_j \mathrm{d}S - \frac{1}{\forall_f}\int_{S_{int}} \nu \frac{\partial \bar{u}_j}{\partial x_i} n_i \mathrm{d}S - \frac{\langle \bar{u}_i \rangle}{\psi}\frac{\partial \psi}{\partial t} \\ &- \frac{1}{\forall_f}\int_{S_{int}} \bar{u}_j u_i^{(I)} n_i \mathrm{d}S - \frac{\langle \bar{u}_j \rangle}{\forall_f}\int_{S_{int}} \bar{u}_i n_i \mathrm{d}S + \frac{1}{\forall_f}\int_{S_{int}} \bar{u}_j \bar{u}_i n_i \mathrm{d}S + \frac{1}{\forall_f}\int_{S_{int}} \overline{u'_j u'_i} n_i \mathrm{d}S\end{aligned} \tag{2.14}$$

By the non-slip condition and considering that the solid-fluid interface is rigid, in time, and non-porous the terms in the last line and the term $\frac{\langle \bar{u}_i \rangle}{\psi}\frac{\partial \psi}{\partial t}$ of the previous equation disappear. Therefore, DANS for rigid boundaries and incompressible fluids are expressed, in force per unit of fluid mass, by (Ferreira *et al.*, 2010; Finnigan, 2000; Nikora *et al.*, 2007a; Raupach *et al.*, 1986)

$$\begin{aligned}\frac{\partial \langle \bar{u}_j \rangle}{\partial t} + \langle \bar{u}_i \rangle \frac{\partial \langle \bar{u}_j \rangle}{\partial x_i} &= g_j - \frac{1}{\psi\rho}\frac{\partial \psi \langle \bar{p} \rangle}{\partial x_j} - \frac{1}{\psi}\frac{\partial \psi \left\langle \overline{u'_j u'_i} \right\rangle}{\partial x_i} - \frac{1}{\psi}\frac{\partial \psi \langle \tilde{u}_j \tilde{u}_i \rangle}{\partial x_i} \\ &+ \frac{1}{\psi}\frac{\partial}{\partial x_i}\left(\psi \left\langle \nu \frac{\partial \bar{u}_j}{\partial x_i} \right\rangle\right) + \frac{1}{\rho \forall_f}\int_{S_{int}} \bar{p} n_j \mathrm{d}S - \frac{1}{\forall_f}\int_{S_{int}} \nu \frac{\partial \bar{u}_j}{\partial x_i} n_i \mathrm{d}S\end{aligned} \tag{2.15}$$

In equation (2.15), terms $\rho\psi\left\langle \overline{u'_j u'_i} \right\rangle$ and $\rho\psi\left\langle \nu \frac{\partial \bar{u}_j}{\partial x_i} \right\rangle$ represent the space-averaged Reynolds and viscous stress tensors, respectively. Due to the spatial variability of the flow, DANS include a new term $\frac{\partial \psi \langle \tilde{u}_j \tilde{u}_i \rangle}{\partial x_i}$, the form-induced flux, which appears due to the non-linearity of the convective acceleration term. Form-induced stresses, also known as dispersive stresses, are defined as $\rho\psi\langle \tilde{u}_j \tilde{u}_i \rangle$ and are due to the spatial variability of the time-averaged velocity field. According to Gimenez-Curto & Corniero Lera (1996), the form-induced stress tensor is non-zero when there is vorticity in the disturbed flow. There are two other terms in the DANS, arising from the non-commutativity of the average and differential operators, the terms $\frac{1}{\rho\forall_f}\int_{S_{int}} \bar{p} n_j \mathrm{d}S$ and $\frac{1}{\forall_f}\int_{S_{int}} \nu \frac{\partial \bar{u}_j}{\partial x_i} n_i \mathrm{d}S$ which represent the pressure and viscous drag, respectively.

Note that in the previous equations, time and space-averaging operators where applied considering a time interval sufficiently large and a control volume defined as an infinite horizontal slab of vanishing thickness. If these conditions are not valid extra stresses appear in the DANS (details in Finnigan, 2000; Leonard, 1974).

The form and viscous drag terms of equation (2.15) can be written as

$$\frac{1}{\forall_f}\int_{S_{int}} \bar{p} n_j \mathrm{d}S = -\left\langle \frac{\partial \tilde{p}}{\partial x_j} \right\rangle + \frac{\langle \bar{p} \rangle}{\psi}\frac{\partial \psi}{\partial x_j} \tag{2.16}$$

and

$$-\frac{1}{\forall_f}\int_{S_{int}} \nu \frac{\partial \bar{u}_j}{\partial x_i} n_i \mathrm{d}S = \left\langle \nu \frac{\partial^2 \tilde{u}_j}{\partial x_i \partial x_i} \right\rangle - \frac{\nu \langle \bar{u}_j \rangle}{\psi}\frac{\partial^2 \psi}{\partial x_i \partial x_i} - \frac{2\nu}{\psi}\frac{\partial \langle \bar{u}_j \rangle}{\partial x_i}\frac{\partial \psi}{\partial x_i} + \frac{1}{\psi}\frac{\partial}{\partial x_i}\psi\nu\left(\frac{1}{\forall_f}\int_{S_{int}} \bar{u}_j n_i \mathrm{d}S\right) \tag{2.17}$$

respectively (Campbell, 2005, pp. 225-231). The last term of equation (2.17) vanishes for rigid, no-slip and non-porous bed conditions. Inserting in equation (2.15) the previous definitions, considering

$$\frac{1}{\psi}\frac{\partial \psi \langle \bar{p} \rangle}{\partial x_j} = \frac{\langle \bar{p} \rangle}{\psi}\frac{\partial \psi}{\partial x_j} + \frac{\partial \langle \bar{p} \rangle}{\partial x_j}$$

and

$$\frac{1}{\psi}\frac{\partial}{\partial x_i}\left(\psi\left\langle \nu \frac{\partial \langle \bar{u}_j \rangle}{\partial x_i} \right\rangle\right) = \left\langle \nu \frac{\partial^2 \bar{u}_j}{\partial x_i \partial x_i} \right\rangle + \frac{\nu \langle \bar{u}_j \rangle}{\psi}\frac{\partial^2 \psi}{\partial x_i \partial x_i} + \frac{2\nu}{\psi}\frac{\partial \langle \bar{u}_j \rangle}{\partial x_i}\frac{\partial \psi}{\partial x_i}$$

an equivalent way to express the DANS is given by

$$\frac{\partial \langle \bar{u}_j \rangle}{\partial t} + \langle \bar{u}_i \rangle \frac{\partial \langle \bar{u}_j \rangle}{\partial x_i} = g_j - \frac{1}{\rho}\frac{\partial \langle \bar{p} \rangle}{\partial x_j} - \frac{1}{\psi}\frac{\partial \psi \left\langle \overline{u'_j u'_i} \right\rangle}{\partial x_i} - \frac{1}{\psi}\frac{\partial \psi \langle \tilde{u}_j \tilde{u}_i \rangle}{\partial x_i} + \nu \frac{\partial^2 \langle \bar{u}_j \rangle}{\partial x_i \partial x_i} - \frac{1}{\rho}\left\langle \frac{\partial \tilde{p}}{\partial x_j} \right\rangle + \nu \left\langle \frac{\partial^2 \tilde{u}_j}{\partial x_i \partial x_i} \right\rangle. \tag{2.18}$$

It should be noticed that often in literature (Finnigan & Shaw, 2008; Nikora *et al.*, 2001; Poggi *et al.*, 2004a; Poggi & Katul, 2008) the drag and viscous drag are presented as $\left\langle \frac{\partial \tilde{p}}{\partial x_i} \right\rangle$ and $\left\langle \nu \frac{\partial^2 \tilde{u}_j}{\partial x_i \partial x_i} \right\rangle$, respectively. That is a simplification, these terms are only one of the components of drag terms.

In the present work, double-averaged quantities are defined as

$$\left\langle \bar{\theta} \right\rangle (z) = \frac{1}{A_f(z)} \int_{\Omega/\Sigma} \overline{\theta}(\xi_1, \xi_2, z)\, \mathrm{d}S \tag{2.19}$$

where Ω is the measuring domain, Σ is the subdomain of Ω occupied by solid elements, $A_f(z)$ is the area of the domain, within Ω, occupied by fluid at a given elevation z. Dummy variables ξ_1 and ξ_2 are such that $0 < \xi_1 < L_x$ and $0 < \xi_2 < L_y$, where L_x and L_y are the characteristic wavelengths of the boundary irregularities in the x and y directions, respectively.

Definition (2.19) is not practical when measurements are spatially discrete, for instance velocity profiles taken at a finite number of points in a given measuring domain. In the latter case, the calculation of the double-averaged velocity at a given elevation z obeys to (Ferreira *et al.*, 2010; Franca *et al.*, 2008)

$$\left\langle \bar{\theta} \right\rangle (z) \approx \frac{\sum_{k=1}^{N-N_0(z)} \bar{\theta}_k(z) A_k(z)}{\sum_{k=1}^{N-N_0(z)} A_k(z)} \tag{2.20}$$

where $A_k(z)$ is the area of the convex subdomain Ω_k, defined as the the area of influence of $(x_k, y_k) \in]0, L_x[\times]0, L_y[$ and such that $\bigcup_{k=1}^{N(z)} \Omega_k = \Omega$, N corresponds to the total number of subdomains and $N_0(z)$ to the number of subdomains, at elevation z, for which the flow variable is not defined in (x_k, y_k). It should be noticed that $\sum_{k=1}^{N-N_0(z)} A_k(z) < A(z)$ for $N_0(z) > 0$.

2.2.6 Space-averaged turbulent kinetic energy equation (SATKE)

In the DAM framework, turbulent kinetic energy conservation is given by the space-averaged turbulent kinetic energy equation (SATKE), which consists on the introduction of spatial decomposition and the application of the space-average operator to the TKE equation, presented above in the equation (2.8). The space-averaged turbulent kinetic energy equation is, thus, expressed by

(Finnigan, 2000; Mignot *et al.*, 2008)

$$\frac{1}{\psi}\frac{\partial \psi\left(\left\langle\overline{u_j}\right\rangle\left\langle\overline{u_i'u_i'}\right\rangle/2\right)}{\partial x_j} = -\underbrace{\left\langle\overline{u_j'u_i'}\right\rangle\frac{\partial\left\langle\overline{u_j}\right\rangle}{\partial x_i}}_{\text{Ps}} - \underbrace{\left\langle\overline{u_j'u_i'}\right\rangle\left\langle\frac{\partial\tilde{\tilde{u}}_i}{\partial x_j}\right\rangle}_{\text{Pm}} - \underbrace{\left\langle\widetilde{\overline{u_j'u_i'}}\frac{\partial\tilde{\tilde{u}}_i}{\partial x_j}\right\rangle}_{\text{Pw}}$$

$$-\frac{1}{\psi}\frac{\partial}{\partial x_j}\left(\underbrace{\psi\frac{\left\langle\widetilde{\overline{u_i'u_i'}}\tilde{\tilde{u}}_j\right\rangle}{2}}_{\text{Td}} + \underbrace{\psi\frac{\left\langle\overline{u_j'u_i'u_i'}\right\rangle}{2}}_{\text{Tt}} + \underbrace{\frac{\psi}{\rho}\left\langle\overline{p'u_j'}\right\rangle}_{\text{Tp}}\right) + \underbrace{\nu\frac{\partial^2\left\langle\overline{u_i'u_i'}\right\rangle/2}{\partial x_i\partial x_i}}_{\text{Tv}} + \langle\bar{\varepsilon}\rangle \quad (2.21)$$

where the term Ps is the shear production, Pw is the wake production term and the term Pm corresponds to the work of the spatial velocity fluctuations against the double-averaged Reynolds stress, and it can be written as $\left\langle\widetilde{\overline{u_j'u_i'}}\right\rangle\frac{\langle\bar{u}_i\rangle}{\psi}\frac{\partial\psi}{\partial x_j}$. The terms Td, Tt, Tp and Tv correspond to the dispersive, turbulent, pressure and viscous transport, respectively, and $\langle\varepsilon\rangle$ is the dissipation term.

2.3 Turbulence

2.3.1 Nature of turbulence

Most of the flows occurring in nature and engineering applications are turbulent, from micro biomedical flows to motions of gases in interstellar nebulae, the number of examples of turbulent flows is almost infinite. Thus turbulence is all around us, therefore its study is extremely important from the practical viewpoint (Monin & Yaglom, 1971, pp. 2-3).

Although turbulence is a rather familiar notion, it is difficult to come up with a definition precise enough to cover all the detailed characteristics comprehended in it (Hinze, 1975, p. 1). The best way is to describe the most common characteristics of turbulent flows. Turbulent flows, occuring at high Reynolds number, are characterized by random fluctuations, in time and in space, of velocity, pressure and other fluid mechanical quantities; they present high diffusivity which causes rapid mixing and increased transfer of momentum, heat and mass; turbulent flows are rotational and three-dimensional and they are characterized by high levels of vorticity fluctuation; turbulent flows are dissipative since viscous shear stresses continuously perform deformation work increasing the internal energy of the fluid by expensing turbulent kinetic energy. Turbulence is a property of the flow and not a fluid property (Tennekes & Lumley 1972, pp. 1-4; Hinze 1975, p. 14).

Turbulent motion can be assumed as a consistent superposition of eddies of various sizes, which strongly interact due to the nonlinear and three-dimensional character of turbulence (Hinze,

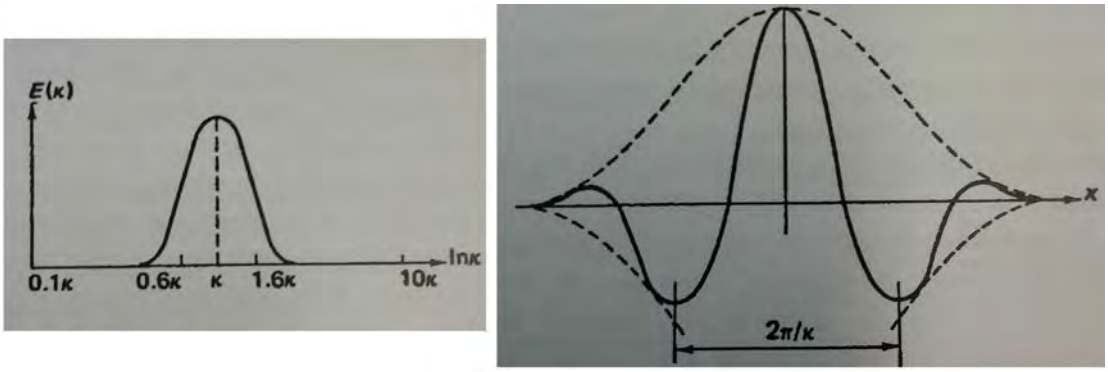

Figure 2.2: Representation of an eddy of wavenumber k and wavelength $2\pi/k$ (from Tennekes & Lumley, 1972, p. 259).

1975, p. 14). Eddies are structures of the turbulent flows characterized by a length scale, l, in the physical domain or by a wavenumber, k, in the spectral domain. A good description of the concept of an eddy is presented by Tennekes & Lumley (1972), who describe, in the spectral space, an eddy as a disturbance containing energy in the vicinity of k. Eddies are expected to interact with other eddies within one or two wavelengths losing their identity. Therefore, the contribution of an eddy to the energy spectrum is a fairly broad spike, wide enough to avoid oscillatory behaviour in the correlation. Tennekes & Lumley (1972) define an eddy of wavenumber k as a disturbance containing energy between $0.62k$ and $1.62k$ (Figure 2.2), which leads to a width of the contribution to the spectrum equal to k ($\ln(1.62) = \ln(0.62) \cong 1/2$), corresponding to an envelope of the eddy of the order of $1/k$. Then, the eddy size l is roughly equal to $2\pi/k$.

In a turbulent flow, the upper limit of the eddies is determined mainly by the size of the physical domain, whereas the lower limit is determined by viscosity effects. Within these smallest eddies the flow is of a strong viscous nature where molecular effects are dominant (Hinze, 1975, pp. 7-8).

Due to the randomness and non-linearity that characterize turbulent flows it is a challenge to find a mathematical expression for time and space dependence of the velocity or pressure field of a flow. A solution is to adopt a statistical description for the turbulence theory, based on the study of specific statistical laws (Monin & Yaglom, 1971, p. 3).

The following subsection presents a brief overview on theory of homogeneous and isotropic turbulence (HIT), where only the definitions pertinent to this work are presented. Complete reviews on statistical fluid mechanics may be found in Tennekes & Lumley (1972), Monin & Yaglom (1971); Monin & Yaglom (1975) or Chassaing (2000).

2.3.2 Homogeneous and isotropic turbulence

The concept of "homogeneous and isotropic turbulence" was introduced by Taylor (1935) as the condition that all the finite-dimensional probability distributions of the fluid mechanical quantities at a finite number of space-time points are invariant under any orthogonal transformation of a system of three-dimensional coordinates (Monin & Yaglom, 1971, p. 13). HIT hypothesis, simplifying the mathematical formulations, allowed for very important advances on the knowledge of turbulence, namely it was the base for the well known Kolmogorov's theories. The conditions of HIT are never fulfilled in real turbulent flows, however they proved to be very valuable for describing small-scale proprieties of real flows. According to Monin & Yaglom (1971), any developed turbulence with sufficiently high Reynolds number may be considered to be locally homogeneous and locally isotropic, this means that a range of scales where homogeneous and isotropic conditions apply may be found in the flow.

In this section the velocity field $u(x,y,z)$ is considered homogeneous and isotropic, thus with constant mean $\langle u \rangle$ and, without loss of generality, it is assumed that $\langle u \rangle = 0$. Note that in HIT conditions the statistics of the velocity field are equal for all the components, so u is here considered as a generic velocity component (scalar random field). It should also be noted that the time dependence of u is not considered since the flow is admitted steady, furthermore the following definitions are presented in terms of space, avoiding to call the Taylor's frozen turbulence theory. The angle brackets, $\langle\rangle$[1], represent here an appropriated ensemble average operator, that due to the assumption done may be a space-average, however, since the processes are considered stationary, it could also be a time-average.

Correlation functions, structure functions and energy spectra are within the most used quantities to characterize turbulent flows. The autocorrelation function, the second-order structure function and the one-dimensional energy spectrum are quantities interrelated, in the sense they are all second-order functions of the fluctuation velocity field.

The correlation function measures the degree to which the velocity at two different points is correlated and how they are correlated (Davidson, 2004, pp. 88-89). In the case of an isotropic field $u(x,y,z)$, the correlation function depends only on the lag r between the two points (Monin & Yaglom, 1975, p. 31). Correlating the scalar field $u(x,y,z)$ with itself at both spatial positions (x,y,z) and $(x+r_x, y+r_y, z+r_z)$, the correlation function can be called autocorrelation and it is defined by

$$B(r) = \langle u(x,y,z)u(x+r_x, y+r_y, z+r_z)\rangle \tag{2.22}$$

where $r = |r_x\vec{e}_x + r_y\vec{e}_y + r_z\vec{e}_z|$. Very often autocorrelation functions are considered in the dimensi-

[1] Later the angular brackets will represent space-averaging.

(a) (b)

Figure 2.3: a) Autocorrelation function and corresponding integral scale, l_0 and Taylor's micro scale, λ (adapted from Chassaing, 2000, p. 55). b) Sketch of the correlation functions B_{LL} and B_{NN}.

onless form, normalizing $B(r)$ by the velocity variance at position (x,y,z):

$$R(r) = \frac{\langle u(x,y,z)u(x+r_x,y+r_y,z+r_z)\rangle}{\langle u(x,y,z)^2\rangle}. \tag{2.23}$$

The typical shape of $R(r)$ is depicted in Figure 2.3a). The integration of this function leads to the definition of the so called integral length scale of the turbulent flow, l_0,

$$l_0 = \int_0^{\text{inf}} R(r)\mathrm{d}r, \tag{2.24}$$

which is the distance where there is an appreciable correlation between the values of the flow field at two points. This distance is of the order of the size of the largest eddies present in the flow field.

Another scale of interest, also based on the autocorrelation function, corresponds to the intersection on the horizontal axis (λ) of the osculating parabola tangent to the autocorrelation function at the origin peak for $r = 0$ (Monin & Yaglom, 1975, p.35). This scale λ, represented in Figure 2.3a), is defined as

$$\left(\frac{\partial^2 R(r)}{\partial r^2}\right)_{r=0} = -\frac{2}{\lambda^2}. \tag{2.25}$$

Monin & Yaglom (1975) named this scale λ as the differential length scale, but it is also often referred as Taylor's micro scale.

The concept of the correlation function was introduced for a scalar field, it is now convenient to extend it to multidimensional isotropic random fields. For that case, a correlation matrix is

defined by

$$\|B_{lj}(r)\| = \| \left\langle u_l(x,y,z)u_j(x+r_x,y+r_y,z+r_z) \right\rangle \| \tag{2.26}$$

in which all the elements depend only on $r = |r_x\vec{e}_x + r_y\vec{e}_y + r_z\vec{e}_z|$ (Monin & Yaglom, 1975, p. 36). When dealing with the tensor B_{lj}, it is convenient to consider a special set of coordinates in which the first axis lies along the direction of the increments, r, while the two other axes are perpendicular to that direction. Due to the isotropic condition it is possible to prove (see Monin & Yaglom, 1975, p. 38) that B_{lj} is a symmetric tensor with only two nonequal components defined by

$$B_{11} = B_{LL}(r) = \langle u_L(\alpha)u_L(\alpha+r)\rangle \tag{2.27a}$$

$$B_{22} = B_{33} = B_{NN}(r) = \langle u_N(\alpha)u_N(\alpha+r)\rangle \tag{2.27b}$$

where α is a generic space point, u_L and u_N denote the projections of the velocity vector on the direction of r and on any perpendicular direction, respectively (see Figure 2.3b). B_{LL} and B_{NN} are called the longitudinal and transverse correlation functions and they relate to each other by (Monin & Yaglom, 1975, p. 49)

$$B_{NN}(r) = B_{LL}(r) + \frac{r}{2}\frac{\partial B_{LL}(r)}{\partial r}. \tag{2.28}$$

For the same referential, the two point longitudinal and transverse second-order structure functions, S_{2L} and S_{2N} respectively, are defined as

$$S_{2L}(r) = \left\langle \left(u_L(\alpha+r) - u_L(\alpha)\right)^2 \right\rangle \tag{2.29a}$$

$$S_{2N}(r) = \left\langle \left(u_N(\alpha+r) - u_N(\alpha)\right)^2 \right\rangle \tag{2.29b}$$

Within HIT conditions, the correlation functions and the second-order structure functions are related as follows (Monin & Yaglom, 1975, p.100)

$$S_{2L}(r) = 2\left(B_{LL}(0) - B_{LL}(r)\right) \tag{2.30a}$$

$$S_{2N}(r) = 2\left(B_{NN}(0) - B_{NN}(r)\right) \tag{2.30b}$$

Concerning second-order structure functions, an important result was analytically devised from Kolmogorov hypotheses, the two-thirds law (Monin & Yaglom, 1975, pp. 353-354). This states that in any turbulent flow with sufficiently large Reynolds number, the mean square of the velocity difference between two points separated by a distance r should be proportional to $\langle\varepsilon\rangle^{2/3} r^{2/3}$, for $l_0 \ll r \ll \eta$, where $\langle\varepsilon\rangle$ is the mean dissipation rate of TKE, and η stands for the

Kolmogorov length scale. Hence, there is a particular range of scales, where HIT conditions are normally valid, for which longitudinal and transverse second-order structure functions can be written as

$$S_{2L}(r) = C_{2L} \langle \varepsilon \rangle^{2/3} r^{2/3} \tag{2.31a}$$

$$S_{2N}(r) = C_{2N} \langle \varepsilon \rangle^{2/3} r^{2/3}, \tag{2.31b}$$

respectively. C_{2L} and C_{2N} are dimensionless constants.

Alternatively to the size of the eddies, one can work with wavenumber, k, passing from the physical to the spectral space by means of Fourier transforms. The energy spectrum, in the spectral domain, is related to the correlation function as follows

$$E_L(k) = \frac{1}{2\pi} \int_{-\infty}^{+\infty} e^{-ikr} B_{LL}(r) \mathrm{d}r \tag{2.32a}$$

$$E_N(k) = \frac{1}{2\pi} \int_{-\infty}^{+\infty} e^{-ikr} B_{NN}(r) \mathrm{d}r \tag{2.32b}$$

where E_L and E_N are longitudinal and transverse one-dimensional energy spectra, respectively, and i is the imaginary unit. The energy spectrum is a convenient way to evaluate how the energy is distributed across the various eddy sizes (Davidson, 2004, p. 91).

An equivalent law to the two-thirds law can be formulated in terms of energy spectrum (Monin & Yaglom, 1975, p.355)

$$E_L(k) = C_L \langle \varepsilon \rangle^{2/3} k^{-5/3} \tag{2.33a}$$

$$E_N(k) = C_N \langle \varepsilon \rangle^{2/3} k^{-5/3} \tag{2.33b}$$

where C_L and C_N are dimensionless constants. This relation, often called $-5/3$ law, is valid only for wavenumbers, k, within a particular range of scales, called the inertial range of scales. Typically, turbulence extracts energy from the mean flow at large scale while viscous dissipation of turbulent energy occurs at very small scales. Between these two extreme eddy scales there is a range of scales which are not directly affected by the energy maintenance and dissipation mechanisms (Tennekes & Lumley, 1972, pp. 248-274). This is the so called inertial range, where both the $2/3$ and the $-5/3$ laws are valid, and where merely transfer of energy, from production processes to dissipation processes, occurs.

Briefly, and in a simplified way, the energy spectrum of turbulence can be defined in three scale ranges. The energy-containing eddies correspond to the range with eddy sizes of the order of the integral length scale, corresponding, normally, to anisotropic scales. Then, there is a flux of energy from larger to smaller eddies, within the inertial range, where the eddies are expected to be isotropic, since the turbulent motion is increasingly "scrambled" at small scales and the

sense of direction is lost. This is the concept of local isotropy proposed by Kolmogorov (1941b). In that range of scales, there are no gains or losses of energy and the total amount of energy transferred down in the cascade process should be equal to the dissipation rate $\langle\varepsilon\rangle$. Therefore, the inertial range is also called the equilibrium range. Finally, at the end of the energy cascade, at very small scales, the energy is dissipated into heat (Tennekes & Lumley, 1972, pp. 248-274).

Kolmogorov (1941a) introduced one of the most important results of the HIT, developing a relation between second- and third-order structure functions and the mean dissipation rate of TKE as follows

$$S_{3L}(r) = -\frac{4}{5}\langle\varepsilon\rangle r + 6\nu\frac{\partial S_{2L}(r)}{\partial r} \tag{2.34}$$

where S_{3L} is the third-order structure function, which is defined by

$$S_{3L}(r) = \left\langle (u_L(\alpha+r) - u_L(\alpha))^3 \right\rangle. \tag{2.35}$$

This is a very important analytical result since it allows the estimation of the dissipation rate of TKE directly from the structure functions, without requiring any constant or major simplifications. Since normally the locally isotropic condition is applied in the inertial range of scales, where viscous friction should not play an important role, the previous equation is often simplified to

$$S_{3L}(r) = -\frac{4}{5}\langle\varepsilon\rangle r, \tag{2.36}$$

which is termed as the "$-4/5$ law" (Frisch, 1995, p. 86). Equation (2.36) provides a straightforward way to calculate the rate of dissipation $\langle\varepsilon\rangle$ provided that there is local isotropy, in the sense of Monin & Yaglom (1975). In that case, there is a sufficiently large range of scales where the linear behaviour of S_{3L} is evident. This estimate of $\langle\varepsilon\rangle$ is particularly interesting since, coming from a third order moment, it is non susceptible to be affected by white noise, typically introduced by most instrumentation.

Chapter 3

Experimental work

3.1 Introduction

The purpose of the experimental work, in the scope of the present doctoral research project, is the characterization of the turbulent flow within arrays of rigid and emergent cylinders, simulating boundaries populated with rigid vegetation. Hence, the experimental tests were designed to measure instantaneous velocities from which turbulent quantities are derived.

The experimental work was carried out in two laboratory facilities: three tests were carried out at the Laboratory of Hydraulics and Environment of Instituto Superior Técnico (IST) in Lisbon, Portugal, acquiring 2D velocity maps with a Particle Image Velocimetry (PIV) system; and one test was reproduced at the Laboratory of Leichtweiß Institute for Hydraulic Engineering and Water Resources at Technische Universität Braunschweig (LWI) in Germany, where 3D point-wise velocity series were acquired with Laser Doppler Anemometry (LDA). The measurements with PIV included velocity acquisitions in horizontal and vertical planes.

Three experimental tests were performed. Two had a constant areal number-density of stems and one presented spatially varying stem areal number-density. The latter was the test reproduced in both facilities. For all tests, the flow was gradually varied, accelerating in the downstream direction.

The present chapter describes the laboratory facilities, instrumentation and experimental tests. It starts with the description of both laboratory facilities and an overview of the instrumentation used. Then, a description of the PIV follows, including a literature review of the key points of this instrumentation, as well as a justification for parameters chosen in the framework of this thesis. The PIV description is followed by a description of the main principles of LDA instrumentation. The last section presents the experimental procedures including the description and characterization of the tests performed.

Figure 3.1: Schematic view of the recirculating tilting flume at IST.

3.2 Laboratory facilities

3.2.1 The flumes

At IST, the experimental work was performed in a recirculating tilting flume (CRIV). This is a 12.5 m long, 40.8 cm wide and 50 cm tall prismatic channel with adjustable slope in the range -0.5% to $+2.5\%$. The channel has side walls made of glass, enabling flow visualization and laser measurements. During the experiments, the channel was horizontal and the bottom was covered with a horizontal layer of gravel and sand. Over the gravel bed, rough, vertical and rigid cylinders with 1.1 cm of diameter were randomly placed to simulate regions populated with rigid vegetation. A general view of the CRIV is shown in Figure 3.1.

The recirculation circuit of CRIV is composed of:

i. four storage and inertia communicating tanks of equal capacity of 1.1 m^3;
ii. a water recirculation PVC pipe system with 200 mm diameter;
iii. a centrifugal pump whose maximum discharge is 28 l/s.

As accessories, the recirculation circuit has (i) a valve upstream of the pump, (ii) a valve in the compression conduit, used to control the discharge and (iii) a 0.01 l/min precision digital electromagnetic flow meter.

At the channel inlet there is a wooden stabilizer to reduce fluctuations of the free-surface due to the upward movement of the flow leaving the pressure circuit. At the outlet, there are two orifices to discharge the flow into one of the inertia tanks. The water is pumped from an intermediate tank minimizing the air entrainment into the recirculation circuit.

CRIV is equipped with a manually operated gate at the outlet. However, during the experimental work the flow was controlled by a coarse gravel weir, avoiding the generation of a recirculation pattern towards upstream of separated flow.

(a) (b)

Figure 3.2: a) View from downstream of the vegetated reach and b) lateral view of the coarse weir, at IST flume.

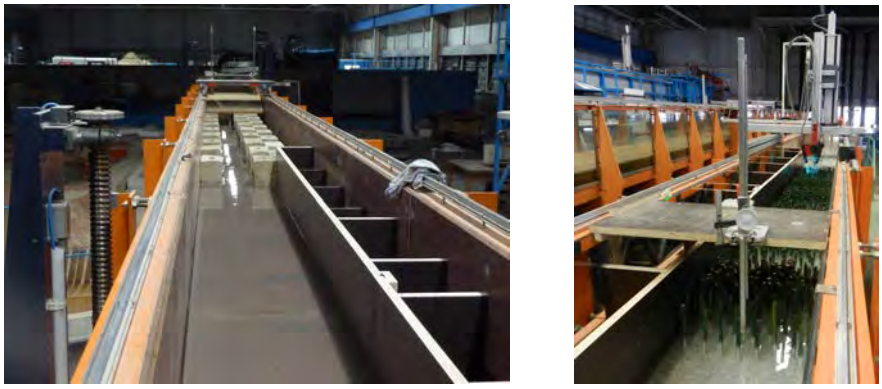

(a) (b)

Figure 3.3: a) Upstream part and b) the vegetated reach of the flume at LWI.

At LWI, the flume where experiments were carried out has a length of 32 m, is 0.6 m wide and 0.4 m high. It is a tilting flume with slope adjustable between -1% and $+4\%$. This channel has also side glass walls. In the experiments the flume was kept horizontal and its width was reduced to 0.40 m in order to reproduce the conditions at IST's laboratory. Figure 3.3a) presents a picture of the upstream part of the flume; it shows the solution applied to narrow the original flume's width. At the entrance of the flume, concrete cubes were alternately place at each side of the flume to destroy the flow structures created by the narrowing of the flume. Figure 3.3b) shows the reach covered with stems, showing also the point gage used to measure the bed topography and the transverse system used to displace the LDA probes. Here, the flow depth was also controlled by a coarse gravel weir positioned downstream, to enforce the same water depths as in the test of the CRIV flume.

The flume is connected to the laboratory recirculating system. At LWI there is a 25 m^3

Figure 3.4: Traverse system used at LWI for positioning the LDA probes.

elevated water reservoir with constant level, from where the water is gravitationally conducted to the flume. The discharge is controlled by a valve and measured by an inductive flowmeter. From the flume's outlet, the water is then conveyed to a reservoir in the underground of the laboratory.

The LWI-flume was equipped with a traverse system which allowed the automatic positioning of the LDA probes during the experiments. This automated system, shown in Figure 3.4, was controlled by the LDA system software, BSA Flow from Dantec®.

Before starting the experiments, preparation works were performed in both flumes to guarantee the adequacy of the experimental conditions. For this purpose, velocity measurements were performed to verify the symmetry of the flumes as well as preliminary tests to evaluate the sensitivity of the instrumentation.

For the experiments in both flumes, arrays of rigid, cylindrical and vertical stems were randomly placed along a 3.5 m long reach simulating rigid vegetation conditions, herein called vegetated reach. The diameter of the cylindrical elements was 1.1 cm. To enable the velocity measurements, gaps (narrow regions without stems in the spanwise direction) were enforced, whose width was equal to the mean inter-stem distance of the upstream reach. These gaps will herein be designated by “measuring gaps".

Upstream of the vegetated reach there was a reach, about 4 m long, where the bed consisted of a horizontal layer of gravel and sand, with the same roughness of the bed in the vegetated reach, to develop the flow. The sand mean diameter was 0.8 mm while the gravel mean diameter was 7.5 mm. Upstream of this reach, at the flume's inlet a reach with larger gravel ($3-5$ cm of diameter) was used to accelerate the development of the flow boundary layer. Figure 3.5 illustrates the longitudinal profile of the flumes during the experiments and shows details on the stem's placement.

All the experiments were carried out with a discharge of 2.3 l/s and the flow was subcritical

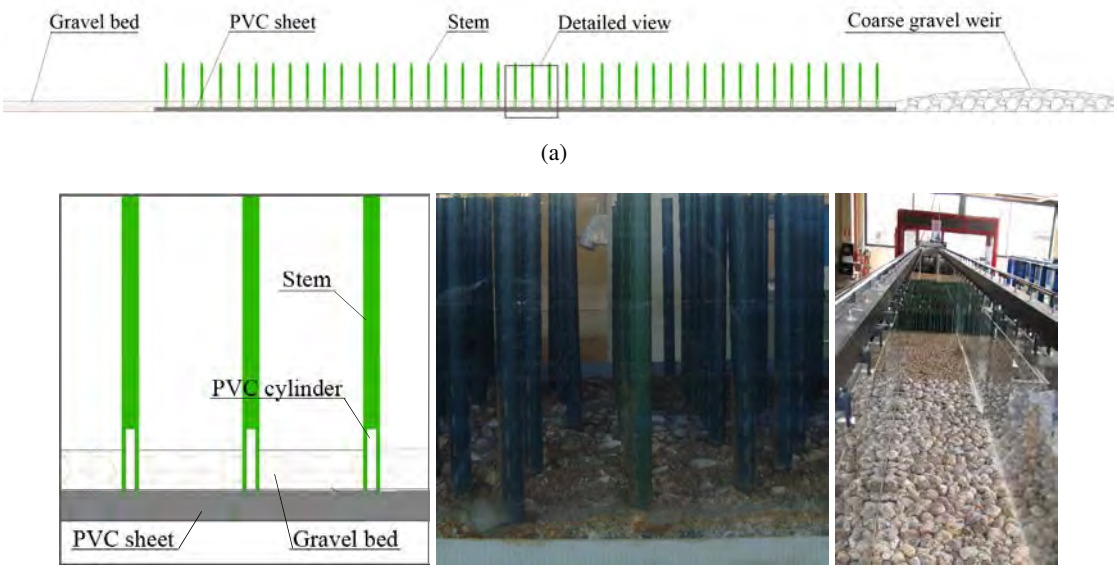

Figure 3.5: a) Scheme of the longitudinal profile of the flumes during the experiments; b) detail of the stem mounting; c) picture of stems and bed during the tests; and d) an view of IST's flume from upstream.

both downstream and upstream of the vegetated reach.

The techniques employed to measure velocities, PIV and LDA, are particle-based techniques, since they rely on the presence of particles following the flow. The corresponding particles were added in the flow during the experiments. At IST, an elevated funnel, equipped with a tap, was filled with a mixture of water and seeding before PIV acquisitions. The seeding mixture is projected against a PVC plate before entering into the flow in order to fasten the mixing with the main flow. The apparatus was placed at the flume's inlet and it is presented in Figure 3.6 a). At LWI, the particles were mixed in water in a 200 l container, where a two-blade mixer was rotating to avoid seeding deposition. The seeding mixture was pumped into the flume at a constant discharge. Also at LWI, the seeding mixture was projected against a plate before entering into the main flow. A picture of this apparatus is shown in Figure 3.6b).

3.2.2 Instrumentation

The experimental work required the measurement of:

i. instantaneous velocity maps;
ii. bed topography;
iii. free-surface elevation;
iv. water temperature.

(a) (b)

Figure 3.6: Apparatus for the introduction of seeding particles in the flow a) at IST and b) at LWI.

Temperatures were regularly measured by means of a digital thermometer (Figure 3.7b) in order to compute the water viscosity according to Likhachev (2003).

Regarding the bed and free-surface elevation, at IST's facility, the measurements were carried out with a high precision laser displacement sensor, the LK-2501 model commercialized by Keyence® (Figure 3.7c). This equipment consists in a IIIb class laser head connected to a high-precision controller. Displacements are obtained by triangulation: the laser beam is reflected off the target surface and is received by a lens system also included in the laser head. The beam is focused on a CCD sensing array which detects the peak value of the light quantity distribution of the beam spot. This equipment has 50 μm of repeatability and the beam spot diameter is 0.3 mm at the reference distance (500 mm). The output is a voltage on the range $\pm$5 V which is linearly converted into the metric system $(50\ \mu\mathrm{m/mV})$. To measure the free-surface level a very small and opaque plastic sheet was placed on the measuring point. It should be noticed that the piece of plastic did not interfere much with the free-surface oscillations.

At LWI, the bed topography was measured with a 0.1 mm precision point gage (Figure 3.3b). The averaged free-surface longitudinal profile was also measured with the point gage. Since the free-surface within the array of cylinders present oscillations, extra measurements were performed acquiring images of the free-surface with a digital camera . During the recordings, there was a ruler on the flume's wall on the field of view (Figure 3.7d). Then, with image processing tools the oscillations of the free-surface were quantified. The digital camera used was a uEye UI-2230RE-M model, commercialized by IDS ®, which has a monochromatic CCD sensor with 1024×768 px^2 of resolution. Its maximum acquisition frequency corresponds to 30 Hz.

Concerning velocity measurements, 2D instantaneous velocity maps were acquired with a Particle Image Velocimetry (PIV) system at IST and 3D point-wise velocity measurements were

(a)

(b)

(c)

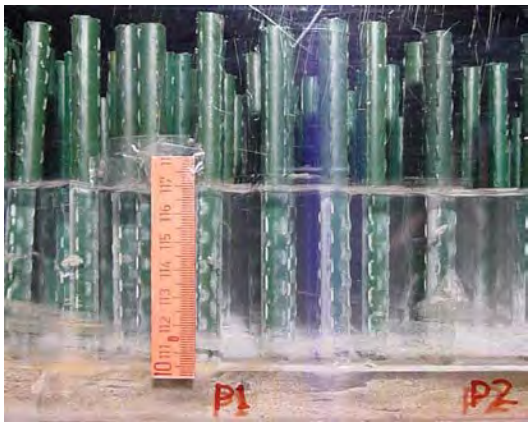

(d)

(e)

Figure 3.7: a) PIV laser head; b) digital thermometer; c) laser displacement sensor; d) ruler used to measure free-surface levels with video images; e) uEye camera used to measure free-surface levels and f) probes during LDA velocity measurements.

performed with Laser Doppler Anemometry (LDA) at LWI. Details about those techniques are presented in the following sections.

3.3 PIV: Particle Image Velocimetry

3.3.1 Historical notes and basic principals of PIV

PIV is an optical technology that allows the recording of instantaneous velocity flow fields, by measuring the displacement of small tracer particles (also called seeding particles) that are carried by the fluid in short time periods. Therefore, the tracer particles must be sufficiently small and density close to the water density in order to accurately follow the fluid motion and not to alter the fluid properties or flow characteristics.

From the operational point of view, PIV is a very simple technique consisting in a laser illuminating a part of the flow and a camera recording the position of the illuminated tracer particles. Therefore, the first form of PIV could be traced far back in history to the first time someone possessing the concept of velocity watched small debris moving on surface of a flowing stream (Adrian, 2005). PIV appeared in literature in the mid-1980s (Adrian, 1984; Lauterborn & Vogel, 1984; Pickering & Halliwell, 1984) when the name *Particle Image Velocimetry* was introduced to distinguish the illumination of particles in fluid flows by a light sheet from laser speckle operation mode. Many researchers became interested in PIV because it offered a new and highly promising means of studying the structure of turbulent flows (Adrian, 2005). In fact PIV enables velocity measurements over a wide dynamic range of scales in length and velocity, to sense flows in more than one direction and to calculate velocity gradients and thus out-of-plane vorticity (Adrian, 2005; Ferreira, 2011). According to Adrian (2005), 30 years ago in the first steps of PIV the major issue concerned the energy necessary to illuminate fine particles and produce images of sufficient exposure and clarity. However promoted by the fast technological growth in computer architecture and digital cameras, PIV has developed significantly in the past 15 years and it is, nowadays, widely used in fluid mechanics in the research of air and water flows.

The classic PIV can only measure the projection of the velocity into the plane of the light sheet. That may result in large errors for measurements of highly 3D flows since the out-of-plane velocity is lost and the in-plane components are affected by perspective transformation (Raffel *et al.*, 2007). Some approaches capable of recovering the 3 velocity components have been proposed, as stereoscopic PIV or holographic PIV, employing an additional camera. However, these approaches increase significantly the cost of a PIV system (which is already expensive) and they are not necessarily easy to implement. Details about stereoscopic PIV can be found in Raffel *et al.* (2007).

PIV has also been extended to microscopic length scales applying the principles of PIV to design systems with spatial resolution of the order of the micron (Raffel *et al.*, 2007, pp. 241-258). This system is known as micro-PIV or μPIV and it is specially interesting in biomedical research.

The description of PIV systems herein presented is based on the 2D "classic" mode as in the reported experimental work was used a classic PIV commercialized by Dantec®. Due to the fact that the quality of PIV measurements depends mostly on data processing there is a considerable body of literature describing PIV hardware, methods and algorithms. Comprehensive reviews can be found in Adrian (1991); Raffel *et al.* (2007); Tropea *et al.* (2007) and references herein can be followed for more specialized issues.

An important advantage of PIV system is its intrusiveness, which is limited to the introduction of the solid targets (seeding) in the flow that may affect flow or fluid particles; in general, no material parts of the instrumentation are needed in the flow region under measurement. Although the acquisition of raw data is relatively simple, PIV relies heavily on software for the analysis of that data, which is a disadvantage of this measuring system. Another weak point of PIV is the large processing time required for the first step of raw data analysis. The process of converting the acquired images into instantaneous velocity fields conveniently calibrated in metric units and referenced to the channel coordinate system is, normally, very slow. This process will be explain in the next subsections.

3.3.2 Components of PIV

The PIV system, schematically represented in Figure 3.8, is typically composed of:

i. laser head and lens (Figure 3.9a);
ii. power supply or laser beam generator (Figure 3.9b);
iii. digital camera (Figure 3.9c);
iv. timing unit (Figure 3.9d);
v. acquisition and control software (Figure 3.9e).

The seeding particles, normally added to the flow, are illuminated twice in a short period of time by means of a thin light sheet from a pulsed laser and the light scattered by the particles is captured by a digital camera onto subsequent image frames by a digital camera. The timing unit ensures the synchronization between the light emission by the laser head and the image acquisition by the camera. The laser beam generator controls the power and the production of the laser light and it includes a cooling system. The whole system is, usually, controlled by means of a software. The PIV system used in this research project was operated with a sampling rate of 15 Hz and its power source is able to generate a pulse of energy of 30 mJ.

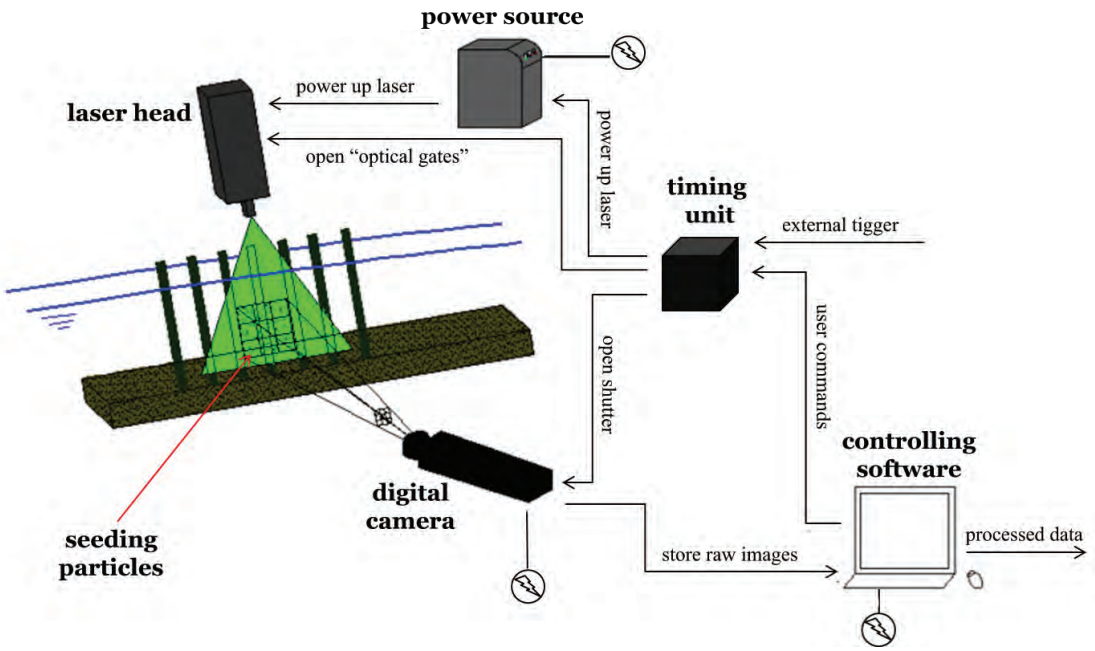

Figure 3.8: Schematic representation of PIV components.

Lasers are widely used due to their ability to emit monochromatic light with high energy density, that can be bundled into thin light sheets allowing the lightning of the seeding particles without chromatic aberrations. A laser consists on the laser material (atomic or molecular gas, semiconductor or solid material), the pump source which excites the laser material and the resonator achieved by mirror arrangement (Raffel *et al.*, 2007, pp. 28-29). The broadly used word *laser* has its origins in the acronym for the expression "Light Amplification by Stimulated Emission of Radiation".

The laser source of the PIV system used in this work is a double-cavity Nd:YAG laser (Neodymium-doped Yttrium Aluminium garnet), which is the most commonly used laser in modern commercial PIV systems. It is a four-level system which has the advantage of relatively low laser threshold. Nd:YAG lasers are solid-state lasers (subjected to optical pumping) with high amplification and good mechanical and thermal proprieties. This type of laser is sensitive to temperature, but for standard operating temperatures it emits at the strongest wavelength, 1064 nm in the infrared spectrum.

A pulsed laser is obtained by a quality switch (Q-switch) inside the cavity, operated in a software-controlled triggered mode. Although Q-switches can be used to generate more than one pulse out of one resonator, PIV lasers are generally associated to double oscillators, which enables the user to adjust the time gap between two illuminations of the tracer particles independently of the pulse strength. The double cavity lasers include a second harmonic generator (nonlinear crystal) which converts infrared light of 1064 nm into green light of 532 nm, during a so called

(a) (b)

(c) (d) (e)

Figure 3.9: Photos of PIV components: a) laser head; b) laser beam generator; c) CCD camera; d) timer box and e) DynamicStudio software.

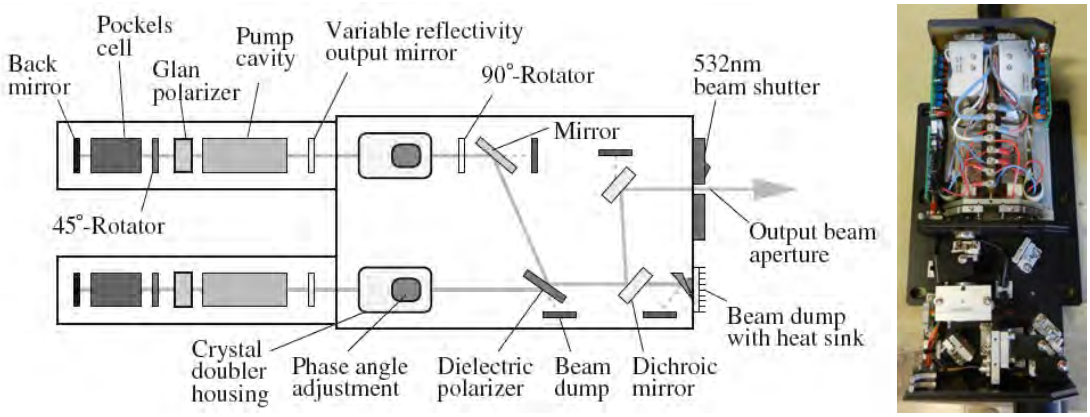

(a) (b)

Figure 3.10: a) Scheme of a double cavity laser head (from Raffel *et al.*, 2007, p. 40); b) Picture of the double cavity laser head o the PIV system used in this work.

phase matching. The cooling system is an essential feature in the phase matching process, as stable temperatures are required due to the refractive index sensitivity to temperature changes (Raffel *et al.*, 2007).

The laser beams from each cavity are then conveyed to the output optics through a system of mirrors, reflectors and shutters, as represented in Figure 3.10. At the output optics, the laser beams are passed through prismatic lenses to generate laser sheets. In the present case, a cylindrical lens produces the laser sheet. This lens is placed in an small cylindrical box attached to the laser head allowing the orientation of the light sheet.

The choice of the cameras used to acquire the images with illuminated seeding particles is very important, since the optical and electronic characteristics of sensors have a direct influence on the technical possibilities in PIV recording and the accompanying error sources (Raffel *et al.*, 2007, p. 69). The camera's sensors most commonly used in PIV systems are charge coupled device (CCD) or complementary metal oxide semi-conductor (CMOS). CCD sensors operate with photoelectric effect at each pixel, converting light (photons) into electric charge (electrons). The charge of each pixel is then transferred through the same output node, which is relatively slow but reliable (not prone to noise). This type of sensor is susceptible to pixel burning due to well saturation (Raffel *et al.*, 2007, p. 69). In CMOS devices each pixel has its own charge-to-voltage conversion node. This type of digital cameras are highly sensitive and fast but tend to be prone to noise and susceptible to image deformation (Raffel *et al.*, 2007, p. 71).

Digital image sensors are, as any electronic device, subject to noise. Thermal and read noise are the most common noise sources in the classic PIV systems. Thermal noise is related to the electron-hole pairs generated by thermal effects which cannot be separated from the electron-hole pairs generated by the photoelectric effect. The consequence is that weak particle images

cannot be distinguished from noise. The read noise (or shot noise) is a direct consequence of the charge-to-voltage conversion during the readout sequence, which increases with the readout frequency (Raffel *et al.*, 2007, p. 72).

In this work, an 8-bit and $1600 \times 1200\text{px}^2$ CCD camera (Figure 3.9c) was used. The sensor is only sensitive to light intensity, *i.e.*, the amount of energy. To maximize the contrast between the bright illuminated particles and the black background in the recorded images, the flume was covered with black fabrics. The camera was positioned perpendicularly to the laser sheet in order to acquire images of the region lightened by the laser minimizing the distortion effects.

The PIV systems used in this work was commercialized by Dantec®, therefore the software used to control the data acquisition and to process the raw data was the DynamicStudio®. This software allows the user to control the acquisition mode, to set the time between consecutive pulses and the acquisition time. It also offers several control variables for the data processing.

3.3.3 Seeding particles

Unquestionably, the solid targets added into the flow play a crucial role in the quality of the data acquired with PIV, since this technique relies on the fact that the solid particles follow all the flow velocity fluctuation. Therefore, the particles' properties have to be carefully examined to avoid significant discrepancies between fluid and particle motion. Seeding particles are ideally neutrally buoyant, non-inertial, non-toxic, non-corrosive, non-abrasive, non-volatile, chemically inactive and clean (Melling, 1997; Raffel *et al.*, 2007). It is desirable that the particles are small enough for a good tracking of the flow and at the same time good light scatters, since this improves the quality of signal. Since light scattering improves with increasing particle size a compromise is required when choosing seeding particles.

For the present work a polymerized material, commercially named Decosoft 60, with a mean diameter of 60 μm in a range from 50 μm to 70 μm was used as seeding. It is a white material with round shaped particles and its chemical composition consists in 73% of polyurethane and 27% of titanium dioxide. The density of this seeding is 1.31g/cm^3.

According to Melling (1997), it is possible to evaluate the suitability of the seeding particles to follow a specific flow and, hence, to determine the smallest turbulent eddies that can be identified, evaluating the ratio r_p defined by

$$r_p = \frac{\overline{V_p^2}}{\overline{V^2}} \tag{3.1}$$

where $\bar{V_p}$ is the modulus of seeding terminal fall velocity and $\bar{V}$ is the modulus of flow velocity. The seeding particles are able to perfectly track the flow when $\overline{V_p^2} = \overline{V^2}$, however Melling (1997)

proposed a threshold of acceptability of $r_p = 0.95$.

This ratio, r_p, can be determined through the solution proposed by Hjemfelt & Mockros (1996) for the limit case in which the density of the seeding particles is much larger than the water density $\left(s^{(p)} \gg s^{(w)}\right)$:

$$\frac{\overline{V_p^2}}{\overline{V^2}} \equiv r_p = \left(1 + \frac{2\pi f_c}{C}\right)^{-1} \tag{3.2}$$

with

$$C = \frac{18\nu}{s^{(p)} d_p^2} \tag{3.3}$$

where f_c is the frequency of the characteristic turbulent structures of the flow, d_p is the diameter of the seeding particles and ν is fluid's kinematic viscosity. Equation (3.2) expresses the ability of the seeding particle to follow the fluid's turbulent micro-structure whose scale is f_c (expressed in terms of frequencies) as a function of the density and the diameter of the particles. The application of equation (3.2) is justifiable for its conceptual simplicity as it retains the most important effects of drag and inertia (Melling, 1997). Since in most cases the density of the seeding particles is not much larger than the water density, this model renders a conservative estimate of the tracers tracking ability.

Figure 3.11 shows the ratio r_p as function of the frequency f_c for the seeding particles used in the present work. The graph represents the curves for the mean $(60\ \mu\text{m})$ as well as the limits of the range $(50$ and $70\ \mu\text{m})$ of particles diameters. As it can be observed in Figure 3.11, $r_p = 0.95$ corresponds , in the graph for $d_p = 60\ \mu$m, to $f_c = 30$ Hz meaning that the employed seeding is suitable to detect turbulent structures with frequencies lower than 30 Hz. Since the PIV was operated at 15 Hz, the Nyquist frequency is equal to 7.5 Hz. Therefore, it can be concluded that the seeding particles used ensure the quality of the data acquired in the time domain. In the space domain, applying Taylor's frozen turbulence hypothesis (Tennekes & Lumley, 1972, p. 253) and considering a mean velocity of 0.10 m/s, the frequency $f_c = 30$ Hz corresponds to a turbulent length scale $\lambda_c = 3.3$ mm. This means that the velocity of eddies smaller than 3.3 mm may be measured with less than 95% confidence employing this material as seeding.

Regarding the scattering behaviour of the seeding particles, it depends on the ratio of particles' refractive index to that of the surrounding medium, the particles' size, shape and orientation, polarization and observation angle. Light scattering by small particles is a complex subject, herein only general aspects are commented. For details Van de Hulst (1957) can be referred to.

Typically seeding particles' diameter used in water flows is of the order of tens of micrometers, thus, larger than the incident light wavelength, λ (532 nm). This means that Mie's scattering theory applies ($d_p > \lambda$). According to this theory, the scattering of light on a particle can be

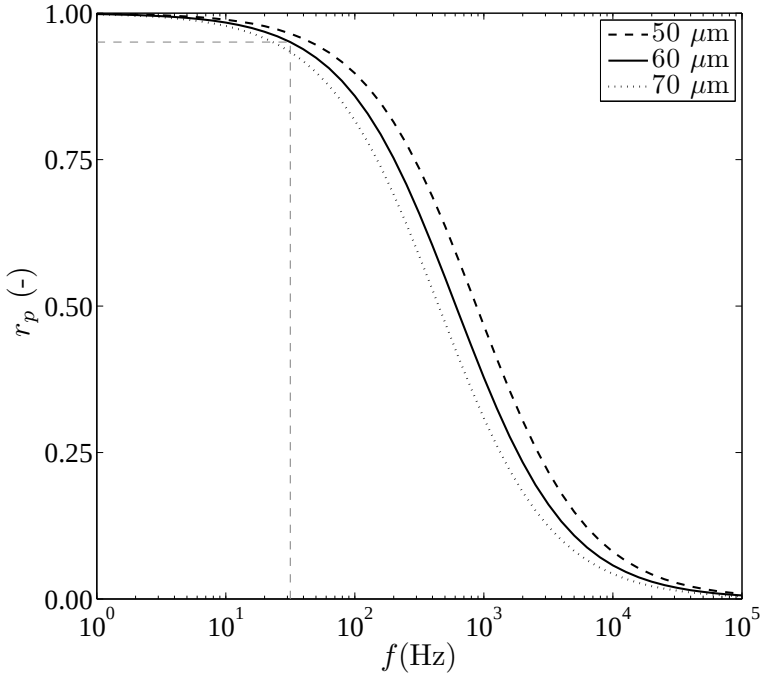

Figure 3.11: Ratio r_p as function of the frequency f_c for the solid targets used in the present experimental work.

characterized by the normalized diameter, q, defined by (Raffel *et al.*, 2007, p. 18)

$$q = \frac{\pi d_p}{\lambda} \tag{3.4}$$

Figure 3.12 exemplifies polar distributions of the normalized scattered light intensity for different diameters of glass particles in water, and an incident light wavelength $\lambda = 532$ nm. For increasing q the ratio of forward to backward scattering intensity increases rapidly, indicating that recording in forward scatter would be a better option, what is impossible in PIV. Scattering is poor at 90° but it is normally the most practical option for PIV, due to the limited depth of field. It can be observed from the Mie's scattering diagrams that there is a clear tendency for the increasing of the scattered light intensity with increasing particle diameter. The scattering efficiency can be increased not only by using larger particles but also by increasing the number of the particles. The light is not blocked by the particles but rather spread in all directions, therefore the light imaged by the recording lens is not only due to direct illumination but also due to light scattered by other neighbouring particles (Raffel *et al.*, 2007, p. 20).

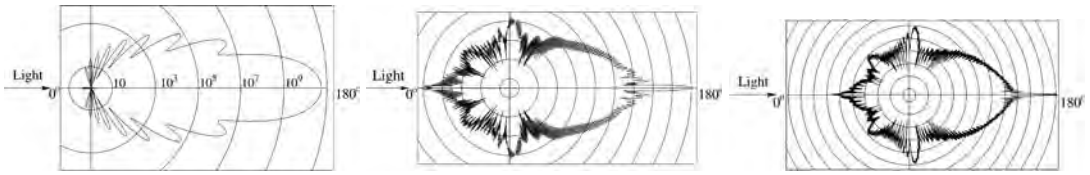

(a) $d_p = 1\ \mu$m (b) $d_p = 10\ \mu$m (c) $d_p = 30\ \mu$m

Figure 3.12: The polar distribution of the scattered light intensity for glass particles of diameter a) $d_p = 1\ \mu$m, b) $d_p = 10\ \mu$m and c) $d_p = 30\ \mu$m with incident light of wavelength $\lambda = 532$ nm, according to Mie's theory (from Raffel *et al.*, 2007, p. 20).

3.3.4 The measuring principle

As it has been mentioned, the PIV system generates quasi-instantaneous velocity maps by means of measuring small displacements of seeding particles between the light pulses, which are determined through the evaluation of the PIV recordings.

The recorded images are divided into small areas, designated interrogation areas (IA), as represented in Figure 3.13a). The displacements of the illuminated particles are obtained through the particles initial and final position within a given IA and for a given time between two consecutive laser pulses. If the lightened particles' mean longitudinal and vertical displacements, Δd_x and Δd_z respectively, in a given interrogation area centred at (x,z) are found, the longitudinal (u) and vertical (w) velocities, relatively to orthogonal axes parallel to the sides, are determined by (Ferreira, 2011)

$$u(x,z) \simeq \frac{(x+\Delta d_x)-x}{\Delta t} \tag{3.5}$$

$$w(x,z) \simeq \frac{(z+\Delta d_z)-z}{\Delta t} \tag{3.6}$$

where Δt is the time between two consecutive laser pulses, herein, referred as time between pulses. Since the time to register images is smaller than time between two pulses, one can assume that the computed velocity is a quasi-instantaneous velocity. Δd_x and Δd_z correspond to the averaged displacement of the particles within a IA, requiring smaller IA in order to minimize the smoothing effects to have velocity fields as much instantaneous as possible. Figure 3.13b) illustrates the measuring principle of PIV.

The key issue in PIV data processing is determining the mean planar displacements Δd_x and Δd_z in each interrogation area, with the least possible errors. Commonly, these mean displacements are determined by cross-correlation algorithms which correlate the gray levels between the two images resulting from two consecutive laser pulses Δt apart from each other. The most straightforward approach consists in dividing each image into non-overlapping square IA with side length N (normally taken as a power of 2) and then perform the two-dimensional

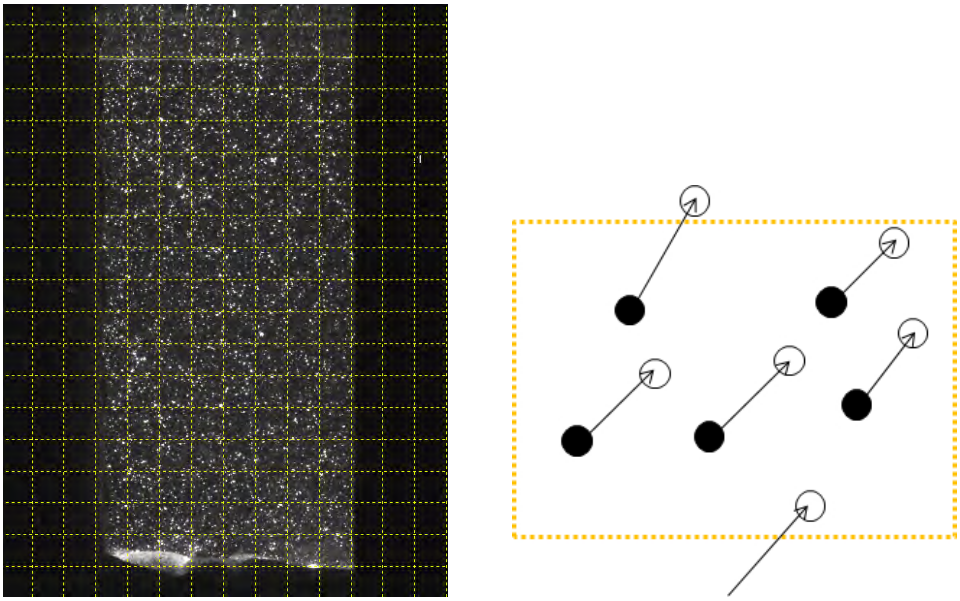

(a) (b)

Figure 3.13: a) Division into interrogation areas (IA) of an image acquired with PIV; b) Illustration of the displacement of particles inside of an interrogation area, where the open circles correspond to the position of the filled circles Δt s later.

cross-correlation of each IA in the image pair. This correlation process is often applied in the spectral domain (Sveen & Cowen, 2004). A cross-correlation algorithm can be, in a simple way, defined as a statistical function that measures the degree of match between two samples for a given shift. In the problem of determining the displacement of seeding particles within an IA, the samples correspond to the gray intensity levels and the cross-correlation function, R can be mathematically expressed by

$$R(x,z) = \sum_{i=-M}^{M} \sum_{j=-N}^{N} I(i,j)I'(i+x,j+z) \tag{3.7}$$

where I is the intensity level on the IA of the first frame, I' is the intensity level on the same IA of the second frame. I is shifted around in I' without extending over edges of the latter. For each choice of sample shift (x,z), the sum of the products of all overlapping pixel intensities produces one cross-correlation value $R(x,z)$. Note that x, z, i and j refer to the referential of the centre of the IA. By applying this operation for the range of shifts $-M \leq x \leq +M$ and $-N \leq z \leq +N$, a correlation plane is obtained, whose size is $(2M+1) \times (2N+1)$ (Raffel *et al.*, 2007, p. 134). The coordinates of the maximum value of R (correlation peak) corresponds to the mean planar displacements Δd_x and Δd_z. Then, the values of the displacements are divided by the time between pulses, Δt, to be converted into velocities. This process is repeated for every IA in the captured images.

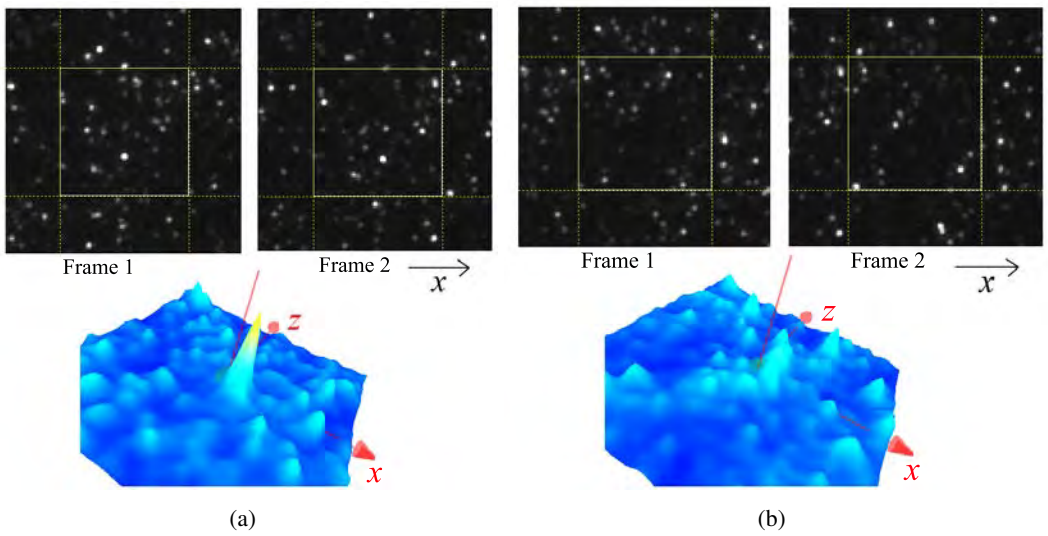

Figure 3.14: Examples of an IA in both frames and the respective correlation map. a) Case with a clear correlation peak corresponding to the particle's displacement; b) case with out-of-plane loss-of-pairs problem, where it is not possible to distinguish the peak of particle's displacement from the noise peaks.

Figure 3.14 shows two examples of correlation functions and the respective IA for both frames. In one of the cases a clear peak can be identified while the other case presents an ambiguous case with low signal-to-noise ratio, where it is not possible to distinguish the peak of particle's displacement from the noise peaks. The goal of this explanation about the cross-correlation was to expose the process required to obtain the velocity maps with PIV. However, it should be noticed that only the basic notions were introduced. The correlation algorithms are constantly improving to enhance their efficiency. There are many algorithms, but the most common are the algorithms based in simple cross-correlation or adaptive correlation.

Adaptive algorithms have been gaining popularity in recent years because they allow improvements on the spatial resolution and spatial accuracy while reducing velocity bias errors, in comparison to cross-correlation algorithms (Wereley & Meinhart, 2000). In adaptive correlation a large IA is employed first and subjected to simple cross correlation. The correlation peak is then used to re-center (offset) a smaller IA, again subjected to correlation. The process can be repeated while there is enough illuminated seeding particles in the IA. This technique is now standard and is especially useful when flow gradients are large. The first steps determine the direction of the flow and the last step finds the correct displacements even with few illuminated particles in the IA.

Often noisy IA conduct to spurious velocity vectors. Then to ensure good results, the last step to obtain the instantaneous velocity maps is applied. It is called validation and it consists in the comparison of the vectors with their neighbours. If they fail a verisimilitude test, they are substituted, generally by the mode or the median of the surrounding 8 vectors. A review on the

validation methods for PIV data is presented by Westerweel (1994) and Nogueira *et al.* (1997).

There are several error sources that may affect the quality of PIV measurements and that can be linked both to experimental conditions or to the processing method. Details on PIV error sources are presented by Keane & Adrian (1990), Westerweel (1993), Sveen & Cowen (2004) or Raffel *et al.* (2007). In general, the loss-of-pairs is the major source of errors, as the name suggests, this problem is caused by the particles that are not found in both of the frames. This problem can occur due to the particles, usually close to the limit of the IA, that leave or arrive to the IA in the interval between pulses. In this case, it is designated in-plane loss-of-pairs and is illustrated in Figure 3.13b). Moreover, particles that leave the laser sheet because of 3D motion are also a loss-of-pairs problem, in this case, named out-of-plane loss-of-pairs (Figure 3.14b). It should also be remarked that the better contrast between the illuminated particles and the background, the less noisy becomes the signal.

Several options can be considered at the processing stage to improve the quality of the results:

- The use of windows or filters may help to correct of in-plane loss of pairs and to enhance peak width.
- Consider overlapped IA results in denser vector map, improving the visualization of the flow field. Particles that were not considered in the correlation process because of in-plane-loss of pairs may be retrieved with mild overlapping. However, this adds little new information, overlapping is generally oversampling for better visualization.
- Adequate subpixel interpolation algorithms allow improvements on the accuracy of the location of the correlation peak (details in Lourenco & Krothapalli, 1995; Roesgen, 2003; Westerweel, 1993).

The data acquired in the scope of this research project was processed with adaptive correlation and a validation method based on the median of the neighbour vectors was applied. Adaptive correlation is time consuming but it renders to much better results that the simple cross-correlation. Simão *et al.* (2009) showed that with cross-correlation large IA would produce considerable errors while adaptive correlation is nearly insensitive to the IA size under the same conditions.

3.3.5 Control parameters of PIV

The quality of the velocity maps acquired with PIV technique depends on three correlated parameters: time between pulses (Δt), quantity of seeding and size of interrogation areas (IA).

In the case of adaptive correlation, a rule-of-thumb states that initial IA should have more than 12 seeding particles and the motion of the particles should be about 25% of the dimension of the final IA (Raffel *et al.*, 2007, p. 137). Therefore, the size of the IA depends on the quantity of particles that are seeding the flow and on the time between pulses; smaller IA require higher

density of seeding particles and lower Δt. The spatial resolution of the velocity maps increases with the decrease of the size of IA. Also the accuracy of the instantaneous velocity improves with smaller IA since the IA work as a filter removing the smallest scales of the turbulent motion. On the other hand, too small IA promote in-plane loss-of-pairs because they will have, in general, less particles which are more likely to be close to the boundary.

Generally, the increase of the quantity of seeding in the flow has a positive impact on the results; the drawback is that seeding particles are expensive. Nonetheless, if a flow can be densely seeded a high valid correlation peak detection is achieved and high signal-to-noise ratio are obtained.

Regarding the time between pulses, short intervals minimize the in-plane and out-of-plane loss-of-pairs but larger Δt increases precision.

Herein, the size of the IA was chosen to start at 128×128 px^2 and to finished at 16×16 px^2 after 3 iterations on the correlation process. This choice intended to maximize the spatial resolution of the velocity field. No overlap of the IA was considered, since it would significantly increase the computational time without improving the results. After choosing the IA's size, a sensitivity analysis was carried out to stablish the time between pulses. For the tested velocities, Δt in the range of $1250 - 1750$ μs satisfied the general rule of displacements around 25% of the dimension of the final IA. First and second order moments were evaluated for $\Delta t = 1250, 1500, 1750$ μs. Figure 3.15 presents time-averaged longitudinal velocity profiles for the tested Δt while Figure 3.16 shows profiles of Reynolds shear stresses. The velocity profiles do not seem very sensitive to the different time between pulses, however the Reynolds shear stresses show that $\Delta t = 1500$ μs renders smoother results. Thus, $\Delta t = 1500$ μs was adopted to all the performed PIV measurements. At last, the quantity of seeding was adjusted in order to have enough seeding particles for the IA's size chosen.

3.4 LDA: Laser Doppler Anemometry

3.4.1 Basic principles

Laser Doppler Anemometry, LDA, is a widespread technique for point-wise instantaneous velocity measurements also referred as Laser Doppler Velocimeter (LDV).

As PIV, LDA is an indirect technique, since it measures the velocity of small particles in the moving fluid. LDA is also a laser based technique, but unlike PIV, LDA employs the laser light in a direct way, making use of the Doppler effect as the laser light is scattered back to the receiver.

Among the advantages of the LDA techniques, the small intrusiveness, which is the result of the tracer particles introduction, the directional-sensitivity, the high temporal resolution and

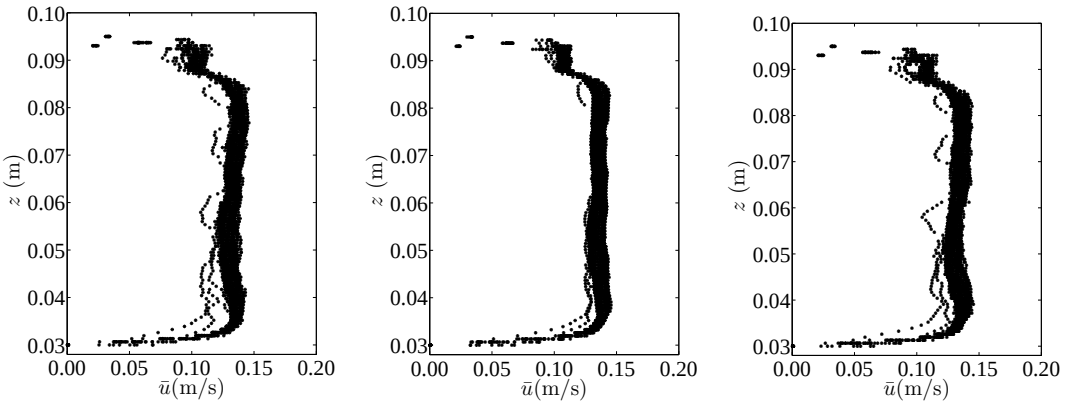

Figure 3.15: Time-averaged longitudinal velocity profiles of a lateral position acquired with time between pulses of a)1250 μs, b)1500 μs and c) 1750 μs.

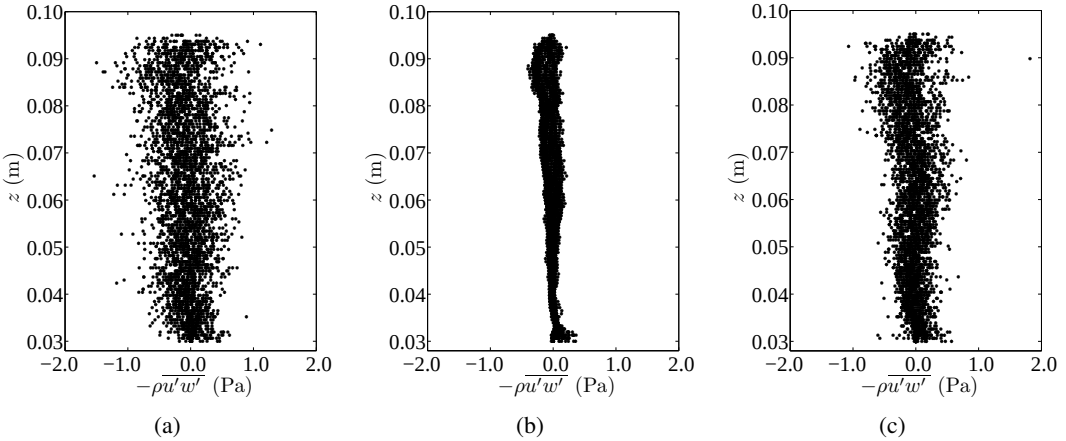

Figure 3.16: Time-averaged Reynolds shear stress profiles of a lateral position acquired with time between pulses of a)1250 μs, b)1500 μs and c) 1750 μs.

the high accuracy can be listed as decisive advantages. LDA techniques are based on complex chemical and electronic units and very sensitive optical systems with little software complexity.

According to Tropea *et al.* (2007) the first laser Doppler instrument was introduced by Cummins *et al.* (1964) and Yeh & Cummins (1964), in which an optical configuration was presented, subsequently known as the reference-beam mode. The dual-beam mode, used nowadays, was introduced few years later by vom Stein & Pfeifer (1969). In this configuration, two in-going laser beams crossing at an intersection angle were applied to create a measurement volume. The scattered light from the two beams was collected on a single detector.

Durst *et al.* (1976) published, in a book format, a comprehensive and detailed review on the measurement of instantaneous velocity by laser Doppler methods. This book, which is still an actual reference concerning LDA principles, outlines principles of geometrical, physical, and quantum optics, analyses light scattering, explains physically the optical measurement of particle velocity and introduces the principles of LDA. Also, optical arrangements for velocity measurement are described, the transform equation for a laser Doppler anemometer is derived, and principles underlying the definition of the measuring control volume are set forth.

Due to technological improvements, LDA systems have continuously been developed and the volume of literature on this technique is large and still increasing (Tropea, 1995). LDA systems started being increasingly applied in the scope of river hydraulics research since the 1980s.

The most common lasers employed in LDA systems are the He-Ne (Helium-Neon), typically at 632.8 nm, Ar-Ion (ions of Argon), normally operated in the blue or green spectra, and Nd:Yag (Neodymium-doped Yttrium Aluminum garnet), in the infrared spectrum. He-Ne and Ar-Ion lasers are gas-lasers, in which coherent light is produced by excitation of a gas by a strong electric current. As mentioned in the PIV section, Nd:Yag is a solid-laser.

An LDA system is composed by a continuous laser source, transmitting optics, receiving optics with photodetector, analogue filters and signal amplifiers, a signal processing unit and memory unit, as schemed in Figure 3.17. The laser beam is split before reaching the transmitting optics, normally by means of a Bragg cell (see Figure 3.17). The Bragg cell is composed of a glass crystal subjected to acoustic vibration, from which the zero and the first-order beams are used. Typical frequency shifts of the first-order beam are 40 MHz or 80 MHz. The shifted beam ensures that directional ambiguity is eliminated. The beams are focused in the transmitting optics in order to intercept in the measurement volume. A pair of beams of a given wavelength is necessary to measure a given velocity component. The receiving optics collects the light scattered by the particles in the measuring volume and conveys it to the photodetector. Generally, the diameter of the tracer particles is larger than the wavelength of the laser light, therefore, the light scattering obeys to the Mie's theory, explained above.

The basic principle of LDA applies the Doppler effect twice. First, when the incident laser

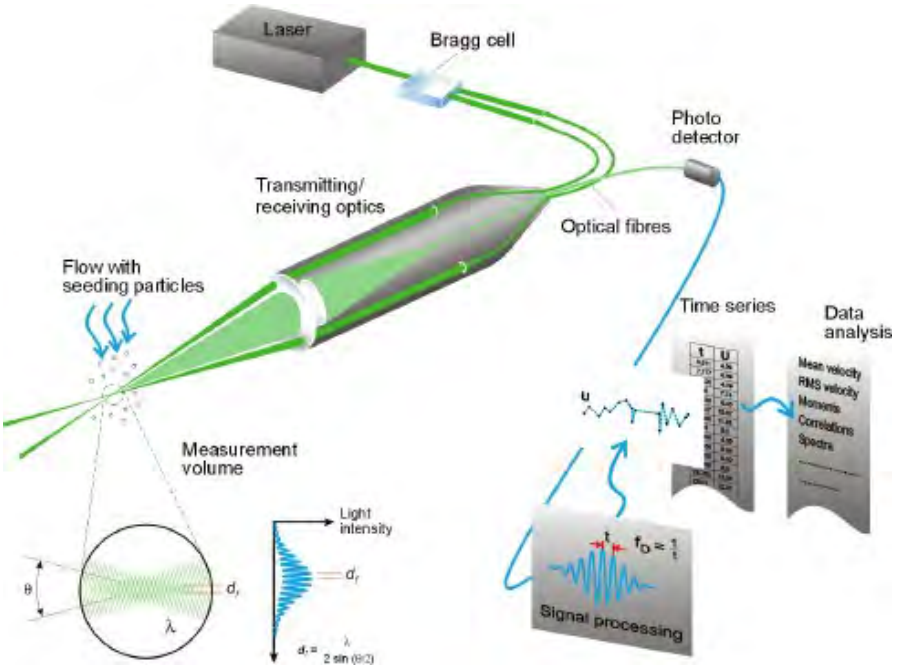

Figure 3.17: General layout of a backscatter LDA system (source: `http://www.dantecdynamics.com/measurement-principles-of-lda`).

light impacts on the moving seeding particle. When the light is scattered from the illuminated particle and received by a stationary detector (Tropea *et al.*, 2007, p. 296). LDA systems can work with the detector placed at any scattering angle with respect to the incident beams, but the configurations commonly used are the forward and back scatter modes, schematically represented in Figure 3.18. As seen in Figure 3.12, the scattered light intensity from seeding particles is usually much stronger in the forward direction. Therefore, from the signal strength point of view, the forward scattering mode is the best, however the back scatter mode is more convenient due to constructive and operative reasons. If the receiving optics can be integrated into the transmitting optics, with the former focused by the manufacturer, it is easier to position the probes and a source of errors is eliminated.

Figure 3.19 illustrates the laser generator, the probes and the intersection of the laser beams during the experiments at LWI. The LDA system used consisted on a 5W Argon-Ion laser, a F80 flow processor and two watertight probes with focal length of 198 mm in water (Aberle, 2006). This system works in back scattering mode. A two-component probe transmits two orthogonal pairs of beams (wavelengths 488 and 514.5 nm) while the one-component probe, positioned at 30° to the two-component probe, transmits the third pair of beams (wavelength 476.5 nm). Due to the focal length larger than the flow depth, an acrylic case with a glass bottom was used to submerge the probes in water and ensure that the laser beams travel in water from the probe casing to the measuring volume, except in the 2 mm glass plate.

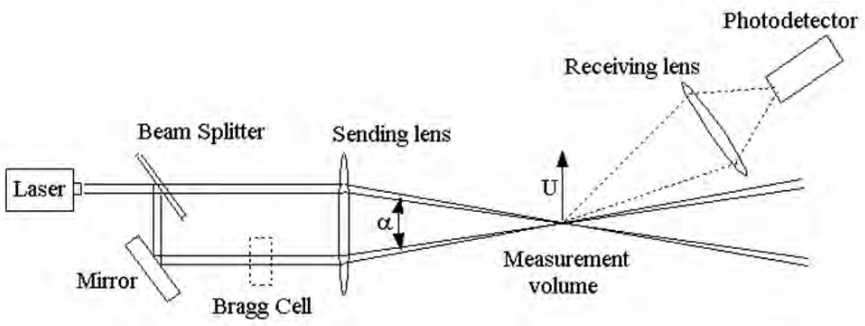

(a)

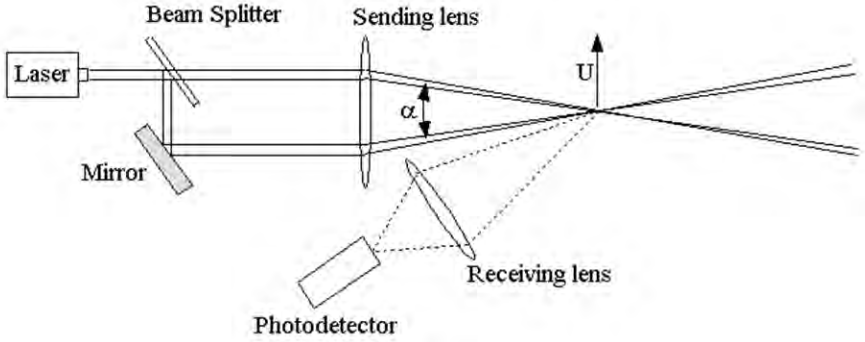

(b)

Figure 3.18: Scheme of a LDA system in a) forward scatter mode and b) back scatter mode.

The Doppler principle by which the LDA operates is better explained by the so called fringe model, represented in Figure 3.20. A fringe pattern is originated when two monochromatic (same wavelength) coherent (same phase for all waves) light beams are superimposed. Where the interfering light waves are in phase, *i.e.*, peak aligned with peak, they add up and a bright fringe is generated; where the waves are out of phase, *i.e.*, peak aligned with trough, they cancel out and a dark fringe occurs. In the LDA case this fringe pattern occurs in the measurement volume and it is parallel to the axis of the transmitting optics.

The spacing between fringes, δ, depends on the wavelength of the crossing beams, λ, and on the angle that they form, θ, according to the following mathematical expression

$$\delta = \frac{\lambda}{2\sin(\theta/2)}. \tag{3.8}$$

A particle crossing the control volume with velocity u normal to the axis of the probe will generate a signal which, in the time domain is a wave packet with frequency f. The interval

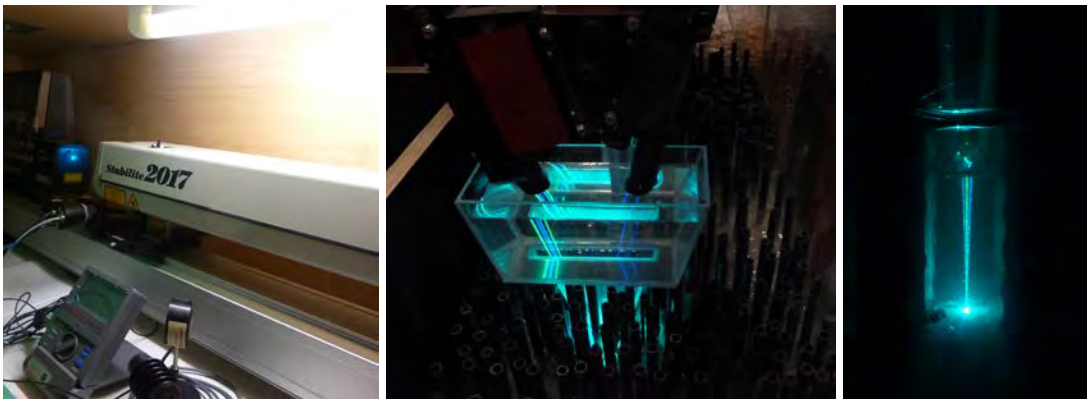

(a) (b) (c)

Figure 3.19: a) The laser generator, b) the probes and the acrylic case and c) the laser light beams during the experiments at LWI.

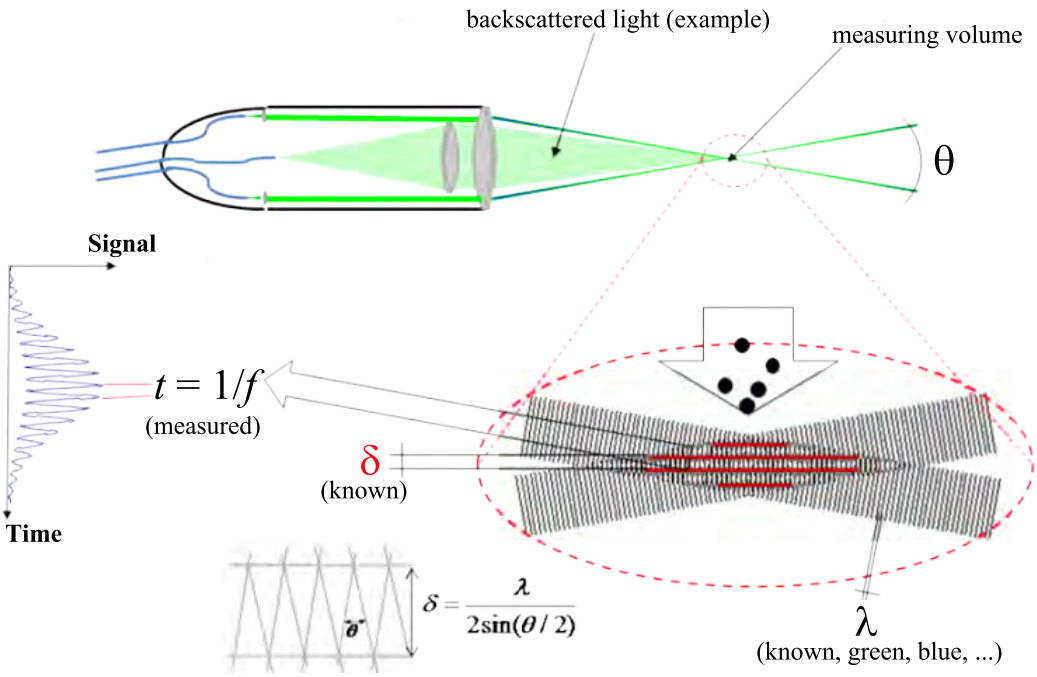

Figure 3.20: Fringe model (Source: Ferreira, 2011).

between peaks is $t = 1/f$, hence, the velocity of the particle that generated the burst is given by

$$u = \frac{\delta}{t} = \frac{\lambda}{2\sin(\theta/2)} f. \tag{3.9}$$

This equation is known as LDA fundamental equation, which combines the imposed arrangement and laser properties, θ and λ, with the detected burst frequency, f to determine the velocity of the particles moving with the fluid.

Each seeding particle passing through the measurement volume results in a signal, referred as burst, at the output of the photodetector. The signal processor has the task of detecting when a burst is present and estimating various signal parameters.

As mentioned before, the frequency shift introduced in the Bragg cell in one of the beams is used to distinguish between positive and negative velocities. The frequency of the shifted beam is changed by an amount proportional to the frequency of the acoustic wave, f_{bragg}. As a result, when the beams cross, the fringe pattern will appear moving with the shift frequency. Detected frequencies smaller than f_{bragg} will result in negative velocities.

Due to the random distribution of the seeding particles, these signals arrive irregularly in time, requiring special considerations in the data processing step, for example, if evenly spaced velocity series are sought polynomial interpolation algorithms for signal reconstruction are needed. The key issue for the LDA signal conditioner and signal processing units is, thus, to identify bursts from background noise and to detect correctly the frequency f. These units are often condensed in the Real-time Signal Analyzer (RSA) unit, which undertake the following main operations:

i. subtraction of the Gaussian pedestal inherent to a coherent laser (the radial distribution of the beam intensity is approximately Gaussian);
ii. amplification;
iii. filtering of noise components (general low-pass filtering);
iv. burst detection, for instance by thresholding in the time-amplitude domain;
v. frequency estimation, normally by inverse-Fourier methods.

3.4.2 Quality of measurements

The signal-to-noise ratio and the transit length are key parameters to verify the quality and to validate a Doppler burst. Naturally, the larger the number of fringes, the easier to detect the burst. The number of fringes increases with increasing angle between beams, θ, and increasing focal distance, F. The time resolution of a LDA velocity series depends on the concentration of the seeding particles in the flow. However, increasing the particle concentration indefinitely does not continue to improve the temporal resolution, because the signal processing may not be reliable in estimating the signal frequency when multiple particles are present simultaneously

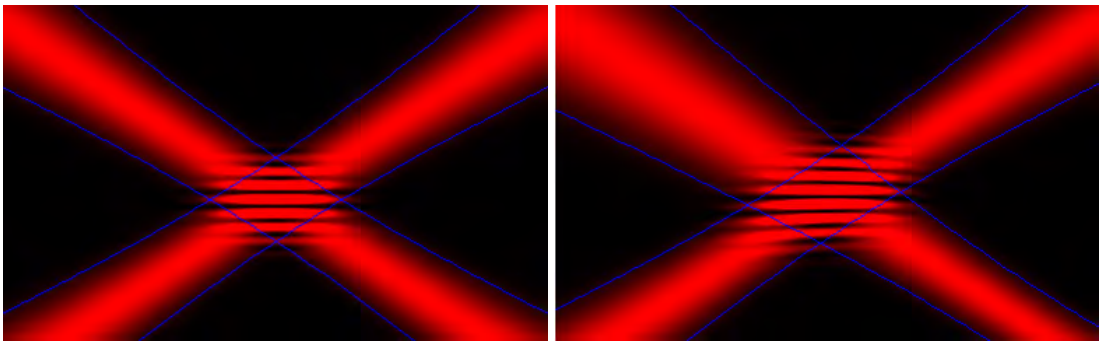

(a) (b)

Figure 3.21: Crossing of laser beams: a) correct crossing with parallel fringe pattern; b) incorrect crossing due to lens aberration (Source: Ferreira, 2011).

in the measurement volume. Furthermore, high particle loads may change the flow properties. More common than errors due to high concentration of seeding, are the errors introduced in the measurements due to scarce seeding, which results in signal spiking or absent counts. Smaller measurement volumes tolerate higher seeding concentrations and, at the same time, the same laser power distributed over a smaller measurement volume leads to higher incident intensity and, thus, higher signal amplitudes and quality. However, reducing the measurement volume excessively may result in fewer particles being seen, reducing the temporal resolution of the measurements.

The Doppler bursts are superimposed by noise associated to the instrumentation, as electric noise due to poor insulation, noise introduced by the photodetector and noise introduced by the laser generation. In general, these sources of noise are uncorrelated corresponding to noise spectrally white, *i.e.*, the total noise power is distributed evenly over all frequencies up to the upper bandwidth of the system.

A common error source in LDA is the positioning of the laser beams, especially in 3D arrangements where the user is required to match the measuring volumes of two different probes. Working in coincidence mode, for which a passing particle must generate a burst recognisable by the detectors associated to each of the three wavelengths, may drastically reduce the frequency count if the measurement volumes are not perfectly aligned. Poor beam focus due to lens aberration causes spatial gradients in the fringe pattern leading to inadequate estimates of the frequency f. This problem of lens aberration is represented in Figure 3.21, where a correct crossing of the beams, resulting in parallel fringe patterns, is compared with incorrect beams crossing.

As a particle-based technique, LDA measurements are affected by errors introduced, especially in turbulent flows, because particles do not follow the fluid exactly. As presented in section 3.3.3 for PIV, Hjemfelt & Mockros (1996) derived and solved the equation that describes particle

motion in a viscous fluid, in which the leading term is Stokes drag. Retaining only this term, the smaller turbulent scale measurable, Δr, for a given velocity increment Δu is

$$\Delta r = \frac{1}{18}\frac{d_p^2(s^{(p)}-1)}{\nu}\Delta u \tag{3.10}$$

where d_p is particle's diameter, $s^{(p)}$ is the specific gravity of the seeding particles and ν is the fluid's kinematic viscosity.

In the present experimental work, at LWI, titanium dioxide, commercialized by AppliChem® under the designation of Titanium (IV) oxide pure, was used to seed the flow. The powder particles were mixed in water in a 200 l container, from which the mixture was pumped into the flume at a constant discharge. The diameter of the particles ranges from 5 to 50 μm and the specific gravity of the titanium dioxide is 4.2 g cm^{-3}. Considering a flow velocity of 0.10 m/s, equation (3.10) indicates the smallest turbulent scale susceptible to be measured with titanium dioxide particles of 50 μm is 4.4×10^{-5} m. For the present experiments this value is much smaller than the spatial resolution of the acquired velocity series, not causing significant errors.

Regarding the quality of turbulent flow measurements wit LDA, the size of the measuring volume must be considered. The dimensions of the measuring volume in the directions normal and parallel to the probe axis are

$$\delta_x = \frac{4F\lambda}{\pi D_L \cos(\theta/2)} \tag{3.11a}$$

$$\delta_y = \frac{4F\lambda}{\pi D_L \sin(\theta/2)} \tag{3.11b}$$

respectively, where F is the focal distance and D_L is the beam's diameter at the beam waist before the lens. The remaining variables were previously defined. Control volumes too large may smooth out small turbulent scales, since particles with symmetric velocities belonging to the same eddy simultaneously present in the measurement volume may disturb burst detection. Large control volumes also generate more noise. If the control volume encompasses strong spatial gradients, particles with different velocities will cross the control volume and will be interpreted as turbulence even if the flow is laminar. Naturally, if the flow is turbulent, this type of noise will also be present but will be very difficult to detect as it may be uncorrelated. In the present study the control volume was characterized by $\delta_x = 0.10$ mm and $\delta_y = 0.38$ mm, for $F = 198$ mm, $\theta = 30°$, $\lambda = 514.5$ nm and $D_L = 1$ mm.

3.5 Experimental tests

3.5.1 Test S1

Test S1 was carried out at IST. This test featured $m = 400$ stems/m^2 randomly distributed all over the vegetated reach, corresponding to a volumetric solid fraction, $\phi = \pi d^2 m/4$, equal to 0.038. Two measuring gaps were considered, distanced 1.0 m from each other. Figure 3.22 shows a plan view of the vegetated reach in test S1. Figure 3.23 illustrates the flume during the experiments.

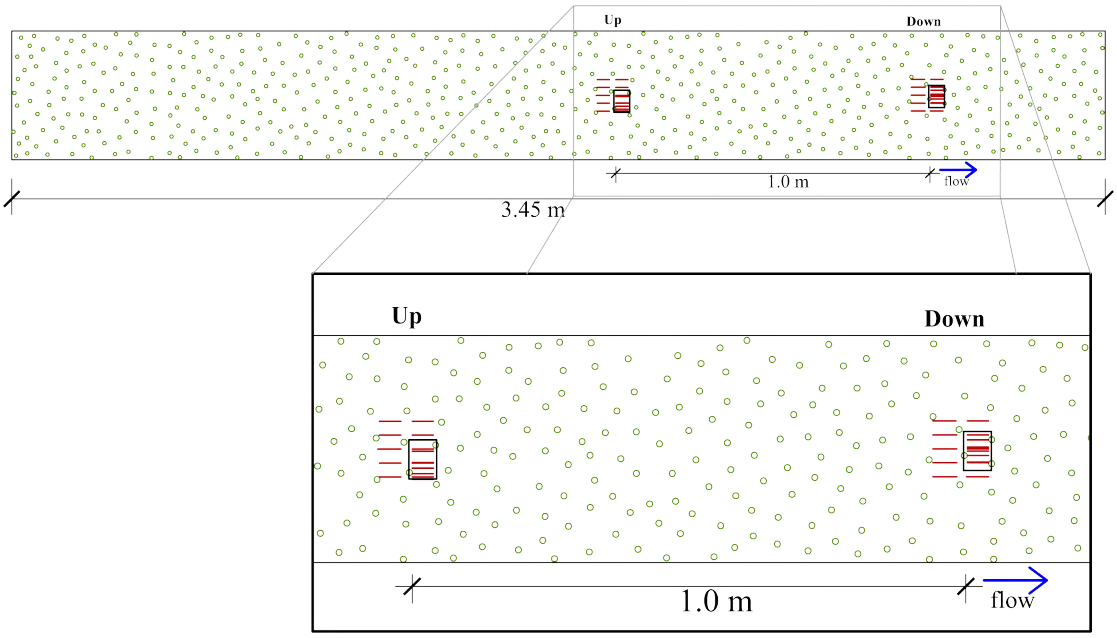

Figure 3.22: Plan view of test S1. The solid lines aligned with flow direction indicate the location of the vertical plans measured with PIV. The rectangles point out the regions where horizontal velocity maps were acquired. The blue arrow indicates the flow direction.

(a) (b)

Figure 3.23: Pictures of the flume during test S1: a) lateral view and b) plan view.

Table 3.1: Features of the experimental measurements and flow properties for test S1.

M.Gap	x (m)	U (m/s)	h (m)	$\mathrm{d}h/\mathrm{d}x$ (−)	$T^{(v)}$ (°C)	$T^{(h)}$ (°C)	Re_p (−)
Up	7.270	0.092	0.066	-	26.2	21.1	1170
Down	8.270	0.109	0.059	-0.007	28.2	25.7	1450

For each measuring gap, vertical (streamwise $\times$ vertical) and horizontal (streamwise $\times$ spanwise) instantaneous velocity maps were measured in the central part of the flume's width, as represented in Figure 3.22. Regarding the measurements in the vertical plane, 21 runs, collecting 486 images couples each, were performed at each lateral position, representing a total acquisition time of $11'20''$. The camera's field of view was adjusted in order to acquire velocity maps of the whole flow depth maximizing the spatial resolution. It yielded to interrogation areas whose size varied between 0.7 and 1.0 mm.

To avoid laser refractions due to the free-surface oscillations, during PIV measurements in the vertical plane, for all tests, a 0.2 mm thick plastic sheet was placed at the free surface on illuminated region.

The horizontal maps were acquired at 6 different heights for each measuring gap. 4×486 image pairs were recorded at each plane. On the upstream measuring gap, the maps were acquired at $0.1, 0.2, 0.6, 1.6, 3.3$ and 5.0 cm above the averaged bed level, while in the downstream gap, the measurements were carried out at $0.1, 0.2, 0.5, 1.0, 3.7$ and 5.3 cm above the average bed level. The interrogation areas were about 0.7 and 0.6 mm large on the upstream and downstream gaps, respectively.

Table 3.1 summarizes the main flow variables for each measuring gap (M.Gap). Herein, x is the longitudinal coordinate of the measuring gap relative to the channel inlet, U is the depth average of the double-averaged longitudinal velocity profile, $\mathrm{d}h/\mathrm{d}x$ is the gradient of the mean flow depth h, $T^{(v)}$ and $T^{(h)}$ are the mean water temperature during vertical and horizontal measurements, respectively and $Re_p = Ud/\nu$ is the stem Reynolds number, where d is the stem diameter and ν is the water kinematic viscosity, which depends on temperature (Likhachev, 2003).

3.5.2 Test S2

Test S2 was first carried out at IST performing velocity measurements with the 2D PIV system and then reproduced at LWI to get 3D velocity fields with the described LDA. For this test, stems were placed in order to create a pattern with seven wavelengths, each 0.5 m long, with varying m. Data acquisition was carried out in eight measuring gaps, distributed along two wavelengths

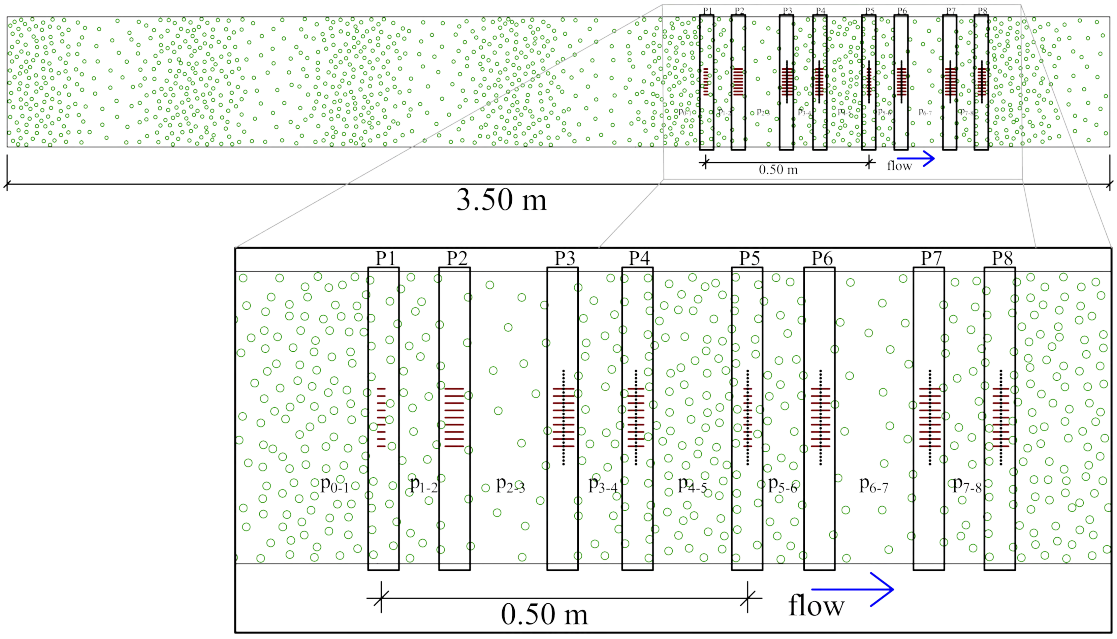

Figure 3.24: Plan view of test S2. The solid lines aligned with flow direction indicate the location of the vertical plans measured with PIV. The rectangles point out the regions where horizontal velocity maps were acquired. The blue arrow indicates the flow direction. The points along lines perpendicular to the flow direction represent the location of LDA measurements (P3 to P8).

- P1 to P4 (first wavelength) and P5 to P8 (second wavelength) as shown in Figure 3.24. Each wavelength features:

  - a 15 cm long patch with $m = 1600$ stems/m^2 (dense patch, herein); this is the case of patch p_{4-5} in the second wavelength;
  - a 10 cm long transition patch with an average m of 980 stems/m^2, divided into two 5 cm reaches with 1200 stems/m^2 and 800 stems/m^2, respectively from upstream to downstream; it is the case of patches p_{1-2} and p_{5-6}, respectively in the first and second wavelengths;
  - a 15 cm long patch of $m = 400$ stems/m^2 (sparse patch, herein); this is the case of patches p_{2-3} (first wavelength) and p_{6-7} (second wavelength);
  - a 10 cm long transition patch with an average m of 980 stems/m^2, divided into two 5 cm reaches with $m = 800$ stems/m^2 and $m = 1200$ stems/m^2, respectively from upstream to downstream; it is the case of patches p_{3-4} (first wavelength) and p_{7-8} (second wavelength).

Figure 3.23 presents pictures showing two views of the flume during the experiments in test S2 at IST.

The velocity measurements with PIV in test S2 consisted, for each measuring gap, in the acquisition of vertical maps at 9 lateral positions and horizontal maps at 4 vertical positions, as represented in Figure 3.24. Regarding the vertical measurements, 10×573 px^2 images couples

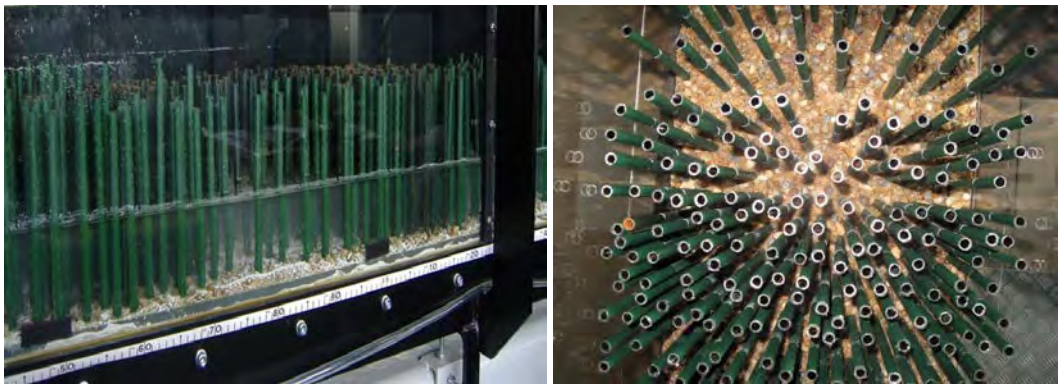

(a) (b)

Figure 3.25: Pictures of the flume during test S2 at IST: a) lateral view and b) plan view.

were collected for each lateral position, representing a total acquisition time of $6'37''$. The spatial resolution yielded to interrogation areas of $0.7-1.0$ mm. For the horizontal measurements, each vertical position consisted in several lateral acquisitions (typically 4) in order to cover the whole flume width. For each lateral position, one run with 5000 image pairs was acquired corresponding to $5'33''$ of consecutive data. The horizontal planes were measured at 90%, 60% and 25% of the flow depth and about 3 mm above the averaged bed elevation. It is difficult to get good measurements very close to the bed due to the laser light refractions. The field of view was $\approx 12 \times 10$ cm^2, corresponding to interrogation areas of $\approx 1.3 \times 1.3$ mm^2.

Table 3.2 presents the main flow variables for each measuring gap (M.Gap) of test S2 at IST, where $\mathrm{d}m/\mathrm{d}x$ is the longitudinal gradient of the stem areal number-density m. The remaining variables are the same as in test S1. It should be noted that, as in the other tests, free surface exhibited an oscillating behaviour, with larger amplitude in the dense patches.

The three-component LDA velocity series were measured at 27 points along spanwise direction, centred in the channel midpoint, with a spatial resolution of 5 mm, as shown in Figure 3.24. These series were collected at 6 elevations for 6 measuring gaps (P3 to P8 - Figure 3.24), approximately at the centre of the measuring gap. The 6 elevations considered were $z = 3$ mm and $z = 7$ mm relatively to the averaged bed elevation and $z = 25, 40, 60, 75\%$ of the flow depth. The sampling time at each point was 3 minutes with sampling frequencies between 50 and 120 Hz.

Table 3.3 presents the main flow variables for each measuring gap (M.Gap) of test S2 at LWI, where the time and space-averaged longitudinal velocity, $\langle \bar{u} \rangle$, is presented for all the vertical positions for each measuring gap. At LWI, the water temperature varied in the range $13.4-14.2$°C, being relatively stable during the experiments.

Table 3.2: Features of the experimental measurements and flow properties for test S2 at IST.

M.Gap	P1	P2	P3	P4	P5	P6	P7	P8
Patch	p_{0-1}	p_{1-2}	p_{2-3}	p_{3-4}	p_{4-5}	p_{5-6}	p_{6-7}	p_{7-8}
x (m)	6.680	6.782	6.935	7.036	7.192	7.293	7.446	7.545
m (stems/m^2)	1600	980	400	980	1600	980	400	980
$\mathrm{d}m/\mathrm{d}x$	0	<0	0	>0	0	<0	0	>0
ϕ $(-)$	0.152	0.093	0.038	0.093	0.152	0.093	0.038	0.093
U (m/s)	0.085	0.083	0.090	0.099	0.103	0.108	0.100	0.106
h (m)	0.065	0.064	0.063	0.062	0.057	0.056	0.054	0.052
$\mathrm{d}h/\mathrm{d}x$ $(-)$	-0.020	-0.017	-0.002	-0.012	-0.031	-0.018	-0.010	-0.017
$T^{(v)}$ (°C)	27.7	30.3	29.9	27.7	25.9	26.3	24.1	22.0
$T^{(h)}$ (°C)	29.2	30.0	29.6	31.9	30.0	30.5	30.1	28.5
Re_p $(-)$	1121	1158	1237	1303	1302	1374	1216	1222

Table 3.3: Features of the experimental measurements and flow properties for test S2 at LWI.

M.Gap		P3	P4	P5	P6	P7	P8
Patch		p_{2-3}	p_{3-4}	p_{4-5}	p_{5-6}	p_{6-7}	p_{7-8}
m (stems/m^2)		400	980	1600	980	400	980
$\mathrm{d}m/\mathrm{d}x$		0	>0	0	<0	0	>0
ϕ $(-)$		0.038	0.093	0.152	0.093	0.038	0.093
h (m)		0.063	0.061	0.056	0.056	0.054	0.052
$\mathrm{d}h/\mathrm{d}x$ $(-)$		-0.001	-0.018	-0.033	0.000	-0.010	-0.028
$\langle\bar{u}\rangle$ (m/s)	$z = 3$ mm	0.107	0.130	0.109	0.109	0.123	0.137
	$z = 7$ mm	0.113	0.123	0.130	0.113	0.126	0.137
	$z = 0.25h$	-	0.115	0.125	0.110	0.123	0.129
	$z = 0.40h$	0.106	0.116	0.123	0.108	0.124	0.128
	$z = 0.60h$	0.109	0.115	0.123	0.112	0.127	0.130
	$z = 0.75h$	0.114	0.122	0.127	0.118	0.138	0.133

3.5.3 Test S3

Test S3 was populated with the same number of stems of test S2 (1366 stems) distributed randomly and uniformly, resulting in $m = 980$ stems/m^2 and $\phi = 0.093$. Two measuring gaps, 1.0 m apart, were considered as represented in Figure 3.26. A lateral and plan view of the flume during the experiments are presented in Figure 3.27.

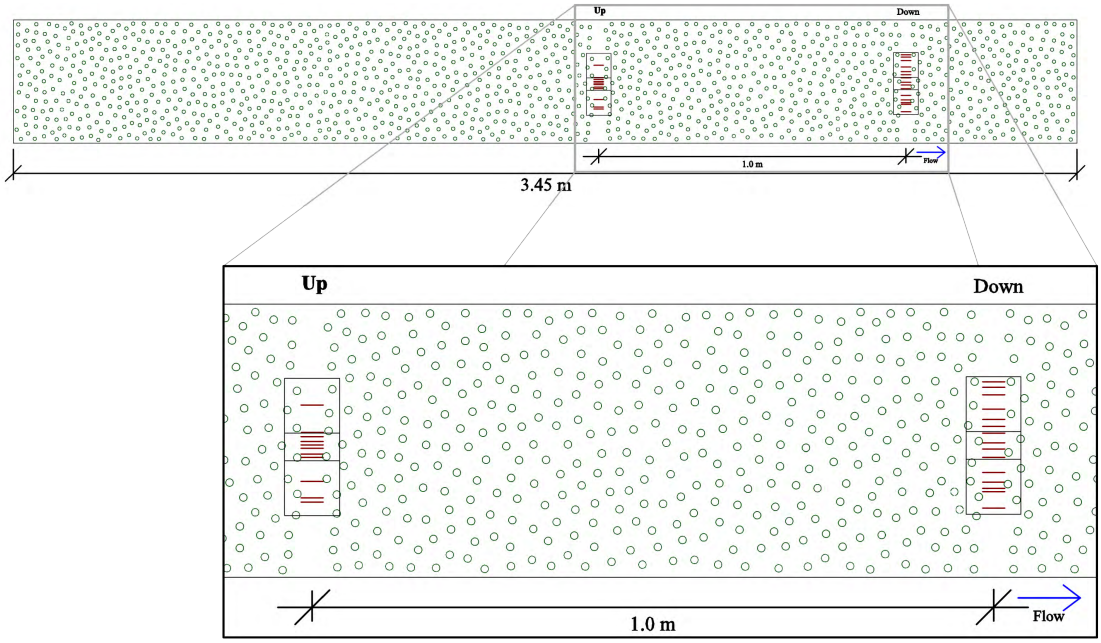

Figure 3.26: Plan view of test S3. The solid lines aligned with flow direction indicate the location of the vertical plans measured with PIV. The rectangles point out the regions where horizontal velocity maps were acquired. The blue arrow indicates the flow direction.

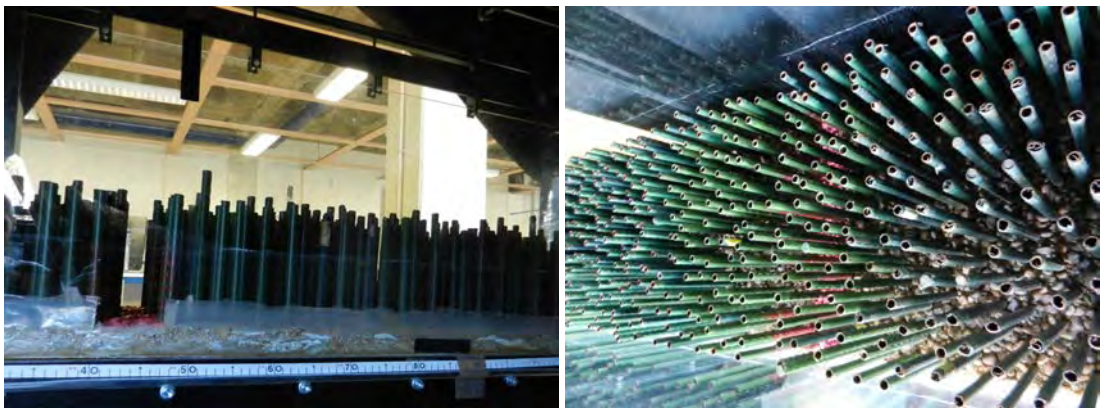

(a) (b)

Figure 3.27: Pictures of the flume during test S3: a) lateral view and b) perspective

Table 3.4: Features of the experimental measurements and flow properties for test S3.

M.Gap	x (m)	U (m/s)	h (m)	$\mathrm{d}h/\mathrm{d}x$ (−)	$T^{(v)}$ (°C)	$T^{(h)}$ (°C)	Re_p (−)
Up	6.900	0.092	0.065	-	19.0	19.0	989
Down	7.900	0.099	0.051	-0.014	19.0	19.0	1064

Also for test S3 the velocity field was characterized with vertical and horizontal maps. Regarding the measurements in the horizontal plane, 5000 instantaneous velocity maps were acquired consecutively in two lateral positions, in the central part of the flume, at each elevation. For each measuring gap, three different elevations were considered, 25%, 60% and 85% of the flow depth. The field of view was $\approx 12 \times 10$ cm^2, corresponding to interrogation areas of $\approx 1.2 \times 1.2$ mm^2. In what concerns vertical velocity maps, the measurements were performed at 11 and 15 lateral positions in the upstream and downstream measuring gaps, respectively (Figure 3.26). At each lateral one run with 5000 image pairs was acquired corresponding to $5'33''$ of consecutive data.

Table 3.4 presents the main flow variables for the measuring gaps of test S3. The presented variables are the same as in test S1.

3.6 Data treatment

3.6.1 Bed topography

The laser displacement sensor described above was employed to measure the bed topography at IST's flume. The laser head was mounted in a mobile support held in the flume's rails, which allows streamwise and spanwise displacements. The goal of the bed topography measurements was a statistical characterization of the bed elevation and fluctuations. This means that a detailed and referenced bathymetry was not sought, instead the measurements were designed to verify the horizontality of the gravel bed and to obtain an average value of the bed elevation in the measuring gaps. The measurements consisted in the acquisition of bed elevation series along a longitudinal or transverse line, moving the laser head with an approximately constant velocity along that line. The laser head was positioned and then pushed manually along the selected line.

To verify the gravel bed covering the flume's bottom was approximately horizontal, longitudinal measurements were performed at several lateral positions, along the vegetated reach. Figures 3.28 and 3.29 exemplify longitudinal bed elevation profiles for tests S1 and S2. Due to the presence of the stems, the laser light was wrongly reflected leading to erroneous values in the longitudinal profile. These spikes were detected applying the phase-space threshold method

presented by Goring & Nikora (2002) and they were not replaced; instead they were simply not considered.

Figure 3.28 shows that the gravel layer in test S1 presented a slight trend. It should be noticed that building of an horizontal layer within the stems was a difficult task. Furthermore, the trend become visible only at the end of the vegetated reach. Therefore, it was accepted as an approximately horizontal bed, but the flow depths were adequately computed.

Bed elevation transverse profiles were acquired to each measuring gap in order to compute the averaged bed elevation characterizing each measuring gap.

3.6.2 Free-surface

The laser displacement sensor was also employed to measure the free-surface level, in a point-wise fashion. A very small and opaque 0.2 mm thick plastic piece was placed on the measuring point to allow the laser light reflection at the free-surface level. The interference of that piece of plastic with the free-surface oscillations was negligible.

Within the scope of the present thesis, the free-surface measurements was aimed at the characterization of the mean flow depth and its longitudinal gradient. Due to the complex oscillatory behaviour of the free-surface, the mean elevation at a given measuring gap was computed from several (7 to 10) points in the spanwise direction. Targeting the longitudinal gradient, the oscillations of the free-surface at several points in along the flume's centreline were acquired. The free-surface elevation series were acquired at 200 Hz during 60 s in test S1 and at 100 Hz during 60 s in test S2. For test S3, the series, which were not evenly spaced, were acquired during 160 s at an average rate of 200 Hz.

Figures 3.30 to 3.33 exemplify two of the free-surface elevation series acquired to each test. Extracts of 10 s are also shown to better visualization of the oscillations. The amplitude of the oscillations varied from point to point in a given cross-section and with the stem areal number-density.

Figure 3.34 presents the longitudinal profile of bed and free-surface elevations for each experimental test, showing that flow was gradually varied accelerating in downstream direction as the flow depth decreases.

3.6.3 Volumetric fluid fraction

To show the relative magnitude of bed and free-surface oscillations over the water column, a vertical profile of the volumetric fluid fraction in the total control volume is presented in Figure 3.35. For the bottom and top layers the statistical information from the bed and free-surface

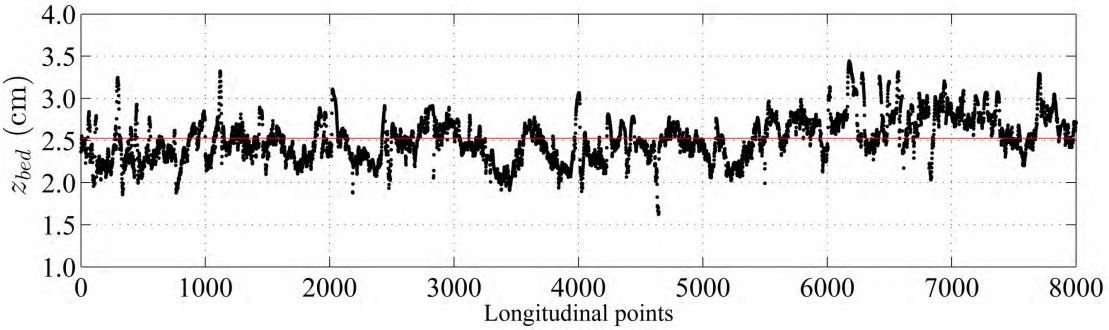

(a)

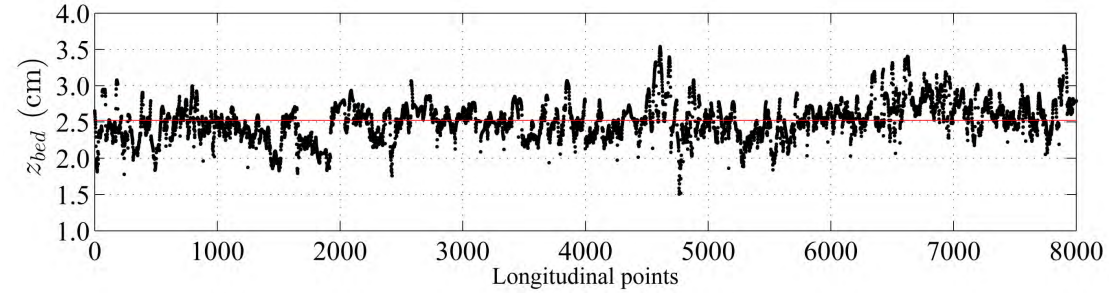

(b)

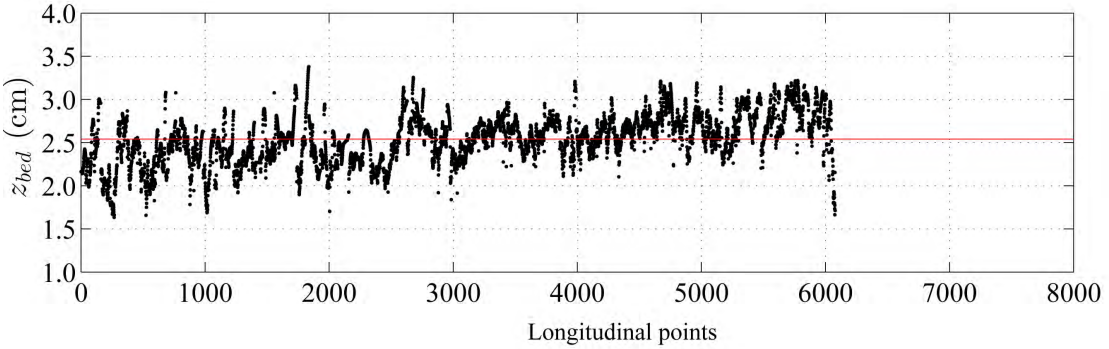

(c)

Figure 3.28: Longitudinal profiles of bed elevation of test S1 at a) $y = 0.100$ m, b) $y = 0.204$ m and c) $y = 0.333$ m. The red lines represent the averaged value of each series.

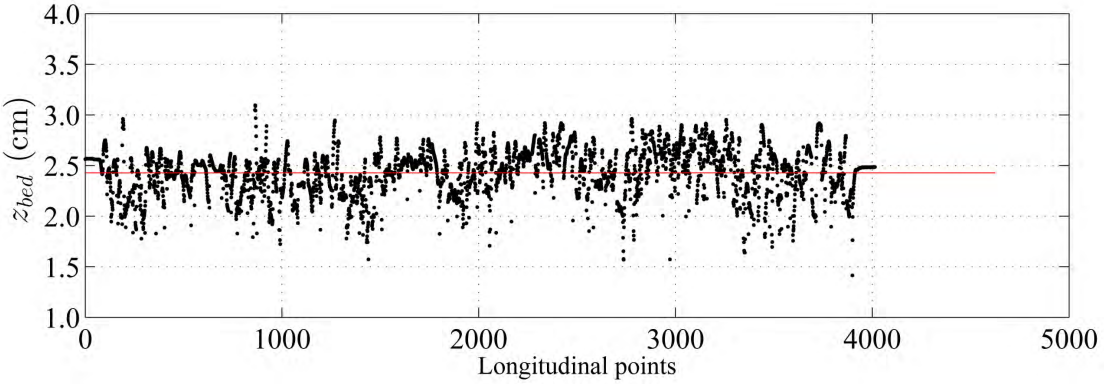

(a)

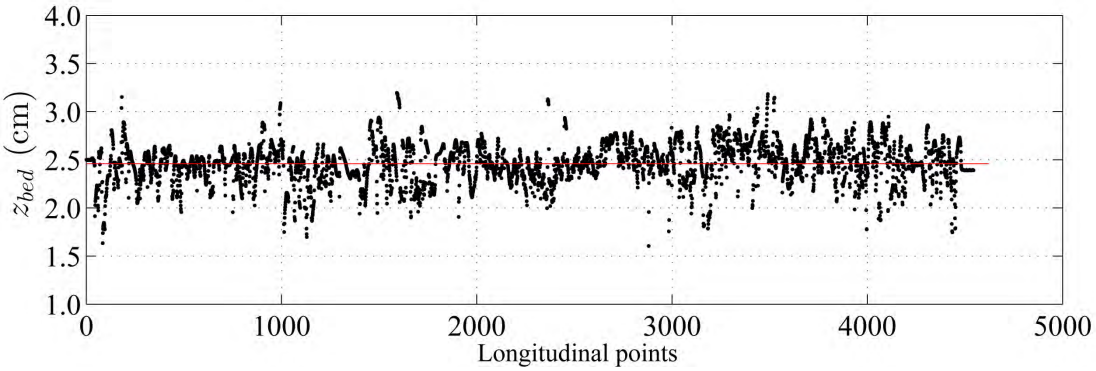

(b)

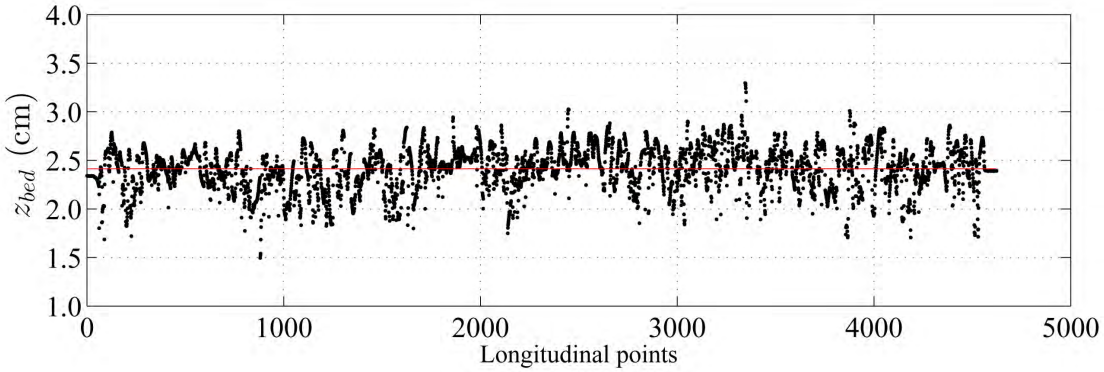

(c)

Figure 3.29: Longitudinal profiles of bed elevation of test S2 at a) $y = 0.164$ m, b) $y = 0.204$ m and c) $y = 0.244$ m. The red lines represent the averaged value of each series.

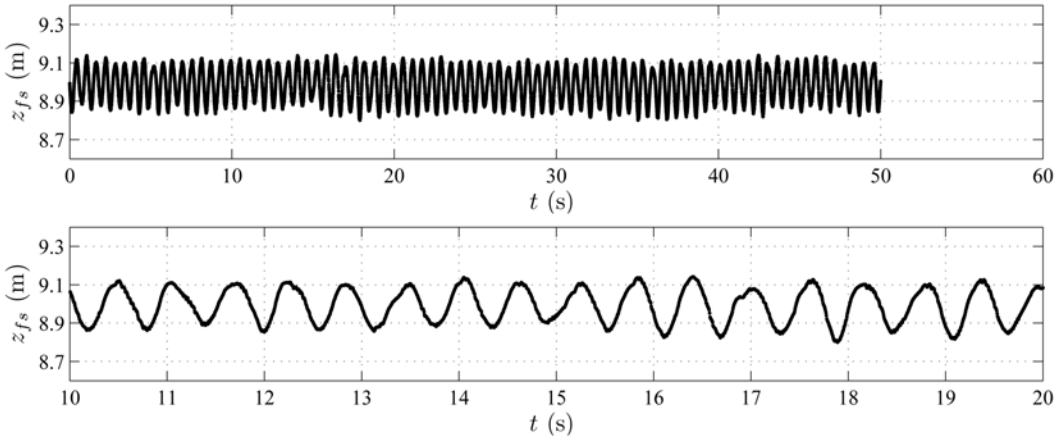

(a)

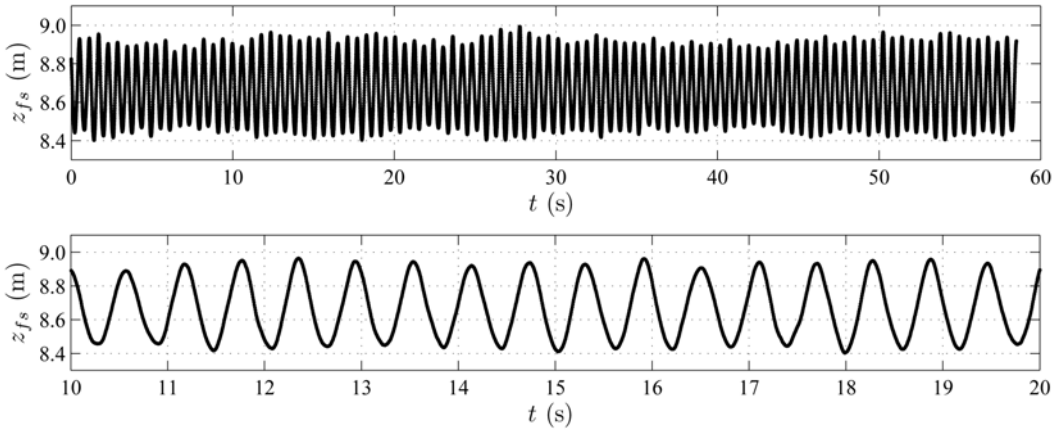

(b)

Figure 3.30: Oscillations of the free-surface at points a) $x = 7.25$ m and $y = 0.275$ m, and b) $x = 8.30$ m and $y = 0.204$ m, in test S1.

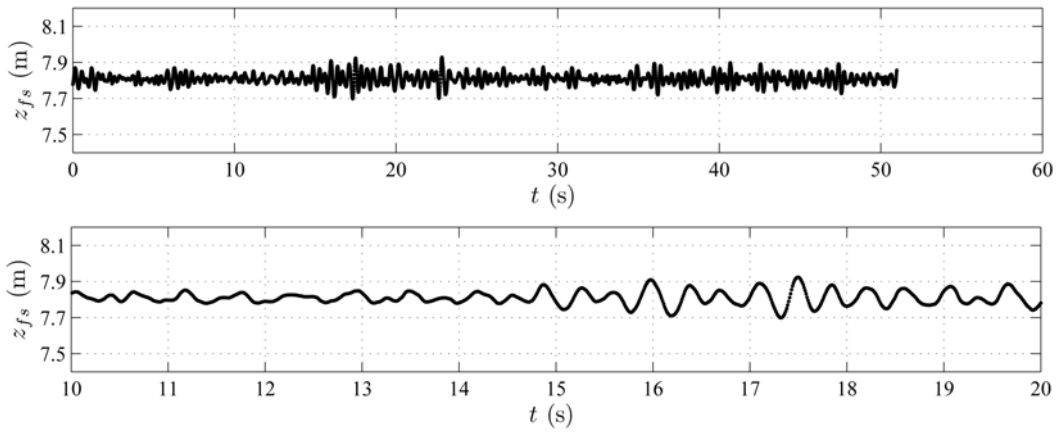

Figure 3.31: Oscillations of the free-surface at the point $x = 7.446$ m and $y = 0.204$ m in the measuring gap P7 of test S2.

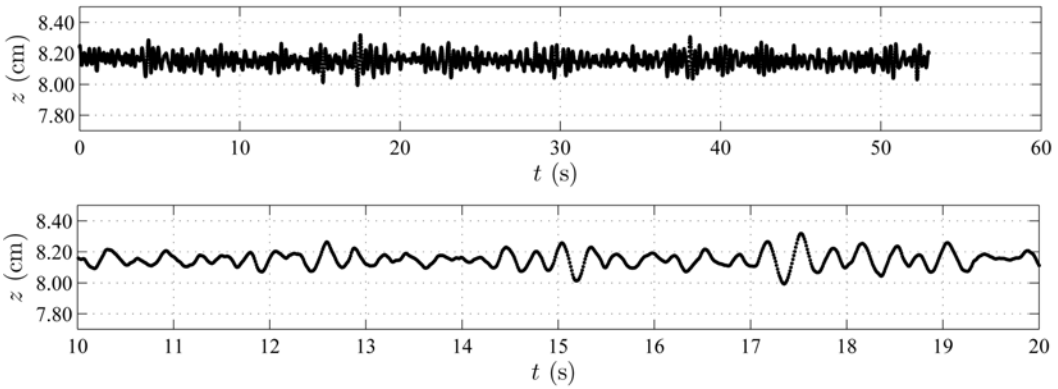

Figure 3.32: Oscillations of the free-surface at the point $x = 7.192$ m and $y = 0.214$ m in the measuring gap P5 of test S2.

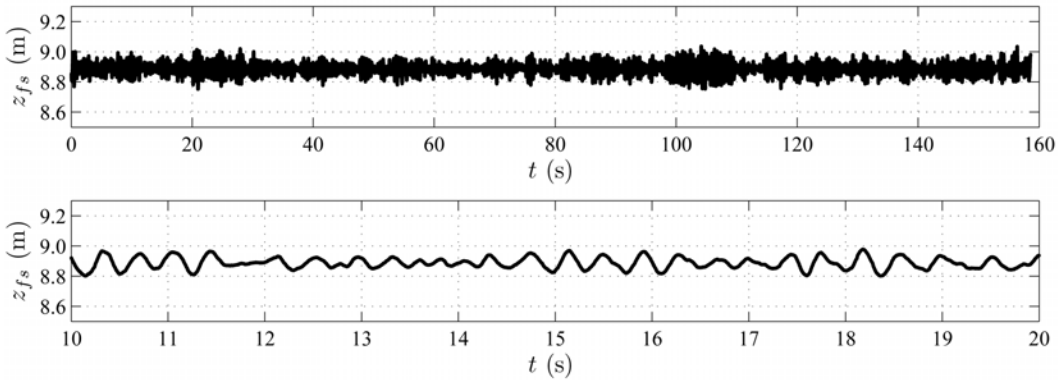

(a)

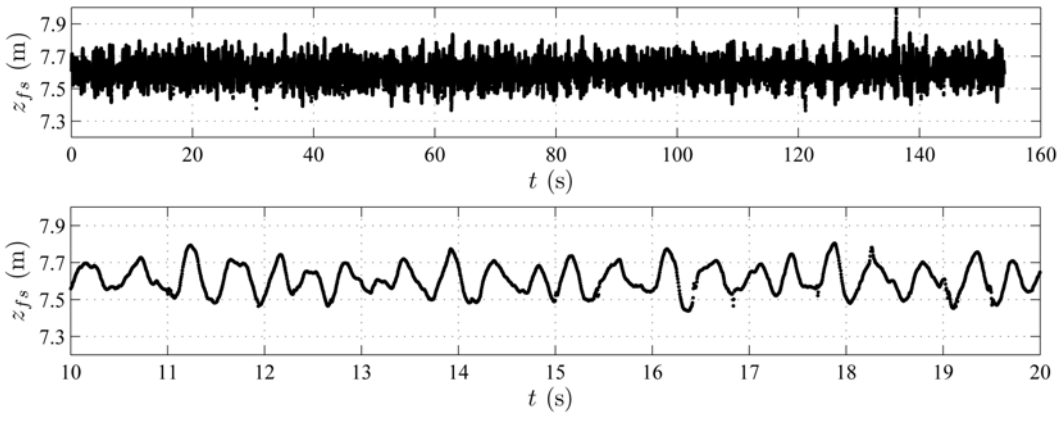

(b)

Figure 3.33: Oscillations of the free-surface at points a) $x = 7.90$ m and $y = 0.302$ m, and b) $x = 8.90$ m and $y = 0.217$ m, in test S3.

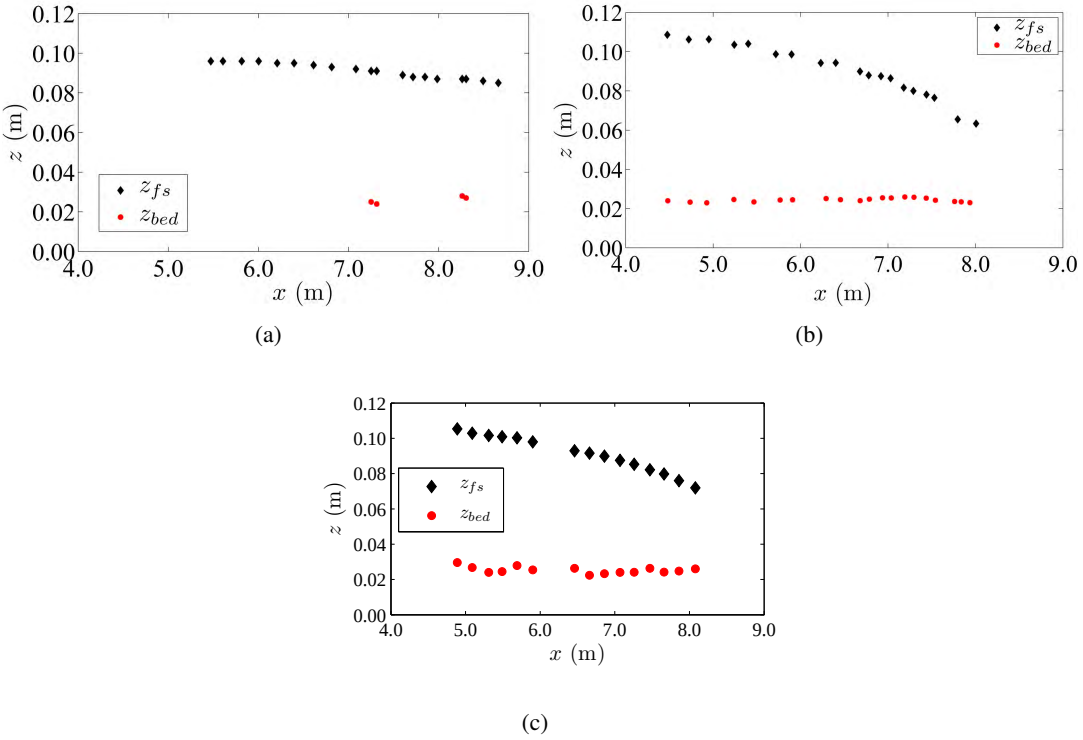

Figure 3.34: Longitudinal profiles of free-surface and bed elevation of tests a) S1, b) S2 and c) S3.

measurements was used and for the layer where the solid fraction corresponds solely to the stems the fluid fraction is defined by

$$\psi = 1 - \pi \frac{d^2}{4} m. \tag{3.12}$$

The volumetric fluid fraction decreases towards zero values due to the oscillations of the free surface. In the layer between the minimum and the maximum of the free surface level, the non-fluid part of the control volume is occupied by stems and air.

3.6.4 PIV velocity maps

Concerning the PIV data treatment, the first step is performed by the PIV software, which applies an adaptive correlation algorithm to convert the images pairs into instantaneous velocity maps. The instantaneous velocity field exported from the PIV software were in image units (px/s), thus a conversion to metric units (m/s) was applied. A simple linear transformation was considered since the field of view was small enough so that it became possible to neglect circular camera distortions. For each acquired plane, before the velocity measurements, a PVC sheet, marked off with a millimetre scale, was placed on measurement's plane and an image was

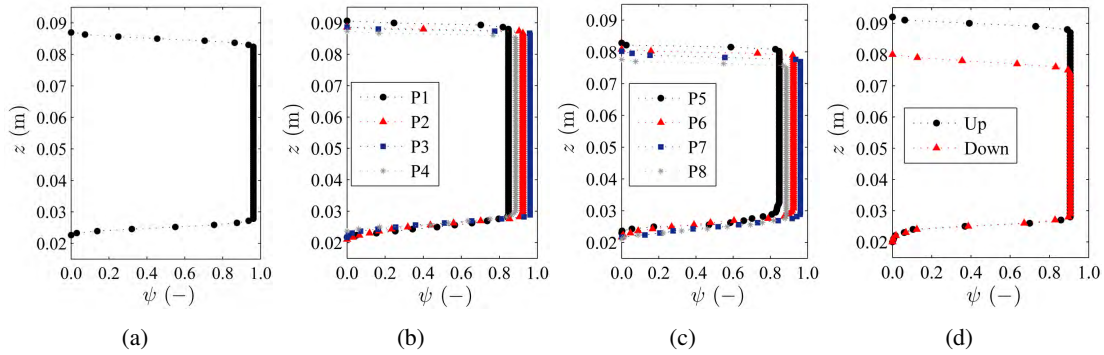

Figure 3.35: Vertical distribution of the volumetric fluid fractions for a) test S1, b) measuring gaps on the first wavelength of the stem distribution of test S2, c) measuring gaps on the second wavelength of the stem distribution of test S2 and d) test S3.

recorded to allow the computation of the calibration coefficient. The marked PVC sheet, shown in Figure 3.36, was also used to focus the camera. Since the camera's field of view included parts which were not flow (bed, stems and air above the free surface), the original velocity maps were masked out to eliminate those parts.

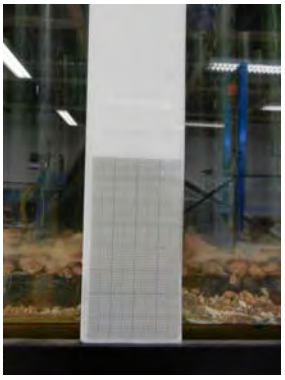

Figure 3.36: PVC sheet used to calculate the calibration factor to convert velocity maps in image units (px/s) into metric units (m/s).

Figures 3.37 and 3.38 present three examples of vertical maps of longitudinal and vertical instantaneous velocity components, respectively, after calibration and mask out procedures. Those maps correspond to the "raw" data in this study and based on the instantaneous flow field a time-averaged characterization of the flow at inter-stem scale was performed. Moreover autocorrelation functions, second and third-order structure functions and energy spectra were computed.

Figure 3.39 presents the time-averaged velocities corresponding to tests in which the instantaneous fields of Figures 3.37 and 3.38 were acquired. The colormaps represent the velocity magnitude, $\left(\bar{u}^2+\bar{w}^2\right)^{1/2}$ and the vector plots correspond the time-averaged velocity field, where only each second vector is represented. The corresponding Reynolds shear stresses and longitudi-

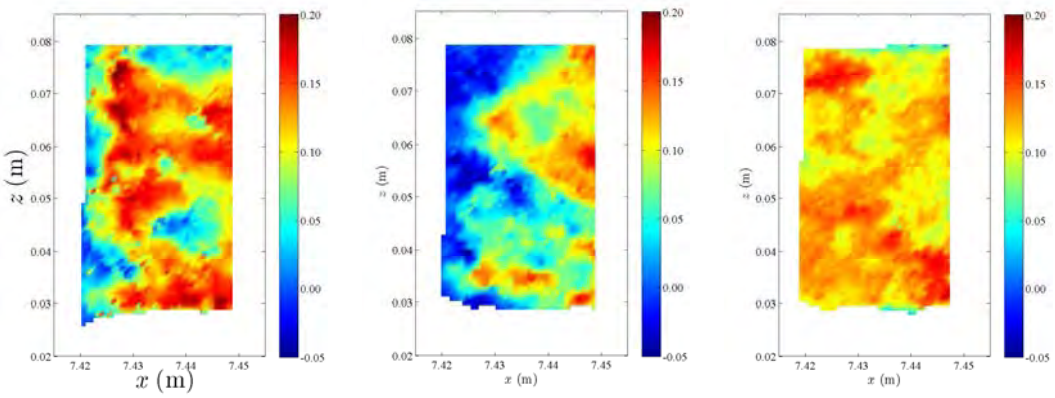

(a) (b) (c)

Figure 3.37: Instantaneous longitudinal velocity, u, maps at measuring gap P7 of test S2 at a) $y = 0.214$ m, b) $y = 0.224$ m and c) $y = 0.234$ m. Units of velocity colormaps are m/s.

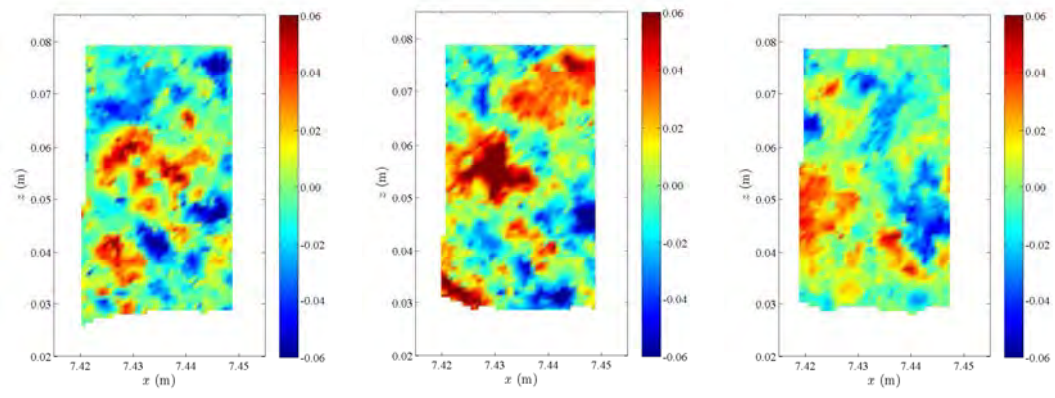

(a) (b) (c)

Figure 3.38: Instantaneous vertical velocity, w, maps at measuring gap P7 of test S2 at a) $y = 0.214$ m, b) $y = 0.224$ m and c) $y = 0.234$ m. Units of velocity colormaps are m/s.

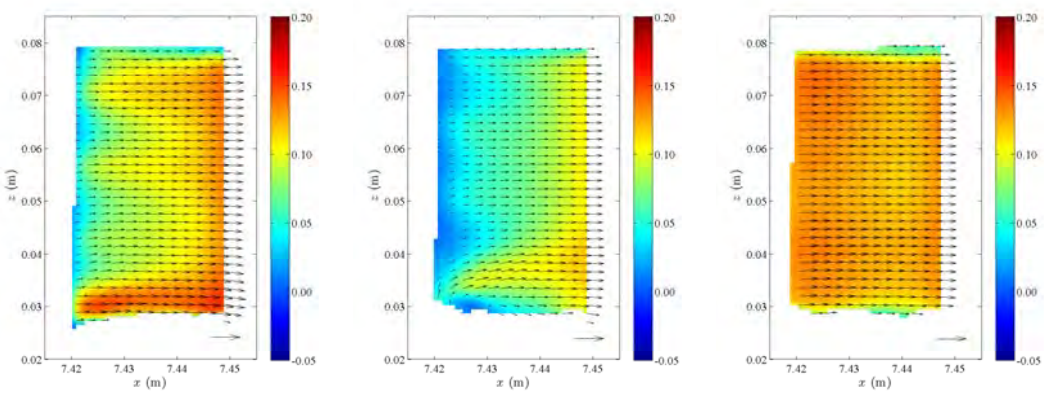

(a) (b) (c)

Figure 3.39: Time-averaged velocity maps at measuring gap P7 of test S2 at a) $y = 0.214$ m, b) $y = 0.224$ m and c) $y = 0.234$ m. The colormap represents the velocity magnitude, $\left(\bar{u}^2 + \bar{w}^2\right)^{1/2}$. Units of velocity colormaps are m/s. The arrow at the graphs bottom is the scale of the vector plot and it corresponds to 0.2 m/s.

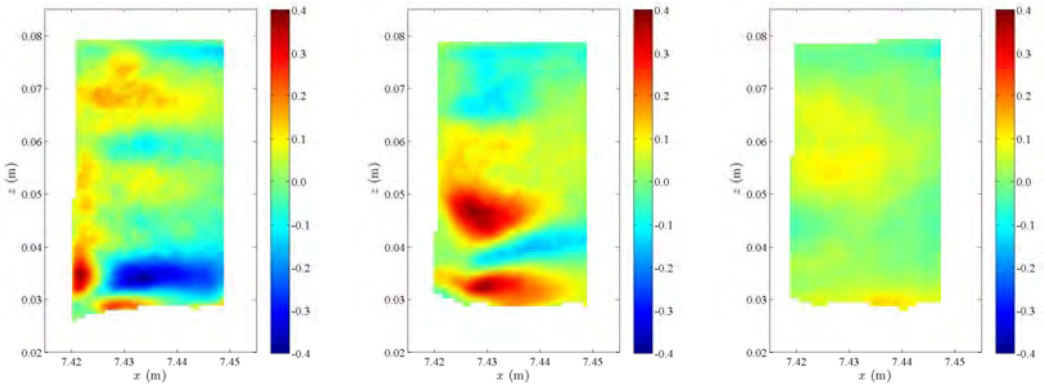

(a) (b) (c)

Figure 3.40: Time-averaged Reynolds shear stress $\left(-\rho\overline{u'w'}\right)$ maps at measuring gap P7 of test S2 at a) $y = 0.214$ m, b) $y = 0.224$ m and c) $y = 0.234$ m. Units of stress colormaps are Pa.

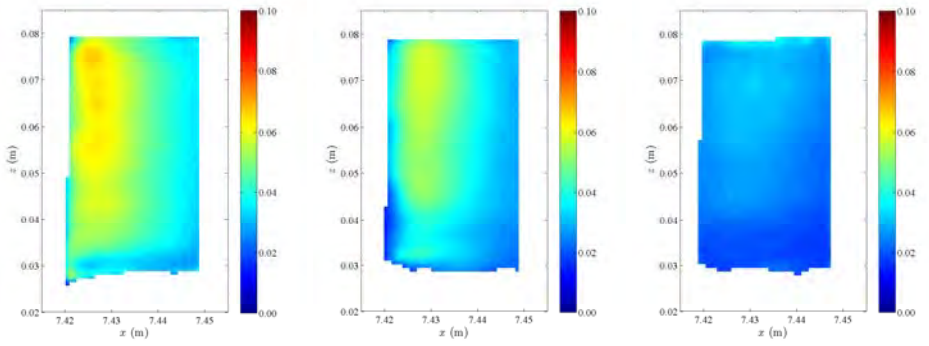

(a) (b) (c)

Figure 3.41: Longitudinal turbulent intensity $\left(\overline{u'u'}^{1/2}\right)$ maps at measuring gap P7 of test S2 at a) $y = 0.214$ m, b) $y = 0.224$ m and c) $y = 0.234$ m. Units of colormaps are m/s.

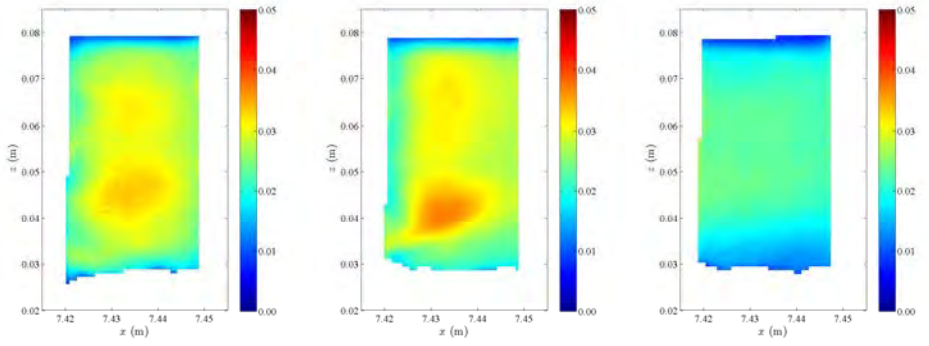

(a) (b) (c)

Figure 3.42: Vertical turbulent intensity $\left(\overline{w'w'}^{1/2}\right)$ maps at measuring gap P7 of test S2 at a) $y = 0.214$ m, b) $y = 0.224$ m and c) $y = 0.234$ m. Units of colormaps are m/s.

nal and vertical turbulent intensities are shown in Figures 3.40, 3.41 and 3.42, respectively.

Data corresponding to vertical planes were mainly applied to compute the double-averaged velocity and stress profiles presented in Chapter 4. The quality of the mean (double-averaged) values depends on the number and on the location of the space-sample points or profiles. The Appendix A presents a conference paper where the issues related to the sufficiently sampling for application of the DAM are discussed.

Regarding the data from horizontal planes, instantaneous velocity series in spanwise direction were used to characterize the turbulence of the studied flows as explained in Chapter 7. The time-averaged flow field allows a qualitative characterization of the flow within the inter-stem space. Figures 3.43 and 3.44 present, for test S2, a time-averaged velocity and vorticity map, respectively, at each measuring gap.

The qualitative time-averaged flow analysis revealed that the inter-stem space is characterized by alternating zones of low velocity in wake regions and high velocity zones between stems, for all the stem areal number-density tested. The time-averaged vorticity maps show a repeating symmetrically paired vortexes pattern caused by the unsteady separation of the flow on the cylinders. These quasi-symmetric high vorticity patterns behind the stems identify von Kármán vortex streets. Comparing vorticity maps for the different longitudinal positions, one can conclude that stems induce a regular structure of vortex patterns independently of the stem areal number-density. However, the space necessary to fully develop the vortex pattern is strongly reduced in dense patches. At sparse patches vorticity has space to decrease its intensity what is not observed at dense patches where the vortices are forced to compress. From the phenomenological point of view, turbulent structure generation in this kind of flow is similar to generation in the case of an isolated cylinder, it is a wake production dominated flow.

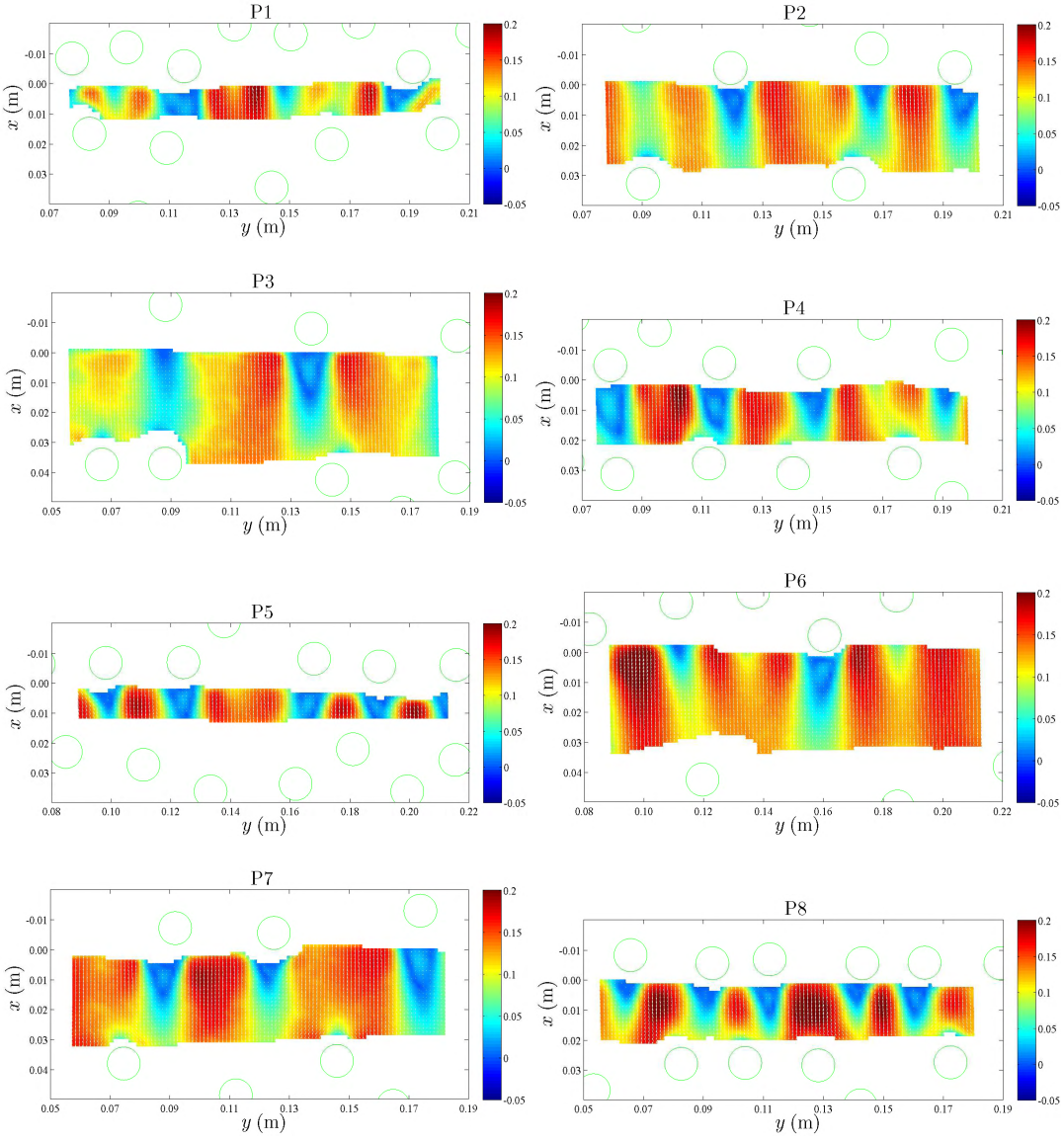

Figure 3.43: Time-averaged velocity maps at the measuring gaps of test S2. Units of colormaps are m/s.

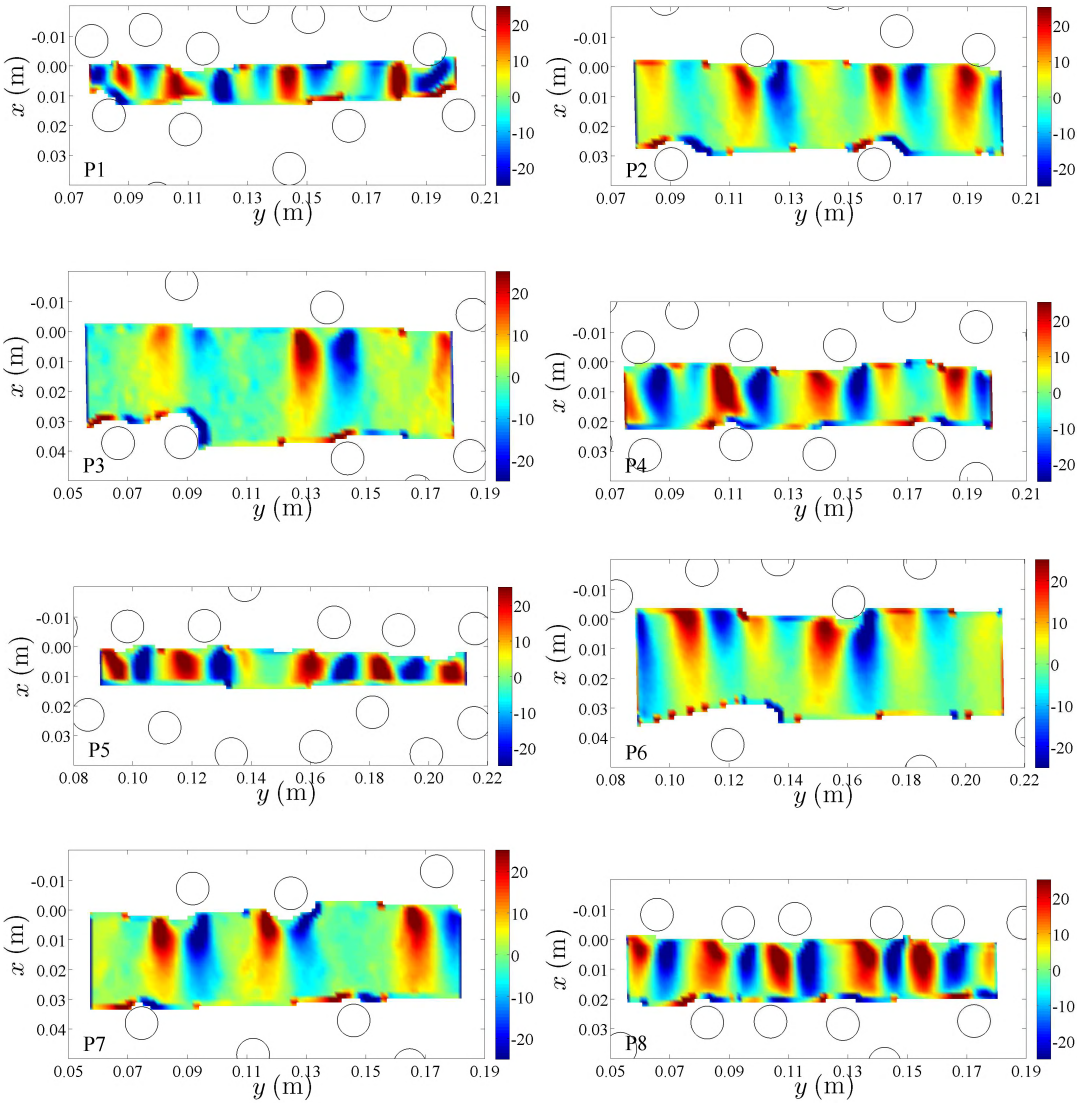

Figure 3.44: Time-averaged vorticity maps at the measuring gaps of test S2. Units of colormaps are s^{-1}.

Chapter 4

Drag coefficient of flows within random arrays of rigid and emergent plant stems

This chapter aims at the quantification of the drag coefficient (C_D) of emergent rigid stems, simulated by vertical cylinders, and at the identification of the parameters to which drag is most sensitive to. Laboratory experiments were performed with rigid and emergent vegetation, featuring constant and varying stem areal number-density (m), under gradually varied flow conditions. Data acquisition consisted in 2D instantaneous velocities maps measured with PIV. Data treatment involved Double-Averaging methods and a dimensional analysis identified the relevant non-dimensional parameters characterizing these flows. At patch scale, the longitudinal increase of m is associated to smaller magnitudes of the drag force per unit of submerged stem length (F_D). However, at wavelength scale, there is no appreciable effect of spatial variability of m and F_D becomes independent of the particular arrangement of stems. For the range of investigated Re_p and m, C_D does not vary with Re_p. C_D seems to increase for lower relative flow depths, revealing the influence of the bottom roughness. It is argued that the drag force should be calculated with the full momentum equation.

Keywords: Vegetation, PIV, Double-Averaging Methodology, Dimensional analysis, Drag coefficient.

4.1 Introduction

River engineering works procure, in a sustainable society, the promotion of high standards of water quality and habitat diversity within good landscape design practices. Vegetation plays a key role in river systems as it affects flow resistance and fluxes of sediments, nutrients and contaminants (Tanino & Nepf, 2008) and it provides a large range of ecosystem services (Aberle & Järvelä, 2013), allied to such economical and safety functions as navigation and flood protection. Promoted by increasing environmental concerns, a large number of scientific works have been carried out during the last decades dealing with flows within vegetation-covered boundaries. These include field studies (Kadlec, 1990; Lee *et al.*, 2004; Nikora *et al.*, 2008; Petryk & Bosmajian, 1975) but most publications report laboratory experiments with arrays of flexible (Dittrich *et al.*, 2012; Fathi-Maghadam & Kouwen, 1997; James *et al.*, 2008; Järvelä, 2002; Nepf & Vivoni, 1999) or rigid stems (Ferreira *et al.*, 2009b; Li & Shen, 1973; Nepf, 1999; Stone & Shen, 2002; Tanino & Nepf, 2008; White & Nepf, 2008). There are also some theoretical works (Cheng, 2013; Lee *et al.*, 2004; Maheshwari, 1992; Yen, 2002) presenting models and respective application domain, and, in the computational realm, an increasing number of numerical databases for flows within vegetation reaches (Koch & Ladd, 1997; López & García, 1998, 2001).

The characterization of drag forces on vegetation elements is one of the most important fields of research, with important applications in civil engineering, namely in the estimation of hydraulic resistance for design of fluvial channels or flood forecasting (Kadlec, 1990; López & García, 1998). Most of the existing design criteria and simulation models employ resistance formulas such as Manning's, necessarily calibrated *ad hoc*. Moving toward physically based design criteria, progresses have been made in the characterization of 3D flows over irregular boundaries and over canopies, mainly due to the application of the Double-Averaging Methodology (DAM), which is a particular form of upscaling in the spatial and temporal sense (Finnigan, 2000; Gimenez-Curto & Corniero Lera, 1996; Nikora *et al.*, 2001, 2007a; Raupach *et al.*, 1986).

Many of the studies aimed at the quantification and parametrization of flow resistance attributable to vegetation are based on the rigid cylinder analogy. On one hand it might be argued that such simplification does not cover most of the wide range of natural conditions; on the other hand some key physical processes governing flow resistance of vegetated areas can be better understood with simple rigid-stem experimental apparatus. This is the case of the effect of changing the number of stems per unit plan area on flow variables such as flow resistance or the relative magnitude of forces acting on the bed boundary and on the stems. Furthermore, floodplains populated by shrubs or trees and wetlands populated by reed-type vegetation, which are cases where vegetation can be simulated by rigid stems, are often found in nature.

The vegetation drag coefficient, C_D, is an empirically derived function of the fluid, flow and vegetation properties. It is of great importance to river engineers who seek for practical models to

evaluate the flow resistance and to some numerical hydrodynamic models. Several authors have computed the vegetation drag coefficient and studied its dependence on characteristic parameters (Ishikawa *et al.*, 2000; Nepf, 1999; Stoesser *et al.*, 2010; Tanino & Nepf, 2008; Tinoco & Cowen, 2013), namely the volumetric solid fraction, ϕ, which is the ratio between the volume occupied by stems and the total control volume, and stem Reynolds number, defined as $Re_p = Ud/\nu$, U being the depth-averaged mean longitudinal velocity, d the stem diameter and ν the fluid kinematic viscosity.

A literature review revealed that there are inconsistencies regarding the dependence of the drag coefficient on the volumetric solid fraction and on the stem Reynolds number: Nepf (1999) presented a negative correlation between drag coefficient and ϕ but most of the authors have found a positive correlation (e.g. Ishikawa *et al.* (2000); Tanino & Nepf (2008); Tinoco & Cowen (2013)); also, positive (Ishikawa *et al.*, 2000) and negative correlations (Tanino & Nepf, 2008) and also lack of correlation (Tinoco & Cowen, 2013) have been reported in what concerns the relation between C_D and Re_p. However, one must note that most of the studies consider the vegetation drag force balanced only by the longitudinal pressure gradient. Although the latter is the dominant term in the horizontal balance of forces, the balance of the other smaller terms might have a non-negligible impact. Particularly, form-induced (or dispersive) stresses, which are often considered negligible in literature, may present magnitudes of the same order as Reynolds stresses (Ferreira *et al.*, 2009b). Bearing these issues in mind, the main objectives of this study are the quantification of the drag coefficient of emergent rigid stems, simulated by vertical cylinders, and to determine to which parameters the value of C_D is most sensitive to.

Since natural systems are rarely homogeneous, the flow within the stem array is influenced by several space scales, determined by the stem diameter, the areal number-density of stems, herein designated by m and expressed in stems/m^2, and its spatial modulation. The present work features the study of a flow with and without spatial variability of m along the streamwise direction. Particular goals include i) a detailed characterization and quantification of the flow within vegetated areas susceptible to be simulated by dense arrays of vertical emergent stems; ii) the quantification of the forces acting on the stems and iii) a discussion on the dependence of the drag coefficient on the non-dimensional parameters that characterize these kind of flows. These objectives lead to a better knowledge of the flow resistance in wetlands and vegetated areas in general.

The objectives are achieved by carrying out in laboratory three tests simulating rigid and emergent vegetation, with constant and varying density of stems. The present study employs rigid, emergent and slightly rough cylinders, randomly placed as a proxy for natural stems in a compromise between laboratory feasibility and physical similitude. The data acquisition consisted mainly in 2D instantaneous velocities maps measured with a Particle Image Velocimetry system (PIV). The data treatment is carried out following the framework of Double-Averaging

Methodology (DAM) and a dimensional analysis is performed to identify the relevant parameters on the characterization of flows within arrays of rigid and emergent stems.

This work is organized in five main sections. After the introduction, the governing equations are presented. Then, it follows the description of the experimental setup. Further, the results are presented and discussed and finally the paper is closed with the main conclusions.

4.2 Governing equations

4.2.1 Double-Averaged Navier Stokes Equations

The Double-Averaging Methodology (DAM) provides the conceptual framework for the calculation of the force acting on the stems and, independently, the force acting on the bed surface. DAM is an upscaling technique that introduces a spatial decomposition of the time-averaged flow variables into a spatial fluctuation component and a double-averaged value. If θ is a generic flow quantity, the time averaged value is decomposed in $\bar{\theta} = \langle\bar{\theta}\rangle + \tilde{\theta}$, where $\tilde{\theta}$ is the spatial fluctuation and $\langle\bar{\theta}\rangle$ is the double-averaged (time- and space-averaged) value, herein simply designated as the mean value of that quantity. The flow is described at larger spatial scales and the effects of spatial variability are expressed as dispersive quantities (Finnigan, 2000; Raupach *et al.*, 1986). The forces acting on the bed and on the stems are calculated from the DANS (Double-Averaged Navier-Stokes) equations (Nikora *et al.*, 2001, 2007a). For steady flows, the DANS equations are written as

$$\begin{aligned}\langle\bar{u}_i\rangle\frac{\partial\langle\bar{u}_j\rangle}{\partial x_i} &= g_j - \frac{1}{\psi\rho}\frac{\partial\psi\langle\bar{p}\rangle}{\partial x_j} - \frac{1}{\psi}\frac{\partial\psi\langle\overline{u_i'u_j'}\rangle}{\partial x_i} - \frac{1}{\psi}\frac{\partial\psi\langle\tilde{u}_i\tilde{u}_j\rangle}{\partial x_i} \\ &+ \frac{1}{\psi}\frac{\partial}{\partial x_i}\left(\psi\left\langle\nu\frac{\partial\bar{u}_j}{\partial x_i}\right\rangle\right) + \frac{1}{\rho\forall_f^{(s)}}\int_{S_{int}^{(s)}}\bar{p}n_j\mathrm{d}S - \frac{1}{\forall_f^{(s)}}\int_{S_{int}^{(s)}}\nu\frac{\partial\bar{u}_j}{\partial x_i}n_i\mathrm{d}S \\ &+ \frac{1}{\rho\forall_f^{(b)}}\int_{S_{int}^{(b)}}\bar{p}n_j\mathrm{d}S - \frac{1}{\forall_f^{(b)}}\int_{S_{int}^{(b)}}\nu\frac{\partial\bar{u}_j}{\partial x_i}n_i\mathrm{d}S, \quad (4.1)\end{aligned}$$

where $i = x, y, z$ are the streamwise, spanwise and vertical directions, respectively, of the Cartesian referential, $\bar{u}_i$ and $\bar{p}$ are the time-averaged velocities and pressure, respectively, $\langle\bar{u}_i\rangle$ and $\langle\bar{p}\rangle$ are the mean (space- and time-averaged) velocities and pressure, respectively, $\tilde{u}_i = \bar{u}_i - \langle\bar{u}_i\rangle$ stands for the spatial velocity fluctuations, $\forall_f^{(k)}$ and $S_{int}^{(k)}$ stand, respectively, for the volume of fluid and for the area of the fluid-solid interface of the control volume k, ψ is the volumetric fluid fraction defined as $\psi = 1 - \phi^{(s)} - \phi^{(b)}$, $\phi^{(k)}$ being the volumetric solid fraction in control volume k. $k = s$ identifies the control volume bounded by the mean bed elevation and the free surface and $k = b$ identifies the control volume bounded by a horizontal plane that contains the crests of the rough bed and by the mean bed elevation. The stress and drag terms in Eq. (4.1) are:

$-\rho\psi\langle\overline{u_i'u_j'}\rangle$, the Reynolds stress tensor; $-\rho\psi\langle\tilde{u}_i\tilde{u}_j\rangle$, the form-induced stress tensor; $\psi\left\langle\nu\frac{\partial\bar{u}_j}{\partial x_i}\right\rangle$, the viscous stresses; $\frac{1}{\rho\forall_f^{(s)}}\int_{S_{int}^{(s)}}\bar{p}n_j\mathrm{d}S$, the form (pressure) drag on the stems; $-\frac{1}{\forall_f^{(s)}}\int_{S_{int}^{(s)}}\nu\frac{\partial\bar{u}_j}{\partial x_i}n_i\mathrm{d}S$, the viscous (skin) drag on the stems; $\frac{1}{\rho\forall_f^{(b)}}\int_{S_{int}^{(b)}}\bar{p}n_j\mathrm{d}S$, the form (pressure) drag on the bed and $-\frac{1}{\forall_f^{(b)}}\int_{S_{int}^{(b)}}\nu\frac{\partial\bar{u}_j}{\partial x_i}n_i\mathrm{d}S$, the viscous drag on the bed (all drag forces per unit mass).

4.2.2 Mean pressure distribution

To obtain the pressure distribution one integrates vertically the vertical component of Eq. (4.1). In the present work only longitudinal and vertical components of the velocity field were measured as it was assumed that $\langle\bar{v}\rangle\approx 0$ (Ricardo *et al.*, 2013). Furthermore, viscous stresses are neglected: due to the small magnitude of the water kinematic viscosity, those stresses are expected to be at least one order of magnitude smaller than the other terms in Eq. (4.1). Under these conditions and further introducing the free-surface kinematic condition, $\partial h/\partial x\,\langle\bar{u}\rangle|_h=\langle\bar{w}\rangle|_h$ (where h stands for the water depth), the integration of the z-component of Eq. (4.1) between a generic level z and the free-surface yields

$$\psi(z)\langle\bar{p}\rangle(z)=\rho g\cos\beta\,[\psi]_z^h+\rho\varkappa(x,z) \tag{4.2}$$

where, simplifying the notation, the square brackets are used to represent the integral variables, $[\theta]_z^h=\int_z^h\theta\mathrm{d}z$ and the function

$$\begin{aligned}\varkappa(x,z)=&\frac{\partial\left[\psi\langle\bar{w}\rangle\langle\bar{u}\rangle\right]_z^h}{\partial x}-\left[\langle\bar{w}\rangle\langle\bar{u}\rangle\frac{\partial\psi}{\partial x}\right]_z^h-\left(\psi\langle\bar{w}\rangle\langle\bar{w}\rangle\right)|_z-\left[\langle\bar{w}\rangle\langle\bar{w}\rangle\frac{\partial\psi}{\partial z}\right]_z^h\\&+\frac{\partial\left[\psi\langle\overline{u'w'}\rangle\right]_z^h}{\partial x}-\frac{\partial h}{\partial x}\left(\psi\langle\overline{u'w'}\rangle\right)|_h+\left(\psi\langle\overline{w'w'}\rangle\right)|_h-\left(\psi\langle\overline{w'w'}\rangle\right)|_z\\&+\frac{\partial\left[\psi\langle\tilde{u}\tilde{w}\rangle\right]_z^h}{\partial x}-\frac{\partial h}{\partial x}\left(\psi\langle\tilde{u}\tilde{w}\rangle\right)|_h+\left(\psi\langle\tilde{w}\tilde{w}\rangle\right)|_h-\left(\psi\langle\tilde{w}\tilde{w}\rangle\right)|_z\end{aligned} \tag{4.3}$$

represents the deviation to the hydrostatic pressure distribution.

4.2.3 Mean drag force

The integration of the longitudinal component of the momentum conservation equation (Eq. 4.1) leads to an equation that allows the computation of the drag force exerted on the stems. With the same assumptions stated for the vertical component, the longitudinal components of DANS

are written as

$$\psi\frac{\partial\langle\bar{u}\rangle\langle\bar{u}\rangle}{\partial x}+\psi\frac{\partial\langle\bar{u}\rangle\langle\bar{w}\rangle}{\partial z}=-\psi g\sin\beta-\frac{1}{\rho}\frac{\partial\psi\langle\bar{p}\rangle}{\partial x}-\frac{\partial\psi\langle\overline{u'u'}\rangle}{\partial x}-\frac{\partial\psi\langle\overline{w'u'}\rangle}{\partial z}$$
$$-\frac{\partial\psi\langle\tilde{u}\tilde{u}\rangle}{\partial x}-\frac{\partial\psi\langle\tilde{w}\tilde{u}\rangle}{\partial z}+\frac{\psi}{\rho\forall_f}\int_{S_{int}^{(b)}}\bar{p}n_x\mathrm{d}S+\frac{\psi}{\rho\forall_f}\int_{S_{int}^{(s)}}\bar{p}n_x\mathrm{d}S$$
$$-\frac{\psi}{\forall_f}\int_{S_{int}^{(b)}}\nu\left(\frac{\partial\bar{u}}{\partial x}n_x+\frac{\partial\bar{u}}{\partial z}n_z\right)\mathrm{d}S-\frac{\psi}{\forall_f}\int_{S_{int}^{(s)}}\nu\frac{\partial\bar{u}}{\partial x}n_x\mathrm{d}S \quad (4.4)$$

Writing the pressure and the viscous forces per unit volume as $I_{px}^{(b)}=-\frac{1}{\forall_f}\int_{S_{int}^{(b)}}\bar{p}n_x\mathrm{d}S$, $I_{px}^{(s)}=-\frac{1}{\forall_f}\int_{S_{int}^{(s)}}\bar{p}n_x\mathrm{d}S$, $I_{\nu x}^{(b)}=\frac{1}{\forall_f}\int_{S_{int}^{(b)}}\mu\left(\frac{\partial\bar{u}}{\partial x}n_x+\frac{\partial\bar{u}}{\partial z}n_z\right)\mathrm{d}S$ and $I_{\nu x}^{(s)}=\frac{1}{\forall_f}\int_{S_{int}^{(b)}}\mu\frac{\partial\bar{u}}{\partial x}n_x\mathrm{d}S$, introducing the previously obtained pressure distribution, carrying out the vertical integration, between zero and h, and introducing the free surface kinematic condition, Eq. (4.4) becomes

$$\frac{\partial\left[\psi\langle\bar{u}\rangle\langle\bar{u}\rangle\right]_0^h}{\partial x}-\left[\langle\bar{u}\rangle\langle\bar{u}\rangle\frac{\partial\psi}{\partial x}\right]_0^h-\left[\langle\bar{u}\rangle\langle\bar{w}\rangle\frac{\partial\psi}{\partial z}\right]_0^h=-g\sin\beta\left[\psi\right]_0^h$$
$$-g\cos\beta\frac{h^2}{2}\frac{\partial\psi}{\partial x}-g\cos\beta h\psi\frac{\partial h}{\partial x}-\frac{\partial\left[\varkappa(x,z)\right]_0^h}{\partial x}+\frac{\partial h}{\partial x}\varkappa(x,h)-\frac{\partial\left[\psi\langle\overline{u'u'}\rangle\right]_0^h}{\partial x}$$
$$+\frac{\partial h}{\partial x}\left(\psi\langle\overline{u'u'}\rangle\right)\big|_h-\left(\psi\langle\overline{w'u'}\rangle\right)\big|_h+\left(\psi\langle\overline{w'u'}\rangle\right)\big|_0-\frac{\partial\left[\psi\langle\tilde{u}\tilde{u}\rangle\right]_0^h}{\partial x}+\frac{\partial h}{\partial x}\left(\psi\langle\tilde{u}\tilde{u}\rangle\right)|_h$$
$$-\left(\psi\langle\tilde{w}\tilde{u}\rangle\right)|_h+\left(\psi\langle\tilde{w}\tilde{u}\rangle\right)|_0-\frac{1}{\rho}\alpha_{b,p}\{\psi\}\langle\bar{f}_x^{(b,p)}\rangle-\frac{1}{\rho}\alpha_{s,p}\{\psi\}\langle\bar{f}_x^{(s,p)}\rangle$$
$$-\frac{1}{\rho}\alpha_{b,\nu}\{\psi\}\langle\bar{f}_x^{(b,\nu)}\rangle-\frac{1}{\rho}\alpha_{s,\nu}\{\psi\}\langle\bar{f}_x^{(s,\nu)}\rangle \quad (4.5)$$

It should be noticed that the last four terms on the right hand side are handled as $\int_0^h\frac{\psi}{\rho}I_{px}^{(b)}\mathrm{d}z\approx\frac{1}{\rho}\{\psi I_{px}^{(b)}\}h=\frac{1}{\rho}\alpha_{b,p}\{\psi\}\{I_{px}^{(b)}\}h=\frac{1}{\rho}\alpha_{b,p}\{\psi\}\langle\bar{f}_x^{(b,p)}\rangle$, where the brackets $\{\}$ stand for the depth-average operator and the constant $\alpha_{b,p}$ represents the deviation of the product of averaged variables and the averaged of the product of the same variables.

The mean quantity $\langle\bar{f}_x^{(s)}\rangle=\langle\bar{f}_x^{(s,\nu)}\rangle+\langle\bar{f}_x^{(s,p)}\rangle$ is the drag force exerted on the stems per unit plan area, susceptible to be expressed as $\langle\bar{f}_x^{(s)}\rangle=F_Dmh$, being F_D the mean drag force per unit of submerged stem length. Note that F_D is not a force (per unit length) acting on any particular stem; it is the mean force acting on the array of stems divided by the number of stems in that array.

4.3 Experimental tests

The experimental work was carried out in a 12.5 m long and 40.8 cm wide recirculating tilting flume of the Laboratory of Hydraulics and Environment of Instituto Superior Técnico. The

flume has glass side walls, enabling flow visualization and laser illumination. The flume bottom was horizontal and covered with a thin horizontal layer of gravel and sand with the thickness of 2 times the mean diameter of the gravel. Arrays of rigid, vertical and cylindrical stems were randomly placed along of a 3.5 m long reach simulating emergent vegetation conditions. The diameter of the cylindrical elements is 1.1 cm. Downstream the reach covered with vegetation, a coarse gravel weir controlled the flow, which was subcritical both downstream and upstream of the vegetated reach.

Three experimental tests were performed, two with a constant areal number-density of stems and one with spatially varying stem areal number-density. To enable the velocity measurements, gaps (narrow regions without stems in the spanwise direction) were enforced, whose width was equal to the mean inter-stem distance of the upstream reach. These gaps will herein be designated as “measuring gaps". The main characteristics of the arrangement of stems and measuring gaps are as follows.

- Test S1 featured 400 stems/m^2 randomly distributed all over the vegetated reach (Fig. 4.1a). The measuring gaps were distanced 1.0 m apart.
- For test S2, stems were placed in order to create a pattern with seven wavelengths, each 0.5 m long, with varying m. Data acquisition was carried out in eight measuring gaps, distributed along two wavelengths - P1 to P4 (first wavelength) and P5 to P8 (second wavelength) as shown in Fig. 4.1b). Each wavelength features
  - a 15 cm long patch with $m = 1600$ stems/m^2 (dense patch, herein); this is the case of patch p_{4-5} in the second wavelength;
  - a 10 cm long transition patch with an average m of 980 stems/m^2, divided into two 5 cm reaches with 1200 stems/m^2 and 800 stems/m^2, respectively from upstream to downstream; it is the case of patches p_{1-2} and p_{5-6}, respectively in the first and second wavelengths;
  - a 15 cm long patch of $m = 400$ stems/m^2 (sparse patch, herein); this is the case of patches p_{2-3} (first wavelength) and p_{6-7} (second wavelength);
  - an ending patch 10 cm long transition patch with an average m of 980 stems/m^2, divided into two 5 cm reaches with $m = 800$ stems/m^2 and $m = 1200$ stems/m^2, respectively from upstream to downstream; it is the case of patches p_{3-4} (first wavelength) and p_{7-8} (second wavelength).
- Test S3 was populated with the same number of stems of test S2 (1366 stems) distributed randomly and uniformly, resulting in $m = 980$ stems/m^2. Measuring gaps were 1.0 m apart (Fig. 4.1c).

The experiments were run with a discharge of 2.3 l/s. The flow is gradually varied, accelerating in the downstream direction. The free surface exhibited an oscillating behaviour with larger amplitudes in dense patches.

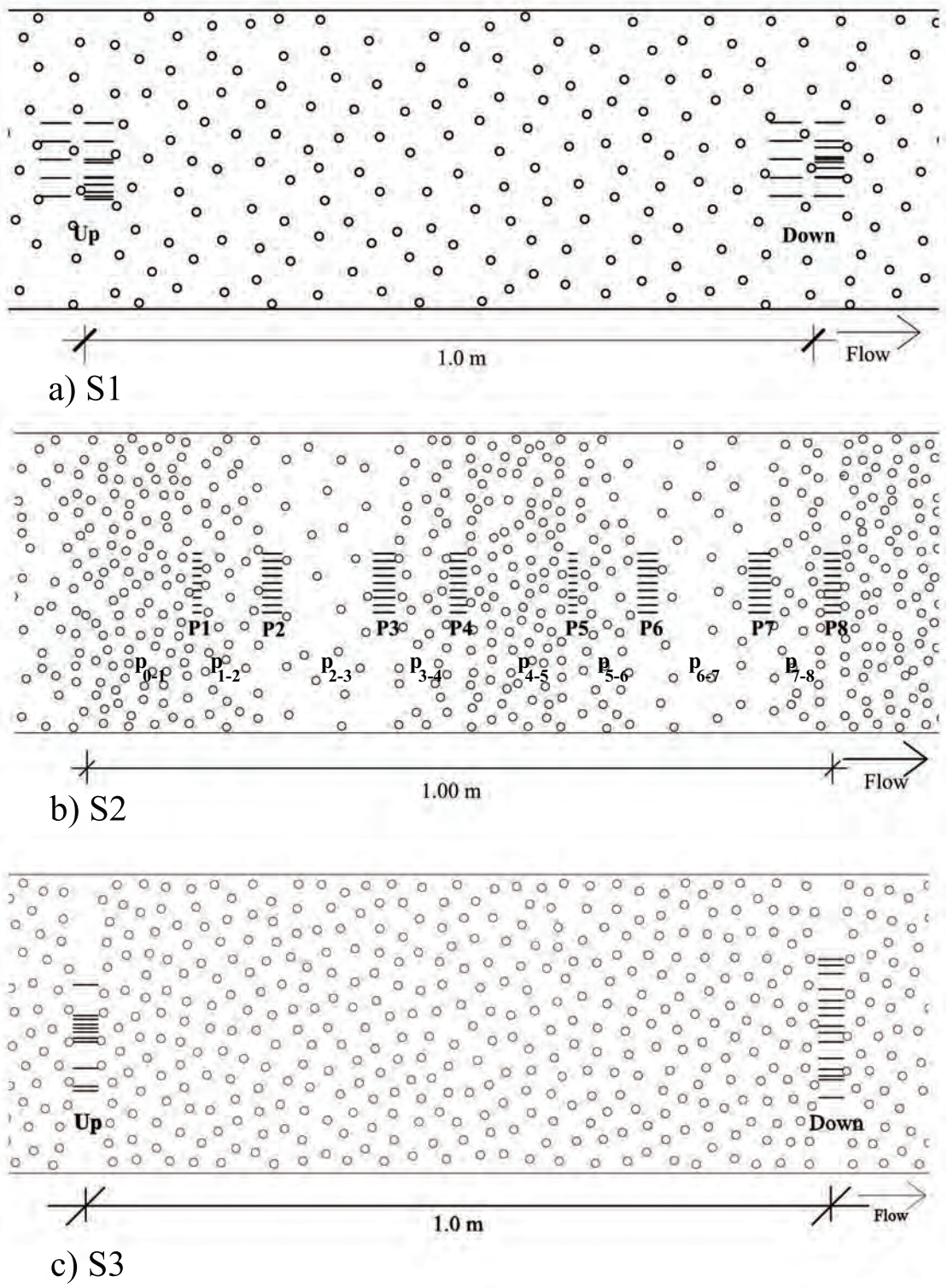

Figure 4.1: Plan view of the stem covered reach where the measurements were carried out for each test: a) test S1; b) test S2 and c) test S3. The solid lines aligned with flow direction indicate the location of the vertical plans measured with PIV.

Table 4.1: Features of the experimental measurements and flow properties for each test.

Test	M.Gap	Patch	x (m)	m (stems/m^2)	dm/dx ($-$)	U (m/s)	h (m)	dh/dx ($-$)	H (m)	Re_p ($-$)
S1	Up		7.270	400	0	0.092	0.066	-	0.044	1170
	Down		8.270	400	0	0.109	0.059	-0.007	0.046	1450
S2	P1	p_{0-1}	6.680	1600	0	0.085	0.065	-0.020	0.046	1121
	P2	p_{1-2}	6.782	980	< 0	0.083	0.064	-0.017	0.045	1158
	P3	p_{2-3}	6.935	400	0	0.090	0.063	-0.002	0.040	1237
	P4	p_{3-4}	7.036	980	> 0	0.099	0.062	-0.012	0.045	1303
	P5	p_{4-5}	7.192	1600	0	0.103	0.057	-0.031	0.038	1302
	P6	p_{5-6}	7.293	980	< 0	0.108	0.056	-0.018	0.036	1374
	P7	p_{6-7}	7.446	400	0	0.100	0.054	-0.010	0.036	1216
	P8	p_{7-8}	7.545	980	> 0	0.106	0.052	-0.017	0.032	1222
S3	Up		6.900	980	0	0.092	0.065	-	0.042	989
	Down		7.900	980	0	0.099	0.051	-0.014	0.041	1064

Table 4.1 summarizes the main flow variables for each test. Herein, x is the longitudinal coordinate of the measuring gap relative to the channel inlet, $\mathrm{d}h/\mathrm{d}x$ is the gradient of the mean flow depth h and H is the depth of the water column where the flow is controlled by the stems. The remaining variables were previously defined. The column label M.Gap identifies the measuring gap where the measurements corresponding to each patch were done.

Measurements consisted in acquisition of 2D (streamwise $\times$ vertical) instantaneous velocity maps with a Particle Image Velocimetry system (PIV), bottom and free surface levels with a laser displacement sensor (Keyence LK-2000) and water temperature with a thermometer. PIV is a technique whose intrusiveness is limited to the introduction of solid targets for flow visualization. The PIV system consisted of an 8-bit 1600×1200 px^2 CCD camera and a double-cavity Nd-YAG laser with pulse energy of 30 mJ at wavelength of 532 nm. PIV image pairs were acquired at a frequency of 15 Hz with a time delay of 1500 μs between frames. The targets were polyurethane particles with a mean diameter of 60 μm in a range from 50 μm to 70 μm and a density of 1.31 g/cm^3. Using this seeding, the cut-off frequency of the turbulent signal, calculated with the theory of Hjemfelt & Mockros (1996), is about 30 Hz. Given that the Nyquist frequency of the PIV measurements is 7.5 Hz, it is concluded that the seeding particles are adequate for the performed laboratory work.

For each longitudinal position, several vertical planes were measured in the central part of the flume width (horizontal lines in Fig. 4.1). For each plane of the test S1 21×486 px^2 images couples were collected, which corresponds to $11'20''$ of total acquisition time. For test S2 10×573 px^2 images couples were collected at each lateral position, representing a total acquisition time of $6'37''$. Concerning the test S3, one run with 5000 image pairs was acquired for each vertical plane, corresponding to $5'33''$ of consecutive data. Image pairs were processed with an adaptive correlation algorithm starting with interrogation area of 128×128 px^2 and ending at 16×16 px^2, without overlap. The spatial resolution of the velocity maps yields to interrogation volumes of $(0.7-1) \times (0.7-1) \times 2$ mm^3, since the laser light sheet is approximately 2 mm thick.

The length scale used in this work to normalize the vertical coordinate in the graphs presented below correspond to the depth of the water column where the flow is controlled by the stems, H. This region is identified by the profile of longitudinal form-induced stress as sketched in Fig. 4.2a).

Fig. 4.2b) shows profiles of the volumetric fluid fraction, or void function, $\psi(x,z)$ showing that the bed and the free-surface oscillations are relatively small. Therefore, the void function is, herein, considered as constant through all the flow depth and determined by the volumetric solid fraction occupied by the stems, $\psi(x) = 1 - \phi^{(s)}$.

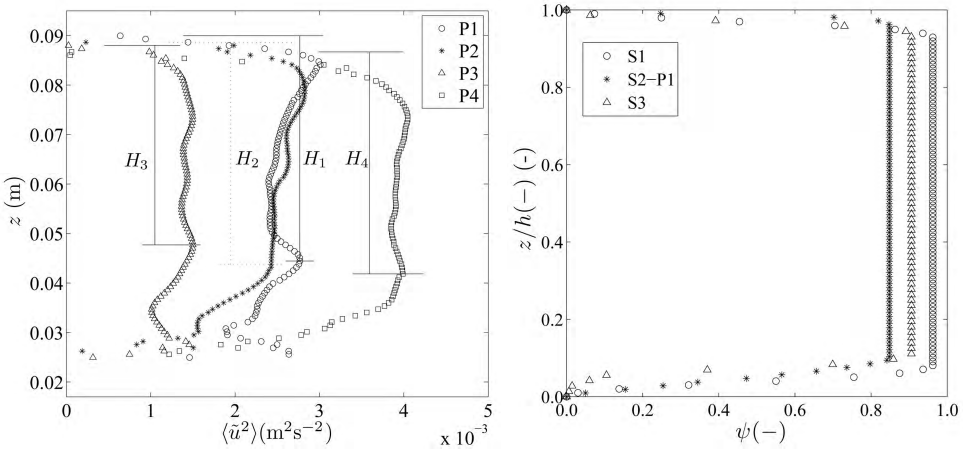

(a) (b)

Figure 4.2: a) Double-averaged profiles of normal longitudinal form-induced stresses for identification of the flow layer controlled by the stems. The data presented correspond to test S2. b) Vertical profiles of void function, $\psi(x,z)$. The vertical axis is normalized by the flow depth, h.

4.4 Results

4.4.1 Dimensional analysis

Any given mean quantity of a physical phenomenon is susceptible to be written as a function of a set of sufficient parameters that fully define that phenomenon (Yalin, 1971, p.6). In this case, the mean drag force on stems and the drag coefficient should depend on:

i) fluid properties, for which the sufficient parameters are the viscosity, μ, and the density, ρ;
ii) vegetation characteristics, which, for rigid stems, are the stem diameter, d, the inter-stem distance s, defined as $s = 1/\sqrt{m}$, its spatial derivative and the roughness of the stems, k_d.
iii) bottom boundary features; in this case the median diameter of the gravel bed d_s stands for a measure of the hydraulic roughness of the immobile boundary;
iv) flow descriptors, for which the necessary and sufficient parameters are the mean depth-averaged longitudinal velocity, U, the flow depth h and their longitudinal derivatives;
v) the acceleration of gravity, g.

Drag forces per unit of submerged stem length are thus completely determined by

$$F_D = f\left(\mu, \rho, d, s, \frac{\partial s}{\partial x}, k_d, d_s, U, h, \frac{\partial U}{\partial x}, \frac{\partial h}{\partial x}, g\right) \tag{4.6}$$

The longitudinal coordinate, x, is not considered since none of the previous parameters varies independently of x.

Applying Vaschy-Buckingham's theorem (also known as π theorem) using U, ρ and d as basic quantities (also called repeating variables), one obtains

$$\Pi_{F_D} = \frac{F_d}{\rho U^2 d} = f_{F_D}\left(Re_p, \frac{s}{d}, \frac{\partial s/d}{\partial x/d}, \frac{d_s}{d}, \frac{k_d}{d}, \frac{h}{d}, \frac{\partial h/d}{\partial x/d}, Fr\right) \tag{4.7}$$

where the stem Reynolds number $Re_p = \frac{U\rho d}{\mu}$ expresses the relative importance of inertial versus viscous effects, the relative inter-stem distance $\frac{s}{d}$ (equivalent to the volumetric solid fraction, ϕ) expresses the influence of flow blockage by stems, the relative grain-size representative diameter $\frac{d_s}{d}$, expresses the influence of bed roughness and $\frac{k_d}{d}$ accounts for the effects stem roughness, the relative flow depth $\frac{h}{d}$ allows for the discussion of the relative influence of the bottom on the flow structure and the Froude number, $Fr = \frac{U}{\sqrt{gh}}$, obtained as (the square root of) a combination of the ratio of $\frac{U^2}{gd}$ and $\frac{h}{d}$, accounts for free-surface effects on the flow structure. Since the areal stem number-density varies longitudinally (patches p_{1-2}, p_{3-4}, p_{5-6}, p_{7-8} in S2) and the flow is gradually varied, the derivatives of the relative inter-stem distance ($\frac{\partial s/d}{\partial x/d}$) and of the relative water depth ($\frac{\partial h/d}{\partial x/d}$) are kept in (4.7).

Figures 4.3 and 4.5 show that the influence of the free-surface over the flow structure are confined to a narrow upper layer, which is compatible with low values of Froude number associated with the investigated flows. Hence, the dependence of C_D on Fr is not discussed. The parameters $\frac{d_s}{d}$ and $\frac{k_d}{d}$ are also not discussed since the properties of the sediments of the gravel bed and the stem roughness are the same for all the tests. One also notices that the derivatives of the dimensionless parameters are the same as the derivatives of the dimensional parameters s and h. Considering that the drag coefficient commonly used in literature is $C_D = 2f_{F_D}$, the functional dependence of the drag force per unit stem length is thus

$$F_D = \frac{1}{2}\rho d U^2 C_D\left(Re_p, \frac{s}{d}, \frac{\partial s}{\partial x}, \frac{h}{d}, \frac{\partial h}{\partial x}\right). \tag{4.8}$$

Equation (4.8) provides the framework for the discussion of the values of F_D and C_D calculated from the PIV database and water depth measurements (shown in the next sub-sections).

4.4.2 Characterization of time- and space-averaged flow

This subsection presents a characterization of the flow for the three experimental tests based on the double-averaged velocity and stress profiles. Note that, hereinafter, for simplification, ρ is omitted in the stress tensors. The quantification of relevant double-averaged quantities allows for the actual calculation of the drag force from Eq. (4.5). Employing discrete measurements, the

calculation of such double-averaged quantities obeys to

$$\langle\bar{\theta}\rangle(z) \approx \frac{\sum_{k=1}^{N-N_0(z)} \bar{\theta}_k(z) A_k(z)}{\sum_{k=1}^{N-N_0(z)} A_k(z)} \tag{4.9}$$

where $\langle\bar{\theta}\rangle = \langle\bar{u}_i\rangle$ or $\langle\bar{\theta}\rangle = \langle\bar{p}\rangle$, $A_k(z)$ is the area of the convex sub-domain Ω_k, defined as the the area of influence of $(x_k, y_k) \in]0, L_x[\times]0, L_y[$ and such that $\bigcup_{k=1}^{N(z)} \Omega_k = \Omega$, N corresponds to the total number of sub-domains and $N_0(z)$ to the number of sub-domains, at elevation z, for which the flow variable is not defined in (x_k, y_k). It should be noticed that $\sum_{k=1}^{N-N_0(z)} A_k(z) < A(z)$ for $N_0(z) > 0$.

Fig. 4.3 presents profiles of longitudinal and vertical velocities. For the longitudinal velocity, one observes that the shape of the profiles is similar for all the tested density of stems. There is a pronounced bulge, at lower layers, in almost all profiles, corresponding to a maximum of the mean longitudinal velocity. Below the maximum, the value of $\langle\bar{u}\rangle$ decreases in fashion typical of a boundary-layer flow. Evidently, near the surface of the gravel elements the no-slip condition applies. Note that the mean flow velocity at the mean trough level is not necessarily zero, it is only required that is is compatible with the mean sub-surface flow which should be negligible. At the free surface, there is a thin boundary layer created by a 0.2 mm thick plastic sheet placed at the free surface to avoid laser refractions during PIV measurements. The main feature of the longitudinal velocity within arrays of rigid stems is its uniformity of the distribution on the region where the flow is controlled by the vertical elements. Regarding its magnitude, the profiles corresponding to downstream positions have higher values than those at upstream expressing the fact that the flow is gradually accelerated.

Profiles of vertical velocity show typically small values, except close to the bottom where, due to the interaction with the bed, the flow shows down- and upward movements (nevertheless presenting values one order of magnitude smaller than the longitudinal velocity). Fig. 4.3b) indicates that the impact of the bed roughness is more important in denser patches. Close to the free surface, the non-zero values might be justified by the vertical oscillations observed. Here, the largest values are observed for the measuring gaps P5 and P8 of S2, which correspond to the densest patches.

Fig. 4.4a) represents Reynolds shear stresses showing that these turbulent stresses have very small magnitudes, almost vanishing on the region controlled by the stems. Close to the bed and the free surface, patches with high stem areal number-density exhibit larger values. The wavy behaviour of this variable, alternating between positive and negative values, is most likely due to

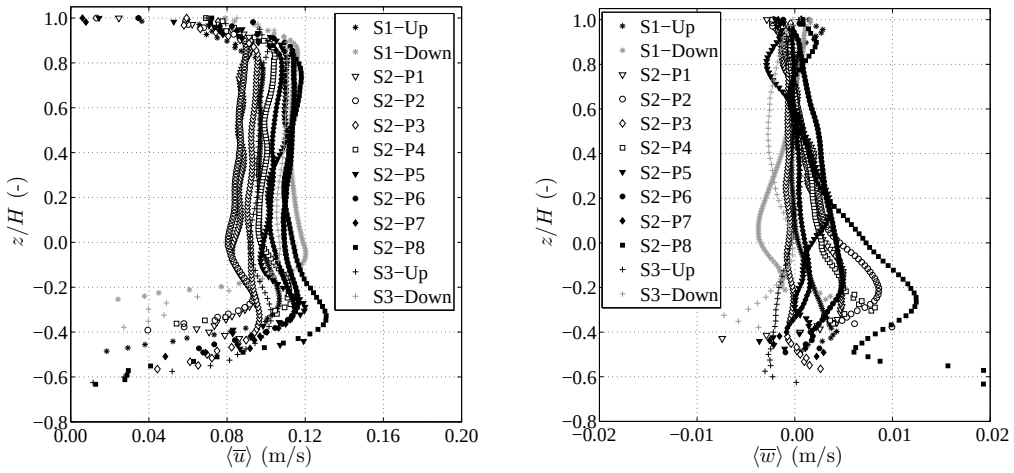

Figure 4.3: a) Double-averaged longitudinal velocity profiles. b) Double-averaged vertical velocity profiles.

the roughness of the vertical stems.

The form-induced shear stresses (Fig. 4.4b) have the maximum values near the bottom and become almost zero at levels close to the free surface. These stresses are, in general, larger than Reynolds stresses and increase with the stem areal number-density.

Normal longitudinal turbulent and dispersive stresses are presented in Fig. 4.5 a) and b), respectively, showing that both have the same order of magnitude. The longitudinal form-induced stress, representing the correlation of the spatial fluctuation of the longitudinal velocity with itself, is a good variable to express the heterogeneity of the flows within vegetation patches. Its magnitude clearly increases with the increasing density of stems. As mentioned above, it allows to identify the region, on the water column, where the flow is controlled by the stems, since its vertical distribution shows an inflection point where the bottom looses importance in the definition of the flow structure.

Fig. 4.6 presents the vertical component of the Reynolds and form-induced stresses showing, in both cases, a correlation between its magnitude and the stem areal number-density. Vertical Reynolds stresses exhibit an almost constant profile at most of the flow depth, decreasing to zero close to the bed and the free-surface. Concerning the dispersive stresses, its magnitude is smaller than the corresponding turbulent stresses and the maximum values are felt close to the bed, decreasing then to zero towards the free-surface. This vertical stress points out that in the region of the interaction with the bed the flow is highly 3D, with important vertical flow components.

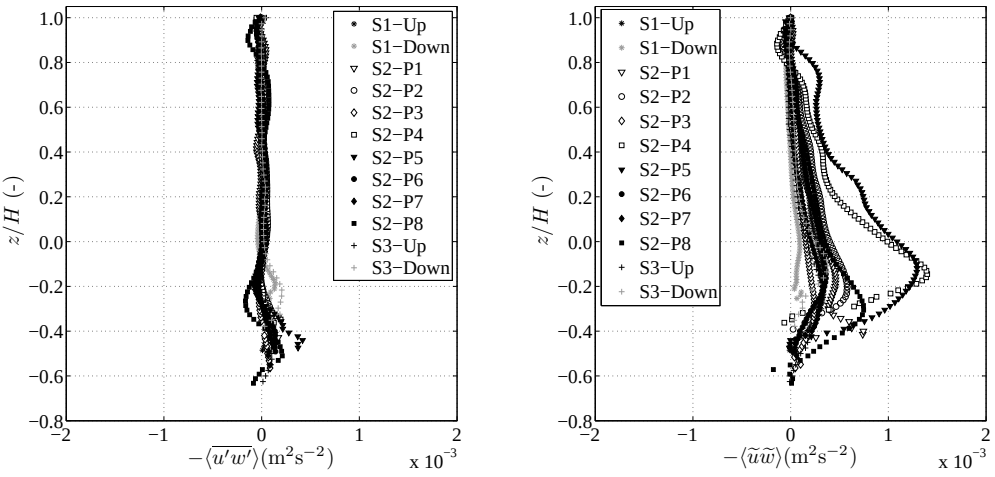

(a) (b)

Figure 4.4: Double-averaged shear stresses: a) Reynolds; b) form-induced.

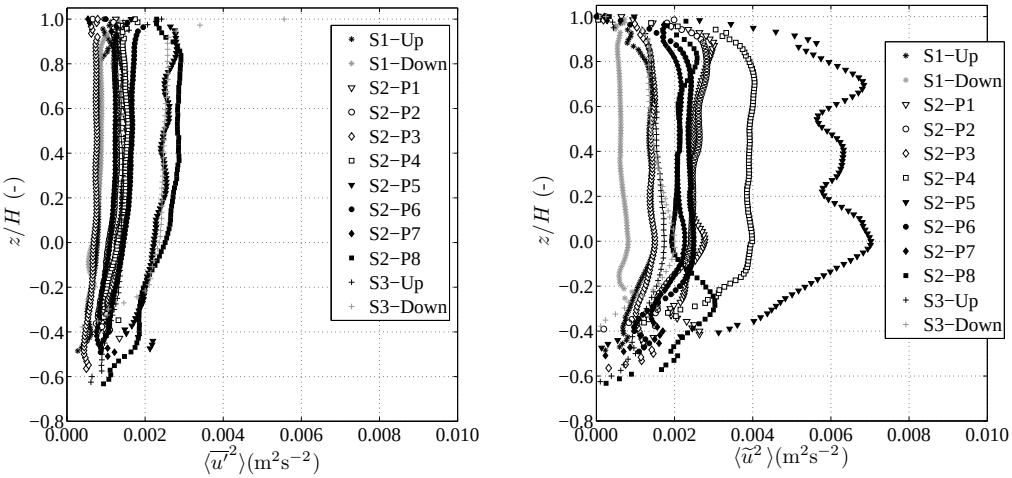

(a) (b)

Figure 4.5: Double-averaged normal longitudinal stresses: a) Reynolds; b) form-induced.

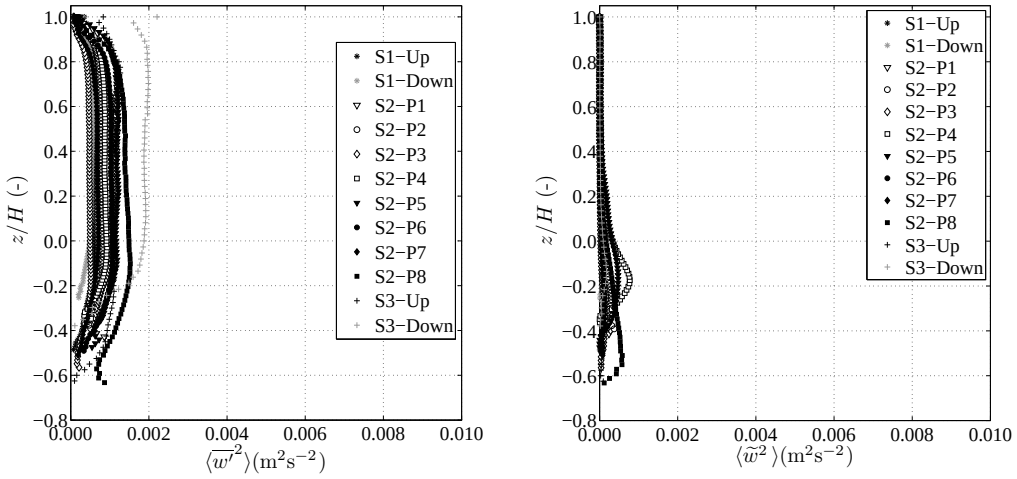

Figure 4.6: Double-averaged normal vertical stresses: a) Reynolds; b) form-induced.

Mean vertical velocity is one order of magnitude smaller that the longitudinal component and does not present important longitudinal gradients (Fig. 4.3b); Reynolds shear stresses proved to be very small through the entire flow depth (Fig. 4.4a); form-induced shear stresses (Fig. 4.4b) and normal vertical form-induced stresses (Fig. 4.6 b) are zero at the free-surface. Therefore, the function $\varkappa(x,z)$ presents values of $\mathscr{O}\left(10^{-4}\right)$, i.e., it is 4 orders of magnitude smaller than the first term of Eq. (4.2). Hence, the pressure distribution is assumed hydrostatic.

4.4.3 Quantification of drag forces and coefficients

The quantification of mean velocities and stresses allows for further simplification of Eq. (4.5), since one notices that some of its terms are negligible: both turbulent and dispersive shear stresses vanish at the bottom and at the free-surface and due to the small amplitude of the bed oscillations; the viscous and pressure drag exerted on the bed per unit plan area, $\langle \overline{f_x^{(b,v)}} \rangle$ and $\langle \overline{f_x^{(b,p)}} \rangle$ respectively, are expected to be very small (Ferreira *et al.*, 2009b), so they were not considered. Therefore, $\langle \bar{f}_x^{(s)} \rangle$ is actually calculated as

$$\langle \bar{f}_x^{(s)} \rangle = \frac{\rho}{\psi} \left(-\frac{\partial \left[\psi \langle \bar{u} \rangle \langle \bar{u} \rangle \right]}{\partial x} + \left[\langle \bar{u} \rangle \langle \bar{u} \rangle \frac{\partial \psi}{\partial x} \right]_0^h - g \frac{h^2}{2} \frac{\partial \psi}{\partial x} - gh\psi \frac{\partial h}{\partial x} - \frac{\partial \left[\psi \langle \overline{u'u'} \rangle \right]_0^h}{\partial x} \right.$$
$$\left. + \frac{\partial h}{\partial x} \left(\psi \langle \overline{u'u'} \rangle \right)\big|_h - \frac{\partial \left[\psi \langle \tilde{u}\tilde{u} \rangle \right]_0^h}{\partial x} + \frac{\partial h}{\partial x} \left(\psi \langle \tilde{u}\tilde{u} \rangle \right)\big|_h \right). \quad (4.10)$$

After computing the force exerted on the stems per unit of plan area, $\langle \bar{f}_x^{(s)} \rangle$, the mean drag

Table 4.2: Values of F_D, C_D and F_D^* for each patch.

Test	S1	S2							S3
		p_{1-2}	p_{2-3}	p_{3-4}	p_{4-5}	p_{5-6}	p_{6-7}	p_{7-8}	
$F_D(\mathrm{N/m})$	0.16	0.19	0.08	0.06	0.17	0.22	0.29	0.13	0.14
$C_D(-)$	2.9	6.3	1.7	0.9	3.0	4.3	5.3	1.8	2.8
$F_D^*(\mathrm{N/m})$	0.17	0.15	0.05	0.11	0.16	0.16	0.24	0.15	0.13

force per unit of submerged stem length, F_D, is obtained by

$$F_D = \frac{\langle \bar{f}_x^{(s)} \rangle}{mh} \tag{4.11}$$

The drag coefficient is defined, from Eq. (4.8), as

$$C_D = 2F_D/(\rho d U^2) \tag{4.12}$$

The mean drag force in the longitudinal direction, for flows over flat beds, is often defined in literature as the force that balances the pressure gradient (Tanino & Nepf, 2008; Tinoco & Cowen, 2013):

$$F_D^* = -\frac{\psi \rho g}{m} \frac{\mathrm{d}h}{\mathrm{d}x} \tag{4.13}$$

The values of F_D, C_D and F_D^* calculated by Eqs. (4.11), (4.12) and (4.13), respectively, for each test are presented in Table 4.2.

The widespread use of F_D^* in the literature justifies a discussion, performed below, of its relation with F_D. The influence of the areal number-density of stems, its modulation and flow variability on the values of F_D and the variation of the values of C_D as a function of the non-dimensional parameters of (4.8) are then discussed.

4.4.4 The use of F_D^* as a proxy for F_D

Equation (4.13) represents the leading term in Eq. (4.11). To better understand the relative contribution of the leading term and remaining terms, F_D is plotted against F_D^* in Fig. 4.7a) and the ratio F_D/F_D^* is shown in Fig. 4.7b) as a function of m. A conspicuous deviation from the identity line is observed in Fig. 4.7a) for large values of F_D. Above all, this means that the approximation error inherent to Eq. (4.13) is not systematic.

Figure 4.7b) allows for a more complete understanding of the relation between the relevant and

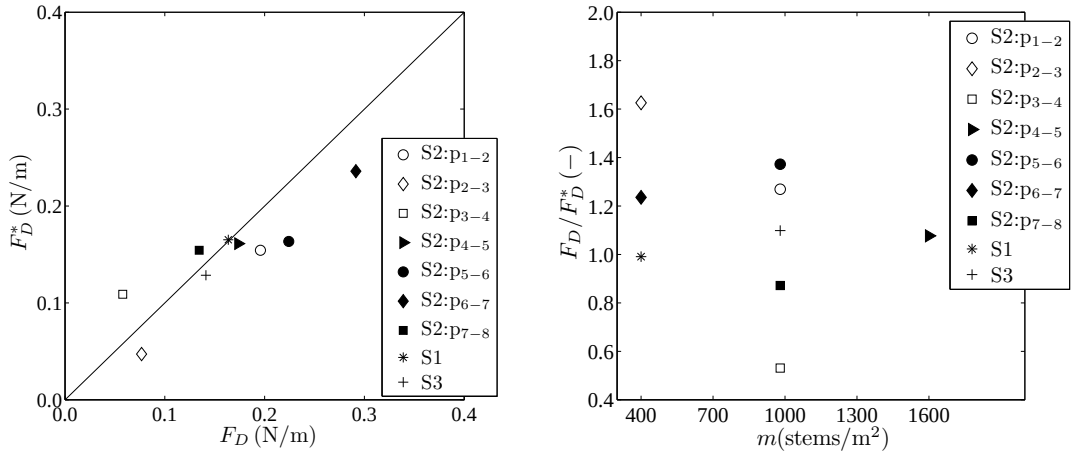

(a) (b)

Figure 4.7: a) Drag force F_D calculated by Eq. (4.11) against the simplification F_D^* expressed by Eq. (4.13); b) the ratio F_D/F_D^* as a function of m.

the secondary terms: for high areal number-density of stems, the dominant term seems sufficient to explain the drag force; on the contrary, for low values of m (400 stems/m^2), the dominant term must be complemented with the secondary terms to avoid blunt errors. Interestingly, it appears that the spatial variability of m can play an important role in the relative magnitude of the terms of Eq. (4.11): for $m = 980$ stems/m^2 and $\frac{\partial m}{\partial x} = 0$, F_D seems satisfactorily described by its dominant term (test S3 in Fig. 4.7b); however, for the same value of m but $\frac{\partial m}{\partial x} < 0$ (or, equivalently, $\frac{\partial s}{\partial x} > 0$) the secondary terms become important and the estimate based solely on the pressure gradient underestimates the true drag force (patches p_{1-2} and p_{5-6}); conversely, for $\frac{\partial m}{\partial x} > 0$ (or, equivalently, $\frac{\partial s}{\partial x} < 0$), secondary terms are also important but the estimate based on the pressure gradient overestimates the true drag force (patches p_{3-4} and p_{7-8}). It is thus concluded that Eq. (4.13) is not a good proxy for the mean drag (per unit length) on plant stems since the approximation error is not systematic and is influenced by gradients in the spatial distribution of stems.

4.4.5 The drag force per unit stem length, F_D

The impact of the variation of the areal number-density of stems on the values of F_D, computed from Eq. (4.11), is shown in Fig. 4.8. The dependence of F_D on m is not conclusive: there seems to be a decreasing trend but only in the highest values of F_D; if one considers the mean of all points for each m, F_D appears approximately constant and thus uncorrelated with m (or s). A closer observation of Fig. 4.8 reveals a dependence on $\frac{\partial m}{\partial x}$; this can be perceived by analysing the values of F_D at $m = 980$ stems/m^2. The relevant points concern test S3 and patches p_{1-2},

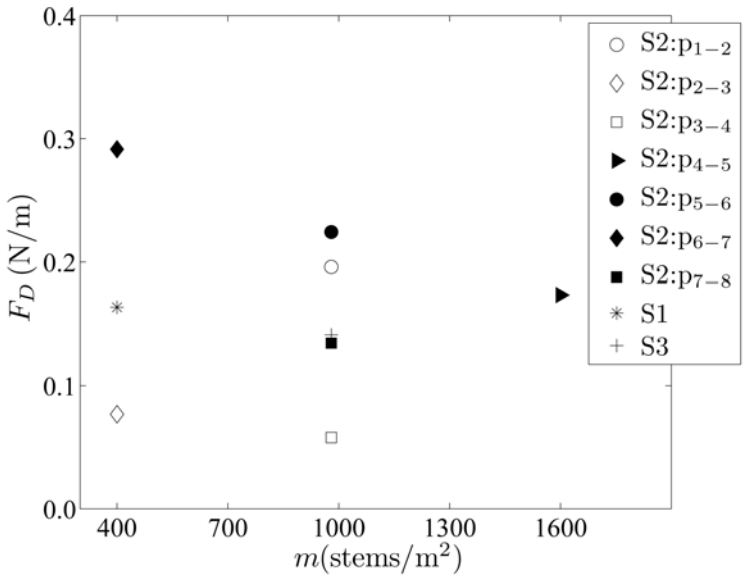

Figure 4.8: Drag force per unit of length of submerged stem, F_D against the stem areal number-density, m.

p_{5-6} $\left(\frac{\partial m}{\partial x} < 0\right)$, p_{4-5} and p_{7-8} $\left(\frac{\partial m}{\partial x} > 0\right)$ of test S2. Patches with $\frac{\partial m}{\partial x} < 0$ exhibit a larger drag force than patches $\frac{\partial m}{\partial x} > 0$. Test S3, with $\frac{\partial m}{\partial x} = 0$, is characterized by an intermediate value of F_D, which contributes to the consistency of this analysis. Hence, the seeming lack of correlation of F_D with s is partially the result of opposite forms of correlation with $\frac{\partial m}{\partial x}$ that cancel out over one wavelength.

To further pursue this issue, the actual drag forces in tests S2 and S3 are calculated and compared. Test S3 was designed to have uniformly distributed the same number of stems between measuring gaps as the two wavelengths of test S2. Furthermore, the submerged stem lengths are comparable in both tests. The total drag force corresponding to the reach between the measuring gaps P1 and P8 on test S2 is 2.9 N, corresponding to 306 stems, while the total force corresponding to the same number of stems in test S3 is 2.6 N. The total drag force is thus practically the same for both tests, although in test S2 its values are sensitive to gradients of m. Interpreting these results one proposes that, in S2, the opposite local influences of $\frac{\partial m}{\partial x} > 0$ and $\frac{\partial m}{\partial x} < 0$ cancel out over each wavelength. One thus concludes that the longitudinal variability of m does not impact the global balance of momentum when its variability is of cyclic nature. This hypothesis can be validated with extra tests featuring the same space-averaged value of m with constant, positive or negative gradients, but this was out of the scope of the present work.

Figure 4.8 also reveals that the values pertaining to the second wavelength, for the same mean value of s and the same value $\frac{\partial s}{\partial x}$, are always larger than the values for the first wavelength. The increase of the drag force from the first to the second wavelength expresses the influence of flow acceleration. Note that this is not a trivial result since, as seen before, drag is not solely

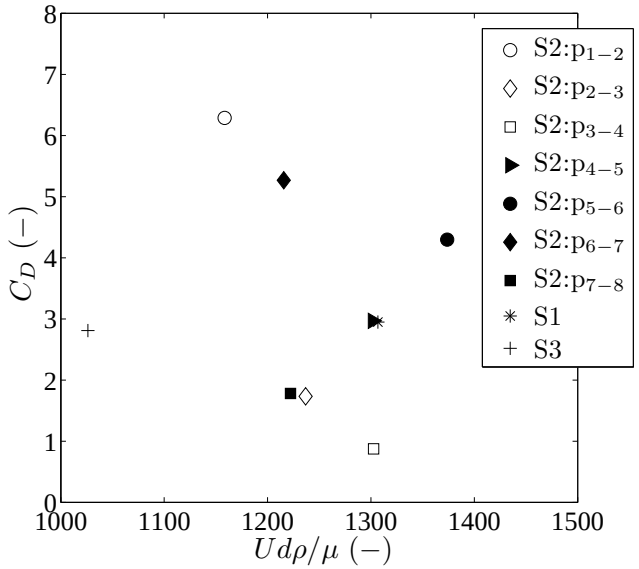

Figure 4.9: Drag coefficient as function of stem Reynolds number $Re_p = Ud\rho/\mu$.

determined by the pressure gradient.

4.4.6 Variation of C_D

Fig. 4.9 shows the dependence of C_D on the stem Reynolds number. It reveals no obvious correlation between the two parameters. As mentioned above, forces acting on stems are mainly pressure drag, as the magnitude of viscosity is sufficiently small to render viscous forces negligible. Therefore, C_D is expected not to change with Re_p, for sufficiently high values of the latter. The somewhat disorganised distribution of values in Fig. 4.9 may be the reflection of the influence of other parameters on C_D (as the randomness of the stem distributions) or it can be due to experimental errors.

The correlation between the drag coefficient and ratio s/d is presented in Fig. 4.10. Although the scatter is high, indicating the influence of other parameters, a tendency for a positive correlation is found, indicating that the drag coefficient should increase with increasing s/d. Since $s = m^{-1/2}$, it means that the presented database reveals a decrease of C_D for increasing stem areal number-density. This is compatible with the study of Nepf (1999), featuring $Re_p = 1000 - 4000$ and $m = 10 - 1000$ stems/m^2. Most of published works claim an inverse trend, notably Tanino & Nepf (2008), Stoesser *et al.* (2010) and Tinoco & Cowen (2013); however it must be underlined that conditions, namely the form of calculating F_D, may vary considerably from one study to another rendering void the direct comparison.

In the case of tests S1 and S3, calculating C_D from F_D^* allows for a direct comparison with the

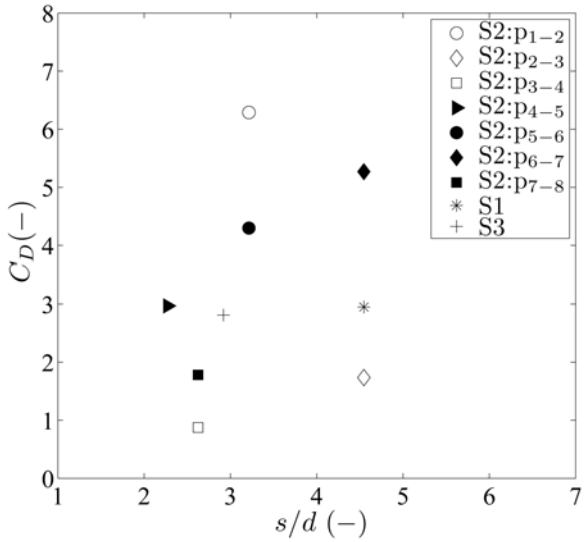

Figure 4.10: Drag coefficient as function of s/d.

results of Tanino & Nepf (2008). They presented curves, represented in Fig. 4.11, showing a parabolic decrease of C_D with Re_p for a given ϕ and an increase of the values of C_D with increasing ϕ. The values of C_D computed from both F_D and F_D^*, are plotted in Fig. 4.11 for tests S1 and S3. These tests have different m, or s, but almost equal values of C_D, 2.9 and 2.8, respectively. According to Tanino and Nepf's curves, a flow with $Re_p \approx 1000$ with $m = 400$ stem/m^2 (as test S1) would have $C_D \approx 1.0$ while for a similar Re_p, with the ϕ of test S3, the drag coefficient would be $C_D \approx 2.0$. The differences between the results are thus large, even for the case of C_D calculated from F_D^*. The fact that the stem Reynolds number is beyond the scope studied by Tanino & Nepf (2008) and the roughness of the stems may justify the differences.

The dependence of C_D on h/d is shown in Fig. 4.12. This parameter expresses the influence of the bed on the definition of the flow structure. Higher values of h/d are associated with a smaller relative influence of the bed. It is envisaged that for very high values of h/d the drag coefficient should not be influenced by this parameter anymore. Fig. 4.12 shows a tendency for the decrease of C_D with increasing h/d. This means that the contributions to the drag force are not uniformly distributed along the water column; the boundary-layer flow near the bottom, subjected to velocities lower than the depth-averaged mean velocity, contributes more than the average. Exceptions for this trend are the patches p_{1-2} and p_{7-8}. It is postulated that the value of C_D in these patches is highly influenced by other parameters: they are transition patches with opposite signs of the gradient of s. In particular the high value of C_D for patch p_{1-2} should be a consequence of its increase for positive gradients of s.

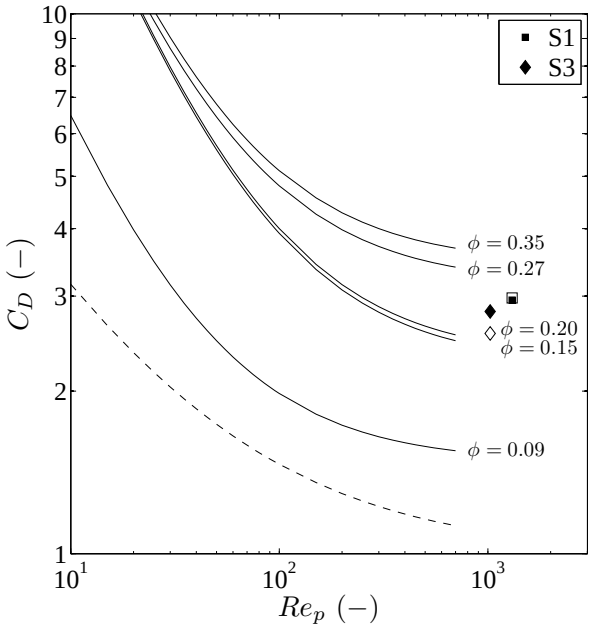

Figure 4.11: C_D against Re_p. The solid curves are the results presented by Tanino and Nepf (2008) for $\phi = 0.091, 0.15, 0.20, 0.27$ and 0.35, the dashed line represents the variation of C_D with Re_p for a smooth isolated cylinder. The markers correspond to the results of the present study from tests S1 and S3. The solid markers represent the C_D computed with F_D calculated by Eq. (4.11) while the open markers with F_D^* expressed by Eq. (4.13).

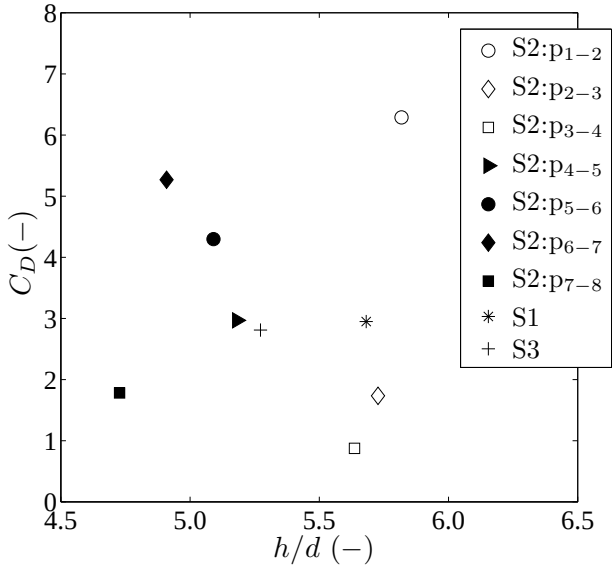

Figure 4.12: Drag coefficient as function of h/d.

4.5 Conclusions

The present study sought progresses on the understanding of the processes governing flow resistance in areas protected by rigid and emergent vegetation through experimental work.

A characterization of the flow was based on vertical profiles of velocity and stresses computed with the Double-Averaging Methodology. Mean longitudinal velocity profiles show a pronounced bulge close to the bottom decreasing like in a typical boundary-layer flow towards the bottom, but its main feature is the constant profile in the region where the flow is controlled by the vertical stems. A strong correlation between stem density and the magnitude of flow variables was observed. Both turbulent and form-induced stresses increase with the stem areal number-density. An important conclusion regarding the magnitude of the dispersive and turbulent stresses is that the former have the same order of magnitude of the latter. Therefore, one should not neglect form-induced stresses, as it is often done in literature arguing that those stresses are much smaller than Reynolds stresses. This is specially important in case of dense patches.

The calculation of the drag force acting on the stems followed a conceptual framework provided by the Double-Averaging Methodology. The drag force per unit plan area was calculated from the depth-averaged longitudinal component of the DANS equations, with no major simplifications.

It was verified that the term corresponding to the pressure gradient is dominant. However, balancing the drag force only with this term, as it is common in literature, may lead to important non-systematic errors. In fact, the relative importance of the dominant term is affected by gradients in the areal number-density of stems. Also, the importance of $\frac{\partial h}{\partial x}$ becomes reduced for high values of the drag force.

A dimensional analysis was carried out identifying the characteristic parameters that influence the drag force. The correlation of those parameters with C_D showed that the dependence of the drag coefficient is complex and may result from a non linear combination of more than one parameter.

The drag force per submerged stem length seems uncorrelated with the stem areal number-density, but it depends on the longitudinal variation of the latter. It was observed that the decrease of the number of stems per unit area is associated to larger flow resistance while the flow resistance is smaller when there is a longitudinal increase of m.

Another progress introduced herein is related to the effect of the patchiness on the drag forces. At patch scale, the longitudinal increase of stem areal number-density is associated to smaller magnitudes of the drag force per unit of submerged stem length. However, at wavelength scale, if the variability of m is cyclic, there might be no appreciable effect of patchiness on the average drag force since the opposite local influences of $\frac{\partial m}{\partial x} > 0$ and $\frac{\partial m}{\partial x} < 0$ cancel out.

The effect of flow acceleration is shown by the increase of the drag force from upstream patches to downstream patches with the same m.

Concerning the dependence of C_D on the stem Reynolds number, for the range of investigated Re_p and m, the drag coefficient does not vary with Re_p.

The observed decrease of C_D with increasing h/d reveals an influence of the bed on the definition of the flow structure. The contribution to the drag force are not uniform along the water column, being the contribution of the bottom boundary layer larger than the average.

This study reveals that experimental tests covering simultaneously a large range of Reynolds numbers and a large range of stem areal number-density, which are still missing, would be the key to understand the flow resistance associated to the vegetation stems.

Chapter 5

The terms of the turbulent kinetic energy budget within reaches of emergent vegetation

This chapter is aimed at quantifying and discussing the relative magnitude of key terms of the equation of conservation of turbulent kinetic energy (TKE) at the inter-stem space of a flow within arrays of vertical cylinders simulating plant stems of emergent and rigid vegetation. The spatial distribution of turbulent quantities and mean flow variables are influenced by two fundamental space scales, the diameter of the stems and the local stem areal number-density. These scales may vary considerably since the areal distribution of plant stems in natural systems is generally not homogeneous; they are often arranged in alternating sparse and dense patches. As a consequence of the complex spatial distribution of the flow field, the magnitude of the terms of the budget of TKE in the inter-stem space has seldom been quantified experimentally and is currently not well-known. Addressing this research need, the calculation of these terms is, in this work, based on new databases consisting of three-component LDA velocity series and two-dimensional PIV velocity maps, obtained in carefully controlled laboratory conditions. It is verified that the main source of TKE is vortex shedding from individual stems. The rates of production and dissipation are not in equilibrium. Regions with negative production, a previously unreported feature, are identified. Turbulent diffusion is particularly important along the von Kármán vortex street. Convective rate of change of TKE and pressure diffusion are most relevant in the vicinity of stems.

5.1 Introduction

Emergent vegetation, featuring a wide range of different species and with different ecological roles, is ubiquitous in coastal and riverine systems. In such systems, herein collected under the general designations of wetland vegetation or wetlands, it is known that there exists a profound interaction of physical, biological and ecological processes, being transport processes especially relevant (Defina & Peruzzo, 2012; Ghisalberti & Nepf, 2004; Tanino & Nepf, 2009). This justifies the recent growth in the volume of research on hydrodynamics of wetland vegetation (Aberle & Järvelä, 2013; Nepf, 2012b).

Progresses have been achieved in the detailed characterization of flow around isolated cylinders or arrays of few cylinders (Sumner, 2010, and references herein), a proxy to the stem scale. However, this scale (whose relevant measure is the stem diameter) is not sufficient to analyse wetlands. The local mean inter-stem distance (the space-averaged distance between neighbouring stems) necessarily plays an important role at intermediate scales since vortex streets emanating from neighbour stems overlap and change the flow characteristics, relatively to the single stem wake flow. Herein, this intermediate scale is termed the inter-stem scale. It should be highlighted that, even for uniform species, the inter-stem scale may vary considerably since the areal distribution of plant stems in natural systems is generally not homogeneous. In fact, they are often arranged in alternating sparse and dense patches (Schoelynck *et al.*, 2012).

The characterization of the flow at scales encompassing several patches, for instance a river reach or a laboratory channel, requires a third geometrical scale: the submerged plant volume divided by the total area occupied by plants (Aberle & Järvelä, 2013). A large amount of research has been carried out at this larger scales (Huthoff, 2012; Kim & Stoesser, 2011; Siniscalchi *et al.*, 2012; Sukhodolova & Sukhodolov, 2012; Tanino & Nepf, 2008), generally aimed at the quantification and parametrization of flow resistance attributable to vegetation.

Currently, one identifies major research needs at the intermediate scale, herein the inter-stem scale, due to the difficulties of acquiring sound empirical data. The key problem concerns the technical difficulties associated with the installation of measuring probes in the reduced void space within arrays of densely packed stems. It is not a coincidence that major recent advances have been attained through numerical data production (Coceal *et al.*, 2007; Defina & Bixio, 2005; Stoesser *et al.*, 2010). These combined with laboratory studies at this scale (Ferreira *et al.*, 2009b; Nepf, 1999; White & Nepf, 2007; White & Nepf, 2003) have mostly advanced the knowledge on fluxes of mass and momentum, for instance clarifying the nature of turbulent and dispersive stresses. The balance of mechanical energy, on the contrary, has received comparatively less attention. Given that in the inter-stem space, the flow is normally turbulent, attention should be directed to the terms of the budget of turbulent kinetic energy (TKE).

Bearing these issues in mind, the main objective of this work is to characterize and to quantify

the spatial distribution of the terms of the equation of conservation of TKE in the inter-stem space of a flow within an array of emergent stems featuring longitudinal patchiness. For steady flows, the equation of conservation of TKE is written, employing a mix of tensor and differential notation,

$$\underbrace{\frac{1}{2}\overline{u_j}\frac{\partial\overline{u_i'u_i'}}{\partial x_j}}_{\text{I}}+\underbrace{\overline{u_i'u_j'}\frac{\partial\overline{u_i}}{\partial x_j}}_{\text{II}}+\underbrace{\frac{1}{2}\frac{\partial\overline{u_i'u_i'u_j'}}{\partial x_j}}_{\text{III}}=-\underbrace{\frac{1}{\rho}\frac{\partial\overline{p'u_j'}}{\partial x_j}}_{\text{IV}}+\underbrace{2\nu\frac{\partial\overline{s_{ij}u_i'}}{\partial x_j}}_{\text{V}}-\underbrace{\bar{\varepsilon}}_{\text{VI}}\quad, \tag{5.1}$$

where i and j are indices running from 1 to 3, x_j stand for three cartesian spatial directions, $\frac{1}{2}\overline{u_i'u_i'}$ (summation of repeated indices intended) is the specific TKE, *i.e*, TKE per mass unit, $\overline{u_j}$ and u_j' are the j^{th} component of, respectively, the time-averaged velocity and the instantaneous time fluctuation, p' is the pressure fluctuation, s_{ij} is the symmetric part of turbulent strain tensor $\frac{\partial u_i'}{\partial x_j}$, $\bar{\varepsilon}$ is the time-averaged dissipation rate of TKE and ν stands for the kinematic viscosity of the fluid. A direct quantification of terms I (convective rate of change of TKE), II (rate of production), III (turbulent diffusion) and VI (dissipation rate of TKE) in equation (5.1) is carried out. Assuming the mean flow Reynolds number is sufficiently high, term V can be neglected and term IV back-calculated from equation (5.1).

To fulfil the aforementioned objectives, a number of practical problems concerning instrumentation and experimental apparatus must be overcome. As a compromise between physical verisimilitude and laboratory feasibility, slightly rough stems, randomly placed, are employed in this laboratory study as an *ersatz* for natural stems. The spatial distribution in the horizontal plane emulates the patchiness often seen in actual wetlands (Schoelynck *et al.*, 2012). A simpler regular spatial distribution would render the results easier to analyse but such simplicity could be misleading as the complexity of wake interactions found in nature is not amenable to be simulated by simple staggered arrays of stems. The key feature of spatial patchiness in the spatial distribution of the stems was simulated by imposing a periodic variation of the stem density in the streamwise direction. Raw data, consisting of instantaneous velocities were acquired with a three-component Laser Doppler Anemometer (LDA) and a two-component Particle Image Velocimetry system (PIV). In both databases the spatial resolution is of the order of magnitude of Taylor's microscale.

The paper is organized in six sections. Laboratory facilities and instrumentation are described in section 2. Section 3 presents the methodology for computing the variables discussed herein. The terms of TKE equation are characterized in section 4. A discussion of the results is expounded in section 5 and the document is ended by a summary of the main conclusions. Throughout this work, a cartesian referential is considered, where x, y and z correspond to the streamwise, spanwise and vertical directions, respectively, and u, v and w are the corresponding velocity components. Concerning the symbology related to turbulent quantities, overlines ($\overline{u_i}$) represent ensemble-

averaging, here simply taken as time-averaging and primes (u_i') represent time fluctuations.

5.2 Laboratory facilities and instrumentation

Two laboratory tests were carried out with identical experimental conditions. They were performed in a 32.0 m long and 0.60 m wide tilting flume at the Leichtweiß-Institute of the Technische Universität Braunschweig (LWI) and in a 12.5 m long and 0.408 m wide recirculating tilting flume at the Laboratory of Hydraulics and Environment of Instituto Superior Técnico (IST). Both flumes have glass side walls, enabling flow visualization and laser illumination. The flume at LWI was adapted to reproduce the same conditions tested at IST, therefore the effective flume were the experiments were carried out had 10.5 m of length and 0.40 cm of width.

The bottom of both flumes was covered with a horizontal layer of gravel and sand. Arrays of rigid, cylindrical and emergent stems with a diameter of 0.011 m were placed in a 3.5 m long reach simulating rigid and emergent vegetation conditions. Patches with 1600 stems/m^2 (dense, herein) were alternated with patches with 400 stems/m^2 (sparse, herein), as shown in Figure 5.1. Both dense and sparse patches are 15 cm long and are separated by 10 cm long transition reaches subdivided into two 5 cm reaches with densities of 1200 stems/m^2 and 800 stems/m^2. Throughout the vegetated reach, i.e. in the dense and sparse patches and in the transition reaches, the areal distribution of stems was random and in accordance with a uniform distribution. Stem density varied periodically with a wavelength of 0.5 m. At the end of the vegetated reach between two consecutive patches there was a gap without stems to enable the velocity measurements (dashed rectangles in Figure 5.1). To minimize its impact, the width of that measuring gap is equal to the mean inter-stem distance of the upstream patch.

The flow was subcritical both downstream and upstream the vegetated reach. A coarse gravel weir downstream of the array of stems controlled the flow depth. Relatively to conventional flap or vertical gates, such weirs do not generate a recirculation pattern of separated flow upstream. The water depth at the end of the vegetated reach was 4.2 cm (in both tests). In the LWI flume, a 3-component Laser Doppler Anemometry system (LDA) was used to acquire instantaneous velocity series at several points. In the IST flume, two-dimensional maps of instantaneous velocities were measured with a Particle Image Velocimetry system (PIV).

LDA technique allows acquisition of three components of instantaneous velocities at high temporal data-rates. If the frozen turbulence hypothesis is applicable, LDA measurements allow long velocity series in the streamwise direction with high resolution. On the other hand, a two-component PIV allows, in general, good spatial resolution and it is much cheaper than LDA, in terms of laboratory time, to obtain spatial variability. Therefore, these two techniques combined can render very good results within a feasible time. For an introduction to these two techniques

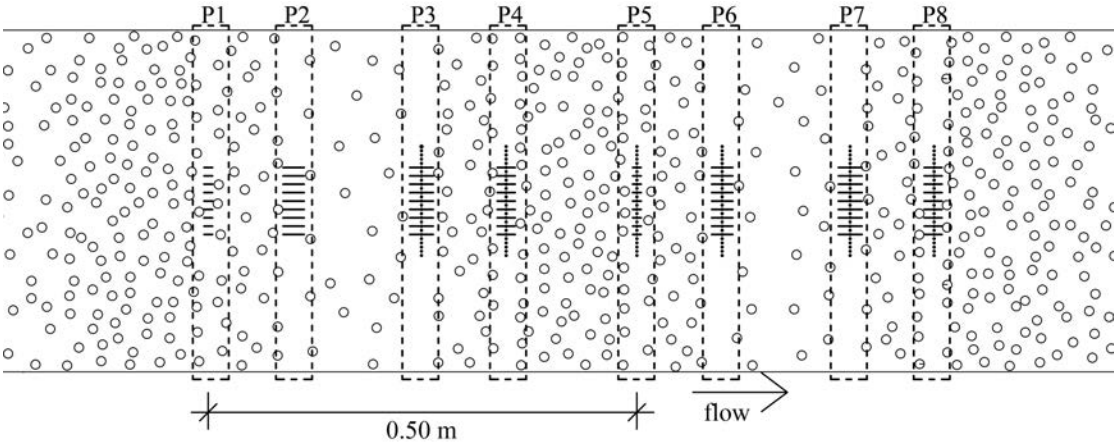

Figure 5.1: Plan view of the stem covered reach where the measurements were carried out. Dashed rectangles point out the regions where horizontal velocity maps (PIV) were acquired for each longitudinal position, P1 to P8. The solid lines aligned with flow direction indicate the location of the vertical plans measured with PIV. The points along lines perpendicular to the flow direction represent the location of LDA measurements (P3 to P8).

see (Tropea *et al.*, 2007, pp. 287-342), or other more specialized literature (Durst *et al.*, 1976; Raffel *et al.*, 1998).

The LDA system consisted in a 5W Argon-Ion laser, a F80 flow processor and two watertight probes with focal length of 198 mm in water and the probes were mounted on an automated transverse system. A two-component probe transmits two orthogonal pairs of beams (wavelengths 514.5 and 488 nm) while the one-component probe, positioned at 30° to the two-component probe, transmits the third pair of beams (wavelength 476.5 nm). Because the focal length is larger than the flow depth, an acrylic case with a glass bottom was used to submerge the probes in water and ensure that the laser beams travel in water from the probe casing to the measuring volume, except in the 2 mm glass plate (Aberle, 2006). The three-component LDA velocity series were measured at 27 points along spanwise direction, centred in the channel midpoint, with a spatial resolution of 5 mm. These series were collected for 6 longitudinal positions (P3 to P8 - Figure 5.1), approximately at the centre of each measuring gap, at 60% of the flow depth. The sampling time at each point was 3 minutes with sampling frequencies between 50 and 120 Hz. Titanium dioxide particles were used as solid targets.

The PIV system consisted of an 8-bit 1600×1200 px^2 CCD camera and a double-cavity Nd-YAG laser with pulse energy of 30 mJ at wavelength of 532 nm. The system was operated at 15 Hz with a time delay of 1500 μm between frames. As solid targets were used polyurethane particles with mean diameter of 60 μm in a range from 50 to 70 μm and density of 1.31 g/cm^3. For this kind of particles the cut-off frequency of the turbulent signal, calculated with the theory of Hjemfelt & Mockros (1996) is about 40 Hz. The Nyquist frequency of the PIV time series is 7.5 Hz, therefore one concludes that the particles were adequate to this experimental work.

Horizontal (u and v) and vertical (u and w) maps of instantaneous velocity were acquired for each longitudinal position (P1 to P8 - Figure 5.1). The vertical measurements were performed in 9 lateral planes, for each position, acquiring 10×573 image couples for each plane which correspond to ≈ 6.5 minutes of acquisition time. Regarding horizontal measurements, maps of $\approx 9.5 \times 12.5$ cm^2 (length $\times$ width) were acquired covering the entire flume width. The spatial resolution yields interrogations volumes of $1.3 \times 1.3 \times 2.0$ mm^3. Each dataset consisted in 5000 image couples performing 5.5 minutes of consecutive data. The horizontal planes were located at about 60% of the flow depth of each longitudinal position.

The discharge was regularly controlled by a digital flowmeter installed on the inlet pipe. Temperatures were measured regularly in order to compute the water viscosity according to Likhachev (2003). For the test at IST, the water temperature varied between 27.6°C and 32.2°C while at LWI water temperature was in the range $13.4 - 14.2$°C.

The bed topography and the free surface elevation were measured with a laser displacement sensor (Keyence LK-2000) at IST. For tests performed at LWI, the free surface elevation was measured with video analysis and the bed topography with a point gage.

Table 5.1 presents key variables that describe the flow at each longitudinal position. In this table, x stands for the longitudinal coordinate of the cross-section representative of each measuring gap, relative to the channel inlet, m is the stem areal number-density, $\langle \bar{h} \rangle$ is the mean (time- and space-averaged in the measuring gap) flow depth, $\mathrm{d}\langle \bar{h} \rangle / \mathrm{d}x$ represents the gradient of the mean flow depth, z is the elevation of the PIV horizontal planes or LDA measurements, $\langle \bar{u} \rangle$ stands for the time- and space-averaged longitudinal velocity and $Re_p = \langle \bar{u} \rangle d / \nu$ is the stem Reynolds number, where d is the stem diameter. The tests were performed with a discharge of 2.33 l/s. The flow is gradually varied, accelerating in the downstream direction as the flow depth decreases. The free surface exhibited an oscillating behaviour, with higher amplitudes within dense patches.

5.3 Methodology for calculations of the terms of TKE equation

5.3.1 Compatibility of PIV and LDA databases

To use LDA and PIV databases complementarily one must first argue for its compatibility. In the present case, the argument relies on the comparison of key terms calculated from both databases, specifically two components of the turbulent production term, $-\overline{u'v'}\frac{\partial \bar{u}}{\partial y}$ and $-\overline{v'v'}\frac{\partial \bar{v}}{\partial y}$. These components are especially relevant for the total production, as it will be discussed in the next section.

Table 5.1: Features of the experimental measurements and flow properties for each longitudinal position.

		P1	P2	P3	P4	P5	P6	P7	P8
x (m)		6.680	6.782	6.935	7.036	7.192	7.293	7.446	7.545
m (stems/m^2)		1600	800	400	1200	1600	800	400	1200
$\langle\bar{h}\rangle$ (m)	PIV	0.066	0.063	0.062	0.061	0.056	0.054	0.054	0.053
	LDA	-	0.063	0.063	0.061	0.056	0.056	0.054	0.052
$\mathrm{d}\langle\bar{h}\rangle/\mathrm{d}x$ $(-)$	PIV	-0.014	-0.029	-0.008	-0.010	-0.035	-0.015	-0.009	-0.007
	LDA	-	-	-0.001	-0.018	-0.033	0.000	-0.010	-0.028
$z/\langle\bar{h}\rangle$ $(-)$	PIV	0.57	0.61	0.61	0.62	0.67	0.69	0.55	0.59
	LDA	-	-	0.60	0.60	0.60	0.60	0.60	0.60
$\langle\bar{u}\rangle$ (m/s)	PIV	0.086	0.093	0.090	0.091	0.092	0.108	0.106	0.100
	LDA	-	-	0.109	0.115	0.123	0.112	0.127	0.130
$Re_p(-)$	PIV	1161	1282	1233	1302	1266	1514	1469	1338
	LDA	-	-	1025	1081	1156	1053	1194	1222

In the case of the LDA database, the spatial resolution is low and, hence, the spatial derivative was computed by means of backward differences, $\frac{\partial\bar{u}_i(y_n)}{\partial y} \approx \frac{\bar{u}_i(y_n)-\bar{u}_i(y_{n-1})}{y_n-y_{n-1}}$, where $n = 1,2,...,27$ is the index of the time-average velocity vector, $\bar{u}_i$ and the y-coordinate, being $y_n - y_{n-1} = 5$ mm. Concerning the PIV database, $\frac{\partial\overline{u}}{\partial y}$ and $\frac{\partial\overline{v}}{\partial y}$ are approximated by central differences for time-averaged velocity maps with the resolution of the PIV interrogation areas without superimposition. It should be noted that the spatial resolution of PIV database is about 5 times larger than that of the LDA database.

The spatial derivatives of the time-averaged velocities are multiplied by the second order moments $-\overline{u'v'}$ and $-\overline{v'v'}$, calculated from time series. In the case of the PIV database, the resolution and the spatial extent is sufficiently high to obtain two-dimensional maps of each production component. In the case of the LDA database, the result is a discrete set of 27 samples of the same production terms that span laterally over a line 13 cm long, centred at the flume axis (see Figure 5.1). In order to compare with the latter, two-dimensional maps obtained from PIV measurements were subsampled at the same line.

The comparison was performed for all measuring gaps. Representative examples are shown in Figures 5.2 and 5.3 for $-\overline{u'v'}\frac{\partial\overline{u}}{\partial y}$ and $-\overline{v'v'}\frac{\partial\overline{v}}{\partial y}$ respectively. Globally, there is a good agreement between the LDA and PIV databases. In the sparser regions (positions P7 in Figure 5.2 and P6 in Figure 5.3) the results are almost coincident. In denser regions (positions P5 in Figure 5.2 and P8 in Figure 5.3), both databases agree qualitatively and, in the case of the space between stems, where the production terms are small, also quantitatively. The quantitative disagreement registered at the wakes of stems are attributed mainly to the low spatial discretization of the

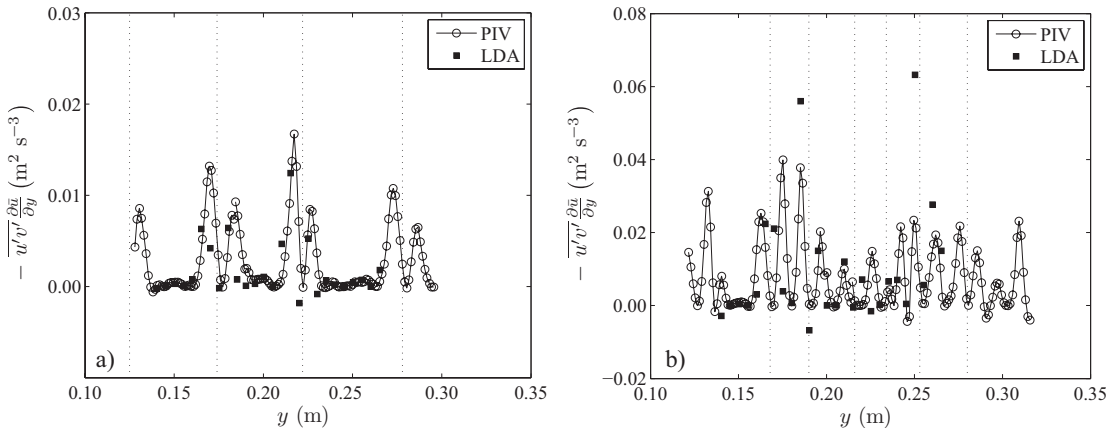

Figure 5.2: Comparison of $-\overline{u'v'}\partial\overline{u}/\partial y$ component of the turbulent production of TKE, computed from PIV and LDA databases for a) P7 and b) P5. Vertical dotted lines identify the y-coordinate of centres of stems close to the upstream limit of the measuring gap (see Appendix C for extra figures).

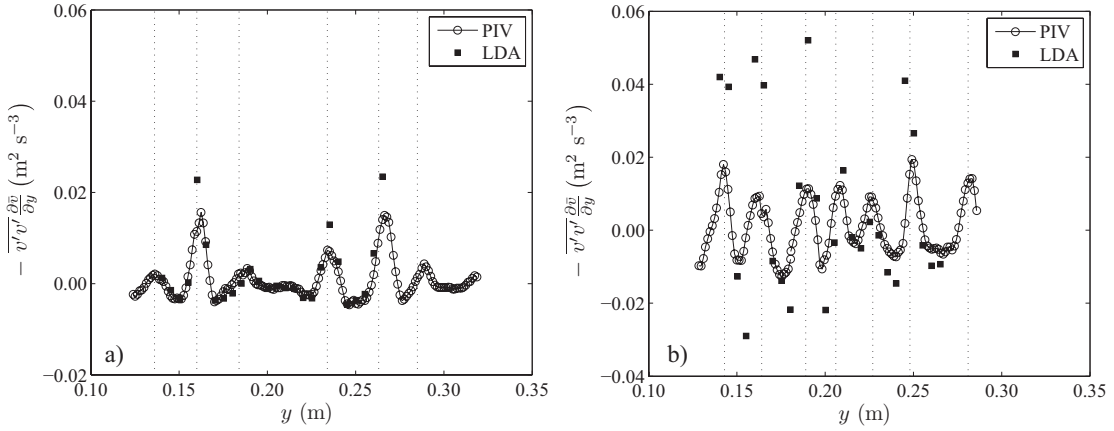

Figure 5.3: Comparison of $-\overline{v'v'}\partial\overline{v}/\partial y$ component of the turbulent production of TKE, computed from PIV and LDA databases for a) P6 and b) P8. Vertical dotted lines identify the y-coordinate of centres of stems close to the upstream limit of the measuring gap (see Appendix C for extra figures).

LDA database, which tends to exacerbate spatial finite-differences. Bias-to-zero characteristic of PIV databases (especially two-component measurements in three-dimensional flows where out-of-plane loss of pairs becomes relevant, Raffel *et al.*, 1998, p. 176) and bias to large velocities, characteristic of LDA databases may also play a role in such disagreement.

Owing to the general good agreement between LDA and PIV databases, these are used in complementarity throughout this work.

5.3.2 Methodology for the calculation of the rate of dissipation of TKE

The mean rate of dissipation of TKE, term VI of equation (5.1), is exclusively calculated from the LDA database. The reason for this option and the methodology for calculation are expounded in this section.

The point-wise time-averaged rate of dissipation of TKE can be easily calculated for homogeneous and isotropic turbulence (HIT), within the theory presented by Kolmogorov (1941a), requiring only a spectral description of the fluctuating motion or the computation of structure functions (see, e.g. Monin & Yaglom, 1975, pp. 351-355). If turbulence is not homogeneous, as is the case of the flow in the inter-stem space, the main results of HIT theory are still valid provided that local isotropy conditions are applicable (Monin & Yaglom, 1975, p. 396). Under these conditions, the mean dissipation rate of energy, $\bar{\varepsilon}$, term VI of equation (5.1), can be computed applying Kolmogorov's equation (Kolmogorov, 1941a)

$$S_{LL}^{(3)}(r) = -\frac{4}{5}\bar{\varepsilon}r + 6\nu\frac{\partial S_{LL}^{(2)}(r)}{\partial r} \tag{5.2}$$

where r stands for the longitudinal increment, $S_{LL}^{(3)}$ is the third-order structure function and $S_{LL}^{(2)}$ is the second-order structure function.

To show that, in this case, there exists a range of isotropic scales, and to identify them, the correlation-coefficient spectra is computed. It is defined as $C_{LN} = |E_{LN}| / (E_{LL}E_{NN})^{1/2}$, where E_{LN} is the shear-stress cospectrum and E_{LL} and E_{NN} are the longitudinal and transverse spectra, respectively (Saddoughi & Veeravalli, 1994). In isotropic conditions no shear stress is originated; hence, scales for which C_{LN} is zero or very small are identified as isotropic and loosely associated with the spectral inertial range, where TKE is not produced or dissipated (Tennekes & Lumley, 1972, chap. 8). Local isotropy in the sense of Monin & Yaglom (1975) can be assumed if there is a range of scales for which C_{LN} is zero or very small.

Figure 5.4 exemplifies correlation-coefficient spectra for two longitudinal positions, P5 and P7. For the point in P5, $C_{LN} < 0.10$ to scales of $f > 3$ Hz; in P7, $C_{LN} < 0.15$ to $f > 10$ Hz. Assuming that for frequencies sufficiently higher than 10 Hz the correlation coefficient is small enough, and

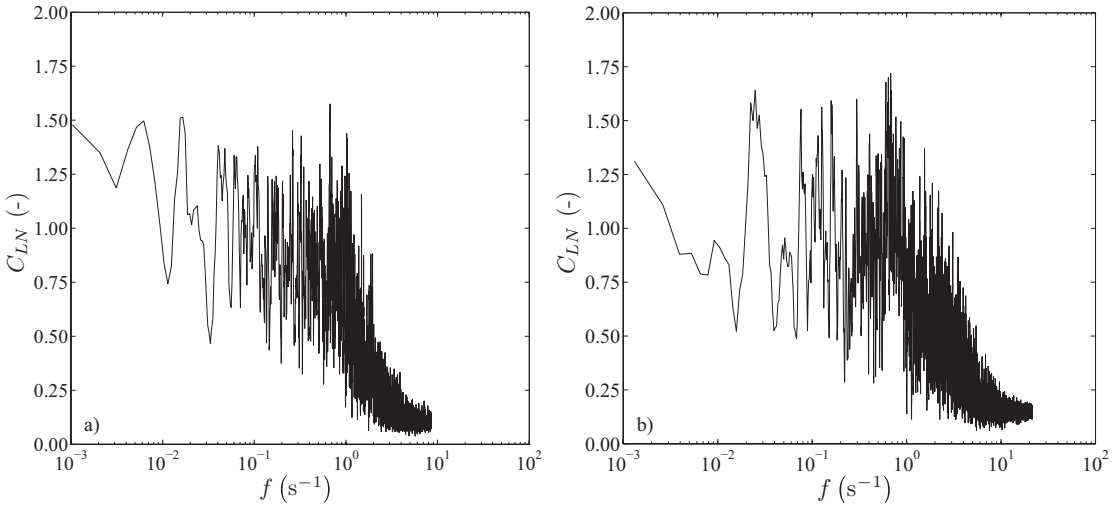

Figure 5.4: Correlation-coefficient spectra at a) $y = 0.215$ m for P5 and b) $y = 0.195$ m for P7. Computed from the LDA database.

applying the frozen turbulence hypothesis proposed by Taylor (1938), with a convection velocity equal to the mean velocity of each gap, one may thus assume that equation (5.2) is valid for scales sufficiently smaller than approximately 8 mm. For practical purposes it will be assumed that scales smaller than half the stem diameter are isotropic.

Having established the range of validity of equation (5.2), the dissipation rate of energy, $\bar{\varepsilon}$, is, herein, computed, from LDA database. The time series are first transformed into spatial series by applying Taylor's hypothesis with the time and space-averaged velocity in each measuring gap as convection velocity. Then, the first plateau of the compensated series $S_{LL}^{(3)}(r) - 6\nu\frac{\partial S_{LL}^{(2)}(r)}{\partial r}$ is identified; the value of the rate of dissipation of TKE is $\bar{\varepsilon} = -\frac{5S_{LL}^{(3)}}{4r} + 6\nu\frac{5}{4r}\frac{\partial S_{LL}^{(2)}(r)}{\partial r}$. It should be noted that the PIV database is not adequate to apply this methodology since the time series were acquired at 15 Hz, a frequency too low to produce power spectral density functions with conclusive information on the existence of an inertial range.

Figure 5.5 exemplifies $S_{LL}^{(3)}$ and $S_{LL}^{(2)}$ for a point in P3 and P8, sparse and dense patches, respectively. Build from the elements shown in Figure 5.5, the third-order structure function corrected by the viscous term (equation 5.2) is shown in Figure 5.6. At small r, there is a linear reach associated with the inertial range of scales, for which the slope is $-4/5\bar{\varepsilon}$. It is noteworthy that, in general, the slope, and therefore the dissipation rate of TKE, increases with the stem density. The example shown in Figure 5.6 is representative of this behaviour.

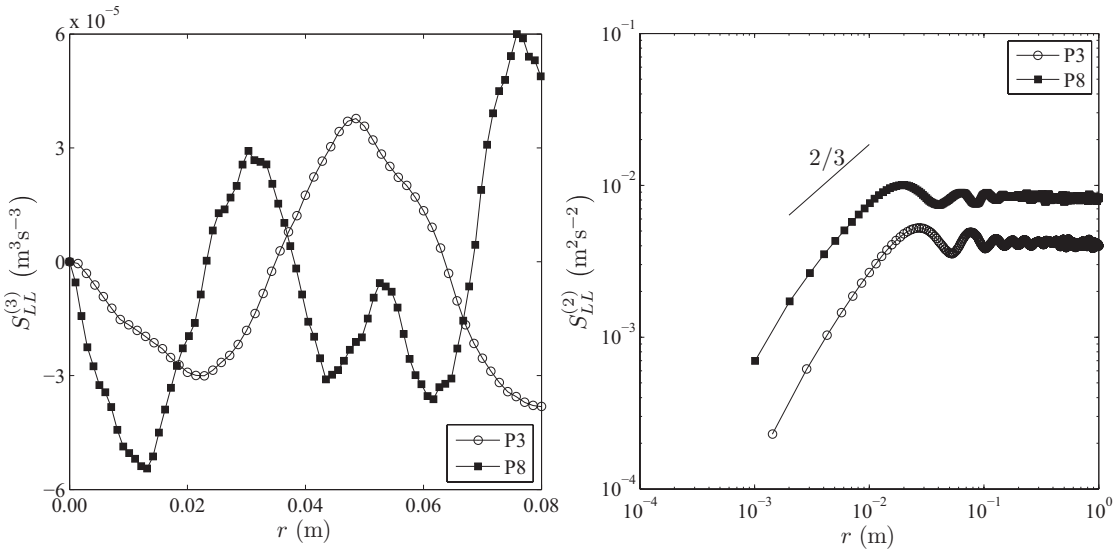

Figure 5.5: a) Third-order structure function $S_{LL}^{(3)}$ and b) second-order structure function $S_{LL}^{(2)}$, for two longitudinal positions, P3 (at $y = 0.180$ m) and P8 (at $y = 0.165$ m).

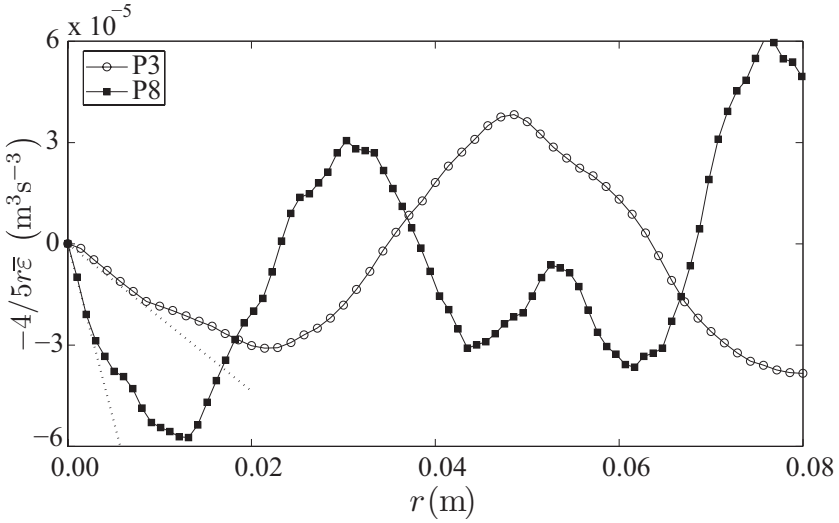

Figure 5.6: Examples of $S_{LL}^{(3)} - 6\nu\partial S_{LL}^{(2)}(r)/\partial r$ for a point in P3 ($y = 0.180$ m) and a point in P8 ($y = 0.165$ m). Dotted lines highlight the linear reach with slope $-4/5\bar{\varepsilon}$.

5.3.3 Methodology for the calculation of convective, productive and turbulent diffusion terms

The convective term, production and turbulent diffusion terms (I, II and III, respectively, in equation 5.1) are computed with PIV measurements taken in the horizontal plane. The order of magnitude of the several contributions that compose these terms is first assessed. At lines corresponding to the intersection of horizontal and vertical planes of PIV measurements (see Figure 5.1) it is possible to compute 7 contributions of terms I, II and III. Representative examples of the calculated contributions and also the sum of all contributions are seen in Figure 5.7. The relative magnitude of contributions involving z-derivatives and correlations involving the w component of time-averaged velocities and fluctuations are much smaller than corresponding terms with $y-$ and $x-$ derivatives and correlations of fluctuating components in the xy-plane.

The available data do not allow the computation of the two terms that require data from the yz-plane. However, the LDA database shows that those terms are much smaller than those pertaining the xy-plane. Indeed, as seen in Figure 5.8a), the Reynolds shear stress in the yz-plane is much smaller than that in xy-plane, $\overline{v'w'} \ll \overline{u'v'}$. Also, Figure 5.8b) shows that $\overline{w}$ is the velocity component with smaller variations in y-component, $\frac{\partial \overline{w}}{\partial y} \ll \frac{\partial \overline{u}}{\partial y}, \frac{\partial \overline{v}}{\partial y}$. Vertical gradients of $\overline{v}$ are not available however they are expected to be small, as $\frac{\partial \overline{u}}{\partial z}$ and $\frac{\partial \overline{w}}{\partial z}$ present also small magnitude (Ferreira *et al.*, 2009b; Ricardo *et al.*, 2012).

One thus concludes that the dominant contributions in terms I, II and III are those calculated from the horizontal PIV database.

Summarizing, in the present work convective, production and turbulent diffusion terms of the TKE budget equation become, respectively,

$$\begin{aligned}
\frac{1}{2}\overline{u_j}\frac{\partial \overline{u_i'u_i'}}{\partial x_j} &\approx \frac{1}{2}\left(\overline{u}\frac{\partial}{\partial x}\left(\overline{u'u'}+\overline{v'v'}\right)+\overline{v}\frac{\partial}{\partial y}\left(\overline{u'u'}+\overline{v'v'}\right)\right) \\
\overline{u_i'u_j'}\frac{\partial \overline{u_i}}{\partial x_j} &\approx \overline{u'u'}\frac{\partial \overline{u}}{\partial x}+\overline{u'v'}\frac{\partial \overline{u}}{\partial y}+\overline{u'v'}\frac{\partial \overline{v}}{\partial x}+\overline{v'v'}\frac{\partial \overline{v}}{\partial y} \\
\frac{1}{2}\frac{\partial \overline{u_i'u_i'u_j'}}{\partial x_j} &\approx \frac{1}{2}\left(\frac{\partial \overline{u'u'u'}}{\partial x}+\frac{\partial \overline{u'u'v'}}{\partial y}+\frac{\partial \overline{v'v'u'}}{\partial x}+\frac{\partial \overline{v'v'v'}}{\partial y}\right).
\end{aligned}$$

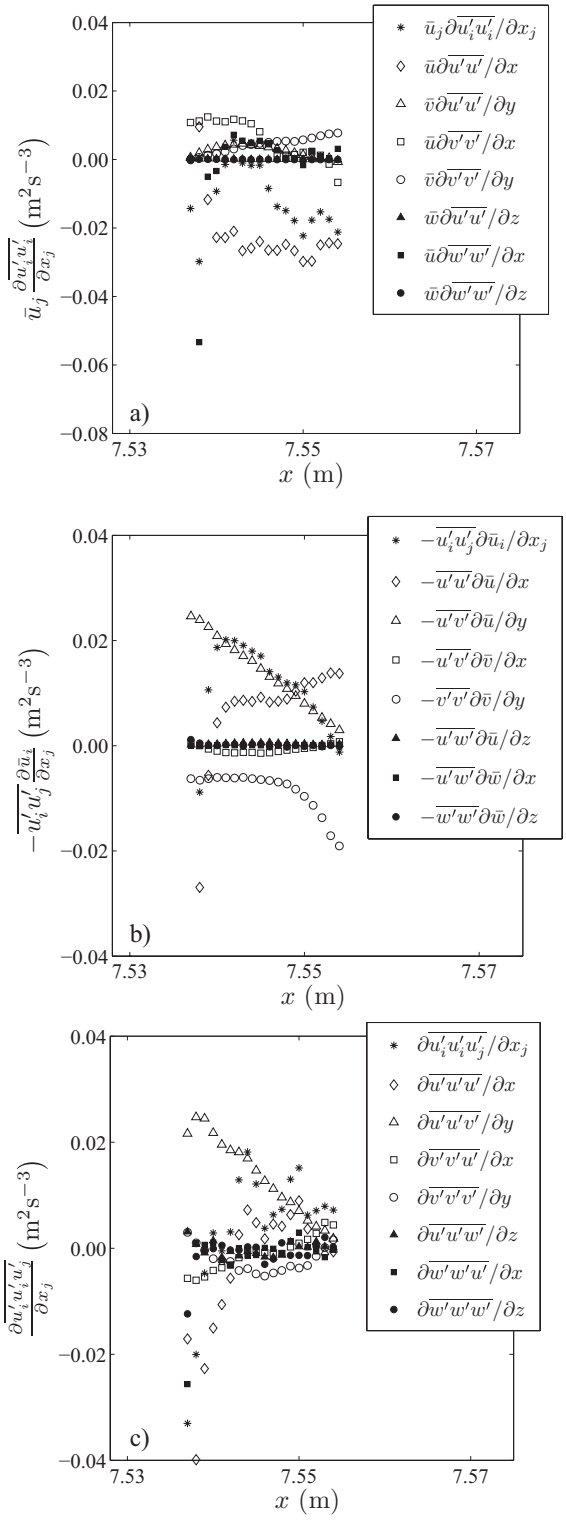

Figure 5.7: Contributions of the a) convective term, b) turbulent production and c) turbulent diffusion of TKE equation for P8 at $y = 24.4$ cm. Open markers represent terms from horizontal database while filled markers are computed with the vertical database. Asterisks represent the sum of the 7 contributions.

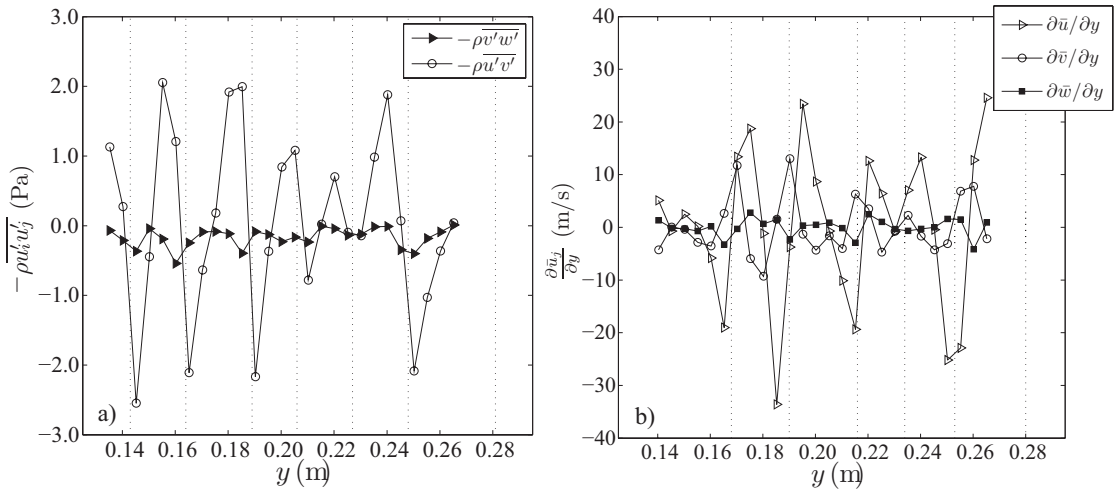

Figure 5.8: a) Reynolds shear stresses $-\rho\overline{u'v'}$ and $-\rho\overline{v'w'}$ for P8. b) Lateral gradients of time averaged velocity components for P5. Both results are computed from LDA database. Vertical dotted lines identify the y-coordinate of centres of stems close to the upstream limit of the measuring gap.

5.4 Quantification of the terms of the equation of conservation of TKE

5.4.1 Computed terms

This section is devoted at presenting and discussing the terms of equation of conservation of TKE (equation 5.1), namely the convective rate of change of TKE (term I), its rate of production (II), its turbulent diffusion (III) and its dissipation rate (VI). Assuming that the mean flow Reynolds number is sufficiently high, term V can be neglected and term IV back-calculated from equation (5.1). Dissipative, convective, productive and turbulent diffusion terms were calculated as explained in section 5.3 for the measuring gaps representative of the patches with different areal number-density of stems identified in section 5.2.

5.4.2 Rate of production of TKE

Spectral analysis of time series of velocity fluctuations obtained in the inter-stem space has revealed that vortex shedding from individual stems is the main source of TKE (Nepf, 1999). The current PIV databases clarify key features of the spatial organization of productive terms, including the preferred location of maxima and minima and the relative importance of the contributions that compose it.

In what concerns the latter issue, quantification of the contributions of turbulent production, exemplified in Figure 5.7b), leads to the conclusion that $-\overline{u'v'}\partial\bar{u}/\partial y$ is the dominant term. Terms

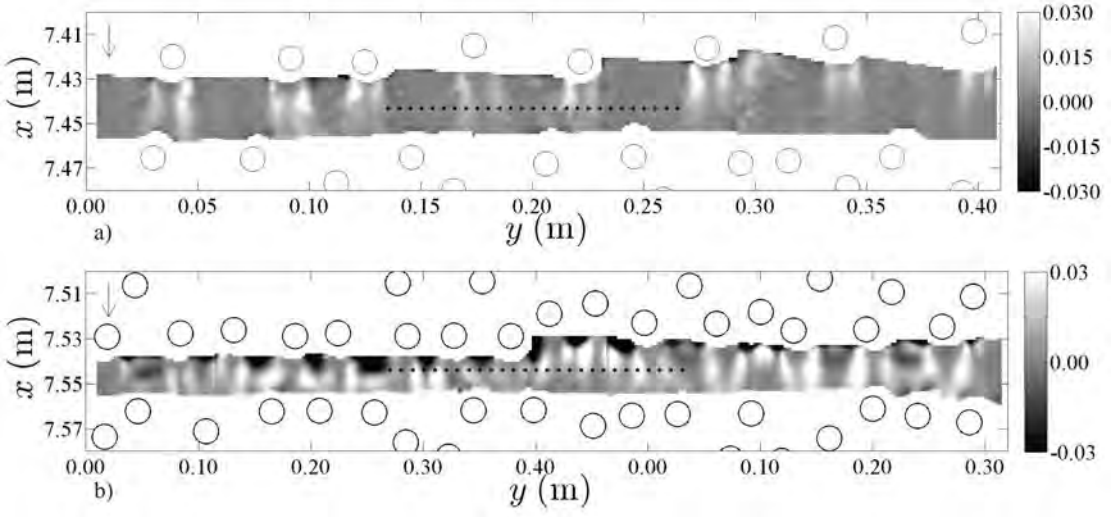

Figure 5.9: Two-dimensional maps of turbulent production, $-\overline{u_i'u_j'}\partial\bar{u}_i/\partial x_j$, $\left(\mathrm{m^2 s^{-3}}\right)$ for positions a) P7 and b) P8. Dots aligned horizontally identify the position of LDA measurements. The arrow indicates the flow direction (see Appendix C for extra figures).

$-\overline{u'u'}\partial\bar{u}/\partial x$ and $-\overline{v'v'}\partial\bar{v}/\partial y$ also have important magnitudes but they tend to cancel each other out. This is observed at all longitudinal positions, irrespectively of their areal number-density of stems. The only exceptions occur in the space between stems at the upstream part of measuring gaps representative of large stem densities. At those locations, $-\overline{u'u'}\partial\bar{u}/\partial x$ shows negative values, as seen in Figure 5.7b).

As for the spatial variation of turbulent production, two-dimensional PIV results in the xy-plane reveal that there is strong production in the wake of each cylinder, accompanying the path of shed vortices (the von Kármán street). Examples of this behaviour are shown in Figure 5.9 for P7, a patch with the smallest stem areal number-density, and for P8, a patch representative of large density of stems. In general, one registers a maximum in TKE rate of production about $1d$ downstream of the shedding stem, where a strong shear rate, mainly $\frac{\partial u}{\partial y}$, produces significant work against non-negligible Reynolds shear stresses.

Moving downstream in each measuring gap, for the cases with large inter-stem space (sparse patches), the magnitude of turbulent production decreases until becoming vanishingly small. This is the case of measuring gap P7, Figure 5.9a). Within the reaches with small inter-stem distance (dense patches), such as P5 and P8 (see Figure 5.9b), as a result of confinement, the maximum can be felt very close to the next array of stems.

Figure 5.9 also shows that not all turbulent rate of production contributes to increase TKE. Negative values of turbulent rate of production were found in-between stems placed sufficiently close to each other in y-direction. The negative production areas are located at the upstream end of the measuring gap in the spaces between adjacent stems, which are regions where the flow is

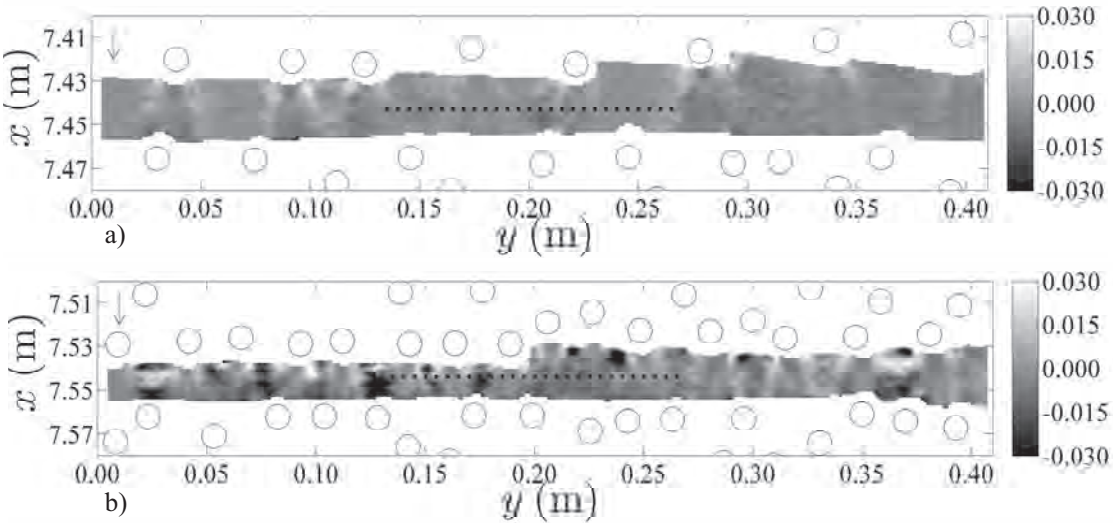

Figure 5.10: Two-dimensional maps of the convective term, $1/2\bar{u}_j\partial\overline{u_i'u_i'}/\partial x_j$, $\left(\mathrm{m^2s^{-3}}\right)$ for positions a) P7 and b) P8. Dots aligned horizontally identify the position of LDA measurements. The arrow indicates the flow direction (see Appendix C for extra figures).

strongly accelerated. Therefore, in this region, the work of the strong positive shear rate $\partial\overline{u}/\partial x$ against the positive $\overline{u'u'}$ is more important than the work generated by other components of shear rate, namely $\partial\overline{u}/\partial y$ against $\overline{u'v'}$ or $\partial\overline{v}/\partial y$ against $\overline{v'v'}$. This previously unreported feature is thus almost absent in the sparse patches, as seen in Figure 5.9a), but is quite evident in Figure 5.9b), representative of a densely populated patch.

5.4.3 Convective transport of TKE

The convective rate of change of TKE (term I in equation 5.1) represents the interaction of the mean and turbulent flow fields. It was observed that the dominate contributions of this term are $\bar{u}\partial\overline{u'u'}/\partial x$ and $\bar{u}\partial\overline{v'v'}/\partial x$, evidencing an important impact of the time-averaged longitudinal velocity on the convective rate of change of TKE. Figure 5.7a) is representative of the relative importance of each contribution composing the convective term of TKE observed for all the studied patches.

The spatial variation of its magnitude is shown in the maps of Figure 5.10. It is higher in the vicinity of the cylinders, both at the upstream and downstream end of the measuring gap, due to the unsteady flow separation around the cylinders. Approaching the stems, the streamlines diverge around the obstacle so that the flow particles, decreasing the longitudinal velocity, travel around the stem without detaching. Maps of the convective rate of change of TKE evidence negative values on the upstream vicinity of the cylinders (downstream of the measuring gap) which are linked to the expected reduction of the longitudinal flow field of the region. Within the inner part of the stems wake, the convective term of TKE presents generally small magnitude

with negative values, since the longitudinal velocity often shows negative values in that regions. While in the outer part of the wakes, the convective term presents its highest positive values. Hence, in the vicinity of the cylinders, both upstream and downstream, the convective term has magnitudes of the same order as the productive term, whereas in the regions between stems it is nearly zero.

5.4.4 Diffusion of TKE

Turbulent diffusion, term III of equation (5.1), accounts for changes in TKE due to its transport by velocity fluctuations. As for the convective and production terms, the dominate contributions of the turbulent diffusion of TKE are those computed from the horizontal database (open symbols in Figure 5.7 c). It was observed that $\frac{\partial \overline{u'u'v'}}{\partial y}$ is, in general, the dominant contribution. However, $\frac{\partial \overline{v'v'v'}}{\partial y}$ and $\frac{\partial \overline{u'u'u'}}{\partial x}$ also show important magnitudes.

Figure 5.11 shows maps of this term at measuring gaps P7 (representative of a sparse reach) and P8 (representative of a dense reach). Globally, turbulent diffusion is large and positive at streaks that loosely reproduce the path of vortices shed behind stems, i.e. the von Kármán street. This is particularly clear in Figure 5.11a) where the streaks are almost perfectly symmetrical relatively to the line in the x-direction that contains the centre of the cylinder that sheds the vortices. Large and negative values are found adjacent to the streaks with positive values, both at the wake behind cylinders but mostly at the outer interface of the von Kármán street, confining with the faster flow regions between stems. In measuring gaps representative of lower stem areal number-densities, the magnitude of diffusion decreases significantly in the downstream direction, before any interaction with the downstream neighbouring stems (see Figure 5.11a).

The main difference between sparse and densely populated patches is that at the latter the positive diffusion streaks and adjacent negative regions are spatially less coherent (see Figure 5.11b). In some cases at P5 and P8, they are superimposed, which is due to the flow patterns imposed by stems further upstream and the interaction of the vortex streets of neighbouring stems. The magnitude of both positive and negative diffusion is larger in the measuring gaps representative of denser regions (Figure 5.11).

5.4.5 Rate of dissipation and overall budget of TKE

As explained in section 5.3, the rate of dissipation of TKE (term VI of equation 5.1) was computed from the LDA database and, hence, results are available at only 27 locations approximately in the centre of each measuring gap. Hence, in this section, to allow for comparison, the maps of the remaining computed terms are sub-sampled on the line, extending spanwise, where $\bar{\varepsilon}$ was calculated (shown as dotted points in Figure 5.1 and in Figures 5.9 to 5.11).

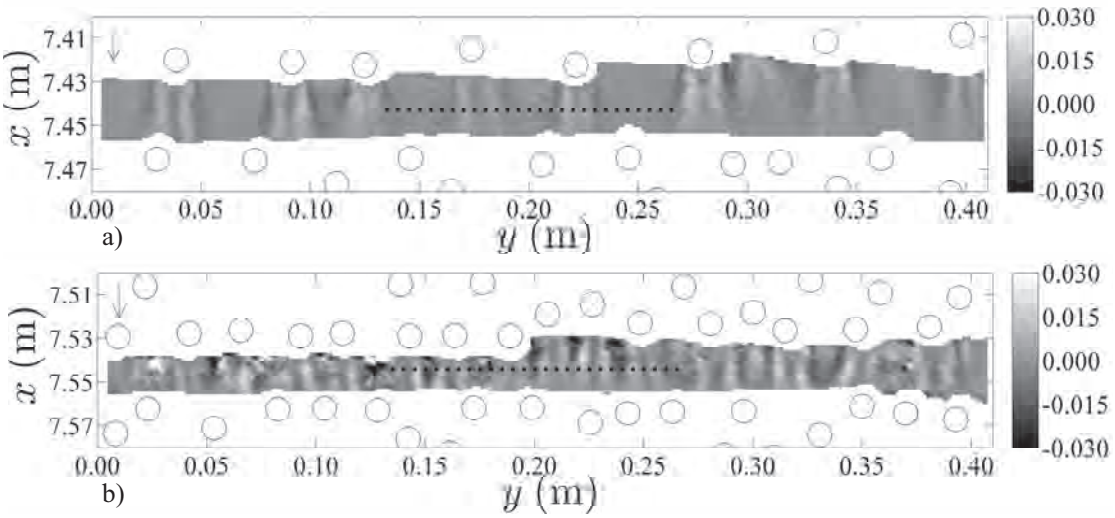

Figure 5.11: Two-dimensional maps of turbulent diffusion, $1/2\partial\overline{u_i'u_i'u_j'}/\partial x_j$, $\left(\mathrm{m^2 s^{-3}}\right)$ for positions a) P7 and b) P8. Dots aligned horizontally identify the position of LDA measurements. The arrow indicates the flow direction (see Appendix C for extra figures).

Figures 5.12 and 5.13 show the spanwise profiles of productive, convective, turbulent diffusion and dissipative terms of equation (5.1) for measuring gaps representative of small (P3 and P7) and large (P5 and P8) stem areal number-density, respectively.

The rate of dissipation of TKE (filled diamonds in Figures 5.12 and 5.13) is seen to increase in wake regions, being negligibly small in regions between stems. As a consequence, $\bar{\varepsilon}$ is higher in measuring gaps with larger stem areal number-density, since the proportion of wake regions is higher.

For variables computed from PIV databases, Figures 5.12 and 5.13 show that all the terms are larger in positions with higher density of stems. This seems to be a consequence of the fact that the terms of equation (5.1) have greater absolute value in the wake of stems.

A comparison of all directly computed terms shows that production and dissipation rates are not in equilibrium, except in the regions between stems where both are negligible. It is also noteworthy that the balance of all directly computed terms is not zero, i.e. the rate of dissipation is not balanced by the sum of the production rate, diffusion and convective rate of change (with respective signs). This is particularly evident in positions with high number of stems per unit of area, like P5 or P8 (see Figure 5.13).

This highlights the role of pressure diffusion (term IV in equation 5.1), i.e. the transport by turbulence of pressure fluctuations. Its magnitude is shown Figure 5.14, for two longitudinal positions, P7 (sparse) and P8 (dense). In the case of small density of stems, P7, term IV is small although not entirely negligible. On another hand, for P8, with a relatively high density of stems, the pressure diffusion has values with the same order of magnitude of the other terms in

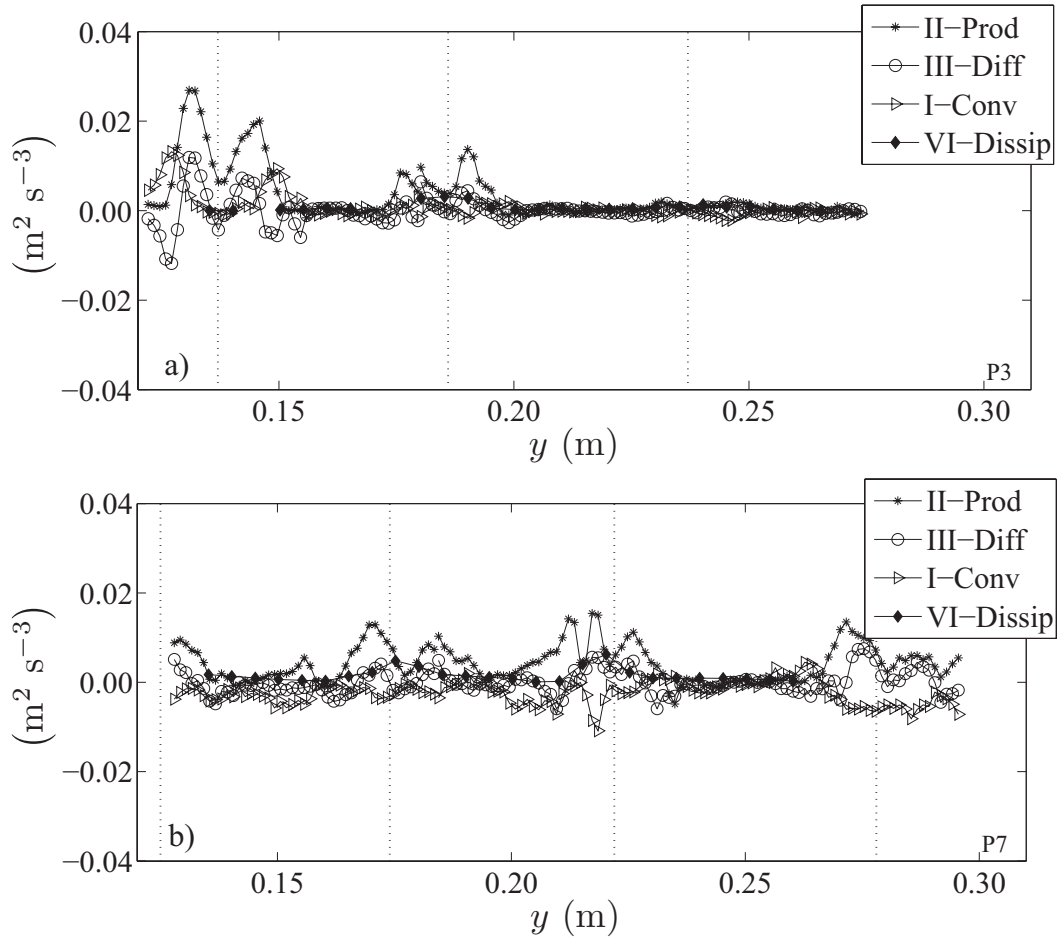

Figure 5.12: Lateral profiles of the terms of TKE budget equation for longitudinal positions a) P3 and b) P7. Vertical dotted lines identify the y-coordinate of centres of stems close to the upstream limit of the measuring reach (see Appendix C for extra figures).

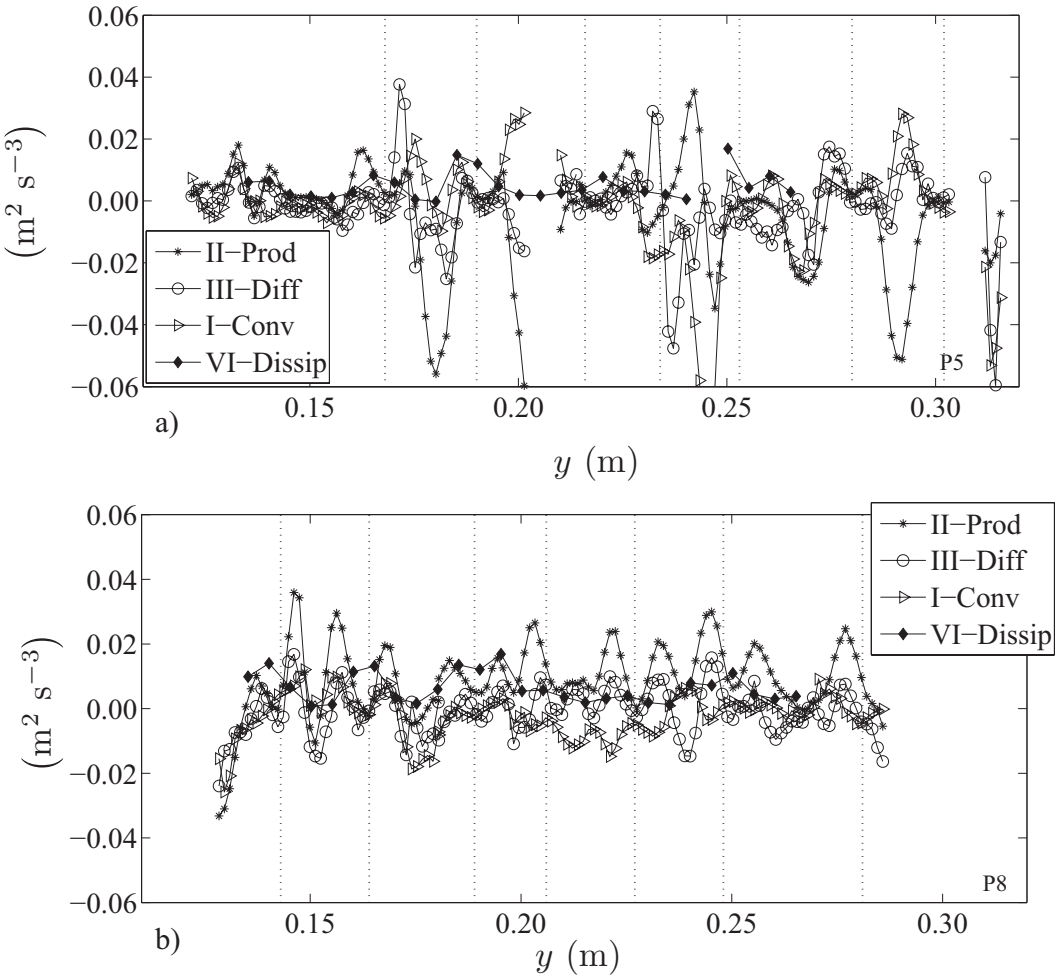

Figure 5.13: Lateral profiles of the terms of TKE budget equation for longitudinal positions a) P5 and b) P8. Vertical dotted lines identify the y-coordinate of centres of stems close to the upstream limit of the measuring reach (see Appendix C for extra figures).

the budget of TKE, presenting larger values in wake regions where dynamics of TKE is more complex. Figure 5.14 shows a correlation between the magnitude of pressure diffusion and the proximity of a cylinder to the downstream limit of the measuring gap. This is possibly associated with the transport by the turbulent field of the pressure that builds up in front downstream stems. This correlation is, obviously, more evident for P8 than for P7, due to narrower width of the measuring gap of the former. It is worth to note that the closest cylinders of the measuring gap for P8 ($y = 0.172$ m and $y = 0.200$ m, see, for example, Figure 5.11b) identify two of the highest negative peaks of the term IV.

The seeming relevance of the role of pressure diffusion must, however be taken with some care, given that it is computed as a derived term, subjected to the hypothesis that viscous diffusion is vanishingly small and incorporating the uncertainty associated with the calculation of $\bar{\varepsilon}$.

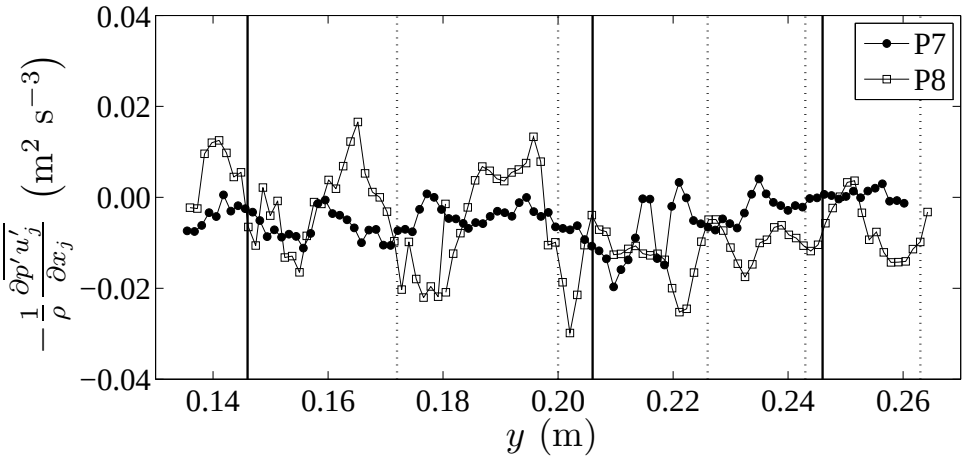

Figure 5.14: Term IV, $\frac{1}{\rho}\frac{\overline{\partial p' u_j'}}{\partial x_j}$, of TKE equation for two longitudinal positions, P7 and P8. Vertical solid and dotted lines identify the y-coordinate of centres of stems close to the downstream limit of the measuring gap of P7 and P8, respectively.

5.5 Discussion

An integrated view of the turbulent energy dynamics of flows through an array of emergent cylinders is attempted in this section.

For the purpose of better organizing the discussion, the wake region can be divided into a near field and a far field. The near field behind individual stems is defined here as the distance behind the stem until the maximum of production is attained, loosely where the von Kármán vortex streets start interacting. From the presented data, it is normally 1 to 1.5d. In the near field, the pattern of production seems essentially determined by the stem diameter and local Re_p and little influenced by the areal number-density of stems. This is a consequence of the fact that, for the range of areal solid-fractions investigated, production in the near field is a consequence of unsteady viscous separation behind individual stems. Hence, the production of TKE in the inter-stem space is mostly associated with vortex shedding from individual stems. Indeed, maps of the rate of turbulent production (Figure 5.9) show that the work of the strong shear rates against Reynolds shear stresses on the wake of the stems originate a clear pattern of positive values, which closely accompany the known path of vortices in the von Kármán street. This is in agreement with the spectral analysis of the flow in the inter-stem space, which reveals a clear peak associated with the shedding frequency in the power spectral density function (Nepf, 1999). In denser regions, the vortex shedding frequency is changed (normally increased) by the proximity of stems upstream (Sumner, 2010). This may be a second-order influence of the number areal-density of stems: an increase of the production rate accompanying an increase of the rate of vortex shedding. In the far field, further downstream in the wake of the stem, turbulent

transport and interaction with mean flow contribute to disrupt the coherence of shed vortices and the rate of production diminishes concomitantly. This effect is clear only in the measuring gaps representative of sparse patches where there is enough space for such interactions to occur. In the dense patches, often no far field is registered, i.e. downstream stems often succeed the locus of maximum production.

The presented data indicate that the rates of production and of dissipation are not in equilibrium in the inter-stem space. One particularly interesting feature is the existence of regions with negative rates of production. This implies interactions of turbulence with the mean flow and with the pressure field as well as a turbulent transport of TKE, the end product of which is the actual spatial distribution of TKE. The latter is presented in Figure 5.15 for sparse (P7) and dense (P8) patches. Herein, TKE is quantified considering only the longitudinal and transverse turbulent intensities, i.e. $1/2\left(\overline{u'u'}+\overline{v'v'}\right)$, since the vertical turbulent intensity is small and its space derivatives are the same as the sum $\overline{u'u'}+\overline{v'v'}$ (the numerical simulation presented by Stoesser *et al.*, 2010, confirms these observations). High values of TKE are found within the wake region, except in the near field very close to the stem. This behaviour is clearly identified in Figure 5.15a) for P7 (sparse patch). This is a consequence of the distribution of its components: the longitudinal is highest on the von Kármán vortex street close to the stem's edge, whereas the highest values of the transverse component are found in the overlapping of von Kármán streets about $1d$ downstream of the shedding stem. For denser patches, as P8 (5.15b), the overlap of the vortex streets occurs closer to the stem, leading to a larger region with high values of TKE.

The key difference between the spatial distributions of TKE and of the rate of production of TKE is that the former is much smoother than the latter, especially in the dense regions (see Figures 5.9b and 5.15b). In common, as observed above, they both peak at the limit of the near field of the wake behind the stems, roughly where von Kármán vortex streets begin (spatially) to interact. This suggests that the imbalance between rates of production and of dissipation is more pronounced in this region. The available results for the rate of dissipation confirm this hypothesis (Figures 5.12 and 5.13), although they are not totally conclusive due to the limited spatial range. Hence, turbulent diffusion and interactions with the mean flow and pressure field surely act to redistribute TKE from the loci of high production-dissipation to adjacent regions.

In the case of turbulent diffusion the redistributive role seems clear: its extreme values, both positive and negative are distributed in a pattern similar to a von Kármán vortex street (Figure 5.11). Since diffusion is obtained from the directional derivatives of the flux of TKE, this suggests that there are important turbulent fluxes of TKE at the loci of peak production that become less important with distance, especially in lateral-outward directions. To clarify this point, these turbulent fluxes were directly quantified. Figure 5.15 shows the flux of TKE represented in vector form $\overline{u'\left(u'u'+v'v'\right)}\vec{i}+\overline{v'\left(u'u'+v'v'\right)}\vec{j}$, where $\vec{i}$ and $\vec{j}$ are the orthogonal unit vectors that define the horizontal plane.

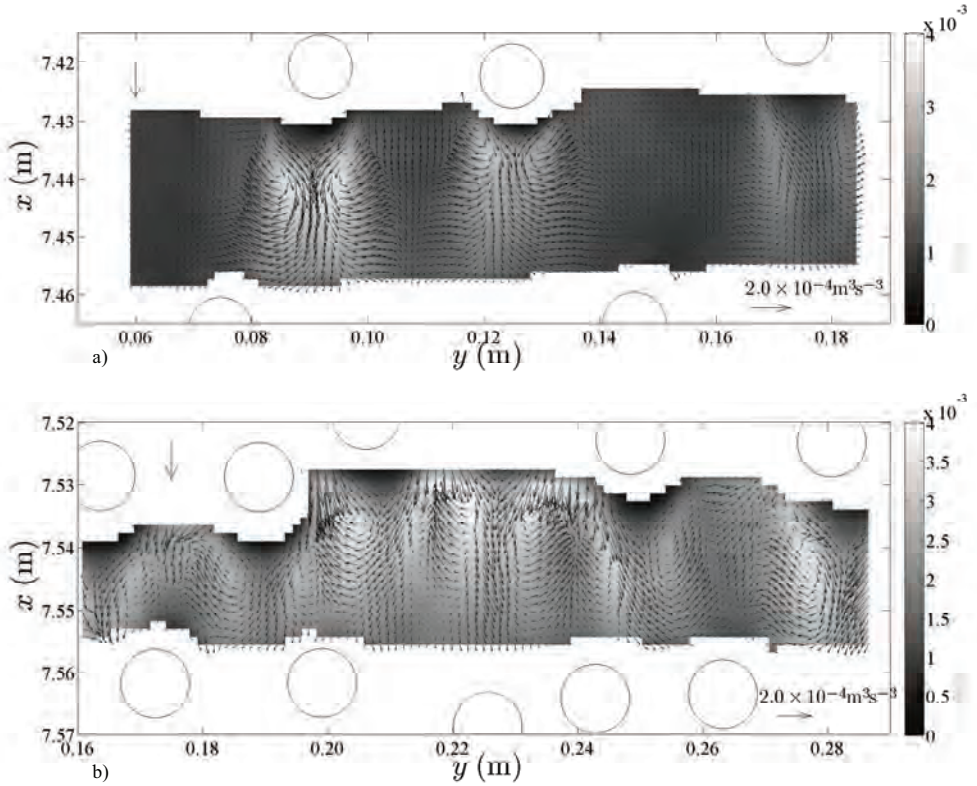

Figure 5.15: Two-dimensional maps of $1/2\left(\overline{u'u'}+\overline{v'v'}\right)$ overlapped by a vector plot of the flux of TKE, for positions a) P7 and b) P8. The colorbar units are m^2s^{-2}. The arrow on the left upper corner indicates the flow direction while the arrow on the bottom indicates the scale of the vector plot (see Appendix C for extra figures).

The key observable features are strong turbulent transport laterally outwards and slightly upstream of the locus of peak production and no laterally-inward turbulent transport. Instead of the latter, strong downstream transport is observed in the inner part of the stems's wake. The result is a quasi-circular pattern of turbulent transport of TKE, around the loci of peak production, more evident in the dense patches (Figure 5.15b). This pattern is compatible with a redistribution of TKE over the inter-stem space. Other features are worth emphasising. In the first place, there is very little turbulent flux directed to the separated flow attached at the lee of the stem, where turbulent intensities are already negligibly small. This is the only exception to the general behaviour that the flux of TKE is directed from regions with high values of TKE to regions with low values. Hence, the turbulent flux seems essentially determined by the gradient of TKE which would classify turbulent diffusion (in the present flow) as a fickian process (the diffusion coefficients were not estimated). Another relevant feature is the absence of turbulent flux directed to regions where the rate of production of TKE is negative. In other words, the conversion of turbulent kinetic energy into kinetic energy of the mean flow is not fed by a turbulent diffusive

mechanism. It was verified that negative production was the result of strong flow acceleration in the corridor between adjacent cylinders, leading to important shear rates, combined with high turbulence intensities in the same region; if turbulent diffusion is indeed a fickian process, there could not be a flux to regions with negative production since they have high turbulent intensities. It is noteworthy that the convective rate of change of TKE is also negative in the regions with negative rate of production, a consequence of the decrease of TKE in the downstream direction corridor between adjacent cylinders. To clarify the role of the mean flow in both the transport of TKE (gradient of TKE in the convective term) and the rate of production of TKE (time-averaged shear rate) further investigation is needed with measurements in the space between laterally placed cylinders.

The interaction of turbulent and mean flow fields, expressed in the rate of convective change of TKE possesses one other interesting feature: high absolute values in front and in the close vicinity of stems (Figure 5.10). Considering that both production and diffusion present small magnitudes in the downstream limit of the measuring gap, it is expected that the observed high values of the convective term are balanced by pressure diffusion and rate of dissipation. Further pursuing this issue, it has been observed that the balance of all the terms of equation (5.1) computed directly from the experiments (terms I, II, III and VI) do not vanish, highlighting the importance of the pressure diffusion term. It is observed that pressure diffusion is larger in the vortex streets and smaller in the corridors between stems (Figure 5.14). More importantly, there seems to be an increase of its absolute value in front of stems, in their close vicinity. This suggests that the turbulent field transports the fluctuating components of the pressure that builds up in front of downstream stems. Balance of TKE would then require a negative gradient of TKE in the longitudinal direction, explaining the strong negative rates of convective change, and a suppression of turbulent intensities in front of cylinders. The latter feature may actually be seen in Figure 5.15b.

It should be noticed that the impact of the Reynolds number is not discussed in the present work. The key role of this parameter on the study of turbulent flows is acknowledge. However, since the range of Re_p is relatively small (see Table 5.1), the present database would not guarantee sufficient contrast to render the discussion fruitful.

5.6 Conclusions

The present study is based on the analysis of three-component LDA velocity series and two-component PIV velocity maps and aimed at the characterization of the key terms of TKE equation. The main goal was to discuss the spatial distribution of the terms within the budget of turbulent kinetic energy, namely turbulent production and diffusion, the convective term and the rate of dissipation, for different stem areal number-density. The compatibility of the two

databases proved to be sufficiently good by leading to similar values of important components of the turbulent production term, $-\overline{u'v'}\partial\bar{u}/\partial y$ and $-\overline{v'v'}\partial\bar{v}/\partial y$.

An important feature of flows through arrays of emergent and rigid cylinders is its conspicuous spatial variability evidencing the importance of vortex shedding and unsteady separation of the flow on the cylinders. Another important feature of this study consisted in the random distribution of the array of stems, due to the impact of the local arrangement of the stems on the results.

The production of TKE in the inter-stem space is mostly associated with vortex shedding from individual stems. The magnitude of the rate of production is higher in the wake region, reaching a maximum about $1d$ downstream of the shedding stem and then decreases towards zero when the inter-stem distance is large enough. Also TKE has a peak of magnitude at the limit of the near field of the stem's wake. However, the spatial distribution of TKE is smoother than the distribution of the rate of production of TKE. Negative production of TKE was identified in the beginning of the measuring gap between close stems, associated with strong accelerations that the flow field is here subjected to.

It was observed that the rates of production and of dissipation are not in equilibrium in the inter-stem space, revealing important interactions of turbulence with mean flow and pressure field and turbulent transport of TKE.

The turbulent diffusion presents important values, both positive and negative, within the von Kármán vortex streets. The turbulent fluxes of TKE revealed strong turbulent transport laterally outwards, slightly upstream of the locus of peak production and in the inner part of the stems's wake, resulting in a quasi-circular pattern of turbulent transport of TKE, around the loci of peak production. The flux of TKE is, generally, directed from regions with high values of TKE to regions with low values indicating turbulent diffusion as a fickian process.

Expressing the interactions between mean and turbulent flow fields, the convective term reveals itself in the vicinity of the array of stems. This term is expected to balance the pressure diffusion term, especially in the downstream limit of the measuring gap where it is associated with to the pressure build-up in front of the following array of stems.

The rate of dissipation was found to increase with the density of stems and to present smaller space variation when comparing to the other terms discussed. However, its magnitude tends to be higher in the wake of the stems than in the regions between adjacent stems.

The integrated analysis of the turbulent kinetic energy dynamics carried out in this work provide further understanding of the complex flows within boundaries covered by emergent and rigid vegetation.

Chapter 6

Adaptation of homogeneous and isotropic turbulence results

6.1 Introduction

This chapter presents the mathematical formalism of a result developed in the scope of this thesis, which was included as Annex of the paper presented in the following chapter. Being on of the innovative points of the present work, it was considered important to include those mathematical developments in a separate chapter before the application of that result.

6.2 Spatial version of Kolmogorov's equation

The two point longitudinal and transverse second-order structure functions, S_{2L} and S_{2N} respectively, are defined herein by

$$S_{2L}(\alpha, r) = \overline{(\tilde{v}(\alpha + r) - \tilde{v}(\alpha))^2} \tag{6.1a}$$

$$S_{2N}(\alpha, r) = \overline{(\tilde{u}(\alpha + r) - \tilde{u}(\alpha))^2} \tag{6.1b}$$

where r is the increment in y-direction, α is any point in the space and $\tilde{v}$ and $\tilde{u}$ are the velocity fluctuations components on the same and the perpendicular direction of the increment, respectively. The over-line stands, here, for the appropriate ensemble-average, since the processes are stationary, this may be a time-average.

The longitudinal third-order structure function is defined as

$$S_3(\alpha, r) = \overline{(\tilde{v}(\alpha + r) - \tilde{v}(\alpha))^3}\ . \tag{6.2}$$

Since turbulence is not homogeneous, the values of the structure functions depend on the point α and not only on the lag r. If the structure functions are space-averaged, the results $\langle S_2 \rangle$ and $\langle S_3 \rangle$ do not depend on any particular α. Instead, they become dependent only on the space lag r:

$$\langle S_{2L} \rangle (r) = \left\langle \overline{(\tilde{v}(\alpha+r) - \tilde{v}(\alpha))^2} \right\rangle \tag{6.3a}$$

$$\langle S_{2N} \rangle (r) = \left\langle \overline{(\tilde{u}(\alpha+r) - \tilde{u}(\alpha))^2} \right\rangle \tag{6.3b}$$

$$\langle S_3 \rangle (r) = \left\langle \overline{(\tilde{v}(\alpha+r) - \tilde{v}(\alpha))^3} \right\rangle . \tag{6.3c}$$

Exploiting the space-averaging of two-point correlations and statistics, we followed the procedure applied by Monin & Yaglom (1975, pp.120-122) to derive an equation akin to Kolmogorov's equation (equation 2.34), from which an estimate of the rate of dissipation of TKE can be obtained. Evidently, turbulence remains non-homogeneous but the formalism that led to the relation between second and third-order structure functions in HIT is now applicable rendering similar results. To show this result, the procedure applied by Monin & Yaglom (1975, pp.120-122) to derive the Kármán-Howart's equation is followed. We start with the incompressible Navier-Stokes equations

$$\frac{\partial u_j}{\partial t} + \frac{\partial u_j u_k}{\partial x_k} = -\frac{1}{\rho}\frac{\partial p}{\partial x_j} + \nu \frac{\partial^2 u_j}{\partial x_k \partial x_k} + g_j \tag{6.4}$$

where u_j is the j^{th} velocity component, p is the pressure field and g_j is the j^{th} gravitational acceleration component. A spatial decomposition is considered

$$\theta(x,t) = \langle \theta \rangle (t) + \tilde{\theta}(x,t)$$

where θ may stand for u_j or p, $\langle \theta \rangle$ is the space average of the variable θ and $\tilde{\theta}$ is the fluctuation to the spatial average. Introducing the spatial decomposition in each term of (6.4) we get:

$$\frac{\partial u_j}{\partial t} = \frac{\partial \langle u \rangle_j}{\partial t} + \frac{\partial \tilde{u}_j}{\partial t} \tag{6.5}$$

$$\frac{\partial u_j u_k}{\partial x_k} = \frac{\partial \langle u \rangle_j u_k}{\partial x_k} + \frac{\partial \tilde{u}_j u_k}{\partial x_k} = \frac{\partial \langle u \rangle_j u_k}{\partial x_k} + \frac{\partial \tilde{u}_j \tilde{u}_k}{\partial x_k} + \frac{\partial \tilde{u}_j \langle u \rangle_k}{\partial x_k} \tag{6.6}$$

$$\frac{\partial p}{\partial x_j} = \frac{\partial \langle p \rangle}{\partial x_j} + \frac{\partial \tilde{p}}{\partial x_j} \tag{6.7}$$

$$\nu \frac{\partial^2 u_j}{\partial x_k \partial x_k} = \nu \frac{\partial^2 \langle u \rangle_j}{\partial x_k \partial x_k} + \nu \frac{\partial^2 \tilde{u}_j}{\partial x_k \partial x_k} \tag{6.8}$$

At a generic instant and at a given point $x_k = x_k^A$, variables will be written $\theta(t, x_k^A) \equiv \theta^A$, time being dropped for simplicity. At point $x_k = x_k^A$, (6.4) can be written

$$\underbrace{\frac{\partial \langle u \rangle_j^A}{\partial t} + \frac{\partial \langle u \rangle_j u_k^A}{\partial x_k^A} - \nu \frac{\partial^2 \langle u \rangle_j}{\partial x_k^A \partial x_k^A} - g_j}_{(1)} + \\ + \underbrace{\frac{1}{\rho} \frac{\partial \langle p \rangle}{\partial x_j^A}}_{(2)} + \underbrace{\frac{\partial \tilde{u}_j^A}{\partial t} + \frac{\partial \tilde{u}_j^A \tilde{u}_k^A}{\partial x_k^A} + \frac{\partial \tilde{u}_j^A \langle u \rangle_k}{\partial x_k^A} + \frac{1}{\rho} \frac{\partial \tilde{p}^A}{\partial x_j^A} - \nu \frac{\partial^2 \tilde{u}_j^A}{\partial x_k^A \partial x_k^A}}_{(3)} = 0 \tag{6.9}$$

Term (1) is equal to the gradient of pressure that balances the result of the application of the Navier-Stokes operator to the (space-averaged) velocity $\langle u \rangle$. This term will be expressed as $-\frac{1}{\rho} \frac{\partial P}{\partial x_j^A}$ and it can be associated to term (2). Together with term (3), (6.9) becomes

$$\frac{1}{\rho} \frac{\partial (\langle p \rangle - P)}{\partial x_j^A} + \frac{\partial \tilde{u}_j^A}{\partial t} + \frac{\partial \tilde{u}_j^A \tilde{u}_k^A}{\partial x_k^A} + \frac{\partial \tilde{u}_j^A \langle u \rangle_k}{\partial x_k^A} + \quad \frac{1}{\rho} \frac{\partial \tilde{p}^A}{\partial x_j^A} - \nu \frac{\partial^2 \tilde{u}_j^A}{\partial x_k^A \partial x_k^A} = 0 \tag{6.10}$$

Then we multiply each term of (6.10) by velocity $\tilde{u}_i^B(t, x_k^B)$, taken at point x_k^B such that $x_k^B = x_k^A + r_k$:

$$\frac{1}{\rho} \frac{\partial (\langle p \rangle - P)}{\partial x_j^A} \tilde{u}_i^B + \frac{\partial \tilde{u}_j^A}{\partial t} \tilde{u}_i^B + \frac{\partial \tilde{u}_j^A \tilde{u}_k^A}{\partial x_k^A} \tilde{u}_i^B + \frac{\partial \tilde{u}_j^A \langle u \rangle_k}{\partial x_k^A} \tilde{u}_i^B + \frac{1}{\rho} \frac{\partial \tilde{p}^A}{\partial x_j^A} \tilde{u}_i^B - \nu \frac{\partial^2 \tilde{u}_j^A}{\partial x_k^A \partial x_k^A} \tilde{u}_i^B = 0 \tag{6.11}$$

Considering that $\tilde{u}_i^B(t, x_k^B)$ does not depend on x_k^A, (6.11) can be written as

$$\frac{1}{\rho} \frac{\partial (\langle p \rangle - P) \tilde{u}_i^B}{\partial x_j^A} + \frac{\partial \tilde{u}_j^A}{\partial t} \tilde{u}_i^B + \frac{\partial \tilde{u}_j^A \tilde{u}_k^A \tilde{u}_i^B}{\partial x_k^A} + \frac{\partial \tilde{u}_j^A \langle u \rangle_k \tilde{u}_i^B}{\partial x_k^A} + \frac{1}{\rho} \frac{\partial \tilde{p}^A \tilde{u}_i^B}{\partial x_j^A} - \nu \frac{\partial^2 \tilde{u}_j^A \tilde{u}_i^B}{\partial x_k^A \partial x_k^A} = 0 \tag{6.12}$$

An equation similar to (6.10) can be written at x_k^B for $\tilde{u}_i^B(t, x_k^B)$. Let this equation be multiplied

by $\tilde{u}_j^A(t,x_k^A)$ and added to (6.12). One obtains

$$\frac{\partial \tilde{u}_j^A \tilde{u}_i^B}{\partial t} + \frac{\partial \tilde{u}_j^A \tilde{u}_k^A \tilde{u}_i^B}{\partial x_k^A} + \frac{\partial \tilde{u}_j^A \langle u \rangle_k \tilde{u}_i^B}{\partial x_k^A} + \frac{1}{\rho}\frac{\partial \tilde{p}^A \tilde{u}_i^B}{\partial x_j^A} - \nu \frac{\partial^2 \tilde{u}_j^A \tilde{u}_i^B}{\partial x_k^A \partial x_k^A} +$$
$$\frac{\partial \tilde{u}_i^B \tilde{u}_k^B \tilde{u}_j^A}{\partial x_k^B} + \frac{\partial \tilde{u}_i^B \langle u \rangle_k \tilde{u}_j^A}{\partial x_k^B} + \frac{1}{\rho}\frac{\partial \tilde{p}^B \tilde{u}_j^A}{\partial x_i^B} - \nu \frac{\partial^2 \tilde{u}_i^B \tilde{u}_j^A}{\partial x_k^B \partial x_k^B} +$$
$$+ \frac{1}{\rho}\frac{\partial \left(\langle p \rangle - P\right) \tilde{u}_i^B}{\partial x_j^A} + \frac{1}{\rho}\frac{\partial \left(\langle p \rangle - P\right) \tilde{u}_j^A}{\partial x_i^B} = 0 \,. \quad (6.13)$$

Equation (6.13) is now a multi-dimensional operator with six independent space variables, x_k^A and $r_k = x_k^B - x_k^A$.

We now average (6.13) over a sufficiently large area. For the problem at hand, this average requires an area larger than twice the mean inter-stem space. In practice, the average can be carried out over a line that encompasses both x_k^A and x_k^B. For the instrumentation at hand, measurements over such lines are discrete which means that, for a given r_k, the average is performed as an arithmetic mean of the values of variables taken at all points r_k apart. Evidently the spatial velocity series thus defined incorporates wavelengths that express the spatial variability of the time-averaged flow, whose classification as turbulence is objectionable. However, one notes that these wavelengths are of the order of magnitude of the inter-stem space and thus much larger than the turbulent scales that will be the focus of the analysis. Equation (6.13) becomes

$$\frac{\partial \left\langle \tilde{u}_j^A \tilde{u}_i^B \right\rangle}{\partial t} + \frac{\partial \left\langle \tilde{u}_j^A \tilde{u}_k^A \tilde{u}_i^B \right\rangle}{\partial x_k^A} + \frac{\partial \left\langle \tilde{u}_i^B \tilde{u}_k^B \tilde{u}_j^A \right\rangle}{\partial x_k^B} + \frac{\partial \left\langle \tilde{u}_i^B \tilde{u}_j^A \right\rangle \langle u \rangle_k}{\partial x_k^B} + \frac{\partial \left\langle \tilde{u}_j^A \tilde{u}_i^B \right\rangle \langle u \rangle_k}{\partial x_k^A} +$$
$$+ \frac{1}{\rho}\frac{\partial \left\langle \tilde{p}^A \tilde{u}_i^B \right\rangle}{\partial x_j^A} + \frac{1}{\rho}\frac{\partial \left\langle \tilde{p}^B \tilde{u}_j^A \right\rangle}{\partial x_i^B} - \nu \frac{\partial^2 \left\langle \tilde{u}_j^A \tilde{u}_i^B \right\rangle}{\partial x_k^A \partial x_k^A} - \nu \frac{\partial^2 \left\langle \tilde{u}_i^B \tilde{u}_j^A \right\rangle}{\partial x_k^B \partial x_k^B} = 0 \,. \quad (6.14)$$

In the above derivation the rules $\left\langle \langle \gamma \rangle \tilde{\theta} \right\rangle = 0$ and $\langle \langle \gamma \rangle \theta \rangle = \langle \gamma \rangle \langle \theta \rangle$, where γ and θ are generic hydrodynamic variables, have been applied.

The variables subjected to derivation are space-averaged, then, since x_k^A and x_k^B belong to same sampling region, all spatial derivatives in (6.14) are independent of the particular point in space where they are evaluated. Thus (6.14) admits only one independent variable, the lag vector r_k. Hence, $\frac{\partial f}{\partial x_k^A} = -\frac{\partial f}{\partial r_k}$, $\frac{\partial f}{\partial x_k^B} = \frac{\partial f}{\partial r_k}$, where f is a generic space-average variable. Including these

derivation rules in (6.14) one obtains

$$\frac{\partial \left\langle \tilde{u}_j^A \tilde{u}_i^B \right\rangle}{\partial t} - \frac{\partial \left\langle \tilde{u}_j^A \tilde{u}_k^A \tilde{u}_i^B \right\rangle}{\partial r_k} + \frac{\partial \left\langle \tilde{u}_i^B \tilde{u}_k^B \tilde{u}_j^A \right\rangle}{\partial r_k} + \\ - \frac{1}{\rho} \frac{\partial \left\langle \tilde{p}^A \tilde{u}_i^B \right\rangle}{\partial r_j} + \frac{1}{\rho} \frac{\partial \left\langle \tilde{p}^B \tilde{u}_j^A \right\rangle}{\partial r_i} - 2\nu \frac{\partial^2 \left\langle \tilde{u}_i^B \tilde{u}_j^A \right\rangle}{\partial r_k \partial r_k} = 0 \quad (6.15)$$

since $\frac{\partial \left\langle \tilde{u}_i^B \tilde{u}_j^A \right\rangle \langle u \rangle_k}{\partial r_k} - \frac{\partial \left\langle \tilde{u}_j^A \tilde{u}_i^B \right\rangle \langle u \rangle_k}{\partial r_k} = 0$.

Considering the correlation tensors, B_{ij}, B_{ip} and $B_{ij,k}$, defined as

$$B_{ji}(r_k,t) = \langle \tilde{u}_j(x_k,t)\tilde{u}_i(x_k+r_k,t) \rangle$$
$$B_{ip}(r_k,t) = \langle \tilde{u}_i(x_k,t)\tilde{p}(x_k+r_k,t) \rangle$$
$$B_{ji,k}(r_k,t) = \langle \tilde{u}_j(x_k,t)\tilde{u}_i(x_k,t)\tilde{u}_k(x_k+r_k,t) \rangle$$

Equation (6.15) may be written as

$$\frac{\partial B_{ji}(r,t)}{\partial t} = \frac{\partial}{\partial r_k} \left(B_{jk,i}(r,t) - B_{j,ik}(r,t) \right) + \frac{1}{\rho} \left(\frac{B_{pi}(r,t)}{\partial r_j} - \frac{B_{jp}(r,t)}{\partial r_i} \right) + 2\nu \frac{\partial^2 B_{ji}(r,t)}{\partial r_k \partial r_k} \quad (6.16)$$

where argument r_k of correlation tensors was replaced by r for simplicity and to avoid misunderstandings with the summation notation.

Considering now the scales at which the local isotropy condition is valid, the functions $B_{pi}(r_k,t)$ and $B_{jp}(r_k,t)$ must vanish and the tensors $B_{ji}(r_k,t)$, $B_{jk,i}(r_k,t)$ and $B_{j,ik}(r_k,t) = B_{ik,j}(-r_k,t)$ can be expressed in terms of the two scalar functions $B_{LL}(r,t)$ and $B_{LL,L}(r,t)$:

$$B_{ji}(r_k,t) = \left(B_{LL}(r,t) - B_{NN}(r,t) \right) \frac{r_j r_i}{r^2} + B_{NN}(r,t)\delta_{ji} \quad (6.17)$$

$$B_{ji,k}(r_k,t) = \left(B_{LL,L}(r,t) - B_{NN,L}(r,t) - 2B_{LN,N}(r,t) \right) \frac{r_j r_i r_k}{r^3} \\ + B_{LN,N}(r,t) \frac{\delta_{ik} r_j + \delta_{jk} r_i}{r} + B_{NN,L}(r,t) \frac{\delta_{ji} r_k}{r} \quad (6.18)$$

where

$$
\begin{aligned}
B_{NN}(r,t) &= B_{LL}(r,t) + \frac{r}{2}\frac{\partial B_{LL}(r,t)}{\partial r} \\
B_{NN,L}(r,t) &= -\frac{1}{2}B_{LL,L}(r,t) \\
B_{LN,N}(r,t) &= \frac{1}{2}B_{LL,L}(r,t) + \frac{r}{4}\frac{\partial B_{LL,L}(r,t)}{\partial r} \\
B_{LL}(r,t) &= \langle \tilde{u}_L(x_k,t)\tilde{u}_L(x_k+r_k,t)\rangle \\
B_{NN}(r,t) &= \langle \tilde{u}_N(x_k,t)\tilde{u}_N(x_k+r_k,t)\rangle \\
B_{LL,L}(r,t) &= \langle \tilde{u}_L(x_k,t)\tilde{u}_L(x_k,t)\tilde{u}_L(x_k+r_k,t)\rangle \\
B_{NN,L}(r,t) &= \langle \tilde{u}_N(x_k,t)\tilde{u}_N(x_k,t)\tilde{u}_L(x_k+r_k,t)\rangle \\
B_{LN,N}(r,t) &= \langle \tilde{u}_L(x_k,t)\tilde{u}_N(x_k,t)\tilde{u}_N(x_k+r_k,t)\rangle
\end{aligned}
$$

$r = |r_k|$, δ_{ji} is the Kronecker delta function, $\tilde{u}_L$ is the velocity fluctuation component on the direction of the increment r and $\tilde{u}_N$ is the velocity fluctuation component normal to that direction (Monin & Yaglom, 1975, pp. 39,64-65,117-118).

Substituting the previous expressions in (6.16) we obtain

$$
\begin{aligned}
&\frac{\partial}{\partial t}\left(-\frac{r}{2}\frac{\partial B_{LL}(r,t)}{\partial r}\frac{r_j r_i}{r^2} + B_{LL}(r,t)\delta_{ji} + \frac{r}{2}\frac{\partial B_{LL}(r,t)}{\partial r}\delta_{ji}\right) = \\
&\frac{\partial}{\partial r_k}\left(B_{LL,L}(r,t)\frac{r_j r_i r_k}{r^3} + B_{LL,L}(r,t)\frac{r_k}{r}\delta_{ji} + \frac{r}{2}\frac{\partial B_{LL,L}(r,t)}{\partial r}\frac{r_k}{r}\delta_{ji}\right. \\
&\left. -r\frac{\partial B_{LL,L}(r,t)}{\partial r}\frac{r_j r_i r_k}{r^3} + \frac{r}{4}\frac{\partial B_{LL,L}(r,t)}{\partial r}\frac{r_j}{r}\delta_{ki} + \frac{r}{4}\frac{\partial B_{LL,L}(r,t)}{\partial r}\frac{r_i}{r}\delta_{kj}\right) \\
&\qquad + 2\nu\frac{\partial}{\partial r_k \partial r_k}\left(-\frac{r}{2}\frac{\partial B_{LL}(r,t)}{\partial r}\frac{r_j r_i}{r^2} + B_{LL}(r,t)\delta_{ji} + \frac{r}{2}\frac{\partial B_{LL}(r,t)}{\partial r}\delta_{ji}\right) \qquad (6.19)
\end{aligned}
$$

If we equate the coefficients of the tensors δ_{ji} and $r_j r_i$ on the left and right hand sides of (6.19), we obtain two scalar equations which are equivalent to each other (Monin & Yaglom, 1975, p.122). Considering, for example, the equation obtained when the coefficients of the tensor δ_{ji} are equate, we find

$$
\frac{\partial B_{LL}(r,t)}{\partial t} = \left(\frac{\partial}{\partial r} + \frac{4}{r}\right)\left(B_{LL,L}(r,t) + 2\nu\frac{\partial B_{LL}(r,t)}{\partial r}\right) \qquad (6.20)
$$

If this equation is time-averaged, over a sufficient large time period, it is no longer time dependent, without loss of generality once we are considering a steady flow and spatial correlation tensors.

Equation (6.20) is now written as

$$\frac{\partial \overline{B_{LL}}(r)}{\partial t} = \left(\frac{\partial}{\partial r} + \frac{4}{r}\right)\left(\overline{B_{LL,L}}(r) + 2\nu\frac{\partial \overline{B_{LL}}(r)}{\partial r}\right) \tag{6.21}$$

being
$\overline{B_{LL}}(r) = \overline{\langle \tilde{u}_L(x_k,t)\tilde{u}_L(x_k+r_k,t)\rangle}$
$\overline{B_{LL,L}}(r) = \overline{\langle \tilde{u}_L(x_k,t)\tilde{u}_L(x_k,t)\tilde{u}_L(x_k+r_k,t)\rangle}$.

In locally isotropic turbulence, structures functions can be determined by means of the correlation functions, $\langle S_{2L}\rangle(r) = 2\left(\overline{B_{LL}}(0) - \overline{B_{LL}}(r)\right)$ and $\langle S_3\rangle(r) = 6\overline{B_{LL,L}}(r)$ (according to our notation).

Within the DAM the conservation of turbulent kinetic energy, DATKE (double-averaged TKE-equation), is written

$$\begin{aligned}
&\frac{\partial}{\partial t}\left(\frac{\left\langle \overline{u_i'u_i'}\right\rangle}{2}\right) + \frac{1}{\psi}\frac{\partial \psi\left(\langle \overline{u}_j\rangle\left\langle \overline{u_i'u_i'}\right\rangle/2\right)}{\partial x_j} = -\left\langle \overline{u_j'u_i'}\right\rangle\frac{\partial\langle \overline{u}_j\rangle}{\partial x_i} - \left\langle \overline{u_j'u_i'}\right\rangle\left\langle \frac{\partial \tilde{\tilde{u}}_i}{\partial x_j}\right\rangle \\
&-\left\langle \widetilde{\overline{u_j'u_i'}}\frac{\partial \tilde{\tilde{u}}_i}{\partial x_j}\right\rangle - \frac{1}{\psi}\frac{\partial}{\partial x_j}\left(\psi\frac{\left\langle \widetilde{\overline{u_i'u_i'}}\tilde{\tilde{u}}_j\right\rangle}{2} + \psi\frac{\left\langle \overline{u_j'u_i'u_i'}\right\rangle}{2} + \frac{\psi}{\rho}\left\langle \overline{p'u_j'}\right\rangle\right) \\
&\qquad + \nu\frac{\partial^2\left\langle \overline{u_i'u_i'}\right\rangle/2}{\partial x_i\partial x_i} - \underbrace{\nu\left\langle \overline{\frac{\partial u_i'}{\partial x_j}}\overline{\frac{\partial u_i'}{\partial x_j}}\right\rangle}_{\langle\overline{\varepsilon}\rangle}
\end{aligned} \tag{6.22}$$

We recall that the overlined variables are time-averaged variables, while primes stand for fluctuations to the time-average, angular brackets for space-averaged variables and tildes for fluctuations to the space-average. In the local isotropy conditions the mean convective fluxes are zero and the dispersive, turbulent and pressure transport terms also vanish. We also assume that the Reynolds number is large enough to have negligible viscous diffusion. So under such conditions the DATKE reduces to

$$\frac{\partial\left\langle \overline{u_i'u_i'}\right\rangle/2}{\partial t} = -\langle\overline{\varepsilon}\rangle \tag{6.23}$$

Once $\frac{\partial\langle S_{2L}\rangle(r)}{\partial t} = 0$ at small scales (Monin & Yaglom, 1975, p.396) and $\frac{\partial\overline{B_{LL}}(0)}{\partial t} = -\frac{2}{3}\langle\overline{\varepsilon}\rangle$ (see 6.3), the (6.21) becomes

$$-\frac{2}{3}\langle\overline{\varepsilon}\rangle = \frac{1}{6}\frac{\partial\langle S_3\rangle(r)}{\partial r} + \frac{2}{3}\frac{\langle S_3\rangle(r)}{r} - \frac{\nu}{6}\frac{\partial^2\langle S_{2L}\rangle(r)}{\partial r\partial r} - \frac{2\nu}{3r}\frac{\partial\langle S_{2L}\rangle(r)}{\partial r} \tag{6.24}$$

If we multiply this equation by r^4 and integrate with respect to r (applying integration by parts theorem) we obtain

$$\langle S_3 \rangle (r) = -\frac{4}{5} \langle \overline{\varepsilon} \rangle r + 6\nu \frac{\partial \langle S_{2L} \rangle (r)}{\partial r} \tag{6.25}$$

This equation is used in the next chapter as a mean to compute the mean dissipation rate of TKE, $\langle \overline{\varepsilon} \rangle$.

6.3 Order of the application of the average operators

There is an important issue behind the assumption $\frac{\partial \overline{B_{LL}}(0)}{\partial t} = -\frac{2}{3} \langle \overline{\varepsilon} \rangle = \frac{2}{3} \frac{\partial \left\langle \overline{u_i' u_i'} \right\rangle / 2}{\partial t}$ which is related with the order of the application of the space- and time-average operators. Since $\overline{B_{LL}}(r) = \overline{\langle \tilde{u}_L(x_k,t) \tilde{u}_L(x_k + r_k, t) \rangle}$ it might not be evident its relation with $\left\langle \overline{u_i' u_i'} \right\rangle / 2$.

Commonly in literature the DATKE is derived applying first the Reynolds decomposition and the time-average operator and then the spatial decomposition and the space-average operator, resulting into (6.22). Let us now introduce the spatial decomposition in the $\left\langle \overline{u_i' u_i'} \right\rangle$ tensor

$$\begin{aligned}
\left\langle \overline{u_i' u_i'} \right\rangle &= \left\langle \overline{\left(\langle u_i' \rangle + \tilde{u}_i' \right) \left(\langle u_i' \rangle + \tilde{u}_i' \right)} \right\rangle \\
&= \left\langle \overline{\langle u_i' \rangle \langle u_i' \rangle + 2 \langle u_i' \rangle \tilde{u}_i' + \tilde{u}_i' \tilde{u}_i'} \right\rangle \\
&= \overline{\langle u_i \rangle' \langle u_i \rangle'} + \overline{\left\langle \tilde{u}_i' \tilde{u}_i' \right\rangle}
\end{aligned}$$

Now considering the inverse order of the average operators we would find the tensor $\overline{\langle \tilde{u}_i \tilde{u}_i \rangle}$. If we now introduce the Reynolds decomposition in this term, we get

$$\begin{aligned}
\overline{\langle \tilde{u}_i \tilde{u}_i \rangle} &= \overline{\left\langle \left(\overline{\tilde{u}_i} + \tilde{u}_i' \right) \left(\overline{\tilde{u}_i} + \tilde{u}_i' \right) \right\rangle} \\
&= \overline{\left\langle \overline{\tilde{u}_i} \overline{\tilde{u}_i} + 2 \overline{\tilde{u}_i} \tilde{u}_i' + \tilde{u}_i' \tilde{u}_i' \right\rangle} \\
&= \langle \bar{\tilde{u}}_i \bar{\tilde{u}}_i \rangle + \left\langle \overline{\tilde{u}_i' \tilde{u}_i'} \right\rangle
\end{aligned}$$

Hence, we are led to the conclusion that

$$\left\langle \overline{u_i' u_i'} \right\rangle - \overline{\langle u_i \rangle' \langle u_i \rangle'} = \overline{\langle \tilde{u}_i \tilde{u}_i \rangle} - \langle \bar{\tilde{u}}_i \bar{\tilde{u}}_i \rangle \tag{6.26}$$

Based in the conservation equation of each of the tensors in (6.26), we get to conclude that

$$\langle \overline{\varepsilon} \rangle - \varepsilon_T = \overline{\langle \varepsilon \rangle} - \varepsilon_G \tag{6.27}$$

where $\langle\overline{\varepsilon}\rangle$ stands for the double-averaged dissipation rate as it is usually presented in literature, $\overline{\langle\varepsilon\rangle}$ is the dissipation rate associated to the tensor $\overline{\langle\tilde{u}_i\tilde{u}_i\rangle}$, which is also a turbulent energy dissipation rate in the Kolmogorov sense. The terms ε_T and ε_G are the dissipation rate corresponding to the tensors $\overline{\langle u_i\rangle'\langle u_i\rangle'}$ and $\langle\bar{\tilde{u}}_i\bar{\tilde{u}}_i\rangle$, respectively, and have a physical meaning more difficult to explain. However, we suppose that in the range of scales we are focus on $\varepsilon_G - \varepsilon_T \approx 0$, and then we can consider $\langle\overline{\varepsilon}\rangle = \overline{\langle\varepsilon\rangle}$.

Hence we can relate $\overline{B_{LL}}$ with the $\langle\overline{\varepsilon}\rangle$ and assume

$$\frac{\partial\overline{B_{LL}}(0)}{\partial t} = -\frac{2}{3}\langle\overline{\varepsilon}\rangle = \frac{2}{3}\frac{\partial\left\langle\overline{u_i'u_i'}\right\rangle/2}{\partial t}$$

Chapter 7

Rate of dissipation of TKE in flows within arrays of rigid emergent stems. Characterisation based on spatial measurements

This chapter presents a detailed spatial description of a flow within an array of rigid and emergent cylinders with varying density. The data used in the flow description consisted in horizontal maps of instantaneous velocity acquired with a Particle Image Velocimetry (PIV) system in a laboratory model simulating a stream with rigid vegetation. The characterization of the flow includes time-averaged velocity and vorticity maps, which allows to see how the mean flow behaves at the inter-stem distance. Autocorrelation functions are presented and they are used to define the characteristic length scales of the flow. Furthermore, second and third order structures functions as well as energy spectra are discussed.

The work exploits the space-averaging of two-point correlations and statistics of the turbulent flow as means to salvage the formalism of homogeneous and isotropic turbulence (HIT), deriving an equation to estimate the dissipation rate of turbulent kinetic energy (TKE).

7.1 Introduction

The physics of flows through arrays of circular cylinders has been investigated in the scope of several fundamental and applied disciplines. In the context of environmental sciences, rigid emergent cylinders represent a convenient ersatz for stems of several wetland species (Lightbody & Nepf, 2006; Nepf & Ghisalberti, 2008), allowing for laboratory work under controlled conditi-

ons. In this context, the study of flows within the array of plant stems is of paramount importance since flow hydrodynamics determines fluxes of suspended sediment, pollutants and nutrients, thus constituting the physical stratum upon which biological and ecological strata are formed (Nepf, 2012a; Tanino & Nepf, 2009; White & Nepf, 2003).

In natural conditions, the flow in the space among stems is normally turbulent. Turbulence is non-homogeneous, being mostly generated by the interaction of vortexes shed by individual stems. For high Reynolds numbers (the appropriate Reynolds numbers will be defined later), second and higher order moments of velocity fluctuations evidence a spatial distribution depending mostly on stem diameter and placement.

Upscaling the analysis to larger spatial scales has allowed for major progresses in the formal definition and characterization of momentum and scalar fluxes (Finnigan, 2000; Poggi *et al.*, 2004a; Raupach *et al.*, 1986; White & Nepf, 2008). The theoretical background allowing for the exact expression of conservation laws at scales larger than the mean inter-stem distance (defined as the averaged distance between a stem and its nearest neighbour) has been laid out by Finnigan (2000); Finnigan & Shaw (2008); Nikora *et al.* (2001); Raupach & Shaw (1982), among others, and has been termed Double-Averaging Methodology (DAM, Nikora *et al.*, 2007a). Conservation equations for mass, momentum and second-order moments of turbulent fluctuations, namely turbulent kinetic energy (TKE), have been developed within the DAM.

Terms in the space-averaged equations of conservation of momentum and TKE, notably space-averaged dispersive stresses, dispersive stresses and wake production terms, require parametrization. It is reasonable to believe, in analogy to turbulence characterization, that combinations of $\langle \bar{k} \rangle$, the space-averaged TKE, and $\langle \bar{\varepsilon} \rangle = \langle \overline{\frac{\partial u'_i}{\partial x_k}} \overline{\frac{\partial u'_i}{\partial x_k}} \rangle$, the space-averaged rate of dissipation of TKE provide length and time scales useful to characterize the averaged flow at the inter-stem scale and to formulate higher order closure models (Juang *et al.*, 2008).

Of particular interest to this research is the quantification of $\langle \bar{\varepsilon} \rangle$, for which existing methods mostly involve space-averaging of point-wise estimates. These may be obtained from characteristic macroscales (Mignot *et al.*, 2009b), from a balance analysis of production and dissipation terms (Finnigan, 2000) or under the assumption of homogeneous and isotropic turbulence (see, e.g. Monin & Yaglom, 1975, pp.351-355). In the latter case, the rate of dissipation can be calculated from the gradient of the longitudinal velocity, from Rice's formula (Sreenivasan *et al.*, 1983) and, in the absence of spectral short-cut typical for submerged canopies, from spectra or structure function scaling laws (e.g. Hsieh & Katul, 1997). These estimates require i) high spatial resolution for direct evaluation of spatial derivatives, ii) sufficient temporal resolution and the validity of Taylor's hypothesis (Taylor, 1938) or sufficient spatial resolution for spectral or structure function analysis.

If turbulence is not homogeneous, as is the case of the flow in the inter-stem space, there are

several competing theories expressing the dissipation tensor (e.g. Moser, 1994; Oberlack, 1997; Perot & Natu, 2004) but they are not analytically tractable for transforming measured velocity fluctuations into dissipation rates and are, therefore, out of the scope of this paper. Furthermore, the use of Taylor's hypothesis in flows that exhibit separation and periodic vortex shedding is problematic, as the correct advection velocity is unknown. In this paper, this issue is addressed as turbulent quantities are derived directly from spatial velocity series.

The objective of the paper is the characterization and quantification of the rate of dissipation of turbulent kinetic energy (TKE) in flows within arrays of emergent, rigid and cylindrical stems at scales of the order of magnitude of the mean inter-stem characteristic length. We do not attempt to employ a non-homogeneous theory. Instead, we assume local isotropy, in the sense of Monin & Yaglom (1975), and we further exploit space-averaging of two-point correlations and statistics as a means to salvage the formalism of HIT. In particular, we derive an equation akin to Kolmogorov's and use it to express the longitudinal $3^{\text{rd}}-$order structure function, from which an estimate of the rate of dissipation of TKE can be obtained. We choose not to calculate it from second-order statistics, namely power spectra and $2^{\text{nd}}-$order structure functions, since we can not presuppose universality of the involved constants under our flow conditions. We also do not employ the direct definition or estimates based on Taylor's micro-scales because the spatial resolution is not sufficiently high to resolve the all relevant gradients of the velocity field.

As a compromise between physical verisimilitude and laboratory feasibility, we employ slightly rough stems randomly placed whose spatial distribution in the horizontal plane emulates the patchiness often seen in actual wetlands (Schoelynck *et al.*, 2012). A simpler regular spatial distribution would render the results easier to analyse. However, such simplicity could be misleading as the complexity of wake interactions found in nature is not amenable to be simulated by simple staggered arrays of stems. We thus assume a wide range of spatial variability in the flow field and seek to explain it as the a result of a, presumably, non-linear combination of space-averaged and local effects.

Horizontal maps of instantaneous velocity were acquired with a particle image velocimetry system (PIV) in a flow within an array of cylinders with different stem areal number-density, herein designated by m and expressed in stems$/\text{m}^2$. The focus of the present study is placed at the scale of the inter-cylinders distance, herein referred as inter-stem distance. A particular feature of the presented characterization of the flow is that it is carried out with a spatial analysis of the flow, avoiding the use of the frozen turbulence approximation, which would be inappropriate for this kind of flows.

The values of the stem-Reynolds number $Re_p = \langle\bar{u}\rangle d/\nu$ (where $\langle\bar{u}\rangle$ stands for the mean longitudinal velocity, d is the stem diameter and ν is the kinematic viscosity) for the particular flow described in this paper range between 1100 to 1700 and the stem density ranges from 400 to 1600 stems m^{-2}. For these densities of stems, the flow in the inter-stem space lies in Type 4B

Strouhal-Reynolds number behaviour presented by Sumner (2010) for staggered configurations.

Depending of its relative location, the flow in the inter space of multiple cylinders may involve complex interactions between the shear layers, vortices, wakes and von Kármán vortex streets. Each cylinder has a viscous boundary layer that stretches and sheds vortices at a frequency, f, that depends on the Reynolds number. Boundary layers of neighbour cylinders may overlap forming a creeping flow. For a single isolated cylinder, the range of Reynolds numbers in the present study would correspond to a Strouhal number ($S_t = fd/\langle\bar{u}\rangle$) of, approximately, 0.21. However, due to the interaction with neighbouring cylinders, the frequency of vortex ejection may be different and may even fluctuate in time. It should be also possible to find cases with more than a single shedding frequency (Sumner, 2010).

Concerning the structure of the paper, the next section describes the experimental facilities, the instrumentation and the laboratory tests carried out. Section 7.3 presents a brief description of the classical tools for turbulence characterization, including the adaptation of the results developed for homogeneous and isotropic turbulence as well as the necessary results to support the simplifications assumed. Section 7.4 is the main section presenting the computation of the dissipation rate of TKE as well as a discussion of the results obtained. To finish, the conclusions of this work are drawn.

7.2 Experimental facilities

The experimental work was carried out in a recirculating tilting flume of the Laboratory of Hydraulics and Environment of Instituto Superior Técnico. It is a 12.5 m long and 40.8 cm wide prismatic horizontal channel. The channel has side walls made of glass, enabling flow visualization and laser measurements. The bottom was covered with a horizontal layer of gravel and sand. Arrays of rigid, cylindrical, vertical and emergent stems, were randomly placed along a 3.5 m long reach simulating rigid vegetation conditions. The stems, randomly but uniformly distributed, were organized in 15 cm long alternated patches with 1600 stems m^{-2} (dense, herein) and 400 stems m^{-2} (sparse, herein), separated by 10 cm long transition reaches featuring 5 cm with a density of 1200 stems m^{-2} and 5 cm with 800 stems m^{-2} (figure 7.1). At the end of the vegetated reach between two consecutive patches there is a gap without stems to enable the velocity measurements (dashed rectangles in figure 7.1). To minimize its impact, the width of that measuring gap is equal to the mean inter-stem distance of the upstream patch. The patchiness of the array of stems presents a wavelength of 0.5 m. Downstream of the vegetation covered reach a coarse gravel weir controlled the flow.

The instantaneous velocity fields were acquired with a 2D Particle Image Velocimetry system (PIV), which is an optical technology which allows obtaining velocity flow fields by measuring

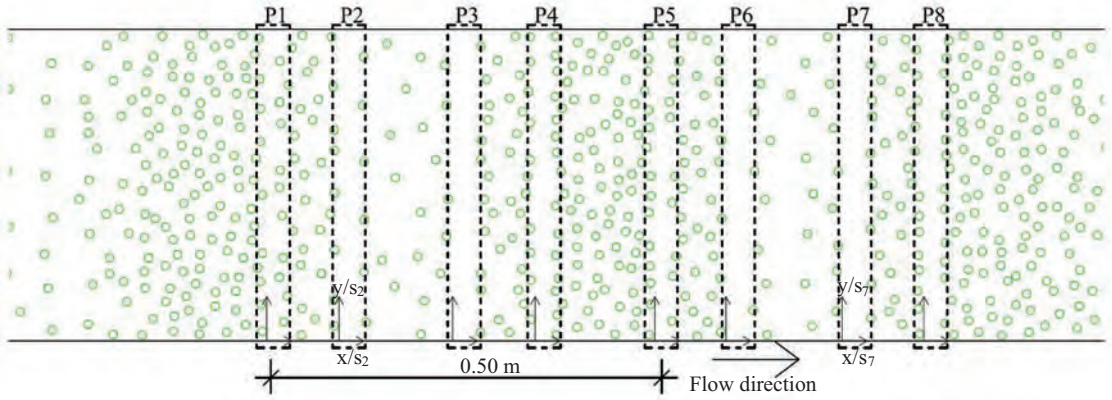

Figure 7.1: Plan view of part of the stem covered reach. Dashed rectangles depict the regions where the horizontal maps of velocity were measured for each patch, from P1 to P8. For each measuring gap a local referential is considered.

seeding particle's velocity. The PIV system consisted of a 8-bit 1600×1200 px^2 CCD camera and a double-cavity Nd-YAG laser with pulse energy of 30 mJ at wavelength of 532 nm. PIV image pairs were acquired at a frequency of 15 Hz with a time delay of 1500 μs between frames. The flow was seeded by polyurethane particles with an averaged diameter of 60 μm in a range from 50 to 70 μm and a density of 1.31g cm^{-3}. The correlation algorithm applied to obtain the instantaneous velocity maps is included in the acquisition software and it incorporates a validation procedure based in the median of the neighbourhood.

Horizontal maps of instantaneous velocity were acquired, at each measuring gap (figure 7.1), covering the entire flume width with maps of ≈ 9.5 cm long and 12.5 cm wide at two different heights (see table 5.1: z_a and z_b). For each acquisition 5000 image couples were collected, what allows computations of turbulence statistics over $5'33''$ of consecutive data. Image pairs were processed with an adaptive correlation algorithm starting with interrogation area of 128×128 px^2 and ending at 16×16 px^2, without overlap. This spatial resolution yields to interrogation volumes of $1.3 \times 1.3 \times 2$ mm^3, since the laser light sheet is approximately 2 mm thick. The spatial resolution of PIV measurements results from a trade off between zooming the image into a small area to solve small scale motion, which leads to a loss of global information and increases noise and capturing the region of the flow field that includes all relevant scales (Lavoie *et al.*, 2007). In this case, the image size is large enough to capture at least twice the mean inter-stem distance, s, which is the most relevant scale for this study. The size of the interrogation area is $\approx 0.4\lambda$ and $\approx 10\eta$, being λ the Taylor's micro scale and η the Kolmogorov length scale.

Tests were performed with a discharge of 2.33 ls^{-1}. In table 5.1, m represents stem areal number-density, $s = 1/\sqrt{m}$ is the mean inter-stem distance, h is the averaged flow depth, $z^{(i)}$, with $i = a, b$, is the elevation of the measurement planes, and $Re_p^{(i)} = \langle \bar{u}^{(i)} \rangle d/\nu^{(i)}$ is the stem Reynolds number, where $d = 0.011$ m is the stem diameter, $\langle \bar{u}^{(i)} \rangle$ is the double-averaged longitudinal

Table 7.1: Features of the experimental tests and flow properties for each longitudinal position.

	P1	P2	P3	P4	P5	P6	P7	P8
m stems m^{-2}	1600	800	400	1200	1600	800	400	1200
s (m)	0.025	0.035	0.050	0.029	0.025	0.035	0.050	0.029
h (m)	0.065	0.064	0.063	0.062	0.057	0.056	0.054	0.052
$z^{(a)}/h$ $(-)$	0.57	0.61	0.61	0.62	0.67	0.69	0.55	0.59
$z^{(b)}/h$ $(-)$	0.84	0.89	0.90	0.91	0.90	0.93	0.94	0.90
$\langle\bar{u}^{(a)}\rangle$ (m s^{-1})	0.086	0.093	0.090	0.091	0.092	0.108	0.106	0.100
$\langle\bar{u}^{(b)}\rangle$ (m s^{-1})	0.091	0.094	0.092	0.092	0.105	0.109	0.104	0.116
$Re_p^{(a)}(-)$	1161	1282	1233	1302	1266	1512	1469	1338
$Re_p^{(b)}(-)$	1281	1268	1242	1301	1473	1533	1462	1564

velocity and $\nu^{(i)}$ stands for the kinematic viscosity, which depends on water temperature at the time of the measurements (Likhachev, 2003). The presented values are averages of the several lateral measurements of each longitudinal and vertical positions.

Throughout this work a Cartesian referential system is considered, where x, y and z correspond to the streamwise, spanwise and vertical directions, respectively, and u, v and w are the corresponding velocity components. However when correlation or structure functions are concerned, it is convenient to consider a special set of coordinates in which the first axis lies along the direction of the increments, r, while the two other axes are perpendicular to that direction. Hence, to avoid misunderstandings concerning spatial directions, it should be noticed that the adjectives streamwise and spanwise are used with a different meaning of longitudinal and transverse, being the latter applied to classify functions evolving increments. Still regarding the symbols used throughout this text, angular brackets ($\langle u\rangle$) denote space-average operator while over-lines ($\bar{u}$) are used as time-average operator, tildes ($\tilde{u}$) represent spatial fluctuations and primes (u') time fluctuations. For example $\tilde{u} = u - \langle u\rangle$ and $u' = u - \bar{u}$. The subscript $p = 1,2,...,8$ is used to identify the measuring gap (then, also the corresponding patch) while the superscript $i = a,b$ identifies the vertical position.

In the present work, the data analysis is performed with an original approach, considering instantaneous velocity series in transversal direction instead of the typical advection direction. That is because the goal is to characterize the flow at at the inter-stem scale and flow heterogeneity due to the presence of the vertical cylinders is highlighted along the spanwise direction. To better understand the results presented in the following sections, some explanations about the data treatment are given hereafter. Figure 7.2a) exemplifies an instantaneous velocity map in the horizontal plane $z^{(a)}$ for the measuring gap P5. The dashed line on that figure represents one spatial series of instantaneous velocity, which is the base for all the analysis herein presented.

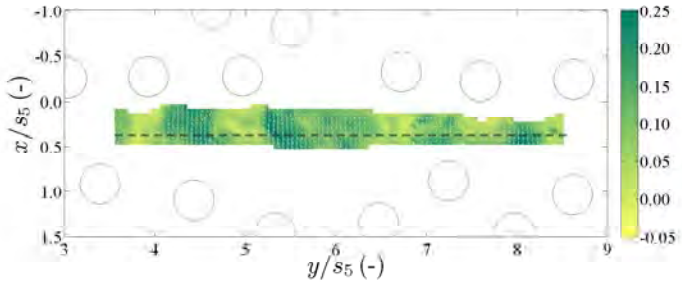

(a)

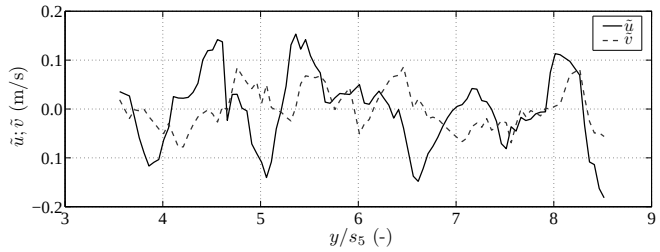

(b)

Figure 7.2: a) Example of an instantaneous velocity map at P5. b) Instantaneous and spatial longitudinal velocity series.

Figure 7.2b) is a graph of the streamwise ($\tilde{u}$) and spanwise ($\tilde{v}$) spatial velocity fluctuation series identified by the dashed line in figure 7.2a). The coordinates are normalized by the mean inter-stem distance, s_p, and a local referential is considered for each longitudinal position (see figure 7.1). With spatial velocity series like these, autocorrelation functions, structure functions and energy spectra are computed for each available cross section and for all time instants. Then a time-average is considered for every cross section.

Figure 7.3 (left hand side) presents time-averaged velocity maps for each measuring gap at height $z^{(a)}$. These maps evidence the great heterogeneity of this kind of flows, at large scales, with zones of low velocity at the cylinder's wake alternated by high velocity zones between cylinders. These low/high velocity patterns are observed for all the tested stem areal number-density. The column on the right hand side of the same figure shows the corresponding time-averaged vorticity maps. Vorticity maps show a repeating symmetrically paired vortexes pattern caused by the unsteady separation of the flow over the cylinders. These *quasi*-symmetric high vorticity patterns behind the stems identify Von Kármán vortex streets. Comparing vorticity maps for patches with m, we conclude that the presence of vertical cylinders induce a regular structure of vortex patterns independently of the stem areal number-density. However, the space necessary to fully develop the vortex pattern is strongly reduced for dense patches. In sparse patches, vorticity has space to decrease its intensity contrarily to what is observed in dense patches where the vortices are forced

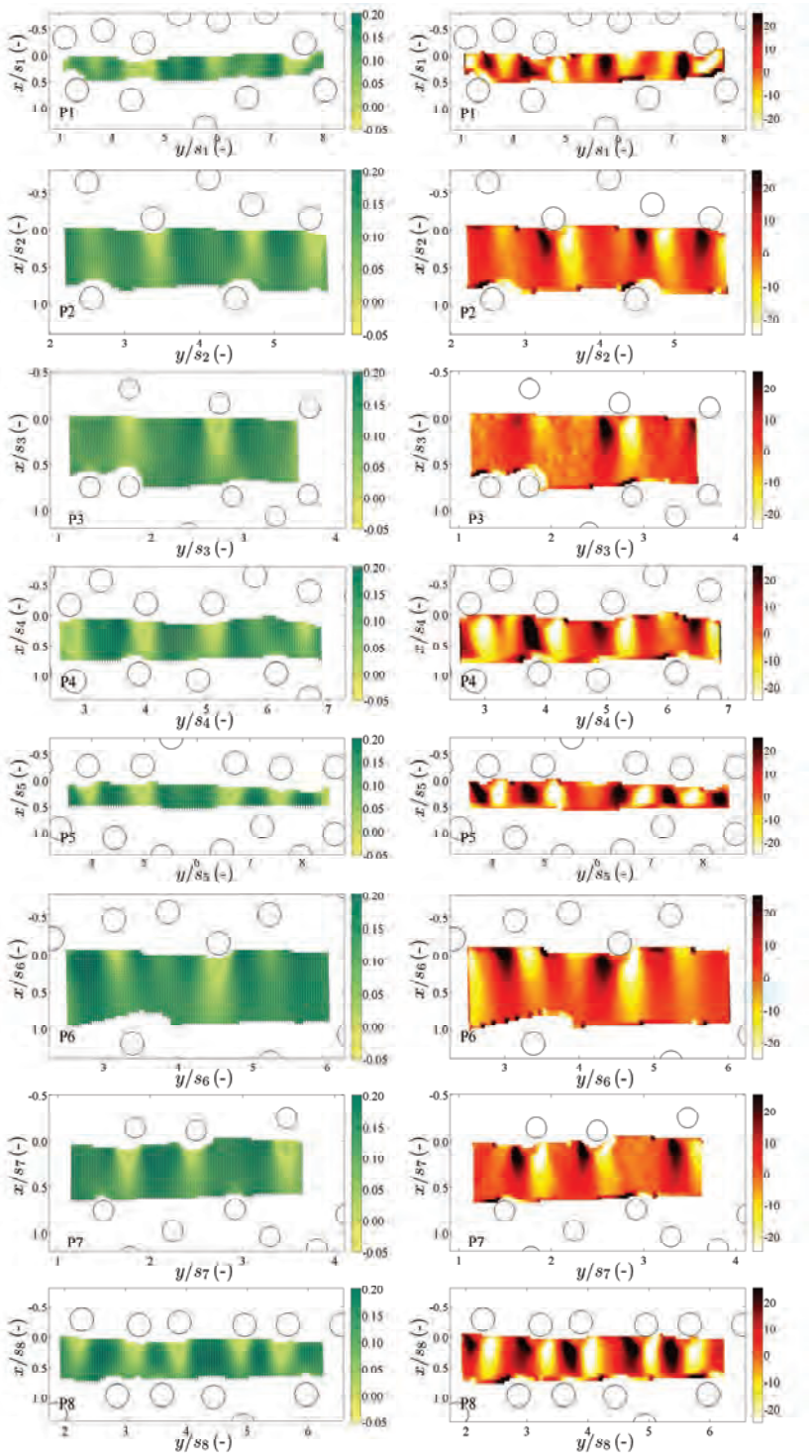

Figure 7.3: Time-averaged velocity maps (left) and time-averaged vorticity maps (right) at $z^{(a)}$ for each longitudinal position (P1 to P8, from the top to the bottom).

to compress. From the phenomenological point of view, turbulent structures generation in this kind of flow is similar to generation in the case of an isolated cylinder, it is a wake production dominated flow. The vortex generation is due to the flow separation around the cylinder, being the size of the vortices dependent on the cylinder diameter. Consequently, the role of the inter-stem distance on the turbulent field is played on density and spatial organization of those vortices. Therefore, a dense patch, having smaller inter-stem distance, leads to higher vortex density which results in stronger spatial velocity fluctuations. Based on that feature, flows within arrays of rigid cylinders can be named as inter-stem flows.

7.3 Adaptation of HIT results

The theory of turbulence is based on statistical analysis of random flow fields. Correlations and moments of the probability distributions are key parameters in characterization of turbulence. Autocorrelation and structure functions are of particular interest.

Autocorrelation functions for spatial velocity series along spanwise direction are presented and applied to estimate a characteristic macro length scale and the Taylor's micro scale of the present flow.

As explained before, sets of instantaneous autocorrelation functions were time-averaged for each cross section and then space averaged for all cross sections, for each dataset. The time-averaged longitudinal and transverse autocorrelation functions are defined, in dimensionless way, by

$$R_L(x,r) = \overline{\left(\frac{\langle \tilde{v}(t,x,y)\tilde{v}(t,x,y+r)\rangle}{\langle \tilde{v}(t,x,y)^2\rangle} \right)} \tag{7.1a}$$

$$R_N(x,r) = \overline{\left(\frac{\langle \tilde{u}(t,x,y)\tilde{u}(t,x,y+r)\rangle}{\langle \tilde{u}(t,x,y)^2\rangle} \right)}, \tag{7.1b}$$

respectively, where t stands for time and r for the space increment. Figures 7.4 and 7.5 exemplify R_L and R_N for sparse and dense patches, P3 and P5, respectively. Theses figures show that both R_L and R_N present an oscillating behaviour around zero, with a wavelength close to s and high amplitude, for R_N, leading to the conclusion that, the inter-stem distance has an important role in the flow energy budget. The definition of integral scale based in the integration of the autocorrelation function proves to be inadequate in flows within arrays of cylinders, since due to this oscillating behaviour it would render to very small values or even to negative values, what does not make physical sense. There is no theoretical definition for the relevant length scales for flows with this level of complexity, nevertheless the previous analysis based on vorticity maps and autocorrelation functions identified the inter-stem distance as a very important scale. Due to the random distribution of cylinders in the present study, it is not possible to have an

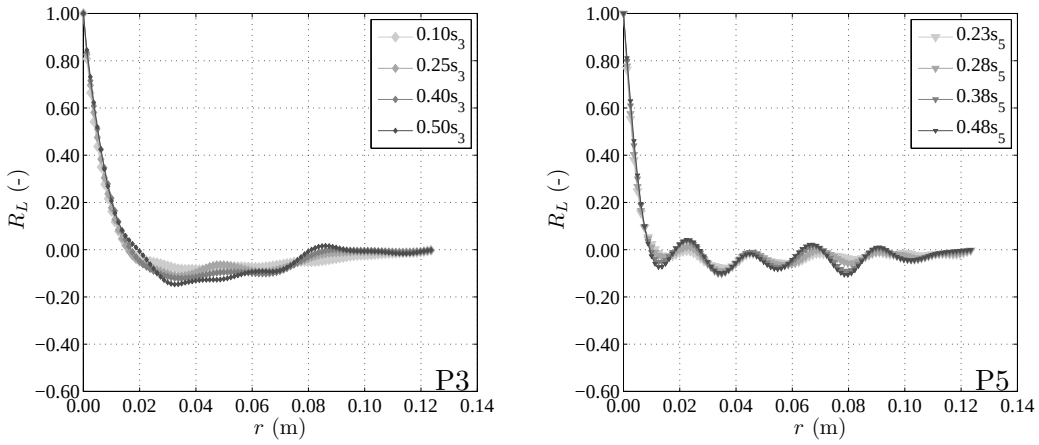

(a) (b)

Figure 7.4: Longitudinal autocorrelation function for a) P3 and b) P5, at 4 different cross sections for a lateral position at height $z^{(a)}$.

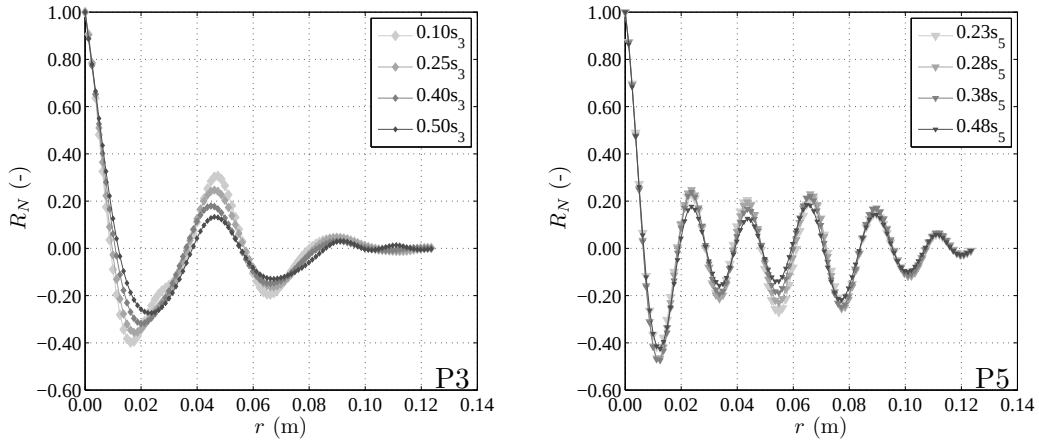

(a) (b)

Figure 7.5: Transverse autocorrelation function for a) P3 and b) P5, at 4 different cross sections for a lateral position at height $z^{(a)}$.

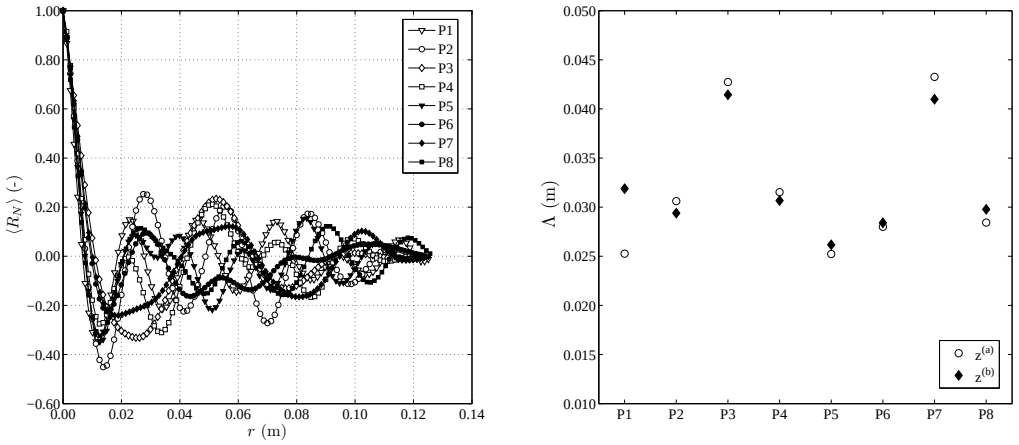

(a) (b)

Figure 7.6: a) Double-averaged transverse autocorrelation function for a lateral position at height $z^{(a)}$. b) Mean macro-scale for each longitudinal and vertical positions.

unambiguous value to the inter-stem space scale. Hence, the present work defines a macro-scale based on the transverse autocorrelation function, instead of using the averaged inter-stem distance s, which would be less sensitive to local flow conditions. The macro-scale, Λ, was defined as the increment r corresponding to the first local maximum of the time- and space-averaged transverse autocorrelation function, $\langle R_N \rangle$, after the origin which corresponds to $\langle R_N \rangle = 1$. Figure 7.6a presents $\langle R_N \rangle$ of each measuring gap for a lateral position at height $z^{(a)}$. The macro-scale is computed for each dataset and then an average of all lateral positions is considered for each longitudinal and vertical position (figure 7.6b). The values of Λ increase from dense patches to sparse ones, supporting the idea that the characteristic length scale is correlated with s.

Another scale of interest corresponds to the length of the segment cut on the horizontal axis by the osculating parabola tangent to the autocorrelation function at its origin peak (Monin & Yaglom, 1975, p.35). This scale is often referred as Taylor's micro scale, and herein is represented by λ_L or λ_N depending whether it is computed from $\langle R_L \rangle$ or $\langle R_N \rangle$, respectively. Formally, this micro scale is defined by (Tennekes & Lumley, 1972, p.211)

$$\left(\frac{\partial^2 R_{L,N}}{\partial r^2} \right)_{r=0} = -\frac{2}{\lambda_{L,N}^2} \tag{7.2}$$

and the numerical definition applied herein to estimate these scales is

$$\lambda_{L,N} = \frac{\Delta r}{\sqrt{\langle R_{L,N} \rangle (r=0) - \langle R_{L,N} \rangle (r=\Delta r)}} \tag{7.3}$$

Table 7.2 presents longitudinal and transverse Taylor's micro scale, λ_L and λ_N, respectively and

Table 7.2: Taylor's micro scales and Reynolds numbers based on the micro and macro scales of the flow.

	P1	P2	P3	P4	P5	P6	P7	P8
$\lambda_L^{(a)}$ (m)	0.0031	0.0031	0.0029	0.0032	0.0027	0.0031	0.0033	0.0031
$\lambda_L^{(b)}$ (m)	0.0033	0.0031	0.0030	0.0034	0.0031	0.0032	0.0033	0.0034
$Re_{\lambda L}^{(a)}$ (−)	152	143	105	159	151	162	160	177
$Re_{\lambda L}^{(b)}$ (−)	167	143	113	163	167	175	159	192
$\lambda_N^{(a)}$ (m)	0.0038	0.0038	0.0036	0.0041	0.0036	0.0037	0.0039	0.0039
$\lambda_N^{(b)}$ (m)	0.0038	0.0038	0.0036	0.0041	0.0040	0.0037	0.0039	0.0040
$Re_{\lambda N}^{(a)}$ (−)	329	278	209	366	385	294	296	387
$Re_{\lambda N}^{(b)}$ (−)	332	271	210	362	440	307	286	401
$Re_{\Lambda}^{(a)}$ (−)	2509	3548	4899	3681	2889	3989	5718	3468
$Re_{\Lambda}^{(b)}$ (−)	3626	3398	4709	3677	3514	4004	5373	4080

the corresponding Reynolds numbers, $Re_{\lambda L} = \lambda_L \overline{\langle \tilde{v}^2 \rangle}^{1/2} / \nu$ and $Re_{\lambda N} = \lambda_N \overline{\langle \tilde{u}^2 \rangle}^{1/2} / \nu$.

It should be noticed that the theoretical result from homogeneous and isotropic turbulence stating that $\lambda_L = \sqrt{2}\lambda_N$ is not verified for this flow, where all reaches have λ_N larger than λ_L, a relation $\lambda_N \approx 1.25\lambda_L$ was found.

The two point longitudinal and transverse second-order structure functions, S_{2L} and S_{2N} respectively, are defined herein by

$$S_{2L}(\alpha, r) = \overline{(\tilde{v}(\alpha + r) - \tilde{v}(\alpha))^2} \tag{7.4a}$$

$$S_{2N}(\alpha, r) = \overline{(\tilde{u}(\alpha + r) - \tilde{u}(\alpha))^2} \tag{7.4b}$$

where r is the increment which has the y-direction, α is any point in the space and $\tilde{v}$ and $\tilde{u}$ are the velocity fluctuations components on the same and the perpendicular direction of the increment, respectively. The over-line stands, here, for the appropriate ensemble-average, since the processes are stationary, this may be a time-average.

The longitudinal third-order structure function is defined as

$$S_3(\alpha, r) = \overline{(\tilde{v}(\alpha + r) - \tilde{v}(\alpha))^3}\,. \tag{7.5}$$

Since turbulence is not homogeneous, the values of the structure functions depend on the point α and not only on the lag r. If the structure functions are space-averaged, the results $\langle S_2 \rangle$ and

$\langle S_3 \rangle$ do not depend on any particular α. Instead, they become dependent only on the space lag r:

$$\langle S_{2L} \rangle (r) = \left\langle \overline{(\tilde{v}(\alpha + r) - \tilde{v}(\alpha))^2} \right\rangle \tag{7.6a}$$

$$\langle S_{2N} \rangle (r) = \left\langle \overline{(\tilde{u}(\alpha + r) - \tilde{u}(\alpha))^2} \right\rangle \tag{7.6b}$$

$$\langle S_3 \rangle (r) = \left\langle \overline{(\tilde{v}(\alpha + r) - \tilde{v}(\alpha))^3} \right\rangle \ . \tag{7.6c}$$

Exploiting the space-averaging of two-point correlations and statistics, we followed the procedure applied by Monin & Yaglom (1975, pp.120-122) to derive an equation akin to Kolmogorov's equation (also referred as Kármán-Howart's equation), from which an estimate of the rate of dissipation of TKE can be obtained. Evidently, turbulence remains non-homogeneous but the formalism that led to the relation between second and third-order structure functions in HIT is now applicable rendering similar results (see Annex I):

$$\langle S_3 \rangle (r) = -\frac{4}{5} r \langle \overline{\varepsilon} \rangle + 6\nu \frac{\partial \langle S_{2L} \rangle (r)}{\partial r} \tag{7.7}$$

where ν stands for the kinematic viscosity and $\langle \overline{\varepsilon} \rangle$ is the mean dissipation rate of energy. This equation is valid within the range of scales where the local isotropy condition is applicable.

Often, when r is in the inertial range of scale, the viscous friction is considered not to play an appreciable role, i.e., $\nu \frac{\partial \langle S_{2L} \rangle (r)}{\partial r} \approx 0$, so (7.7) is very often found in literature written as:

$$\langle S_3 \rangle (r) = -\frac{4}{5} r \langle \overline{\varepsilon} \rangle \tag{7.8}$$

which corresponds to the known four-fifth law in homogeneous and isotropic turbulence theory (Monin & Yaglom, 1975, pp.395-397; Frisch, 1995, p.76).

Normalized third order structure functions, $\langle S_3 \rangle$, for two measuring gaps, P7 and P5, are presented in figure 7.7. Analysing the measured third order structure functions we conclude that it is difficult to identify a common pattern for these functions, what may be related to the difficulty associated to estimate third order moments from the measurements. However, the main interest of third order structures functions is found at small scales, where these are related to energy dissipation rate according to (7.8). On that reach of interest, for all the datasets we found the expected behaviour, since $\langle S_3 \rangle$ presents a linear decrease with r until reaching a minimum value. The analysis of $\langle S_3 \rangle$ herein is focused on the reach $r/\Lambda_p < 0.5$. The linear reach is longer in dense patches than in sparse patches (figure 7.7). In general, the number of points over the linear part of the graph decreases toward downstream.

Recent studies, investigating the finite Reynolds number effect (Antonia & Burattini, 2006; Danaila *et al.*, 2002; Qian, 1999; Tchoufag *et al.*, 2012), have evidenced that for flows encoun-

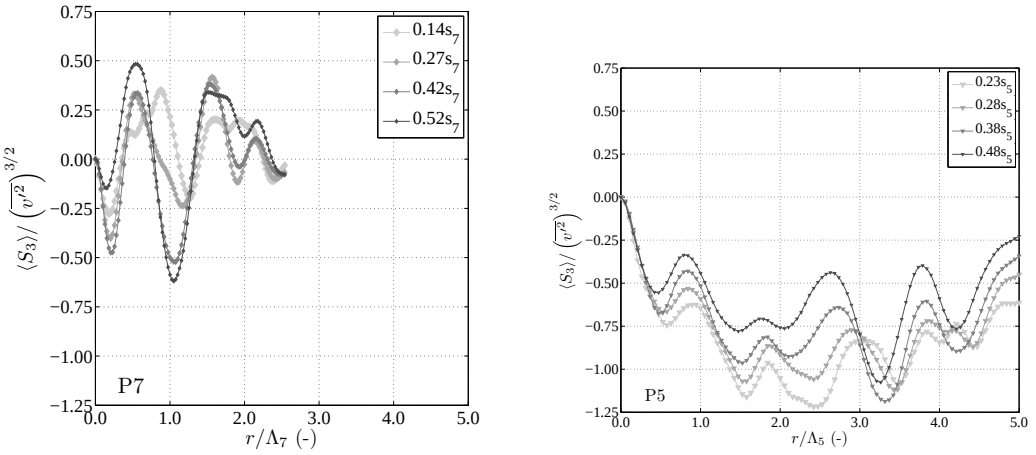

(a) (b)

Figure 7.7: Dimensionless third order longitudinal structure function, $\langle S_3 \rangle$, for a lateral position at height $z^{(a)}$ for a) P7 and b) P5.

tered in the laboratory, the effect of a finite Reynolds number and of the non-stationarity or inhomogeneity associated with large scales can affect significantly the behaviour of the scales in the inertial range. These advances show that small Reynolds numbers maintain the magnitude of the third order structure function below its asymptotic value of $4\overline{\varepsilon}r/5$. Thus, the estimation of $\langle \overline{\varepsilon} \rangle$ by (7.8) may lead to overestimated values. Most of these recent studies require a known dissipation rate, which is often estimated by other theoretical assumptions. So when the goal is to estimate turbulent dissipation rate, a certain degree of uncertainty is still inevitable.

Another important result from Kolmogorov hypotheses is the two-thirds law (Monin & Yaglom, 1975, pp. 353-354), stating that in any turbulent flow with sufficiently large Reynolds number, the mean square of the velocity difference between two points separated by a distance r should be proportional to $\langle \overline{\varepsilon} \rangle^{2/3} r^{2/3}$, for $l_0 \ll r \ll \eta$, where l_0 and η stand for integral and Kolmogorov length scale, respectively. The mean square of velocity increments corresponds to the second order structure function. Hence, supposing that our data have enough spatial resolution, we should find the following relations within the inertial range of scales

$$\langle S_{2L} \rangle (r) = C_{2L} \langle \overline{\varepsilon} \rangle^{2/3} r^{2/3} \tag{7.9a}$$

$$\langle S_{2N} \rangle (r) = C_{2N} \langle \overline{\varepsilon} \rangle^{2/3} r^{2/3} \tag{7.9b}$$

where C_{2L} and C_{2N} are dimensionless constants. Figure 7.8 exemplifies longitudinal second order structures functions, $\langle S_{2L} \rangle$, for a dense patch (P5) and sparse one (P3). Graphs are presented in dimensionless form, being increments normalized by the macro-scale, Λ_p and structure functions normalized by the variance of the velocity series, $\overline{\langle \tilde{v}^2 \rangle}$ and $\overline{\langle \tilde{u}^2 \rangle}$. The black crosses plotted in these

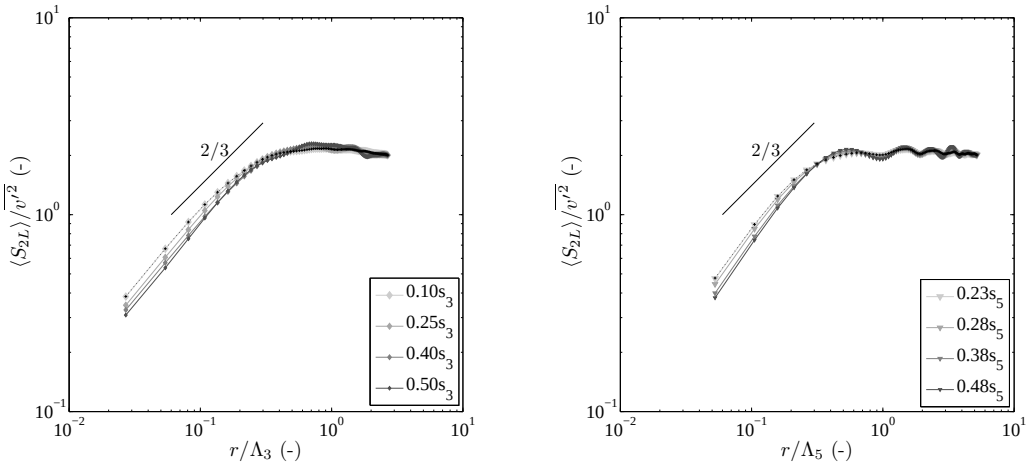

Figure 7.8: Dimensionless second order longitudinal structure function,$\langle S_{2L}\rangle$, for a lateral position at height $z^{(a)}$ for a) P3 and b) P5. The black dotted line with $+$-marker represents the relation given by (7.10a) for the upstream cross section.

figures represent an estimation of the structure function based on the autocorrelation functions by the following relation for HIT (Monin & Yaglom, 1975, p.100)

$$\langle S_{2L}\rangle(r) = 2\left(R_L(0) - R_L(r)\right) \tag{7.10a}$$

$$\langle S_{2N}\rangle(r) = 2\left(R_N(0) - R_N(r)\right) \tag{7.10b}$$

We observed that this estimation agrees well with measured $\langle S_{2L}\rangle$ and $\langle S_{2N}\rangle$, corroborating the local isotropy approach. $\langle S_{2L}\rangle$ and $\langle S_{2N}\rangle$ reveal an oscillating shape, more pronounced for dense patches, which expresses the characteristic pattern of high and low velocity of the flow field. In both, longitudinal and transverse functions, the reach corresponding to the inertial range is identified, where graphs have a $2/3$ slope spanning about half decade for $\langle S_{2L}\rangle$ and a bit less for $\langle S_{2N}\rangle$. The structure functions are practically constant along streamwise direction.

An equivalent law to the two-thirds law can be formulated in terms of energy spectrum (Monin & Yaglom, 1975, p.355)

$$E_L(k) = C_L\,\langle\overline{\varepsilon}\rangle^{2/3}\,k^{-5/3} \tag{7.11a}$$

$$E_N(k) = C_N\,\langle\overline{\varepsilon}\rangle^{2/3}\,k^{-5/3} \tag{7.11b}$$

where E_L and E_N are longitudinal and transverse one-dimensional energy spectrum, respectively and C_L and C_N are dimensionless constants. This relation, often called $-5/3$ law, is valid only for wavenumbers, k, within the inertial range. Figure 7.9 shows transverse spectra for P3 (sparse patch) and P1 (dense patch). The computed spectra exhibit the inertial range, typically spanning

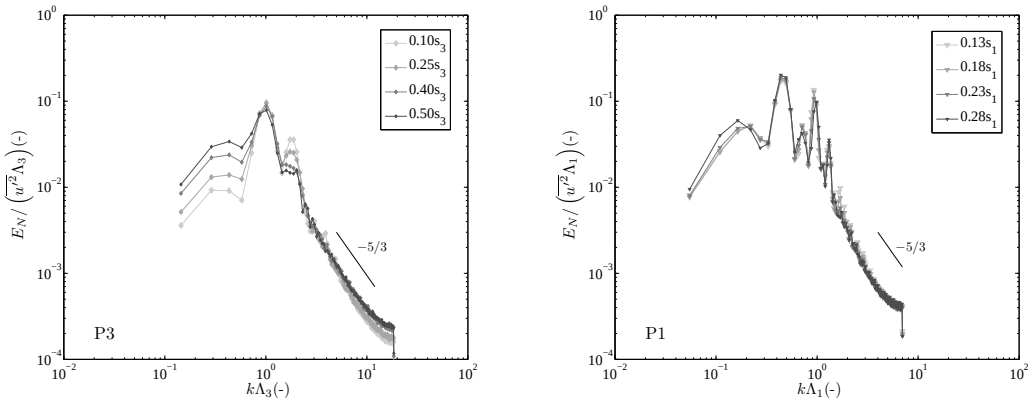

(a) (b)

Figure 7.9: Dimensionless spatial transverse spectra for a lateral position at height $z^{(b)}$ for patches a) P3 and b) P1.

about half decade, where a $-5/3$ slope reach is visible (Appendix B presents transverse and longitudinal spectra for all measuring gaps).

Flows within arrays of cylinders require heterogeneity and anisotropy. However, the heterogeneity of those kind of flows is on the time-averaged field. Considering translations in spanwise direction, the flow is statistically invariant due to the periodic distribution of cylinders (Frisch, 1995, p.73). Since the turbulence of such kind of flow is governed by the inter-stem distance, it reveals a strong tendency to isotropy, as presented by Ricardo *et al.* (2011). Assuming that the collected data present enough resolution to include increments within the inertial range of scales, and assuming local isotropy in the studied flow, (7.7) will be employed to estimate the mean dissipation rate of the flow within arrays of different m. Nevertheless, an evaluation of the suitability of the local isotropy approach is presented by means of the correlation-coefficient spectrum, C_{LN}, which is defined by

$$C_{LN}(k) \equiv \frac{|E_{LN}(k)|}{[E_N(k)E_L(k)]^{1/2}} \tag{7.12}$$

where $E_{LN}(k)$ is the shear-stress cospectrum and $E_L(k)$ and $E_N(k)$ are the longitudinal and transverse one-dimensional spectra, respectively. For local isotropy, $C_{LN}(k)$ should fall to zero at high wavenumbers (Saddoughi & Veeravalli, 1994). Log-linear plots of correlation-coefficient spectra, C_{LN} are shown in figure 7.10, for two patches, P5 and P7. For other patches similar behaviour is found. After the greatest peak at macro scale wavenumber, C_{LN} starts decreasing towards zero. In the inertial range of scales $C_{LN} < 0.05$, revealing that the local isotropy condition is satisfied.

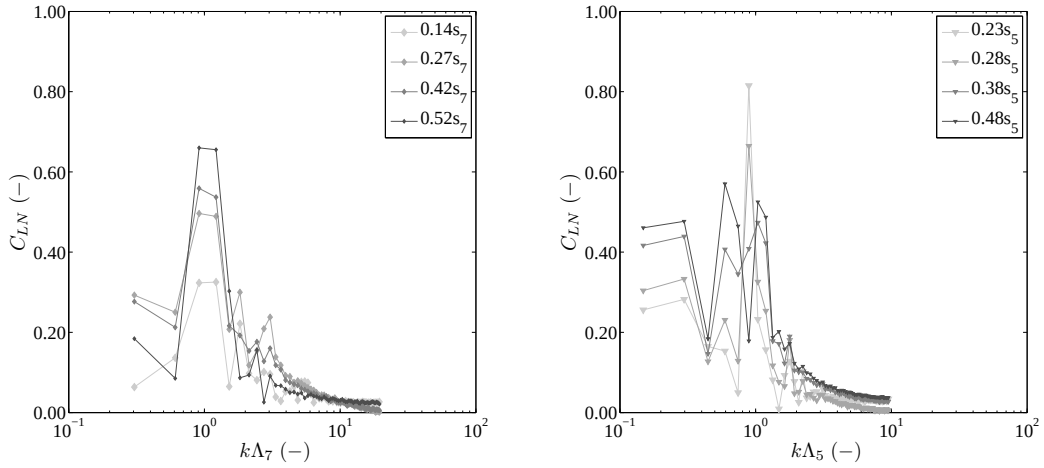

(a) (b)

Figure 7.10: Correlation-coefficient spectra a lateral position at height $z^{(a)}$ for a) P7 and b) P5.

7.4 Dissipation rate

To attempt an estimation of the dissipation rate of turbulent kinetic energy, the methodology described above was followed. The dissipation rate was estimated by identifying the first plateau of the compensated version of (7.7):

$$\langle \overline{\varepsilon} \rangle = -\frac{5}{4r}\left(\langle S_3 \rangle (r) - 6\nu \frac{\partial \langle S_{2L} \rangle (r)}{\partial r} \right) \tag{7.13}$$

Once the second order structure functions may be affected by uncorrelated noise and the noise level is specially important for small increments, the second term on the right hand side of the previous equation may introduce errors on the estimate of the energy dissipation rate. On other hand, it is a non sense to neglect this term when it can be computed from the experimental data avoiding additional simplifications on (7.7). For that reason, we adopt a compromised solution identifying with spectral analysis the range of scales where the noise is significant, and therefore neglecting the term of the second order structure function derivative only for those scales. Typically, the noise gets important for scales smaller than 5 mm, which correspond to scales within the linear reach of the third order structure function. Another remark on the estimate of the dissipation rate concerns the definition of the plateau, which is considered valid only when it is defined by 3 or more points.

A careful analysis of the results led to the conclusion that the $\langle \overline{\varepsilon} \rangle$ is very sensitive to local conditions, i.e., the local arrangement of the cylinders impacts strongly the behaviour of the dissipation rate. Figure 7.11 illustrates the variation of $\langle \overline{\varepsilon} \rangle$ with x for four of the studied datasets,

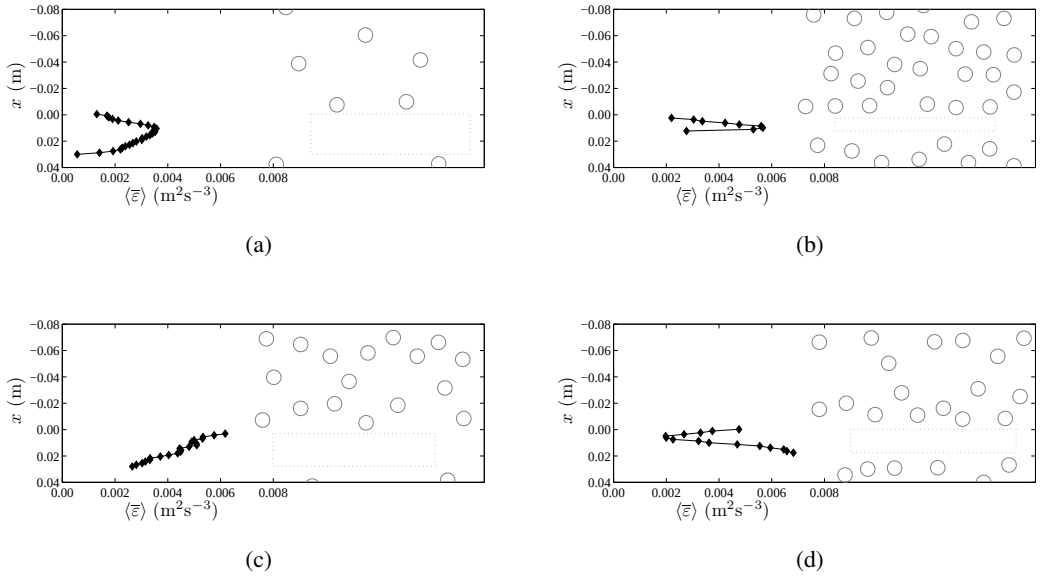

Figure 7.11: Dissipation rate of kinetic energy along streamwise direction for several datasets: a) P3 for $y = 0.29 - 0.41$ cm at $z^{(b)}$, b) P5 for $y = 0.10 - 0.22$ cm at $z^{(b)}$, c) P6 for $y = 0.0.09 - 0.21$ cm at $z^{(a)}$ and d) P8 for $y = 0.23 - 0.35$ cm at $z^{(a)}$. The dashed rectangles indicate the measurement reach while the circles represent the cylinders. It should be noticed that plan views represented in these graphs preserve the geometrical scale indicated by the x-axis.

representing also the corresponding local distribution of the cylinders. In most of the cases, $\langle\overline{\varepsilon}\rangle$ progresses downstream as in the cases a) and b)of figure 7.11, increasing towards a maximum value and then decreasing. Such behaviour is due to the gap without cylinders where the velocity measurements were carried on.The production of each cylinder is not felt immediately downstream of it but rather slightly further downstream, however that distance may not be determined easily. So, the initial increasing of $\langle\overline{\varepsilon}\rangle$ reflects the input of the upstream cylinders, then the flow finds a region without any obstacles where its dissipative potential decreases until the flow enters again in an area with cylinders. The pattern of decreasing $\langle\overline{\varepsilon}\rangle$ presented in figure 7.11 c) was found only for P6 in two of the lateral positions at both heights. For this case, the relatively low amount of cylinders within the close neighbourhood of the measuring gap explains that $\langle\overline{\varepsilon}\rangle$ is already within its decreasing reach. Furthermore, the impact of the closest cylinders can be identified on the two local maxima found on the graph of $\langle\overline{\varepsilon}\rangle$ against x corresponding to this dataset. The last case herein presented corresponds to a first decreasing reach of $\langle\overline{\varepsilon}\rangle$ followed by an increasing one, which may be more difficult to explain. However, the example of figure 7.11 d) shows that the particularly dense array of cylinders on the upstream limit of the measuring gap following a sparser region should indicate that first five points of the graph are not impacted by the "last row" of cylinders yet, while the remaining points show an increase of $\langle\overline{\varepsilon}\rangle$ due to the presence of those closest cylinders.

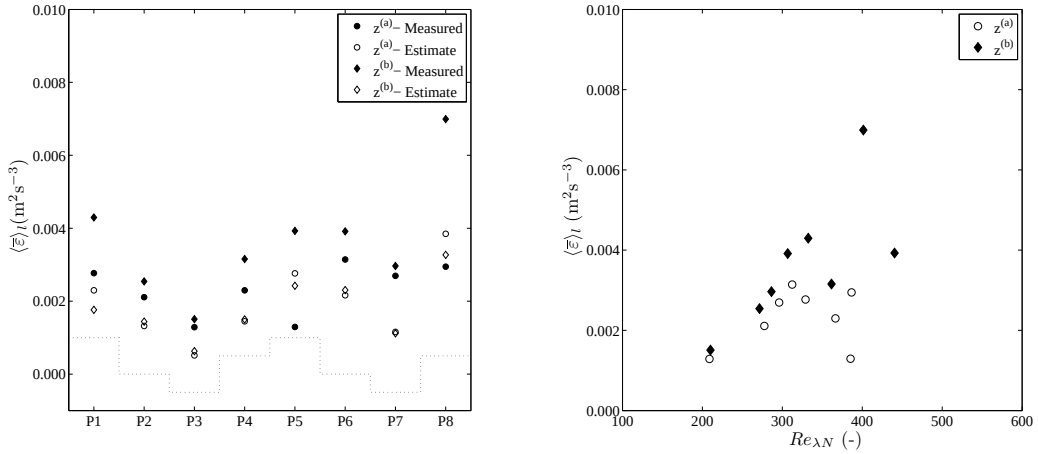

(a) (b)

Figure 7.12: a) Measured and estimated mean dissipation rate, $\langle\overline{\varepsilon}\rangle_l$, for each longitudinal position. The dashed line at the bottom stand for relative stem density; b) Mean dissipation rate, $\langle\overline{\varepsilon}\rangle_l$, against the Taylor's micro scale based Reynolds number, $Re_{\lambda N}$.

Equation (7.13) was applied for each cross section of all available datasets, as presented in figure 7.11, then an average of the dissipation rate for each dataset was considered, $\langle\overline{\varepsilon}\rangle_x$ as well as an average of the dissipation rate of all the lateral positions for the same patch and the same height, $\langle\overline{\varepsilon}\rangle_l$. Figure 7.12a) shows that dissipation rate has a strong correlation with the stem areal number-density, since the former increases when the later increases. There is an increase of the dissipation rate from the first to the second wavelength of the array modulation, i.e. from P1-P4 to P5-P8, due to the pressure gradient. This figure also presents estimates $\langle\overline{\varepsilon}\rangle_l$ based in a characteristic scales of velocity, u_c and length, L, $\varepsilon \approx u_c^3/L$, as is commonly used in literature, assuming that production is equal to dissipation. Herein, the estimative was computed by $\langle\overline{\varepsilon}\rangle \approx \overline{\langle\tilde{v}^2\rangle}^{(3/2)}/\Lambda$ (empty symbols in figure 7.12a) and one can observe that it leads to values of dissipation rate close to the measured ones. We also computed an estimative based in the streamwise velocity component, $\langle\overline{\varepsilon}\rangle \approx \overline{\langle\tilde{u}^2\rangle}^{(3/2)}/\Lambda$. However, this estimate leads to values one order of magnitude higher than the measured ones. This difference is due to the anisotropy of the flow at the macro scale. Hence, it should be highlighted that the application of this simple estimative requires some caution since it can lead to values with different orders of magnitude depending in the characteristic velocity chosen.

Given the importance of the Reynolds number based on Taylor's micro scale, figure 7.12b) represents mean dissipation rate of energy against this dimensionless parameter. The dissipation rate increases with increasing Reynolds number, being this behaviour clearer at height $z^{(b)}$ than at $z^{(a)}$. This may indicate that the proximity to the free surface has an impact on the energy budget of the flow.

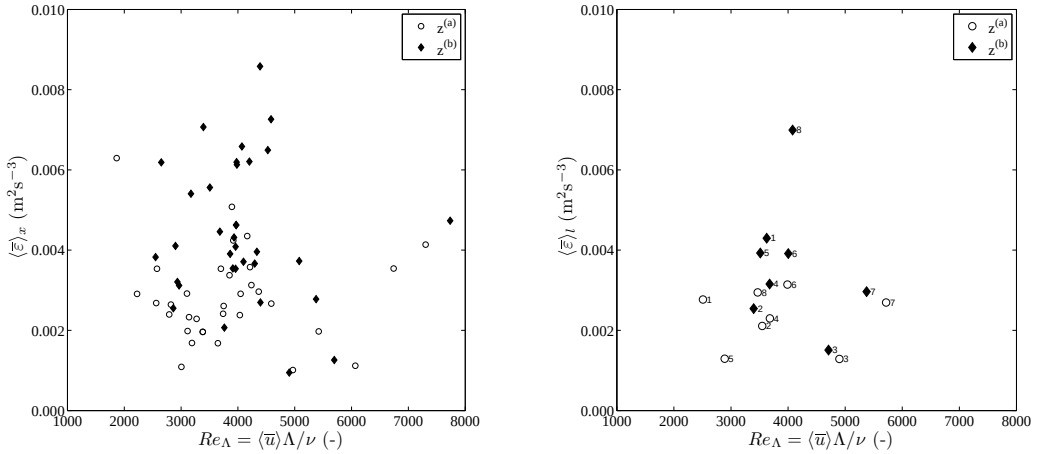

(a) (b)

Figure 7.13: a) Mean dissipation rate $\langle\overline{\varepsilon}\rangle_x$ against the macro scale based Reynolds number, Re_Λ, for each lateral position. b) Mean dissipation rate $\langle\overline{\varepsilon}\rangle_l$ against the macro scale based Reynolds number, Re_Λ, average of all lateral position for each longitudinal and vertical positions. The numbers indicate the corresponding longitudinal position.

Figure 7.13 presents the mean dissipation rate $\langle\overline{\varepsilon}\rangle_x$ and $\langle\overline{\varepsilon}\rangle_l$ as function of the Reynolds number based in the macro-scale of the flow, $Re_\Lambda = \langle\bar{u}_h\rangle\Lambda/\nu$. The dispersion of the points presented in those graphs lead us to the conclusion that the correlation between these variables is weak and depends of the height of the measured plane. For $z^{(a)}$ the dissipation rate does not change much for a large range of Reynolds number while closer to the free surface similar values of Reynolds number present large differences on the value of $\langle\overline{\varepsilon}\rangle$.

7.5 Conclusion

The present work carried out, for a turbulent flow within an array of emergent and rigid cylinders with varying areal number-density, a flow characterization in spatial domain with a pertinent and innovative approach. A spatial analysis of this kind of flows is particularly interesting since it avoids the approximation of the frozen turbulence theory. The innovative approach consisted in the application of the common tools for turbulent analysis with spatial velocity series in the spanwise direction instead of considering it along the direction of advection. The focus of the present study is the region, of the flow depth, where the flow is controlled by the vertical elements, so the effect of the bottom roughness and the free surface were not discussed herein.

The qualitative time-averaged flow analysis revealed that the inter-stem space is characterized by alternating zones of low velocity in wake regions and high velocity zones between stems

and by quasi symmetric high vorticity patterns around the stem, independently of the stem areal number-density. However, the inter-stem distance plays a very important role on the turbulent field, since that scale controls the density and the spatial organization of those vortices. Also, transverse autocorrelation functions corroborate the importance of this length scale presenting oscillations with wavelengths close to that scale and amplitudes of ≈ 0.2. Hence, flows within arrays of rigid cylinders are inter-stem flows. Autocorrelation functions were applied to define the macro-scale, Λ, a characteristic length scale which was defined as the increment r corresponding to the first local maximum of $\langle R_N \rangle$, after the origin. Second and third order structure functions were presented. A linear relation was found, for the smallest scales, between the increment r and the structure function, $\langle S_3 \rangle$, evidencing that the measurement resolution was small enough to measure within the inertial range of scales.

The main goal of this work was the computation and discussion of the mean dissipation rate of TKE. Within the framework of the Double-Averaging Methodology, and following a similar procedure to the one applied by Monin & Yaglom (1975) to obtain the Kolmogorov equation, we showed that the formalism that leads to the relation between second and third-order structure functions in HIT is applicable to non-homogeneous turbulence rendering similar results (see equation 7.7); this represents the main contribution of our work. Despite to the great heterogeneity at the large scales of the studied flow, the present work proved that the results of the isotropic turbulence theory may be applied to study the small scales. Obviously some caution is needed. It should be remarked that we are not claiming the validity of the local isotropy for each instantaneous velocity series but instead we confirm that averages of sufficient long time series of the structures functions and energy spectra lead to the conclusions of the well known isotropic turbulence theory. We have shown that an average of 5000 spatial spectra, at the same cross section, presents a clear $-5/3$ slope reach, while $\langle S_3 \rangle$ presents a linear reach and $\langle S_2 \rangle$ a reach of $2/3$ slope. Furthermore, correlation-coefficient spectra, C_{LN}, decrease towards zero for small scales, reinforcing the validity of the local isotropy condition. Equation (7.13) was employed to compute the rate of dissipation of TKE, $\langle \overline{\varepsilon} \rangle$. We conclude that behaviour of $\langle \overline{\varepsilon} \rangle$ is very sensitive to the local arrangement of the cylinders. For most of the datasets studied herein , $\langle \overline{\varepsilon} \rangle$ increases on the first cross-sections, reflecting the production input of upstream obstacles and when the closest cylinders are far enough, it decreases towards downstream due to the gap without cylinders where the measurements where carried on. Several exceptions to this comportment of the dissipation rate were found and explained by the local arrangement of the random array of cylinders. Concerning the patterns of a global average, $\langle \overline{\varepsilon} \rangle_l$ exhibits a spatial variation close to that of the cylinder areal number-density, m. In both wavelength of the array modulation, the rate of energy dissipation increased with m. We also conclude that $\langle \overline{\varepsilon} \rangle_l$ increases with the Reynolds number based on Taylor's micro scale. However, no strong correlation was found between the dissipation rate and Reynolds number based on the macro scale, Re_Λ.

The present work, based in detailed 2D PIV measurements and in a non-conventional approach, allowed some advances in the complex task of understanding the dissipation rate of TKE of a flow in a presence of random array of cylinders.

Chapter 8

Conclusions

8.1 Summary

The present research study, based on experimental measurements of instantaneous velocities, aimed at a detailed description of a turbulent flow within arrays of emergent stems with constant and varying density. This study brings innovation in what concerns the detailed spatial description of the budget of turbulent kinetic energy and the terms of the double-averaged momentum conservation equation. Innovative experimental procedures are also introduced, particularly in what concerns data treatment for which the use of spatial measurements avoids the use of the frozen turbulence approximation. This work introduces a new techniques to deal with the non-homogeneity of flows within vegetation. The phenomenological length scales with most interest to this work were the inter-stem and patch scales. Furthermore, the focus was on the region of the flow depth where the flow is controlled by the vertical stem. Bottom roughness and free surface effects were not discussed.

Two measuring techniques were employed for obtaining the empirical data: 3D Laser Doppler Anemometry (LDA) and 2D Particle Image Velocimetry (PIV). LDA technique allows acquisition of three components of instantaneous velocities at high temporal data-rates in one point of the flow. Being a point-wise technique, a thorough spatial characterization of the velocity flow field with LDA is extremely time consuming. On the other hand, a two-component PIV allows, in general, good spatial resolution and in a less expensive fashion than LDA, in terms of laboratory time, to obtain spatial variability. If the spatial resolution is good enough, PIV databases allow turbulence analysis without the application of the frozen turbulence approximation. These two techniques were thus combined to allow complementary results within a feasible time.

8.2 Main results

The main conclusions of the core chapters of this thesis are summarized hereafter.

Chapter 4

The characterization of the flow based on vertical profiles of velocity and stresses computed with the Double-Averaging Methodology revealed that:

- there is a strong correlation between stem areal number-density and the magnitude of flow variables;
- mean longitudinal velocity vertical distribution have a pronounced bulge close to the bottom, decreasing then like in a typical boundary-layer flow towards the bottom;
- mean longitudinal velocity profiles are characterized by a uniform distribution in the region where the flow is controlled by the vertical stems;
- dispersive and turbulent stresses have the same order of magnitude, and therefore, the former should not be neglected by on basic conservation equations describing these flows.

The calculation of the drag force acting on the stems followed the conceptual framework provided by the Double-Averaging Methodology. The drag force per plane unit area was calculated from the depth-averaged longitudinal component of the DANS equations, with no major simplifications, showing that the term corresponding to the pressure gradient is dominant. However, balancing the drag force only with this term, as it is common in literature, may lead to important non-systematic errors. In fact, the relative importance of the dominant term is affected by the gradients in the areal number-density of stems, and the importance of the flow depth gradient, $\frac{\partial h}{\partial x}$, becomes reduced for high values of the drag force.

A dimensional analysis identified, among the variables assessed in this study, stem Reynolds number, Re_p, ration between inter-stem distance and stem diameter, $\frac{s}{d}$, longitudinal gradient of the inter-stem distance, $\frac{\partial s}{\partial x}$, ration between flow depth and stem diameter, $\frac{h}{d}$, and longitudinal flow depth gradient, $\frac{\partial h}{\partial x}$ as the characteristic parameters that control the drag force. The correlation of those parameters with drag coefficient, C_D, showed that the dependence of the drag coefficient is complex and may result from a non linear combination of more than one parameter. The main achieved conclusions include:

- the drag force per submerged stem length seems uncorrelated with the stem areal number-density, m, and with the stem Reynolds number, Re_p, for the range of Re_p and m investigated;
- the drag force depends on the longitudinal variation of the stem areal number-density. It was observed that the decrease of the number of stems per unit area, m, is associated to larger flow resistance while the flow resistance is lower with the longitudinal increase of m;
- the drag coefficient increases with the relative roughness defined as h/d, revealing an influence of the bed on the definition of the flow structure;

At patch the scale, it was observed that the longitudinal increase of stem areal number-density is associated to smaller magnitudes of the drag force per unit of submerged stem length. However, at the representative scale of the longitudinal variation of the stem areal number-density, m, if the variability of m is cyclic, there might be no appreciable effect of patchiness on the average drag force since the opposite local influences of $\frac{\partial m}{\partial x} > 0$ and $\frac{\partial m}{\partial x} < 0$ cancel out in overall.

Chapter 5

An integrated view of the turbulent energy dynamics of flows through an array of emergent cylinders was described based in the spatial characterization of the terms of the TKE budget equation. The spatial distribution of the convective rate of change, the rate of turbulent production, the turbulent diffusion and the dissipation rate of TKE were presented. Assuming that the mean flow Reynolds number is sufficiently high, the viscous term could be neglected and the pressure diffusion term was back-calculated from the TKE conservation equation. The following conclusions are drawn in accordance to the analysis of the TKE budget terms:

- The production of TKE is mostly associated to vortex shedding from individual stems; the magnitude is higher in the wake region, reaching a maximum about one stem diameter downstream of the shedding stem, decreasing towards zero, when the inter-stem distance is large enough.
- As the rate of production, TKE quantity has a peak of magnitude at the limit of the near field of the stem wake, but the spatial distribution of TKE is smoother.
- Negative production of TKE is observed between close stems, associated to strong accelerations combined with high turbulent intensities that the flow field is here subjected to. The data analysis confirmed that this conversion of turbulent kinetic energy into mean kinetic energy is not fed by any turbulent diffusive mechanism.
- The rates of production and of dissipation are not in equilibrium at the inter-stem space, revealing important interactions of turbulence with mean flow, turbulent transport of TKE and pressure diffusion.
- The turbulent diffusion of TKE presents important values, both positive and negative, within the von Kármán vortex streets.
- The turbulent fluxes of TKE revealed strong turbulent transport laterally, slightly upstream of the locus of peak production and in the inner part of the stems wake, resulting in a quasi-circular pattern of turbulent transport of TKE.
- There is evidence that turbulent diffusion may be a Fickian process since the flux of TKE is, generally, directed from the regions with higher values of TKE to the regions with lower values.
- The highest values of the magnitude of the convective term are located in the vicinity of the array of stems.
- The convective rate of change of TKE is expected to balance the pressure diffusion term;

- The rate of dissipation was found to increase with the density of stems and to present smaller spatial variation when compared to the other terms of the TKE budget equation. However, the magnitude of the rate of dissipation tends to be higher in the wake of the stems than in the regions between adjacent stems.

A conspicuous spatial variability was found evidencing the importance of vortex shedding and unsteady separation of the flow on the cylinders. In this study a random distribution of the array of stems highlighted the impact of the local arrangements of the stems on the budget of TKE.

Chapter 6 and 7

A spatial analysis of turbulence in these flows is particularly relevant since it avoids applying the approximation of the frozen turbulence theory. An innovative approach is herein presented, consisting in the application of the common tools for turbulent analysis to the instantaneous spatial velocity series in the spanwise direction of the flow,instead of considering it along the direction of main advection. Inspired on the framework of the Double-Averaging Methodology, and following a similar procedure to the one applied by Monin & Yaglom (1975) to obtain Kolmogorov's equation, it is shown that the formalism that leads to the relation between second and third-order structure functions in HIT is applicable to non-homogeneous turbulence, rendering similar results. An equation similar to Kolmogorov's equation, relating the space-averaged second- and third-order structure functions and the mean dissipation rate of energy, is proposed. This equation was applied to compute the mean dissipation rate of energy for patches with different stem areal number-density.

Despite the great heterogeneity at the larger scales of the studied flow, the present work proved that an average of 5000 spatial spectra obtained instantaneously at the same cross section, presents a clear $-5/3$ slope reach, while third-order structure functions present a linear reach and second-order structure functions a reach of $2/3$ slope, as expected when performing the equivalent analysis using Kolmogorov's equations for time series. Therefore, it is clear that long time series of the structures functions and energy spectra show, at small-scales, the expected results of the isotropic turbulence theory. Furthermore, correlation-coefficient spectra decrease towards zero for small scales, reinforcing the validity of the local isotropy condition.

Concerning the dissipation rate of turbulent kinetic energy, it was seen that

- in most cases, it increases in the downstream near-field of stems, reflecting the strong production input of stems in the upstream limit of the measuring gap and then it decreases towards downstream, as the distance to upstream stems increases, in a way similar to the decay observed in grid turbulence. However, exceptions to this behaviour were found and explained by the local arrangement of the random array of cylinders;
- the dissipation rate of TKE it is very sensitive to the local arrangement of the cylinders;
- the dissipation rate increases with the cylinder areal number-density;
- the dissipation rate of TKE increases with the Reynolds number based on Taylor's micro

scale although the relation is not exactly quadratic;
- there is not a correlation between the dissipation rate and Reynolds number based on the macro scale.

Summing up the achievements of the present work, advances on the understanding of the complex flow within random arrays of rigid and emergent stems, at the inter-stem scale, were reached in three relevant topics: flow resistance, budget of TKE and computation of dissipation rate of TKE.

8.3 Recommendations for future work

The characterization of flows within wetlands is a relevant topic for river engineering and simultaneously a challenging fluid mechanics problem. Although a considerable amount of research has been carried out, the open questions are still numerous and the practical applications, sought by river engineers, are not appropriately answered yet. In that sense, many recommendations for future work could be envisaged. Herein, special attention is given to the natural extension of the present work.

A large experimental database was created with this PhD research project, which is yet far from completely explored. Therefore, the most natural recommendation for future work is a further exploitation of that database, namely,

- applying proper orthogonal decomposition (POD) to quantify the relevant scales of this type of flows;
- determining the velocity of propagation of the vortexes shed by the cylinders based on the instantaneous vorticity maps;
- computing the dissipation tensor and the rate of dissipation of TKE in accordance to different theories for non-homogenous turbulence;
- analysing the equation of conservation of the Reynolds stress tensor;
- determining the appropriate constants for spectral density functions and second order structure functions.

Regarding the flow resistance associated to the vegetation stems, the present study revealed that experimental tests covering simultaneously a large range of Reynolds numbers and a large range of stem areal number-density, are still missing.

Also, in the characterization of the terms of the TKE conservation equation, the impact of the Reynolds number could not be discussed in the present work. The key role of this parameter on the study of turbulent flows is acknowledged and justify additional experimental tests.

Closure models for form-induced stresses and for the production terms in conservation

equation associated to these stresses, are not available for flows with vegetated boundaries yet. Determining these closures is a rather difficult task due to the complexity that these flows present. That is, definitely, a demanding research challenge and represents a decisive step in the path towards physically based design criteria for vegetated channels.

References

ABERLE, J. (2006). Spatially averaged near-bed flow over rough armor layers. In: *River Flow 2006* (R.M.L. FERREIRA, E. A., J.G.B. LEAL & CARDOSO, A., eds.), vol. 1. Taylor and Francis, London.

ABERLE, J. & JÄRVELÄ, J. (2013). Flow resistance of emergent rigid and flexible floodplain vegetation. *Journal of Hydraulic Research* **51**(1), 33–45.

ADRIAN, R. J. (1984). Scattering particle characteristics and their effect on pulsed laser measurements of fluid flow: speckle velocimetry vs particle image velocimetry. *Appl. Opt.* **23**(11), 1690–1691.

ADRIAN, R. J. (1991). Particle-imaging techniques for experimental fluid mechanics. *Annual review of fluid mechanics* **23**(1), 261–304.

ADRIAN, R. J. (2005). Twenty years of particle image velocimetry. *Experiments in Fluids* **39**(2), 159–169.

ANTONIA, R. & BURATTINI, P. (2006). Approach to the 4/5 law in homogeneous isotropic turbulence. *Journal of Fluid Mechanics* **550**(1), 175–184.

CAMPBELL, L. J. (2005). *Double-Averaged open-channel flow over regular rough beds*. Ph.D. thesis, University of Aberdeen, Aberdeen.

CHASSAING, P. (2000). *Turbulence en Mécanique des Fluides*. Cépaduès Éditions.

CHENG, N. (2013). Calculation of drag coefficient for arrays of emergent circular cylinders with pseudofluid model. *Journal of Hydraulic Engineering* **139**(6), 602–611.

COCEAL, O., DOBRE, A., THOMAS, T. G. & BELCHER, S. E. (2007). Structure of turbulent flow over regular arrays of cubical roughness. *Journal of Fluid Mechanics* **589**, 375–409.

CUMMINS, H. Z., KNABLE, N. & YEH, Y. (1964). Observation of diffusion broadening of rayleigh scattered light. *Phys. Rev. Lett.* **12**, 150–153.

CURRIE, I. G. (1993). *Fundamental Mechanics of Fluids*. Toronto: McGraw Hill.

DANAILA, L., ANSELMET, F. & ANTONIA, R. A. (2002). An overview of the effect of large-scale inhomogeneities on small-scale turbulence. *Physics of Fluids* **14**(7), 2475–2484.

DAVIDSON, P. A. (2004). *Turbulence: An Introduction for Scientists and Engineers: An Introduction for Scientists and Engineers*. Oxford University Press.

DEFINA, A. & BIXIO, A. C. (2005). Mean flow and turbulence in vegetated open channel flow. *Water Resources Reseach* **41**(7), W07006.

DEFINA, A. & PERUZZO, P. (2012). Diffusion of floating particles in flow through emergent vegetation: Further experimental investigation. *Water Resources Research* **48**(3), W03501.

DITTRICH, A., ABERLE, J., SCHONEBOOM, T., RODI, W. & UHLMANN, M. (2012). Drag forces and flow resistance of flexible riparian vegetation. In: *Environmental fluid mechanics: Memorial colloquium on environmental fluid mechanics in honour of Professor Gerhard H. Jirka*. CRC Press London.

DURST, F., MELLING, A. & WHITELAW, J. (1976). *Principles and practice of laser-Doppler anemometry*. Academic Press.

FATHI-MAGHADAM, M. & KOUWEN, N. (1997). Nonrigid, nonsubmerged, vegetative roughness on floodplains. *Journal of Hydraulic Engineering* **123**(1), 51–57.

FERREIRA, R. L., FERREIRA, L. M., RICARDO, A. M. & FRANCA, M. J. (2010). Impacts of sand transport on flow variables and dissolved oxygen in gravel-bed streams suitable salmonid spawning. *River Research and Applications* **26**(10), 414–438.

FERREIRA, R. M. (2011). Turbulent flow hydrodynamics and sediment transport: Laboratory research with LDA and PIV. In: *Experimental Methods in Hydraulic Research*. Springer, pp. 67–111.

FERREIRA, R. M., FRANCA, M. J., LEAL, J. & CARDOSO, A. H. (2009a). Mathematical modelling of shallow flows: Closure models drawn from grain-scale mechanics of sediment transport and flow hydrodynamics. *Canadian J. of Civ. Eng.* **36**, 1604–1621.

FERREIRA, R. M. L., FRANCA, M. J. & LEAL, J. G. A. B. (2008). Flow resistance in open-channel flows with mobile hydraulically rough beds. In: *River Flow 2008 - Vol. 1*.

FERREIRA, R. M. L., RICARDO, A. M. & FRANCA, M. J. (2009b). Discussion of " Laboratory investigation of mean drag in a ramdom array of rigid, emergent cylinders" by Heydi M. Nepf and Yukie Tanino, Journal of Hydraulic Engineering, vol. 134, no 1, 2008. *Journal of Hydraulic Engineering* **135**(8), 690–693.

FINNIGAN, J. (2000). Turbulence in plant canopies. *Annu. Rev. Fluid Mech.* **32**, 519–571.

FINNIGAN, J. J. & SHAW, R. H. (2008). Double-averaging methodology and its application to turbulent flow in and above vegetation canopies. *Acta Geophysica* **56**(3), 534–561.

FRANCA, M. J. & CZERNUSZENKO, W. (2006). Equivalent velocity profile for turbulent flows over gravel riverbeds. In: *River Flow 2006* (R. M. L. FERREIRA, J. G. A. B. L., E. C. L. ALVES & CARDOSO, A. H., eds.). Taylor and Francis.

FRANCA, M. J., FERREIRA, R. M. L. & LEMMIN, U. (2008). Parametrization of the logarithmic layer of double-averaged streamwise velocity profiles in gravel-bed river flows. *Advances in Water Resources* **31**, 915–925.

FRISCH, U. (1995). *Turbulence. The legacy of A. N. Kolmogorov.* Cambridge, UK: Cambridge University Press.

GHISALBERTI, M. & NEPF, H. M. (2004). The limited growth of vegetated shear layers. *Water Resources Reseach* **40**(W07502), W07502.

GIMENEZ-CURTO, L. A. & CORNIERO LERA, M. A. (1996). Oscillating turbulent flow over very rough surfaces. *J. Geophys. Res.* **101**(C9), 20745 – 20758.

GORING, D. & NIKORA, V. I. (2002). Despiking acoustic doppler velocimeter data. *J. Hydraul. Eng* **128**(1), 117–126.

GRAY, W. G. & LEE, P. C. Y. (1977). On the theorems for local volume averaging of multiphase systems. *International Journal of Multiphase Flow* **3**, 333–340.

HINZE, J. O. (1975). *Turbulence*. McGraw Hill, 2nd ed.

HJEMFELT, A. T. & MOCKROS, L. F. (1996). Motion of discrete particles in a turbulent fluid. *Applied Science Research* **16**, 149–161.

HSIEH, C.-I. & KATUL, G. G. (1997). Dissipation methods, Taylor's hypothesis, and stability correction functions in the atmospheric surface layer. *Journal of Geophysical Research* **102**(D14), 16391–16405.

HUTHOFF, F. (2012). Theory for flow resistance caused by submerged roughness elements. *Journal of Hydraulic Research* **50**(1), 10–17.

ISHIKAWA, Y., MIZUHARA, K. & ASHIDA, S. (2000). Effect of density of trees on drag exerted on trees in river channels. *Journal of Forest Research* **5**(4), 271–279.

JAMES, C. S., GOLDBECK, U. K., PATINI, A. & JORDANOVA, A. A. (2008). Influence of foliage on flow resistance of emergent vegetation. *Journal of Hydraulic Research* **46**(4), 536–542.

JÄRVELÄ, J. (2002). Flow resistance of flexible and stiff vegetation: a flume study with naural plants. *Journal of Hydrology* **269**, 44–54.

JUANG, J.-Y., KATUL, G. G., SIQUEIRA, M. B., STOY, P. C. & MCCARTHY, H. R. (2008). Investigating a hierarchy of Eulerian closure models for scalar transfer inside forested canopies. *Boundary-layer meteorology* **128**(1), 1–32.

KADLEC, R. H. (1990). Overland flow in wetlands: Vegetation resistance. *Journal of Hydraulic Engineering* **116**(5), 691–705.

KEANE, R. D. & ADRIAN, R. J. (1990). Optimization of particle image velocimeters. i. double pulsed systems. *Measurement Science and Technology* **1**(11), 1202.

KIM, S. J. & STOESSER, T. (2011). Closure modeling and direct simulation of vegetation drag in flow through emergent vegetation. *Water Resources Research* **47**(10), W10511.

KOCH, F. L. & LADD, A. J. C. (1997). Moderate reynolds number flows through periodic and random arrays of aligned cylinders. *Journal of Fluid Mechanics* **349**, 31–66.

KOLMOGOROV, A. (1941a). Dissipation of energy in the locally isotropic turbulence. *Dokl. Akad. Nauk SSSR* **32**, 16–18. English translation in, Proc. R. Soc. London, Ser. A 434, 15-17 (1991).

KOLMOGOROV, A. (1941b). The local structure of turbulence in incompressible viscous fluid for very large Reynolds numbers. In: *Dokl. Akad. Nauk SSSR*, vol. 30.

LAUTERBORN, W. & VOGEL, A. (1984). Modern optical techniques in fluid mechanics. *Annual Review of Fluid Mechanics* **16**(1), 223–244.

LAVOIE, P., AVALLONE, G., DE GREGORIO, F., ROMANO, G. & ANTONIA, R. (2007). Spatial resolution of piv for the measurement of turbulence. *Experiments in Fluids* **43**, 39–51.

LEE, J. K., ROIG, L. C., JENTER, H. L. & VISSER, H. M. (2004). Drag coefficients for modeling flow through emergent vegetation in the Florida Everglades. *Ecological Engineering* **22**, 237–248.

LEONARD, A. (1974). Energy cascade in large-eddy simulations of turbulent fluid flows. *Advances in Geophysics* **18A**, 237–248.

LI, R.-M. & SHEN, H. W. (1973). Effect of tall vegetations on flow and sediment. *Journal of the Hydraulics Division* **99**(HY5), 793–814.

LIGHTBODY, A. F. & NEPF, H. M. (2006). Prediction of velocity profiles and longitudinal dispersion in emergent salt marsh vegetation. *Limnol. Oceanogr.* **51**(1), 218–228.

LIKHACHEV, E. (2003). Dependence of water viscosity on temperature and pressure. *Technical Physics* **48**(4), 514–515.

LÓPEZ, F. & GARCÍA, M. (1998). Open-channel flow through simulated vegetation: Suspended sediment transport modeling. *Water Resources Research* **34**(9), 2341–2352.

LÓPEZ, F. & GARCÍA, M. (2001). Mean flow and turbulence structure of open-channel flow through emergent vegetation. *J. Hydraul. Eng.* **127**(5), 392–402.

LOURENCO, L. & KROTHAPALLI, A. (1995). On the accuracy of velocity and vorticity measurements with PIV. *Experiments in Fluids* **18**(6), 421–428.

MAHESHWARI, B. L. (1992). Suitability of different flow equations and hydraulic resistance parameters for flows in surface irrigation: A review. *Water Resources Research* **28**(8), 2059–2066.

MANES, C., POKRAJAC, D. & MCEWAN, I. (2007). Double-averaged open-channel flows with small relative submergnce. *Journal of Hydraulic Engineering* **138**, 896–904.

MELLING, A. (1997). Tracer particles and seeding for particle image velocimetry. *Measurement Science and Technology* **8**, 1406–1416.

MIGNOT, E., BARTHÉLEMY, E. & HURTHER, D. (2008). Turbulent kinetic energy budget in a gravel-bed channel flow. *Acta Geophysica* **56**(3), 601–613.

MIGNOT, E., BARTHÉLEMY, E. & HURTHER, D. (2009a). Double-averaging analysis and local flow characterization of near-bed turbulence in gravel-bed channel flows. *Journal of Fluid Mechanics* **618**, 279–303.

MIGNOT, E., HURTER, D. & BARTHÉLEMY, E. (2009b). On the structure of shear stress and turbulent kinetic energy flux across the roughness layer of a gravel-bed channel flow. *Journal of Fluid Mechanics* **638**, 423–452.

MONIN, A. S. & YAGLOM, A. M. (1971). *Statistical Fluid Mechanics: Mechanics of Turbulence.*, vol. I. MIT Press.

MONIN, A. S. & YAGLOM, A. M. (1975). *Statistical Fluid Mechanics: Mechanics of Turbulence.*, vol. II. MIT Press.

MOSER, R. (1994). Kolmogorov inertial range spectra for inhomogeneous turbulence. *Physics of Fluids* **6**, 794.

NAZARENKO, S., KEVLAHAN, N. & DUBRULLE, B. (1999). WKB theory for rapid distortion of inhomogeneous turbulence. *Journal of Fluid Mechanics* **390**(1), 325–348.

NEPF, H. (1999). Drag, turbulence, and diffusion in flow through emergent vegetation. *Water Resources Research* **35**(2), 479–489.

NEPF, H. (2012a). Flow and transport in regions with aquatic vegetation. *Annual Review of Fluid Mechanics* **44**, 123–142.

NEPF, H. (2012b). Hydrodynamics of vegetated channels. *Journal of Hydraulic Research* **50**(3), 262–279.

NEPF, H. & GHISALBERTI, M. (2008). Flow and transport in channels with submerged vegetation. *Acta Geophysica* **56**, 753–777.

NEPF, H. M. & VIVONI, E. R. (1999). Turbulence structure in depth-limited, vegetated flow : transition between emergent and submerged regimes. In: *Conference Proceedings of the 28th International IARH Conference*. Graz, Autria.

NIKORA, V., BALLIO, F., COLEMAN, S. & POKRAJAC, D. (2013). Spatially averaged flows over mobile rough beds: Definitions, averaging theorems, and conservation equations. *Journal of Hydraulic Engineering* **139**(8), 803–811.

NIKORA, V., GORING, D., MCEWAN, I. & GRIFFITHS, G. (2001). Spatially averaged open-channel flow over rough bed. *Journal of Hydraulic Engineering* **127**(2), 123–133.

NIKORA, V., KOLL, K., MCEWAN, I., MCLEAN, S. & DITTRICH, A. (2004). Velocity distrubution in the roughness layer of rough-bed flows. *Journal of Hydraulic Engineering* **130**(10), 1036–1042.

NIKORA, V., LARNED, S., NIKORA, N., DEBNATH, K., COOPER, G. & REID, M. (2008). Hydraulic resistance due to aquatic vegetation in small streams: Field study. *Journal of Hydraulic Engineering* **134**(9), 1326–1332.

NIKORA, V., MCEWAN, I., MCLEAN, S., COLEMAN, S., POKRAJAC, D. & WALTERS, R. (2007a). Double-averaging concepts for rough-bed open-channel and overland flows: Theoretical background. *Journal of Hydraulic Engineering* **133**(8), 873–883.

NIKORA, V., MCLEAN, S., COLEMAN, S., POKRAJAC, D., MCEWAN, I., CAMPBELL, L., ABERLE, J., CLUNIE, D. & KOLL, K. (2007b). Double-averaging concepts for rough-bed open-channel and overland flows: Applications. *Journal of Hydraulic Engineering* **133**(8), 884–895.

NOGUEIRA, J., LECUONA, A. & RODRIGUEZ, P. (1997). Data validation, false vectors correction and derived magnitudes calculation on PIV data. *Measurement Science and Technology* **8**(12), 1493.

OBERLACK, M. (1997). Non-isotropic dissipation in non-homogeneous turbulence. *Journal of Fluid Mechanics* **350**, 351–374.

PATEL, V. C., NEZU, W. & SCHEUERER, G. (1985). Turbulence models for near-wall and low reynolds number flows: a review. *AIAA Journal* **23**, 1308–1319.

PEROT, B. & NATU, S. (2004). A model for the dissipation rate tensor in inhomogeneous and anisotropic turbulence. *Physics of fluids* **16**, 4053.

PETRYK, S. & BOSMAJIAN, G. (1975). Analysis of flow through vegetation. *Journal of the Hydraulics Division* **101**(HY7), 871–884.

PICKERING, C. J. & HALLIWELL, N. A. (1984). Laser speckle photography and particle image velocimetry: photographic film noise. *Applied Optics* **23**(17), 2961–2969.

POGGI, D., KATUL, G. & ALBERTSON, J. (2004a). Momentum tranfer and turbulent kinetic energy budgets within a dense model canopy. *Boundary Layer Meteorology* **111**, 589–614.

POGGI, D., KATUL, G. & ALBERTSON, J. (2004b). A note on the contribution of dispersive fluxes to momentum transfer within canopies. *Boundary Layer Meteorology* **111**, 615–621.

POGGI, D. & KATUL, G. G. (2008). Micro- and macro-disperdive fluxes in canopy flows. *Acta Geophysica* **56**(3), 778–800.

POKRAJAC, D., MCEWAN, I. & NIKORA, V. (2008). Spatially averaged turbulent stress and its partitioning. *Exp Fluids* **45**, 73–83.

POPE, S. B. (2000). *Turbulent Flows*. Cambridge University Press.

QIAN, J. (1999). Slow decay of the finite reynolds number effect of turbulence. *Phys. Rev. E* **60**, 3409–3412.

RAFFEL, M., WILLERT, C. E. & KOMPENHANS, J. (1998). *Particle Image Velocimetry: A Pratical Guide*. Springer.

RAFFEL, M., WILLERT, C. E., WERELEY, S. T. & KOMPENHANS, J. (2007). *Particle Image Velocimetry: A Practical Guide*. 2nd edition. Springer.

RAHMEYER, W., WERTH, D. & CLEERE, R. (1995). The study of resistance and stability of vegetation in flood channels. Lab report usu-376, Utah State University.

RAUPACH, M. & THOM, A. (1981). Turbulence in and above plant canopies. *Annual Review of Fluid Mechanics* **13**(1), 97–129.

RAUPACH, M. R., ANTONIA, R. & RAJAGOPALAN, S. (1991). Rough-wall turbulent boundary layers. *Applied Mechs. Rev.* **44**(1), 1–25.

RAUPACH, M. R., COPPIN, P. A. & LEGG, B. J. (1986). Experiments on scalar dispersion within a model plant canopy - Part I: Turbulence structure. *Boundary Layer Meteorology* **35**, 21–52.

RAUPACH, M. R. & SHAW, R. H. (1982). Averaging procedures for flow within vegetation canopies. *Boundary-Layer Meteorology* **22**, 79–90.

RICARDO, A. M., FRANCA, M., SCHLEISS, A. J. & FERREIRA, R. (2012). Interaction of different wavelengths in a turbulent flow within a random array of rigid and emergent stems. In: *2nd European Congress of the International Association for Hydraulic Research and Engineering (IAHR)*.

RICARDO, A. M., FRANCA, M. J. & FERREIRA, R. (2011). Anisotropic turbulent flow in flows within emergent rigid vegetation. In: *Geophysical Research Abstracts, Vol. 13*, EGU 2011-1294-1. Vienna: EGU General Assembly.

RICARDO, A. M., KOLL, K., FRANCA, M. J., SCHLEISS, A. J. & FERREIRA, R. M. L. (2013). The terms of the turbulent kinetic energy budget within reaches of emergent vegetation. *Water Resources Research* **(under revision)**.

RICARDO, A. M. C. (2008). *Caracterização do escoamento turbulento em canais com vegetação emersa rígida. Aplicação ao estudo da resistência hidráulica.* Master's thesis, Instituto Superior Técnico - Universidade Técnica de Lisboa, Lisboa. (in Portuguese).

RIGHETTI, M. & ARMANINI, A. (2002). Flow resistance in open channel flows with sparsely distrubuted bushes. *Journal of Hydrology* **269**, 55–64.

ROESGEN, T. (2003). Optimal subpixel interpolation in particle image velocimetry. *Experiments in Fluids* **35**(3), 252–256.

SADDOUGHI, S. G. & VEERAVALLI, S. V. (1994). Local isotropy in turbulent boundary layers at high Reynolds number. *Journal of Fluid Mechanics* **268**, 333–372.

SCHLICHTING, H. (1968). *Boundary - Layer Theory*. McGraw Hill, 6th ed.

SCHOELYNCK, J., DE GROOTE, T., BAL, K., VANDENBRUWAENE, W., MEIRE, P. & TEMMERMAN, S. (2012). Self-organised patchiness and scale-dependent bio-geomorphic feedbacks in aquatic river vegetation. *Ecography* **35**(8), 760–768.

SIMÃO, J. G., RICARDO, A. M. & FERREIRA, R. M. (2009). Análise de sensibilidade a medições PIV para a caracterização de escoamentos hidraulicamente rugosos com moderada submersão relativa. In: *3ª Conferencia Nacional em Mecânica de Fluidos, Termodinâmica e Energia*. (in Portuguese).

SINISCALCHI, F., NIKORA, V. & ABERLE, J. (2012). Plant patch hydrodynamics in streams: Mean flow, turbulence, and drag forces. *Water Resources Research* **48**(1), W01513.

SMITH, J. & MCLEAN, S. (1977). Spatially averaged flow over a wavy surface. *J. Geophys. Res.* **83**(12), 1735–1746.

SREENIVASAN, K., PRABHU, A. & NARASIMHA, R. (1983). Zero-crossings in turbulent signals. *Journal of Fluid Mechanics* **137**, 251–272.

STOESSER, T., KIM, S. & DIPLAS, P. (2010). Turbulent flow through idealized emergent vegetation. *Journal of Hydraulic Engineering* **136**(12), 1003–1017.

STONE, B. M. & SHEN, H. T. (2002). Hydraulic resistance of flow in channels with cylindrical roughness. *Journal of Hydraulic Engineering* **128**(5), 500–506.

SUKHODOLOVA, T. A. & SUKHODOLOV, A. N. (2012). Vegetated mixing layer around a finite-size patch of submerged plants: Part 1. Theory and field experiments. *Water Resources Research* **48**(10), W10533.

SUMNER, D. (2010). Two circular cylinders in cross-flow: A review. *Journal of Fluids and Structures* **26**(6), 849–899.

SUMNER, D., RICHARDS, M. & AKOSILE, O. (2005). Two staggered circular cylinders of equal diameter in cross-flow. *Journal of Fluids and Structures* **20**(2), 255 – 276. URL `http://www.sciencedirect.com/science/article/pii/S0889974604001331`.

SVEEN, J. K. & COWEN, E. A. (2004). Quantitative imaging techniques and their application to wavy flows. *Advances in Coastal and Ocean Engineering* **9**, 1.

TANINO, Y. & NEPF, H. M. (2008). Laboratory investigation of mean drag in a random array of rigid, emergent cylinders. *Journal of Hydraulic Engineering* **134**(1), 34–41.

TANINO, Y. & NEPF, H. M. (2009). Laboratory investigation of lateral dispersion within dense arrays of randomly distributed cylinders at transitional reynolds number. *Physics of Fluids* **21**(046603), 1–10.

TAYLOR, G. (1938). The spectrum of turbulence. *Proceedings of the Royal Society of London. Series A-Mathematical and Physical Sciences* **164**(919), 476.

TAYLOR, G. I. (1935). Statistical theory of turbulence. *Proceedings of the Royal Society of London. Series A, Mathematical and Physical Sciences* **151**(873), 421–444.

TCHOUFAG, J., SAGAUT, P. & CAMBON, C. (2012). Spectral approach to finite reynolds number effects on Kolmogorov's 4/5 law in isotropic turbulence. *Physics of Fluids* **24**(1), 015107.

TENNEKES, H. & LUMLEY, J. (1972). *A first course in turbulence*. The MIT press.

TINOCO, R. O. & COWEN, E. A. (2013). The direct and indirect measurement of boundary stress and drag on individual and complex arrays of elements. *Experiments in Fluids* **54**(4), 1–16.

TROPEA, C. (1995). Laser doppler anemometry: recent developments and future challenges. *Measurement Science and technology* **6**(6), 605.

TROPEA, C., YARIN, A. & FOSS, J. (2007). *Springer handbook of experimental fluid mechanics*. Springer Verlag.

VAN DE HULST, H. C. (1957). *Light scattering: by small particles*. Courier Dover Publications.

VOM STEIN, H. & PFEIFER, H. (1969). A doppler difference method for velocity measurements. *Metrologia* **5**(2), 59.

WERELEY, S. T. & MEINHART, C. D. (2000). Accuracy improvements in particle image velocimetry algorithms. In: *10th International Symposium on Applications of Laser Techniques to Fluid Mechanics*. Fundação Calouste Gulbenkian/Centro de Estudos em Inovação, Tecnologia e Políticas de Desenvolvimento (IST).

WESTERWEEL, J. (1993). *Digital particle image velocimetry: theory and application*. Ph.D. thesis, University of Delft, Delt, Netherlands.

WESTERWEEL, J. (1994). Efficient detection of spurious vectors in particle image velocimetry data. *Experiments in Fluids* **16**, 236–247.

WHITAKER, S. (1967). Diffusion and dispersion in porous media. *AIChE Journal* **13**(3), 420–427.

WHITE, B. & NEPF, H. (2007). Shear instability and coherent structures in shallow flow adjacent to a porous layer. *Journal of Fluid Mechanics* **593**, 1.

WHITE, B. L. & NEPF, H. M. (2003). Scalar transport in random cylinder arrays at moderate reynolds number. *Journal of Fluid Mechanics* **487**, 43–79.

WHITE, B. L. & NEPF, H. M. (2008). A vortex-based model of velocity and shear stress in a partially vegetated shallow channel. *Water Resources Research* **44**(W01412), WR005651.

WILSON, N. R. & SHAW, R. H. (1977). A higher order closure model for canopy flow. *Journal of Applied Meteorology* **16**, 1197–1205.

YALIN, M. S. (1971). *Theory of hydraulic models*, vol. 266. Macmillan London.

YEH, Y. & CUMMINS, H. Z. (1964). Localized fluid flow measurements with an he-ne laser spectrometer. *Applied Physics Letters* **4**(10), 176–178.

YEN, B. C. (2002). Open channel flow resistance. *Journal of Hydraulic Engineering* **128**(1), 20–39.

Appendix A

Optimizing the location of sampling points for double-averaged turbulent quantities in flows within arrays of rigid emergent stems

Abstract: [1] In engineering applications concerning the flow in vegetated channels such as the quantification of flow resistance it is desirable to upscale the analysis. The proper geometrical scale for the quantification of the turbulent flow variables is the mean inter-stem space. Double-averaging methods (time and space averaging, herein DAM) become a relevant conceptual tool to express the conservation equation describing spatially heterogeneous flows within a space domain the flow. The quality of the mean (double-averaged) values depends on the number and on the location of the space-sample points or profiles. No systematic and rational approaches have been dedicated to the impacts of the number and location of the sample points on the quality of the mean quantities. The objective of this work is to study the positioning of a limited set of samples so to describe the system in an optimal way. The placement of sampling points results from an optimization procedure seeking the empirical probability distribution of the time-averaged longitudinal velocity, obtained with 8 samples, that best reproduces the complete distribution. The results of the optimization are shown to be robust and applicable to situations where flow characterization is performed with little detail.

Keywords: Emergent rigid vegetation, Double-Averaging Methods, velocity maps, optimization algorithm

[1] Ricardo, A. M. (2009), Optimizing the location of sampling points for double-averaged turbulent quantities in flows within arrays of rigid emergent stems, 33th IAHR Congress, Vancouver.

Introduction

Emergent vegetation covering floodplains and wetlands has an important role in fluvial ecosystems, influencing hydrodynamic behaviour, ecological equilibrium and environmental characteristics of water bodies (Ghisalberti & Nepf, 2004). Plant stems affect flow depth, flood conveyance, sediment transport capacity, and other hydraulic parameters. In addition, vegetation plays an important role in maintaining the water quality by filtering nutrients from the water column (White & Nepf, 2008).

The main characteristic of the flow through arrays of rigid stems is the great spatial variability in the inter-stem space. Most applications, notably mathematical simulation, require some form of spatial upscaling, averaging out smaller scales. The contribution of the latter will be given by closure equations whose formulations must be determined empirically. One of the most successful upscaling techniques is the Double-Average Methodology (DAM) (Nikora *et al.*, 2001, 2008). It reveals that, at the scale of the mean inter-stem distance, the effect of smaller scales is expressed through form-induced stresses. For instance, their spatial gradients explain a considerable part of drag on plant stems (Ferreira *et al.*, 2009b; Ricardo, 2008).

In practice, the space-averaging procedure is planar and discrete: at a given z level, a number of time-averaged samples of a given quantity is taken to compute the double-average value of that quantity. The quality of the double-averaged values depends on the number and on the location of the sample points or profiles. The sufficient number of sampling points and its location has, to the author's knowledge, never been the object of a systematic study. If no attempts are made is taken to optimize these, the application of DAM may result in a considerable expenditure of time for measuring and process data and of data storage space.

This work addresses the issue of the location of the sampling points. The objective is to devise simple criterion to optimize the location of a limited number of sampling points so that they are representative of the flow at a given space scale. This can be seen as the basis of a technique to determine the sufficient number of sampling points for DA analysis.

To meet the proposed objective laboratory work was performed. PIV was used to characterize the flow in a region whose dimensions are of the order of magnitude of the desired spatial scale - the inter-stem spacing (sections 2 and 3). The probability density functions of the time-averaged spatial fluctuations of the longitudinal velocity is obtained in a region whose area scales with the square of the inter-stem spacing. An empirical distribution with 8 samples is generated so that its four moments are optimal relatively to those of the true distribution (section 4). The location of the sampling points in the horizontal plane is determined by finding longitudinal velocities in the 2D plane equal to those of optimal distribution. The work herein proposed rests on the following premise: in order to reduce data collection time and data storage volume and to ensure a good quality space averaged quantities, it is necessary to perform a preliminary characterization of the flow before performing the actual tests. This means finding zones of quasi-homogeneity to be articulated with the results of the optimized distribution (section 5).

Laboratory facilities and instrumentation

The data used in the present study was produced in the 10 m long and 0.409 m wide Recirculating Tilting Flume at the Laboratory of Hydraulics and Environment of Instituto Superior Técnico, TULisbon (Figure A.1). The flume has glass side walls, enabling flow visualization and laser measurements.

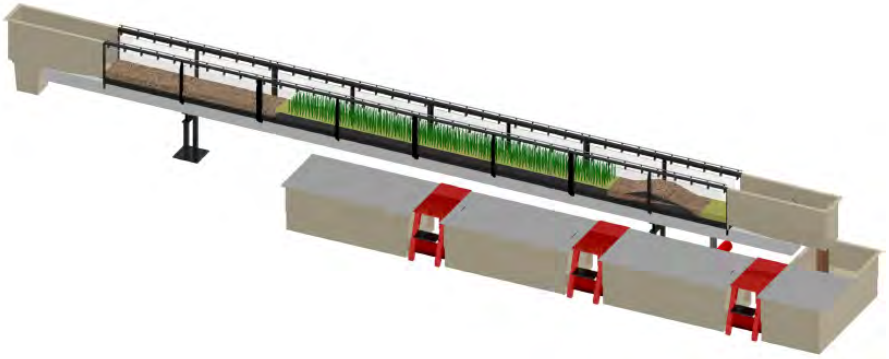

Figure A.1: Schematic view of the flume.

Laboratory tests were carried out to characterize the flow within a dense array of vertical emergent stems that reproduce the natural conditions in wetlands (Figure A.1). The flume bottom was covered with a uniform sand layer with mean diameter $d_{50} = 0.008$ m. Arrays of stems with 1.1 cm of width randomly placed in the sand bed simulated emergent vegetation conditions. Downstream the stems reach, coarse gravel weir controlled the flow. To develop the turbulent boundary layer, a gravel-bedded reach was laid upstream of the stems.

Instantaneous velocity maps were obtained with a 532 nm, 30 mJ 2D *Particle Image Velocimetry* (PIV) system, operated at a sampling rate of 15 Hz and an interval between consecutive laser pulses of 1500 μs. Each acquisition period contained 490 samples, corresponding to about 33 s. The velocity fields were measured in vertical planes at 3 different lateral positions aligned with the flow direction and in horizontal planes at 6 different vertical positions. Figure A.2 depicts a plan view of the flume with the measuring reach.

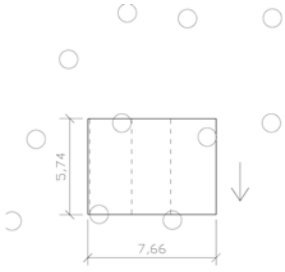

Figure A.2: Plan view of working reach. The measuring region is the dot-dashed rectangle in horizontal plane and dashed lines in vertical plane). Point 1 and 2 are sample points that will be refereed latter for spectral analysis.

The particles employed for flow visualization and measuring were 50 μm Polyamide Seeding Particles with a specific gravity of 1.03. The cut-off was 100 Hz, much greater than the Nyquist frequency of the PIV measurements (details in Ricardo, 2008).

The free-surface elevation was measured with a 1 mm precision ruler and the bed topography was measured with a 0.1 mm precision point gage.

Characterization and description of the flow

Before introducing the optimization procedure for the location of the sampling points, it is necessary to characterize the flow in the measuring area in order to assess the type of variability to be dealt with. The experiments were performed with a discharge of $Q = 2.33$ ls^{-1} and the stem distribution was characterized by density $n = 399$ stems/m^2 and a solid volume fraction $\phi = 0.038$. At the measuring reach, the mean velocity was $U = 0.106$ ms^{-1}, the flow depth was $\langle \bar{h} \rangle = 0.055$ m, the free-surface slope was $\mathrm{d}\langle \bar{h} \rangle / \mathrm{d}x = -0.0056$ and the stem Reynolds number was $Re_p = Ud/\nu = 1162$. Scour holes developed at the base of the stems and sand deposits with 0.4 cm of maximum elevation above the initial bed formed downstream the stems. The impact of these on the flow structure consisted on the development of an inner layer influenced by bed-form oscillations. The flow exhibits a thin inner boundary layer, influenced by the bed forms and grain roughness. This layer extend to about 10 % of the flow depth and is characterized by a sharp longitudinal velocity gradient. In most of the depth, the longitudinal velocity is constant and the flow is mainly influenced by turbulence generated at the stem array.

Maps of 2DH mean spatial velocity fluctuations (Figure A.3) and maps of mean vorticity

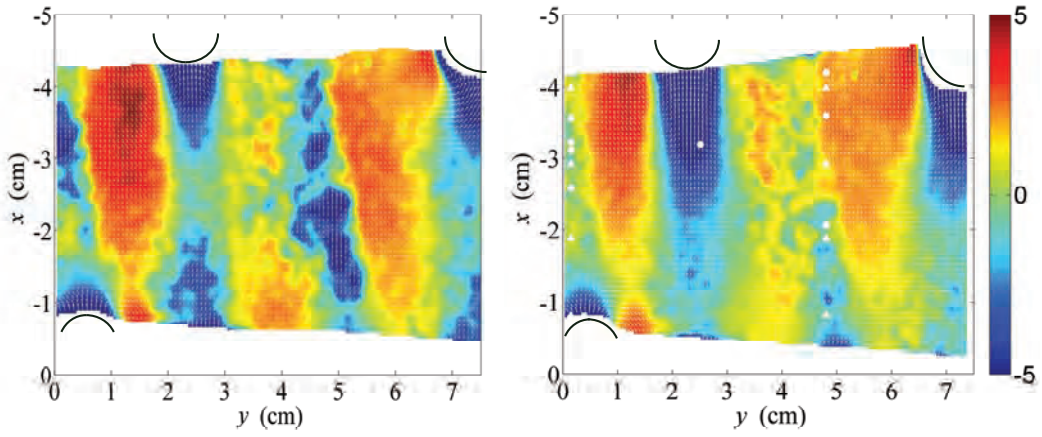

Figure A.3: Maps of time-average velocity fluctuations (cm/s) measured in the horizontal planes at level: a) $z = 0.95$ cm and b) $z = 1.95$ cm. Circles stand for placement of the sample points of optimal solution and triangles of the uniform solution (section 5).

(Figure A.4) were computed to characterize the flow in the inter-stem region. The spatial velocity fluctuations were obtained from $\widetilde{u} = \bar{u} - \langle \bar{u} \rangle$, where $\bar{u}$ and $\langle \bar{u} \rangle$ are, respectively, the time-average and the double-averaged longitudinal velocity. Figure A.3 shows that the flow within vegetated areas is extremely heterogeneous. As expected, velocity is lower in the wake of the stems and higher in regions between two stems. Between $y = 5$ cm and $y = 6$ cm, it is possible to observe a shear layer dividing regions of relative low and high velocity. One may expect that Kelvin-Helmholtz instabilities may form in this in this region. In fact, the mean vorticity maps seems to corroborate the existence of this kind of instabilities. However, due to the tridimensional character of the flow, they are difficult to distinguish. A careful observation of instantaneous map

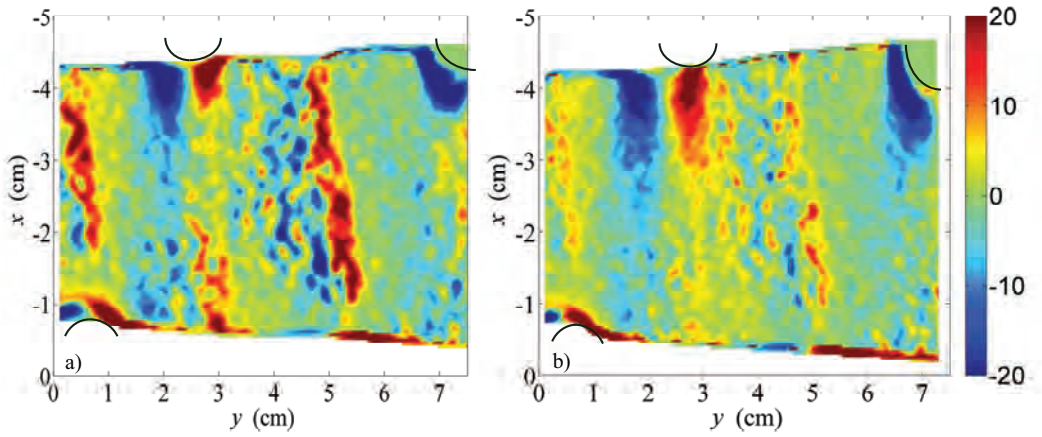

Figure A.4: Mean vorticity fields (s^{-1}). (Remaining caption as in Figure A.3)

of velocity and streamlines, reveals that the flow is marked by coherent upward and downward fluid motion. Indeed, streamlines merge and disappear in sinks or appear in sources (Figure A.5). These events are probably turbulent ejections and sweeps.

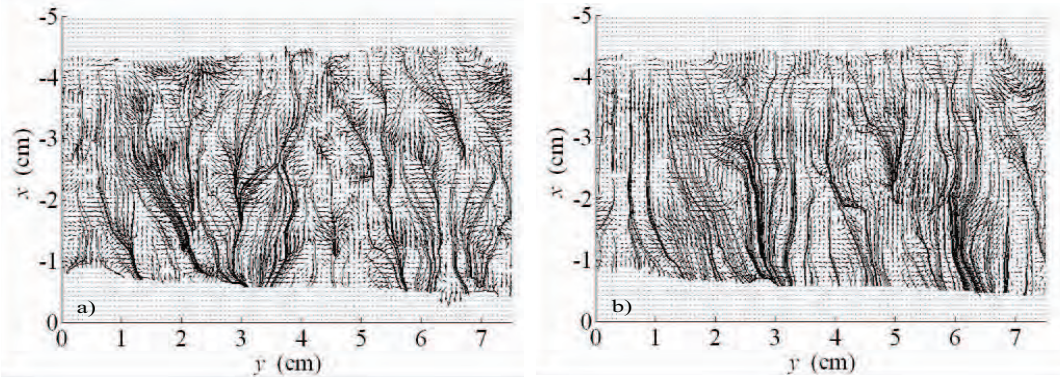

Figure A.5: Instantaneous fluctuation velocity quiver and streamlines in a a) event of upward velocity and b) event of downward velocity.

The Von Kármán vortex street is observed downstream the stem situated at the top left of the measuring reach (stem A on Figure A.2). In this region there is a repeating pattern of paired vortexes caused by the unsteady separation of flow over the stem. The Von Kármán vortex street may be identified on maps of mean vorticity, which clearly shows a quasi-symmetric high vorticity pattern behind the stems.

The Strouhal number of the vortexes in a Kármán vortex street is given by (Schlichting, 1968, pp. 31-32) $S = fd/U$, where f is the dimension frequency and U is the flow velocity. For an isolated cylinder, the Strouhal number depends uniquely on the Reynolds number. For a Reynolds number of 5574, the Strouhal number is 0.205. Hence, the frequency of the Von Kármán vortex street would be 1.98 Hz.

Figure A.6 shows the power spectrum on two points of the flow at level $z = 1.95$ cm (indicated in Figure A.2). It was assumed that the array of stems is sparse enough to be applied the results of a isolated cylinder. Hence, the spectrum corresponding to point 1, exhibits the highest

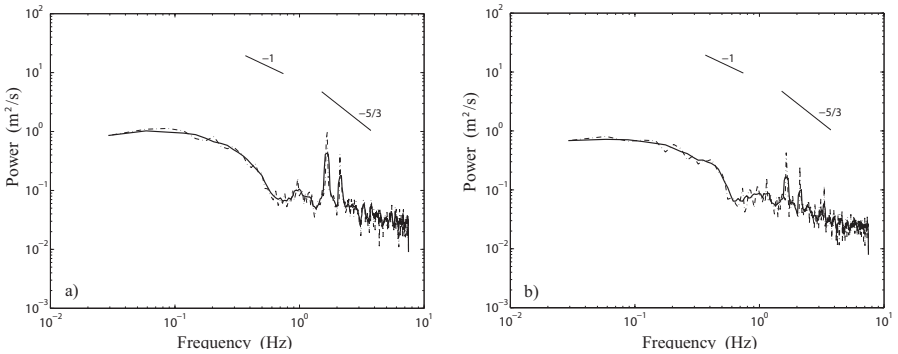

Figure A.6: Log-log plot of the power spectra of the flow at 1.95 cm above the bed in a) point 1 and b) point 2 (see Figure A.2). The continuous line is a moving average of the periodogram (dot-dashed line).

peak corresponding to the frequency 2 Hz corroborating the existence of a predominant and persistent flow structure in the wake of the stem A. The lower peak, in this spectrum may represent the interaction between cylinders. About the second spectrum, it is possible that the two peaks corresponding to frequencies 1.6 and 2.2 Hz are an impression of the Kelvin-Helmholtz instabilities.

Optimization procedure

Due to economic and time limitations it is usual to have a limited number of sampling points to characterize the flow. In the previous section the particular forms of spatial heterogeneity that characterize flows within arrays of rigid emergent stems were identified. It is now explained how to best capture the observed heterogeneity with a limited number of samples, i.e. how to obtain good DA quantities with a small number of samples. The analysis will be restricted to double-averaged velocities, but it can easily be extended to other DA quantities.

The procedure begins with a statistical analysis of the data of the horizontal plane. The spatial probability density function (pdf) of the longitudinal velocity is determined. Then, it is applied the principle that the empirical distribution obtained with a limited set of velocities should have the same 1st, 2nd, 3rd and 4th order moments.

The mean velocity field of the studied flow, at level $z = 1.95$ cm, is characterized by mean of 8.88 cm/s, variance of 5.94 $\mathrm{cm^2 s^{-2}}$, third central moment of -23.02 $\mathrm{cm^3 s^{-3}}$ and forth central moment of 226.57 $\mathrm{cm^4 s^{-4}}$. Figure A.8-a) presents the pdf of this mean velocity map. In this work, it is proposed that the number of sampling points is restricted to 8. The optimization algorithm is based on a guided generation system states, each characterized by a 8 velocities, and for which the statistical descriptors are calculated. The algorithm chooses the solution that minimizes the following objective function:

$$OF = \alpha \left(\frac{M_2^{(x)}}{\mu_x^2} - \frac{M_2^{(t)}}{\mu_t^2} \right)^2 + \beta \left(\frac{M_3^{(x)}}{\mu_x^3} - \frac{M_3^{(t)}}{\mu_t^3} \right)^2 + \gamma \left(\frac{M_4^{(x)}}{\mu_x^4} - \frac{M_4^{(t)}}{\mu_t^4} \right)^2 \tag{A.1}$$

where $M_i^{(x)}$ stand for the ith moment of the set of 8 points about the mean of the total population,

$M_i^{(t)}$ is the ith central moment of the population, μ_x and μ_t are, respectively, the mean of the set of 8 points and the population. The weighting factors are $\alpha = 0.6$, $\beta = 0.3$ and $\gamma = 0.1$ since, for the frequency distribution of velocity field, statistical dispersion is more important than asymmetry and asymmetry is more important than flatness. Since the set of all possible system states is extremely large (of order of 10^{12}), the optimization algorithm selects only states for which the mean is optimal (reducing to order of 10^9 system states). The latter condition is implemented as the threshold condition $|\frac{\mu_t - \mu_x}{\mu_x}| \leq 0.05$.

Thus, the algorithm tests all possible combinations of 8 sampling points in a chosen number of bins of the discretized velocity pdf that verify the condition optimal 1st moment. In Figure A.7 is showed a plot of a part of the objective function.

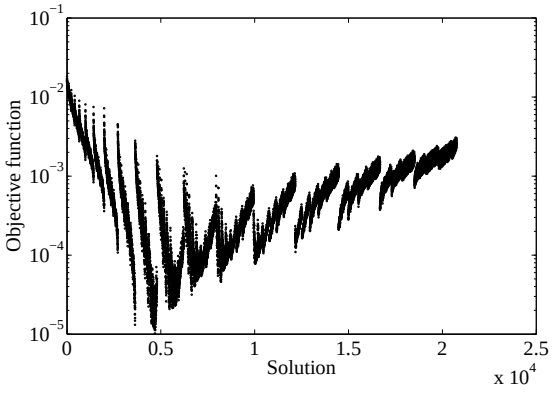

Figure A.7: Plot of part of the objective function.

Results and discussion

The results were obtained with a discretization of velocity pdf of 0.09 cm/s, compatible with an acceptable computing time. Figure A.8 exhibits the pdf of the population (left) and the histogram obtained with the optimal system state (right). The value of the objective function of

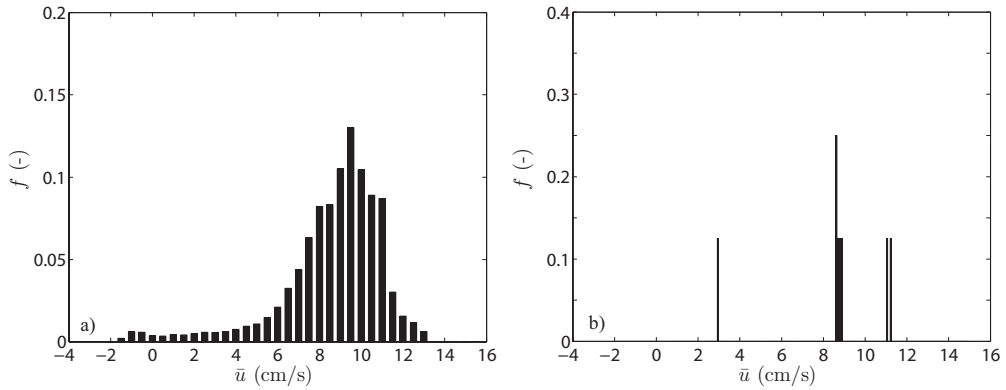

Figure A.8: Frequency distribution of the a) velocity map at level $z = 1.95$ cm b) and its best fit with only 8 points.

the best solution is 8.14×10^{-6}.

The velocities of the optimal solution were searched in the 2DH velocity plot (Figure A.3) to find the location of the sampling points. Profiles of DA longitudinal velocities were computed in these locations. The results, showed in Figure A.9a, were compared with the integration of mean velocity of each horizontal plane and with reference results of a DAM presented in Ricardo (2008) with 60 sampling points. To clarify the importance of the optimization procedure, the results of a "primitive" (uniform) distribution of sampling points (Figure A.3b) are compared with the optimal distribution in Figure 9b. In absence of previous flow characterization, the tendency will be to distribute uniformly the sampling points. As seen in Figure 9b, such distribution would underestimate the values of the DA longitudinal velocity.

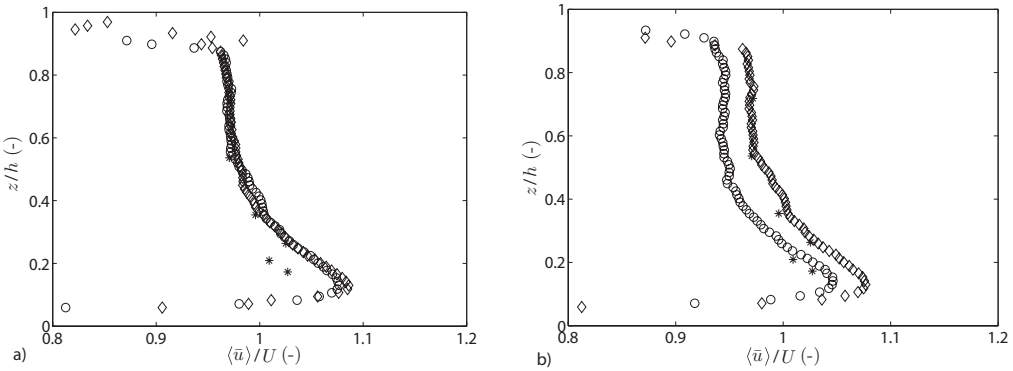

Figure A.9: a) Double-average longitudinal velocity profiles resulting of a DAM with the best set of 8 points (circles), a DAM presented in Ricardo (2008) (diamonds) and the integration on horizontal planes (asterisks). b) Velocity profile resulting of a uniform placement of the sample points (circles) compared with optimal solution (diamonds).

This procedure may seem non-applicable in most practical applications, as it requires extra information prior to the commencement of the tests. However, it is stressed that some previous knowledge of the flow will allow for better estimates of DA variables. Furthermore, the procedure does not require a too detailed flow information and it can be shown to be robust. One concludes, observing the pdf and the distribution of Figures 8a and b, that the results may be interpreted as an indication that 5 sample points are needed in regions of intermediate velocities, 2 sample points in regions of high velocity and 1 sample point in regions of low velocity. To show the

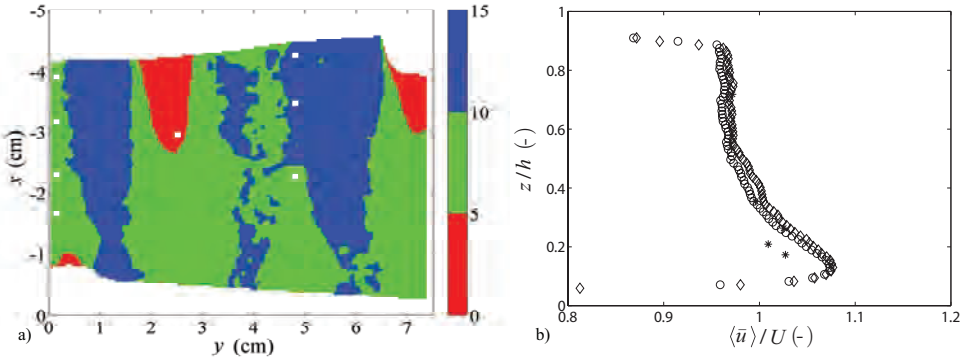

Figure A.10: a) Longitudinal velocity map (cm/s) and placement of the sample points of the simpler solution (squares). b) Velocity profile resulting of a placement of the sample points with a simpler criterion (circles) compared with the best solution of placement algorithm (diamonds).

robustness procedure, these flow regions are shown in Figure A.10a. With this simpler criterion a DA velocity profile was computed with 5 points on mean values (green), 2 points on higher values (blue) and 1 point on a wake (red). The result of this test is very similar to the best solution (Figure A.10-b), confirming that this is a robust procedure.

Conclusions

This work was performed under the premise that it is necessary to acquire some information of the heterogeneity of the flow before collecting data for DA descriptions. It was thus proposed a methodology for a rational use of that preliminary information. The optimizing procedure was designed for the spatial distribution of the longitudinal velocity and verified with the DA longitudinal velocity but can be applied to other DA variables.

The procedure was applied to a highly heterogeneous flow, within an array of emergent rigid stems, featuring vortical structures of different nature and interactions between vortical structure emitted from neighboring stems. This complexity was sufficiently capture in the pdf of the spatial fluctuations of the longitudinal velocity. The optimal distribution of the limited number of sampling points preserved the four main moments of the pfd of the population. This procedure is robust in the sense that a coarse description of the flow variability would conduct to near-optimal solutions.

This procedure can be seen as a first step for a sufficient sampling algorithm, that will allow for time and data storage savings in the context of DA applications.

Appendix B

Spectral analysis

The present appendix presents spatial transverse, $\overline{E_N}$, and longitudinal, $\overline{E_L}$, energy spectra for the two lateral positions at the flume's center at height $z^{(b)}$ (see Table 7.1) in all the measuring gaps of test S2. The energy spectrum is obtained by a power spectral density of a spatial series of velocity fluctuations, using the periodogram as spectral estimator. Instantaneous spatial series were used along y direction and then time-averaged spectra are considered. Graphs are presented in dimensionless form, being wavenumbers normalized by the macro-scale, Λ and energy power normalized by the macro-scale and the variance of the velocity series.For each figure a comparison of the energy spectrum at different cross sections is shown. The subscript i of Λ_i and s_i specifies the measuring gap. Vertical lines indicate scales of interest: dotted lines for averaged macro scale of P3 and P7; solid lines for averaged macro scale of P2 and P6, and P4 and P8; dashed lines for averaged macro scale of P1 and P5; thicker dot-dashed lines for $k\Lambda_i = 1$; thinner dot-dashed lines for stem diameter. An averaged macro-scale was considered for patches with the same stem areal number-density, to avoid an overload of lines.

The presented transverse spectra show an inertial range, typically spanning about half decade, a $-5/3$ slope reach is visible. About the productive range of scales, it should be highlighted that the fingerprint of different scales in the flow are visible in the energy spectra. The spectra indicates that the most energetic scale corresponds to the macro-scale of the region immediately upstream of the measuring section, but the other densities also contribute to the energy balance. Comparing, for each patch, spectra at different streamwise locations one can observe that they remain nearly the same, only at high wavenumbers there is an increase of energy towards downstream. Also comparing spectra of different measuring patches, one can conclude that both magnitude and shape are similar, only a slight increase of the peak values can be noticed for dense patches when compared with sparse patches.

Regarding longitudinal spectra, the peaks are less pronounced than in $\overline{E_N}$ and they decrease with the stem areal number-density. However, one can still identify in $\overline{E_L}$ the signature of the different scales in the flow as well as the $-5/3$ slope identifying the inertial range of scales.

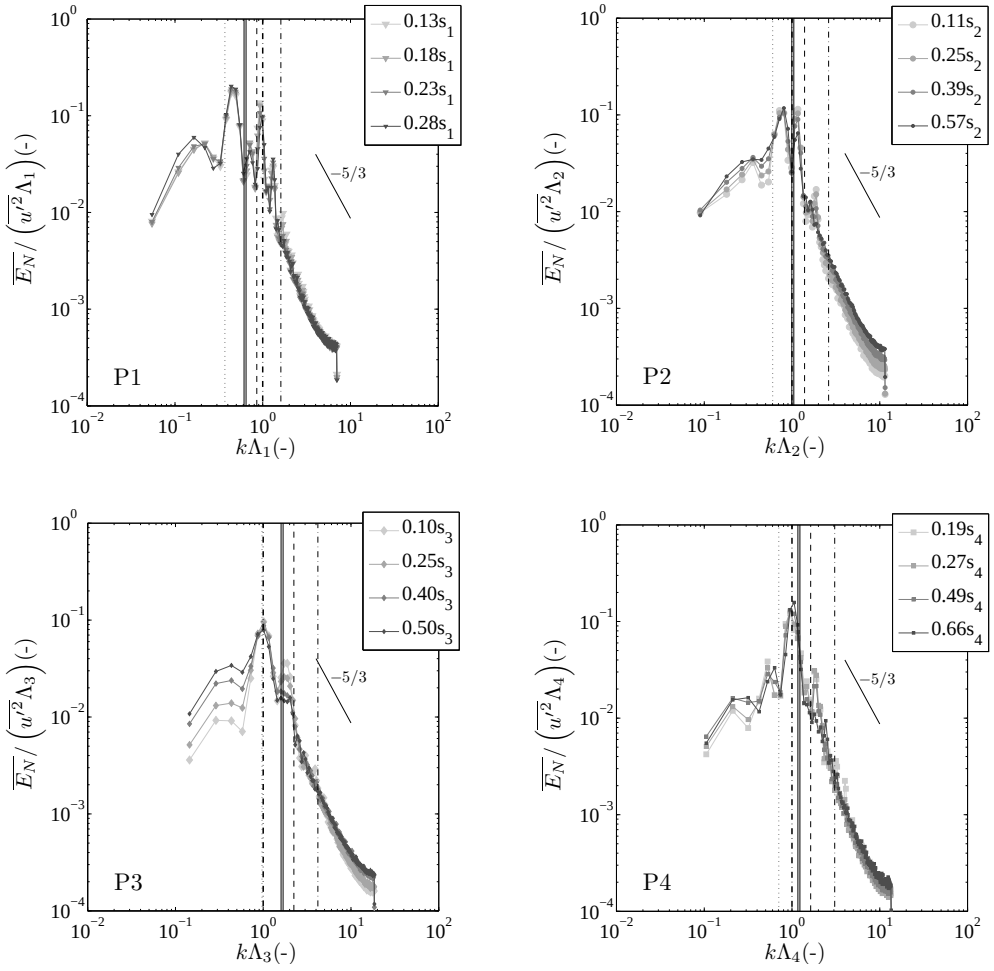

Figure B.1: Dimensionless spatial transverse spectra for the lateral position between $y = 0.10$ m and $y = 0.22$ m at height $z^{(b)}$, for the measuring gaps P1 to P4 of test S2. Vertical lines indicate scales of interest: dotted – average macro scale of P3 and P7; solid – average macro scale of P2 and P6, and P4 and P8; dashed – average macro scale of P1 and P5; thicker dot-dashed – $k\Lambda_i = 1$; thinner dot-dashed – stem diameter.

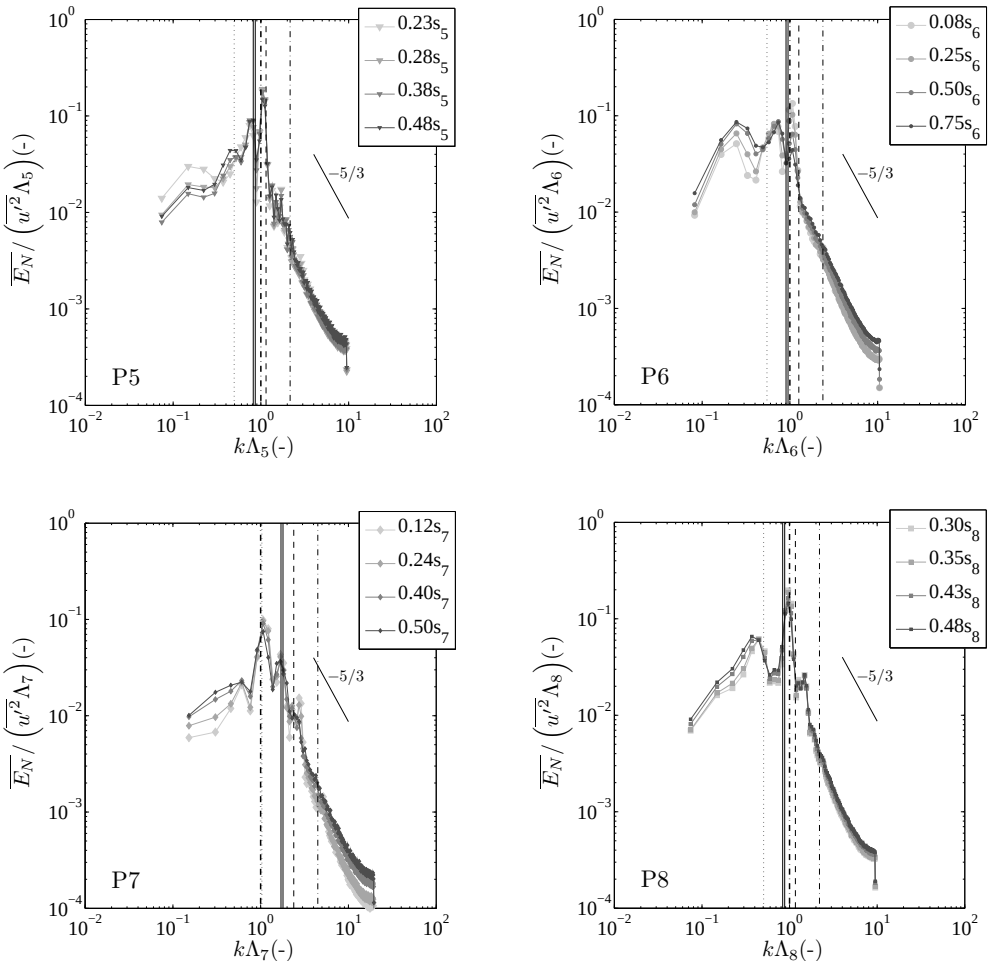

Figure B.2: Dimensionless spatial transverse spectra for the lateral position between $y = 0.10$ m and $y = 0.22$ m at height $z^{(b)}$, for the measuring gaps P5 to P8 of test S2 (*cf.* Fig. B.1 for meaning of vertical lines).

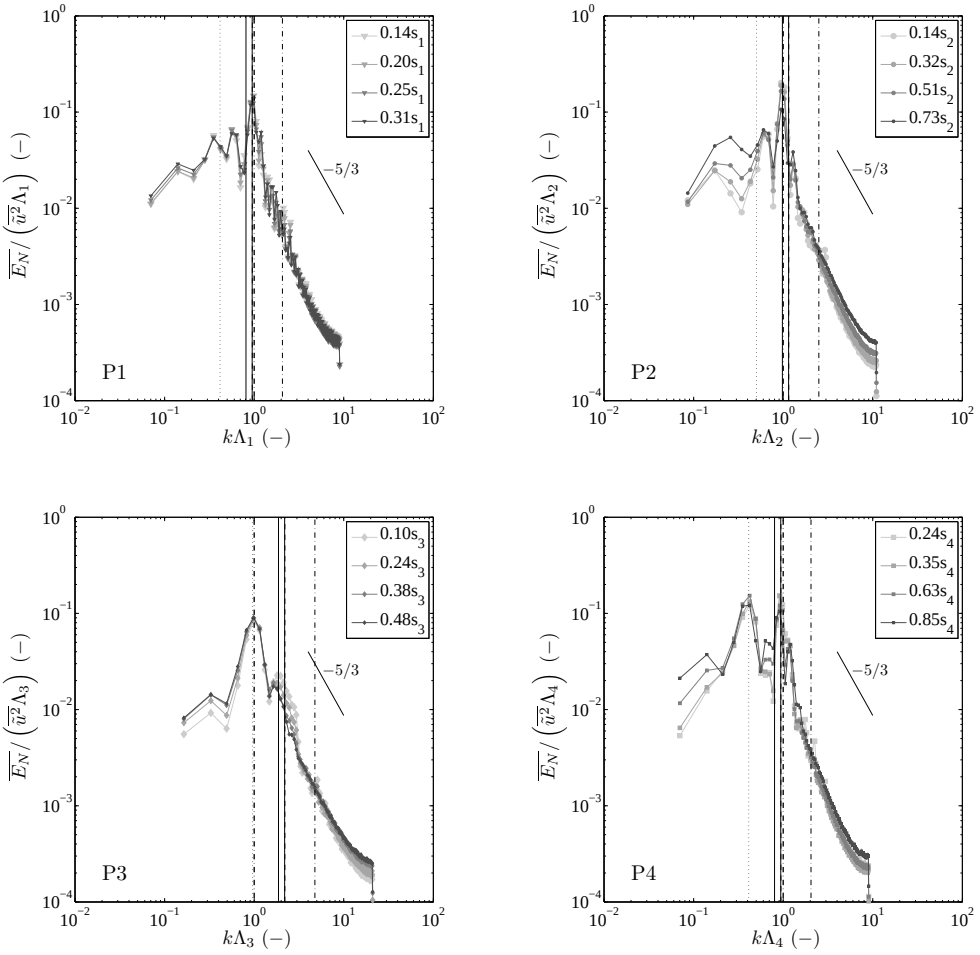

Figure B.3: Dimensionless spatial transverse spectra for the lateral position between $y = 0.18$ m and $y = 0.30$ m at height $z^{(b)}$, for the measuring gaps P1 and P4 of test S2 (*cf.* Fig. B.1 for meaning of vertical lines).

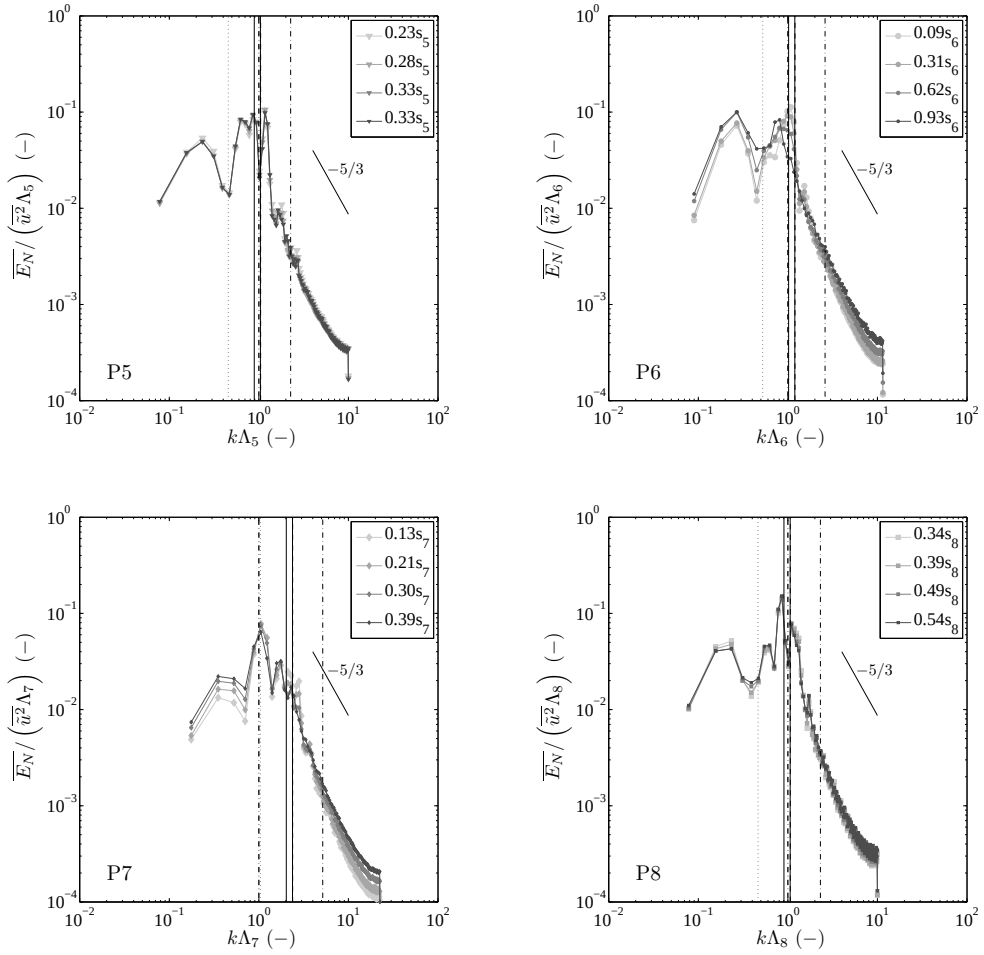

Figure B.4: Dimensionless spatial transverse spectra for the lateral position between $y = 0.18$ m and $y = 0.30$ m at height $z^{(b)}$, for the measuring gaps P5 to P8 of test S2 (*cf.* Fig. B.1 for meaning of vertical lines).

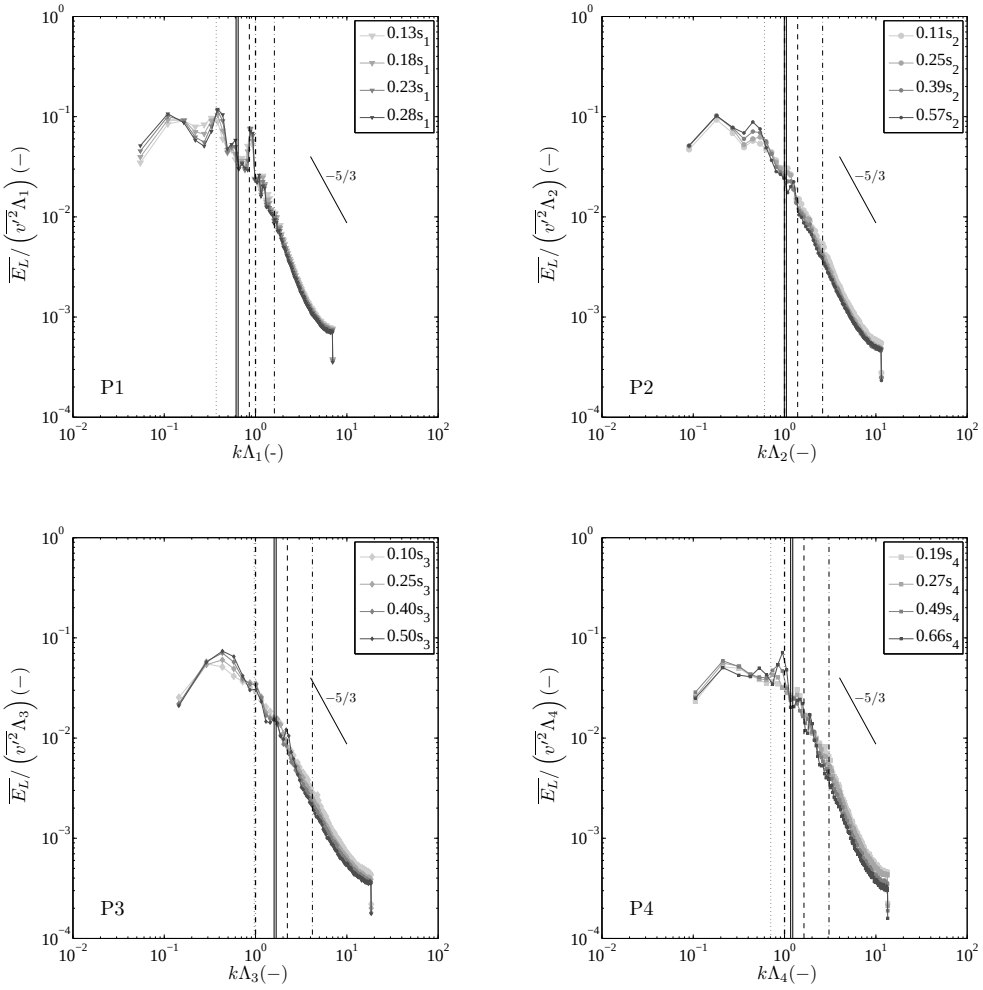

Figure B.5: Dimensionless spatial longitudinal spectra for the lateral position between $y = 0.10$ m and $y = 0.22$ m at height $z^{(b)}$, for the measuring gaps P1 to P4 of test S2 (*cf.* Fig. B.1 for meaning of vertical lines).

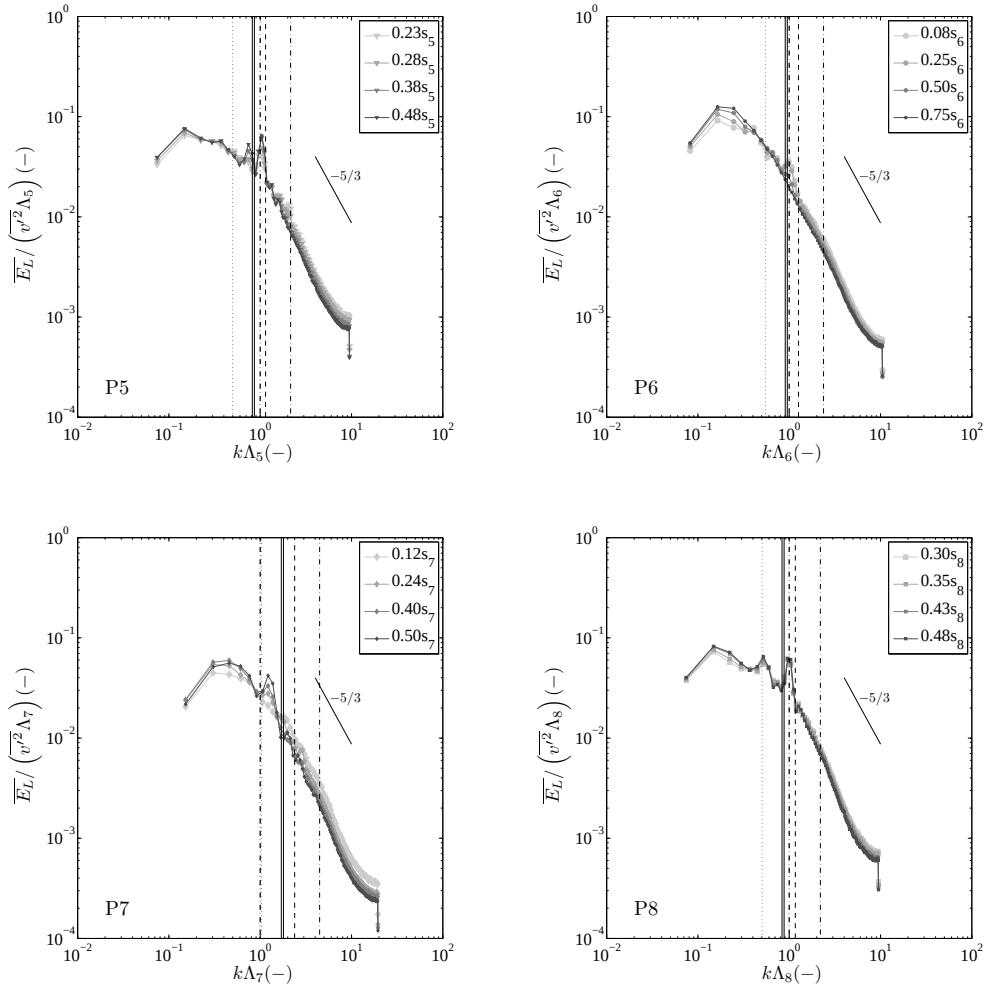

Figure B.6: Dimensionless spatial longitudinal spectra for the lateral position between $y = 0.10$ m and $y = 0.22$ m at height $z^{(b)}$, for the measuring gaps P5 to P8 of test S2 (*cf.* Fig. B.1 for meaning of vertical lines).

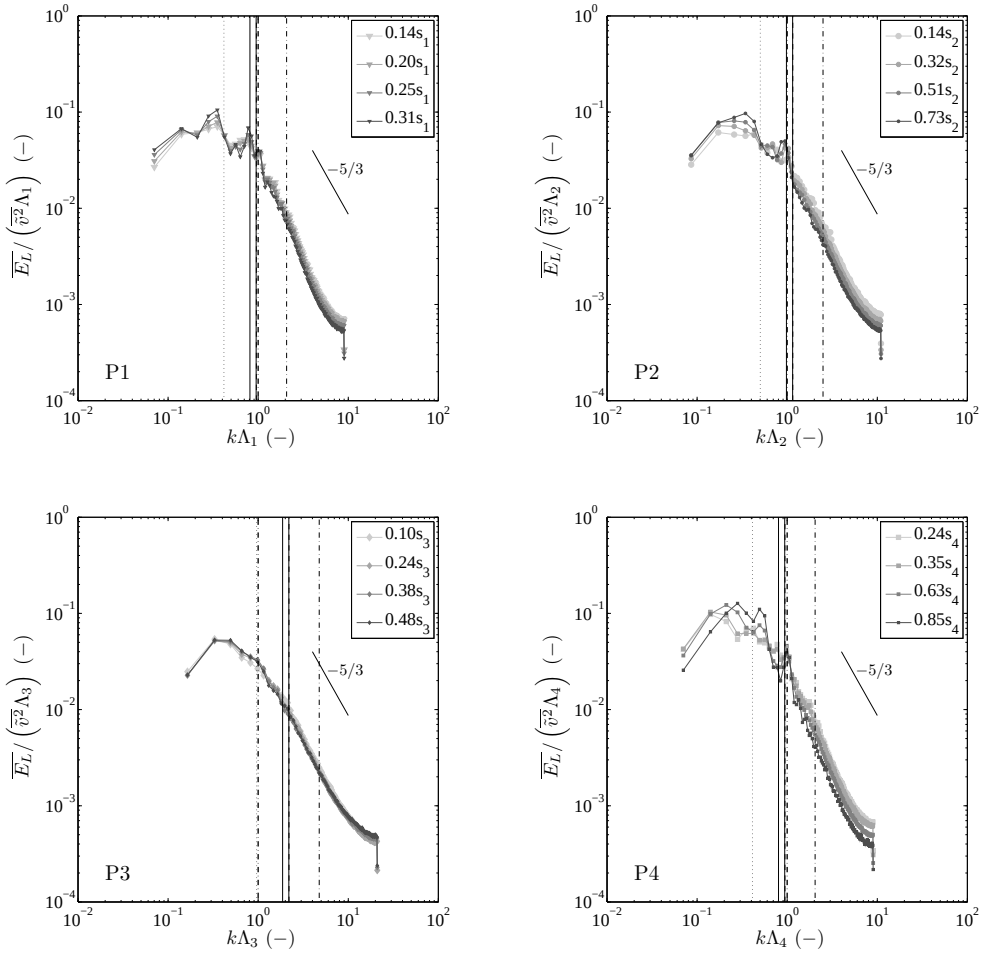

Figure B.7: Dimensionless spatial longitudinal spectra for the lateral position between $y = 0.18$ m and $y = 0.30$ m at height $z^{(b)}$, for the measuring gaps P1 to P4 of test S2 (*cf.* Fig. B.1 for meaning of vertical lines).

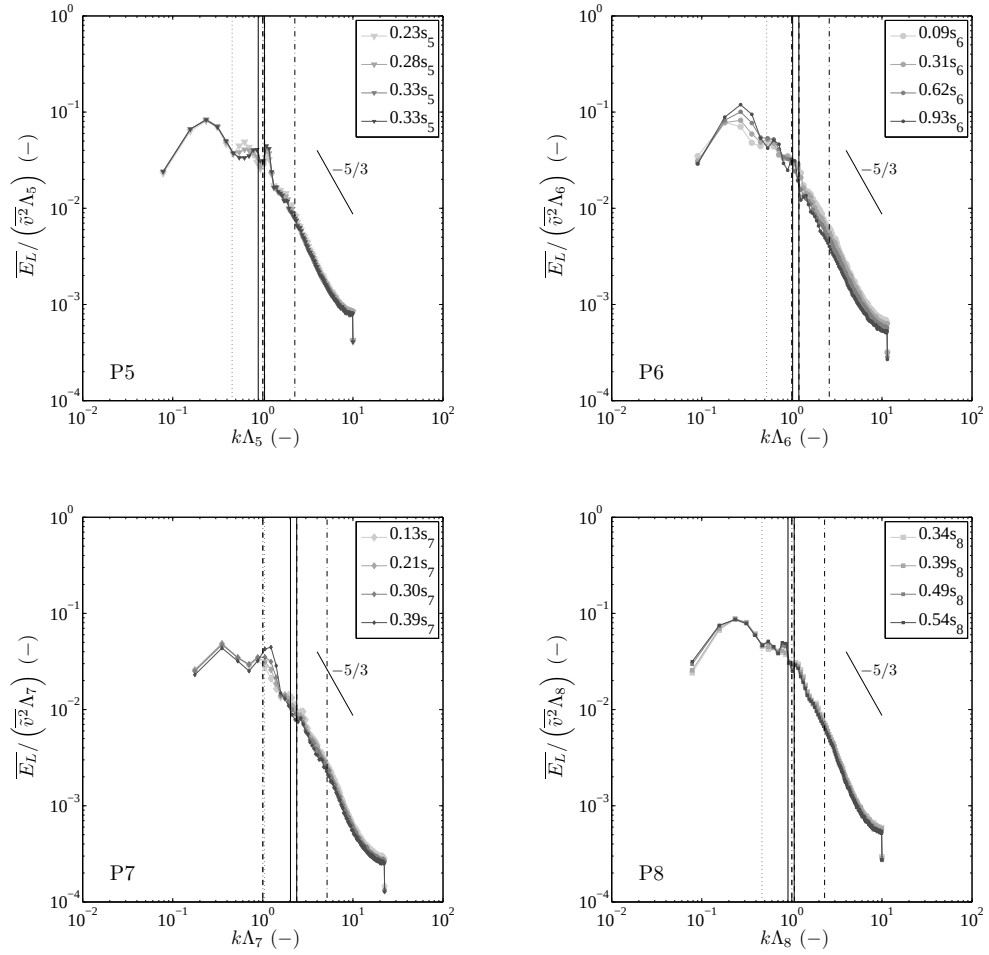

Figure B.8: Dimensionless spatial longitudinal spectra for the lateral position between $y = 0.18$ m and $y = 0.30$ m at height $z^{(b)}$, for the measuring gaps P5 to P8 of test S2 (*cf.* Fig. B.1 for meaning of vertical lines).

Appendix C

Additional figures for the characterization of TKE budget within arrays of cylinders

This appendix is aimed at presenting for all the measuring gaps of test S2 part of the figures exemplified in Chapter 5 only for some patches. All the data presented here correspond to the database identified in Chapter 5.

Figure C.1 and C.2 show $-\overline{u'v'}\partial\overline{u}/\partial y$ and $-\overline{v'v'}\partial\overline{v}/\partial y$ components of the turbulent production of TKE, respectively, computed from PIV and LDA databases for measuring gaps where LDA measurements were performed.

Figures C.3 and C.4 present maps of turbulent production for all measuring gaps of test S2. Figures C.5 and C.6 show maps of the convective term of TKE budget and Figures C.7 and C.8 show maps of turbulent diffusion, also to the measuring gaps P1 to P8.

Lateral profiles of the terms of TKE budget equation are presented in Figures C.9 and C.10.

In Figures C.11 to C.14 two-dimensional maps of $1/2\left(\overline{u'u'}+\overline{v'v'}\right)$ overlapped by a vector plot of TKE flux are shown for the two lateral positions in the flume's center, for each measuring gap of test S2.

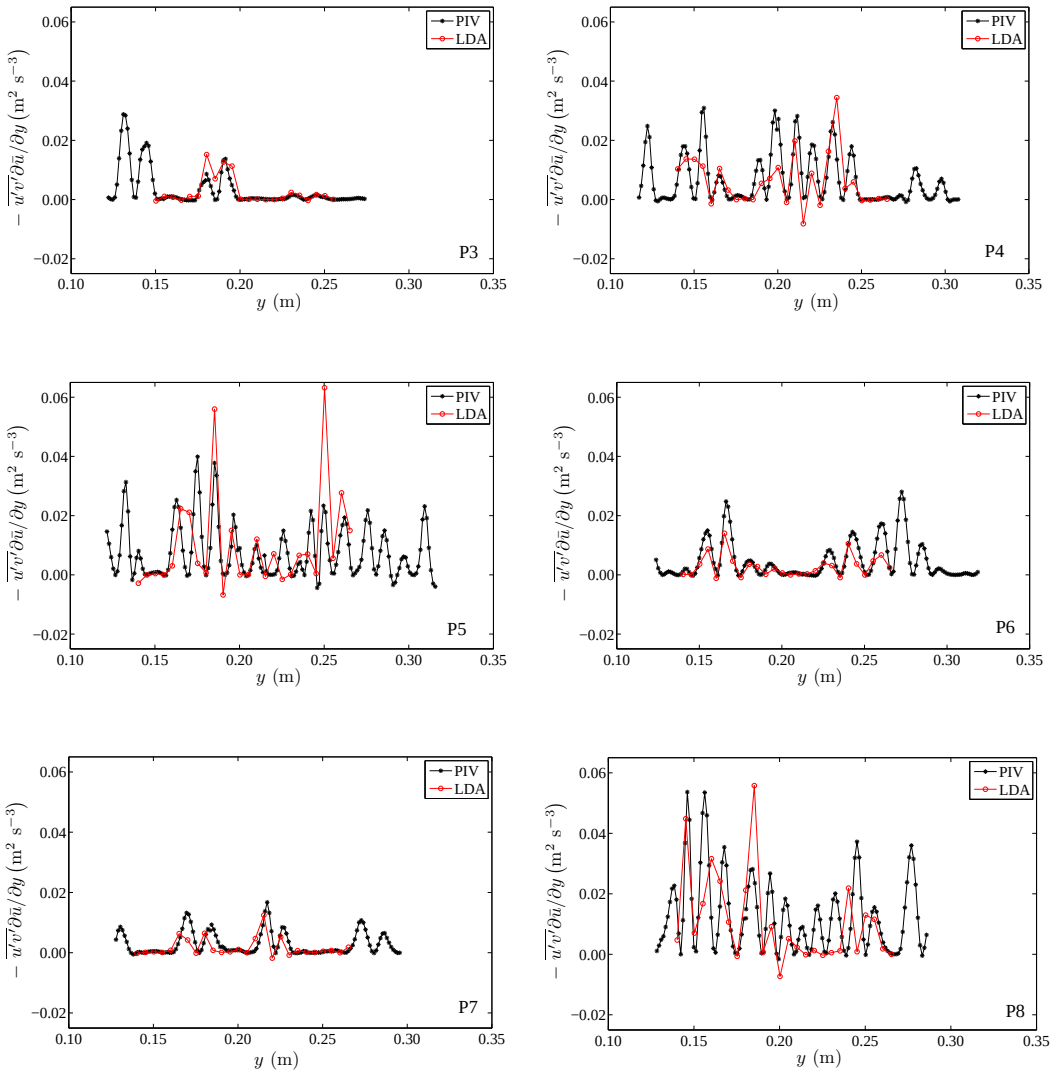

Figure C.1: Comparison of $-\overline{u'v'}\partial\overline{u}/\partial y$ component of the turbulent production of TKE, computed from PIV and LDA databases for measuring gaps P3 to P8. Vertical dotted lines identify the y-coordinate of centres of stems close to the upstream limit of the measuring gap.

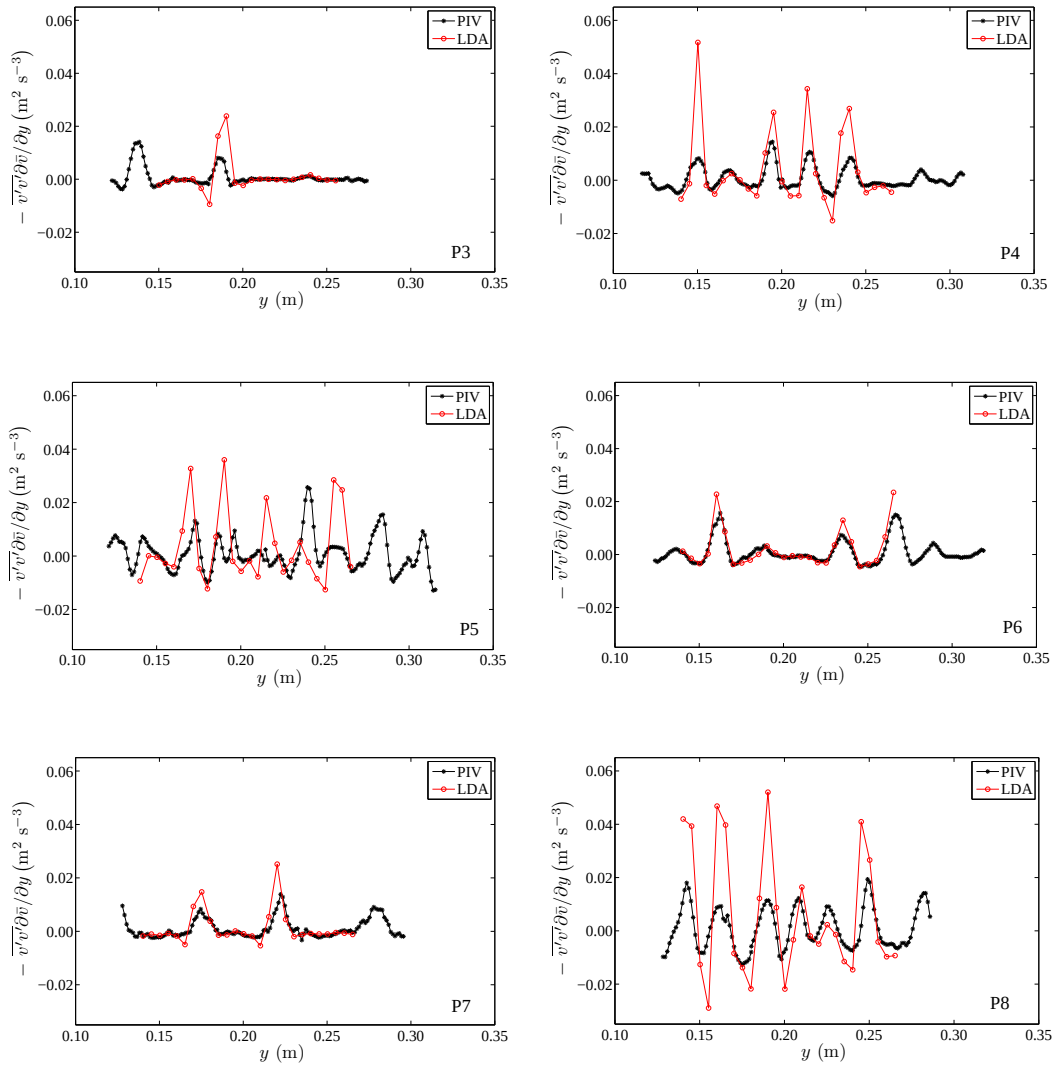

Figure C.2: Comparison of $-\overline{v'v'}\partial\overline{v}/\partial y$ component of the turbulent production of TKE, computed from PIV and LDA databases for measuring gaps P3 to P8.

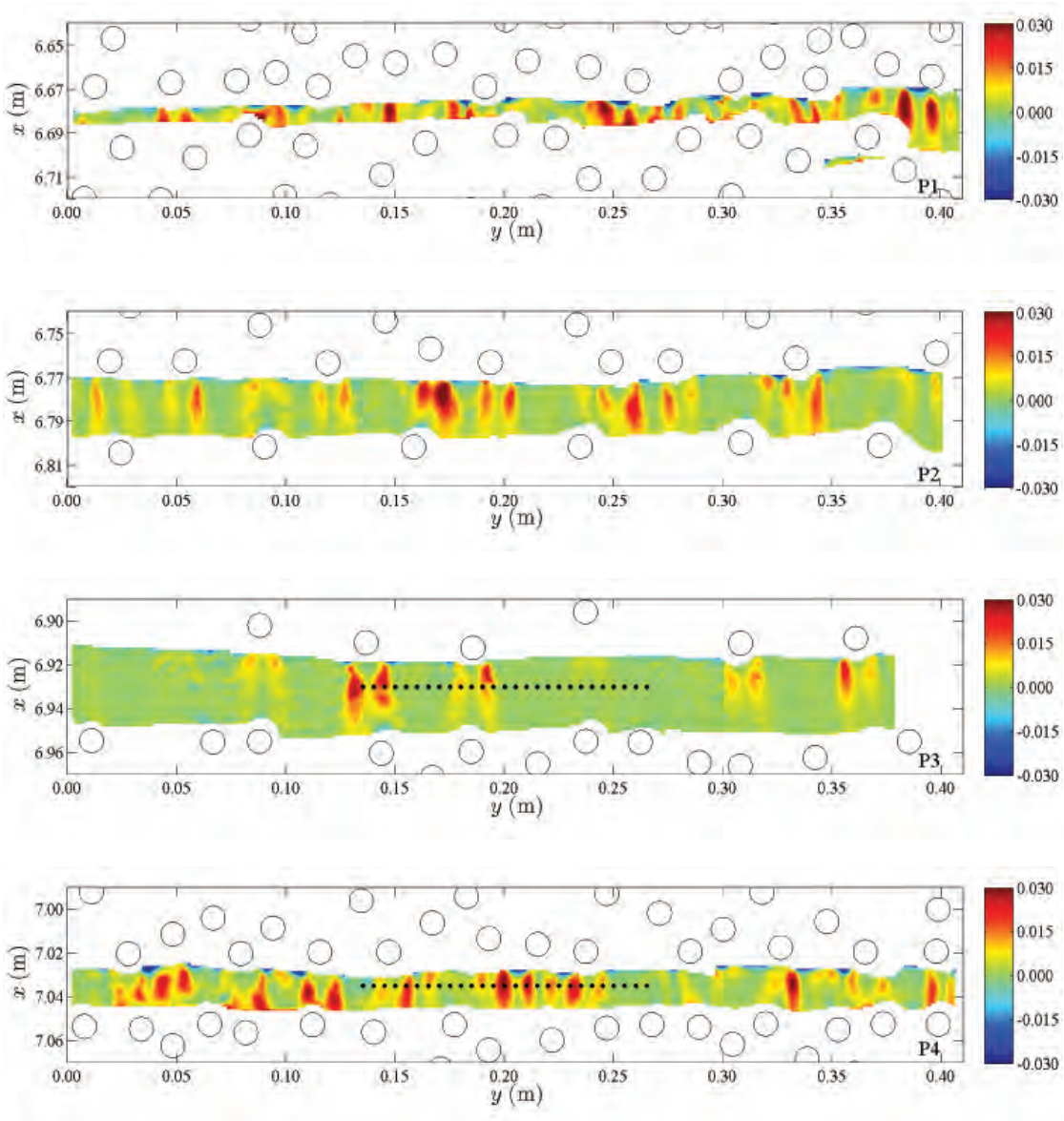

Figure C.3: Two-dimensional maps of turbulent production, $-\overline{u_i' u_j'} \partial \bar{u}_i / \partial x_j$, $\left(\mathrm{m^2 s^{-3}}\right)$ for measuring gaps P1 to P4. Dots aligned horizontally identify the position of LDA measurements.

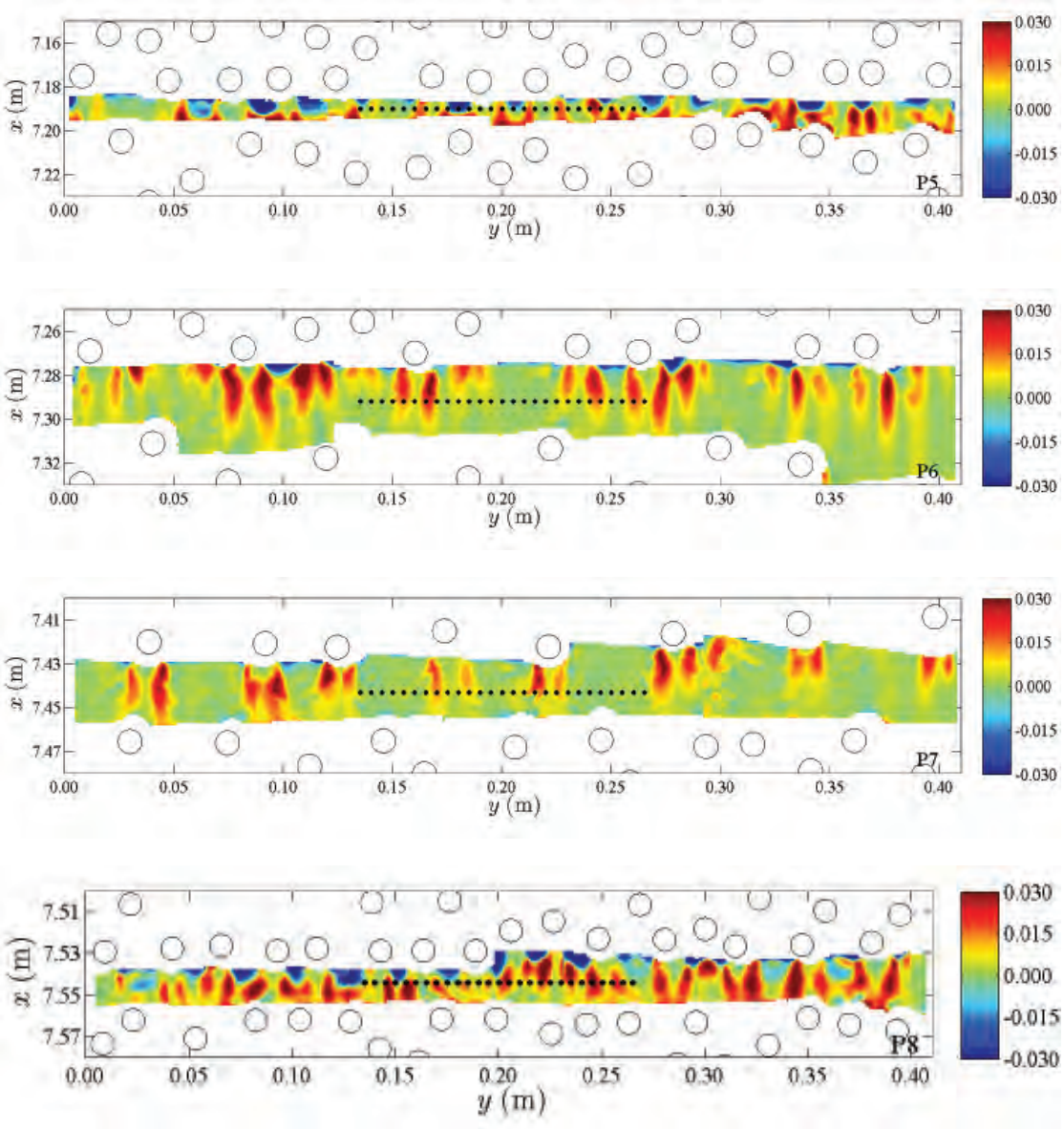

Figure C.4: Two-dimensional maps of turbulent production, $-\overline{u_i' u_j'} \partial \bar{u}_i / \partial x_j$, $\left(\mathrm{m^2 s^{-3}}\right)$ for measuring gaps P5 to P8. Dots aligned horizontally identify the position of LDA measurements.

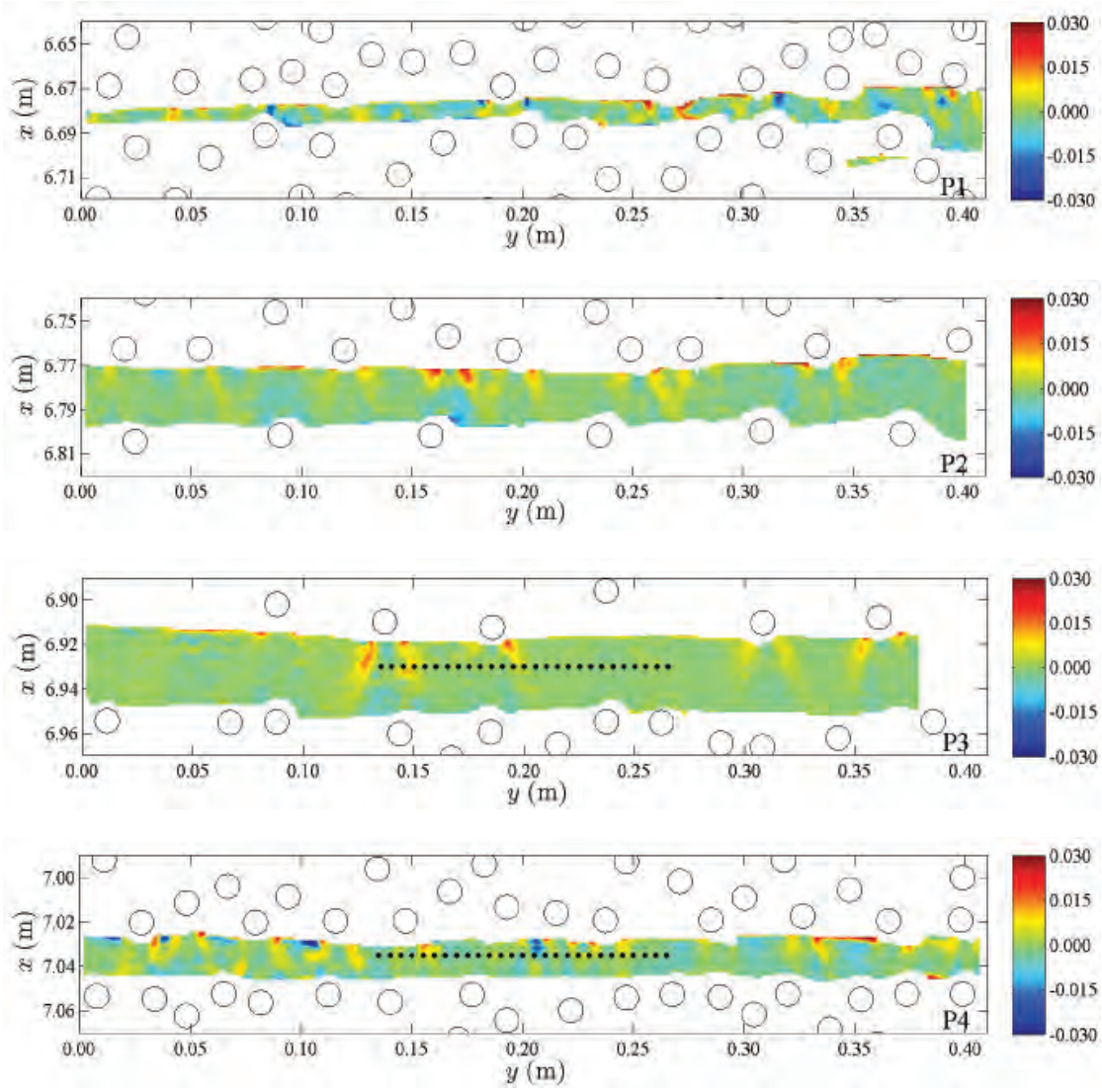

Figure C.5: Two-dimensional maps of the convective term, $1/2\bar{u}_j \partial \overline{u_i' u_i'} / \partial x_j$, $\left(\mathrm{m^2 s^{-3}}\right)$ for measuring gaps P1 to P4. Dots aligned horizontally identify the position of LDA measurements.

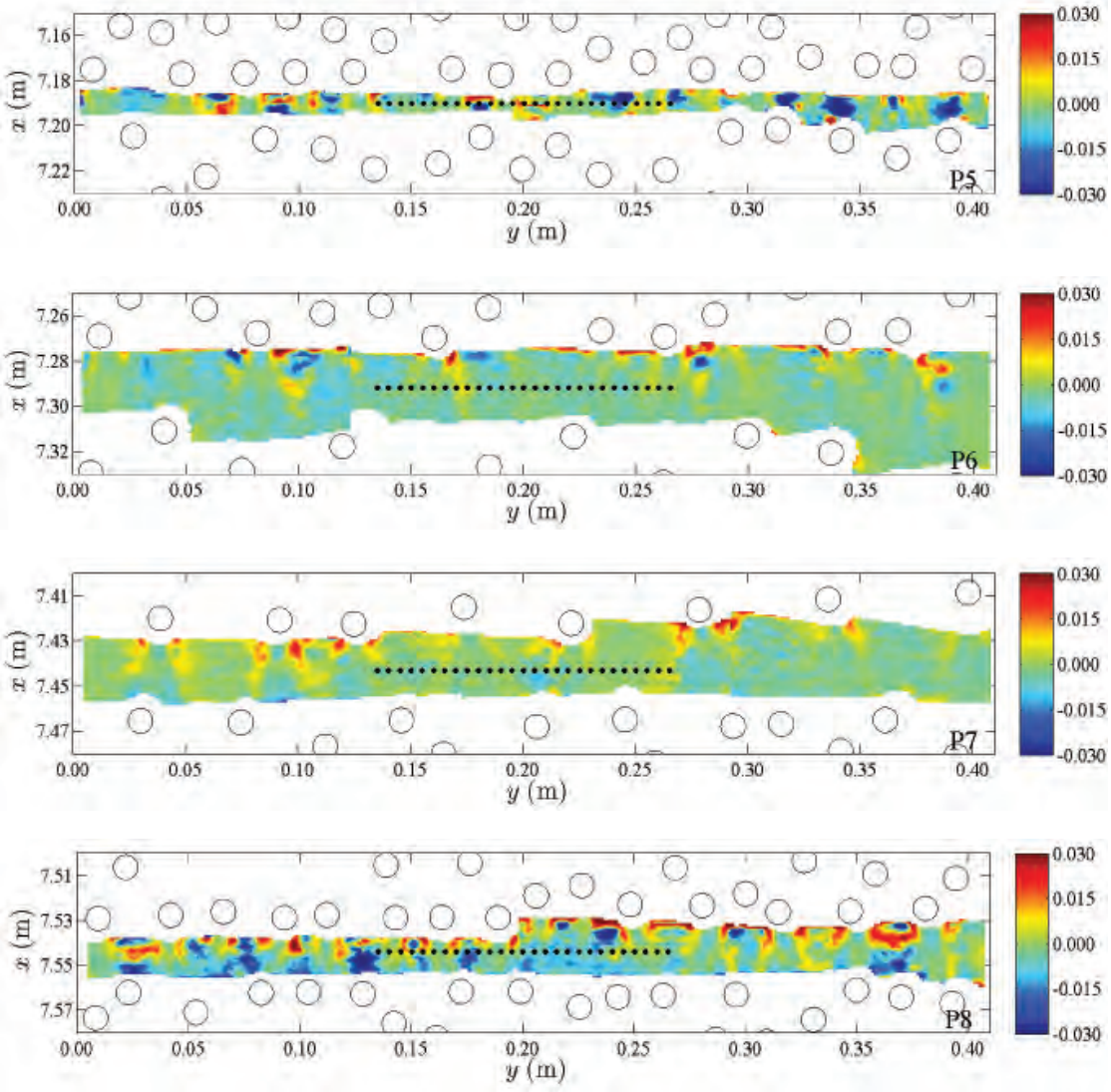

Figure C.6: Two-dimensional maps of the convective term, $1/2\bar{u}_j \partial \overline{u_i' u_i'} / \partial x_j$, $\left(\mathrm{m^2 s^{-3}}\right)$ for measuring gaps P5 to P8. Dots aligned horizontally identify the position of LDA measurements.

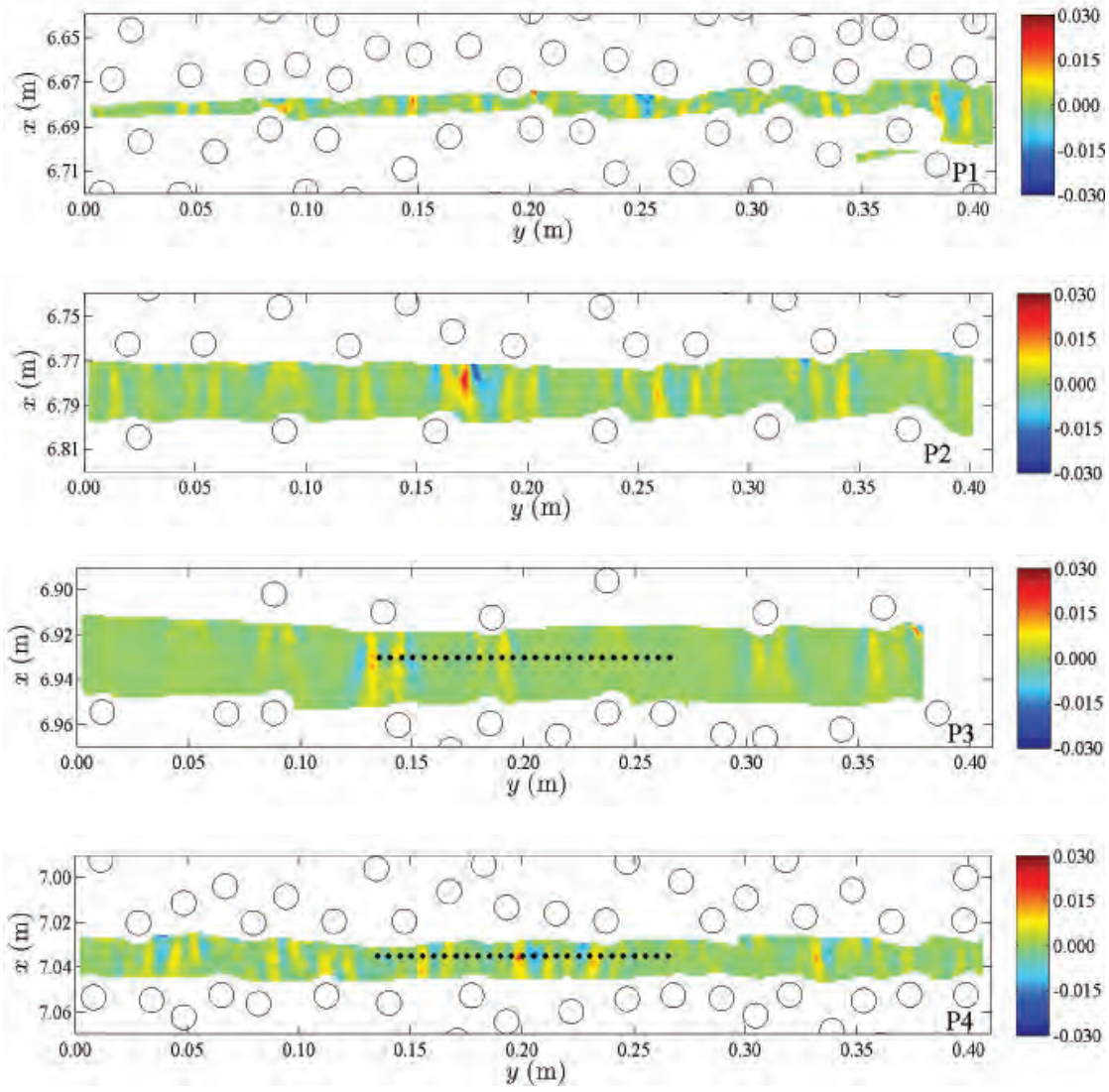

Figure C.7: Two-dimensional maps of turbulent diffusion, $1/2\partial\overline{u_i'u_i'u_j'}/\partial x_j$, $\left(\mathrm{m^2 s^{-3}}\right)$ for measuring gaps P1 to P4. Dots aligned horizontally identify the position of LDA measurements.

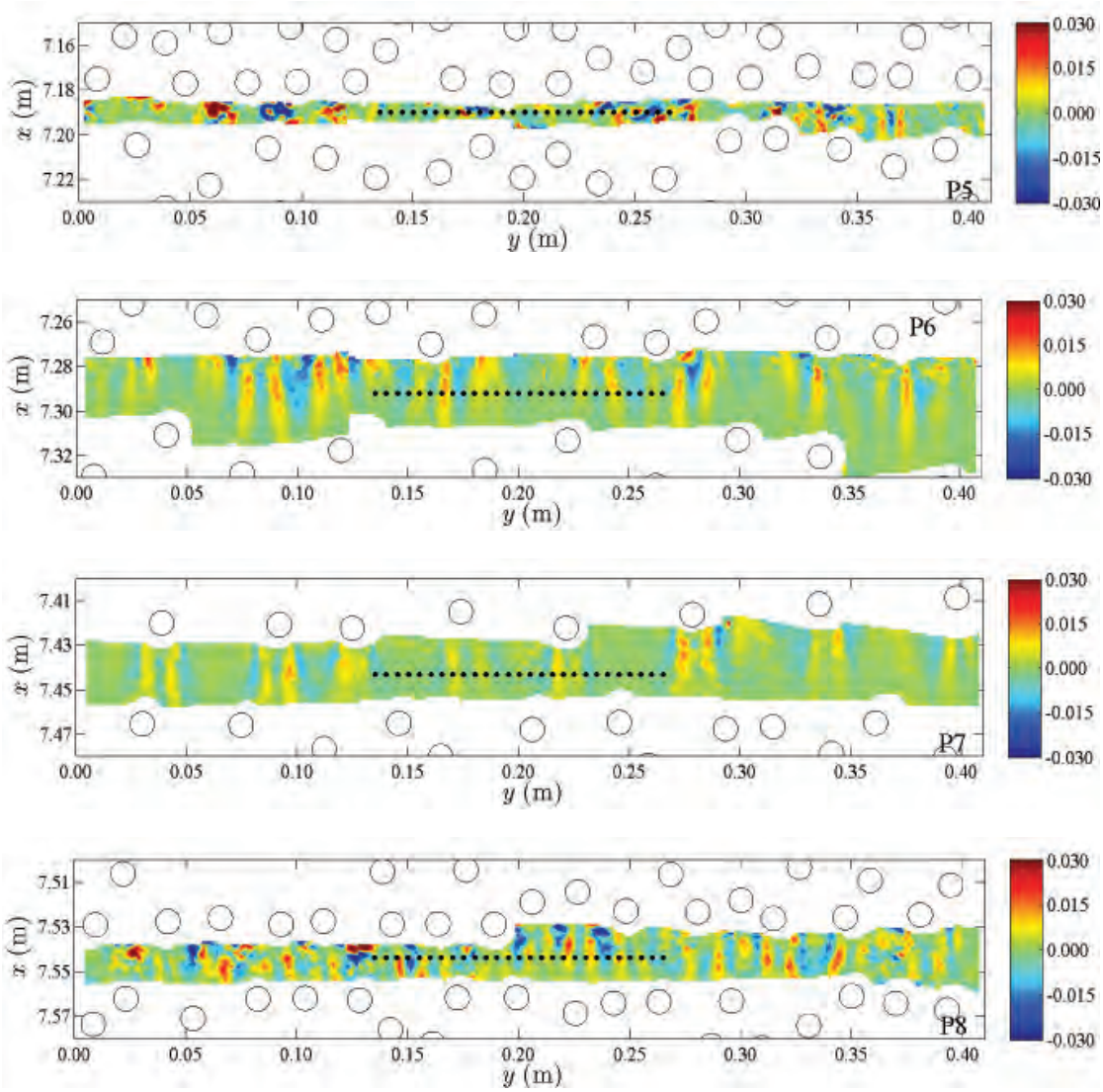

Figure C.8: Two-dimensional maps of turbulent diffusion, $1/2\partial\overline{u_i' u_i' u_j'}/\partial x_j$, $\left(\mathrm{m^2 s^{-3}}\right)$ for measuring gaps P5 to P8. Dots aligned horizontally identify the position of LDA measurements.

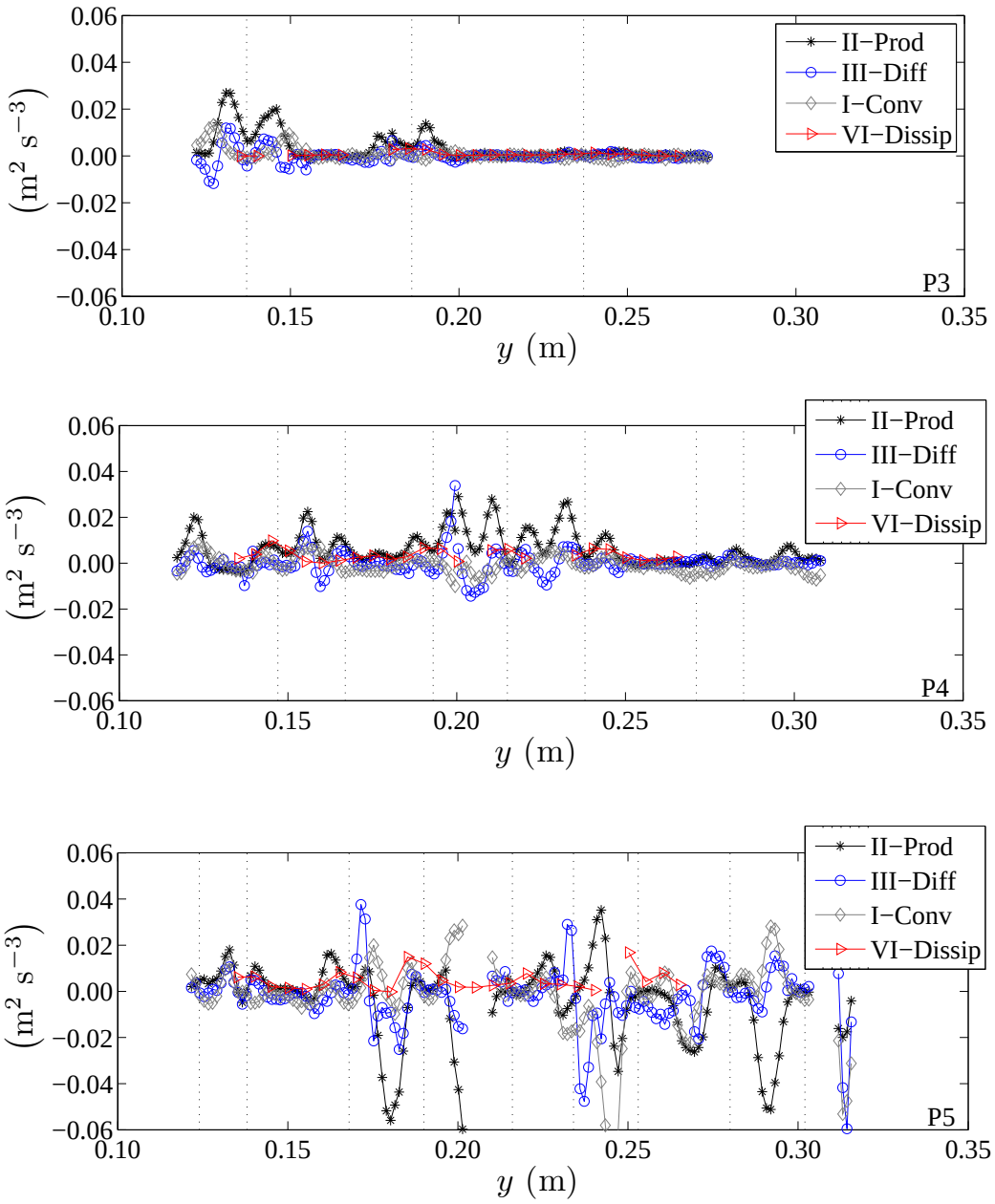

Figure C.9: Lateral profiles of the terms of TKE budget equation for measuring gaps P3 to P5.

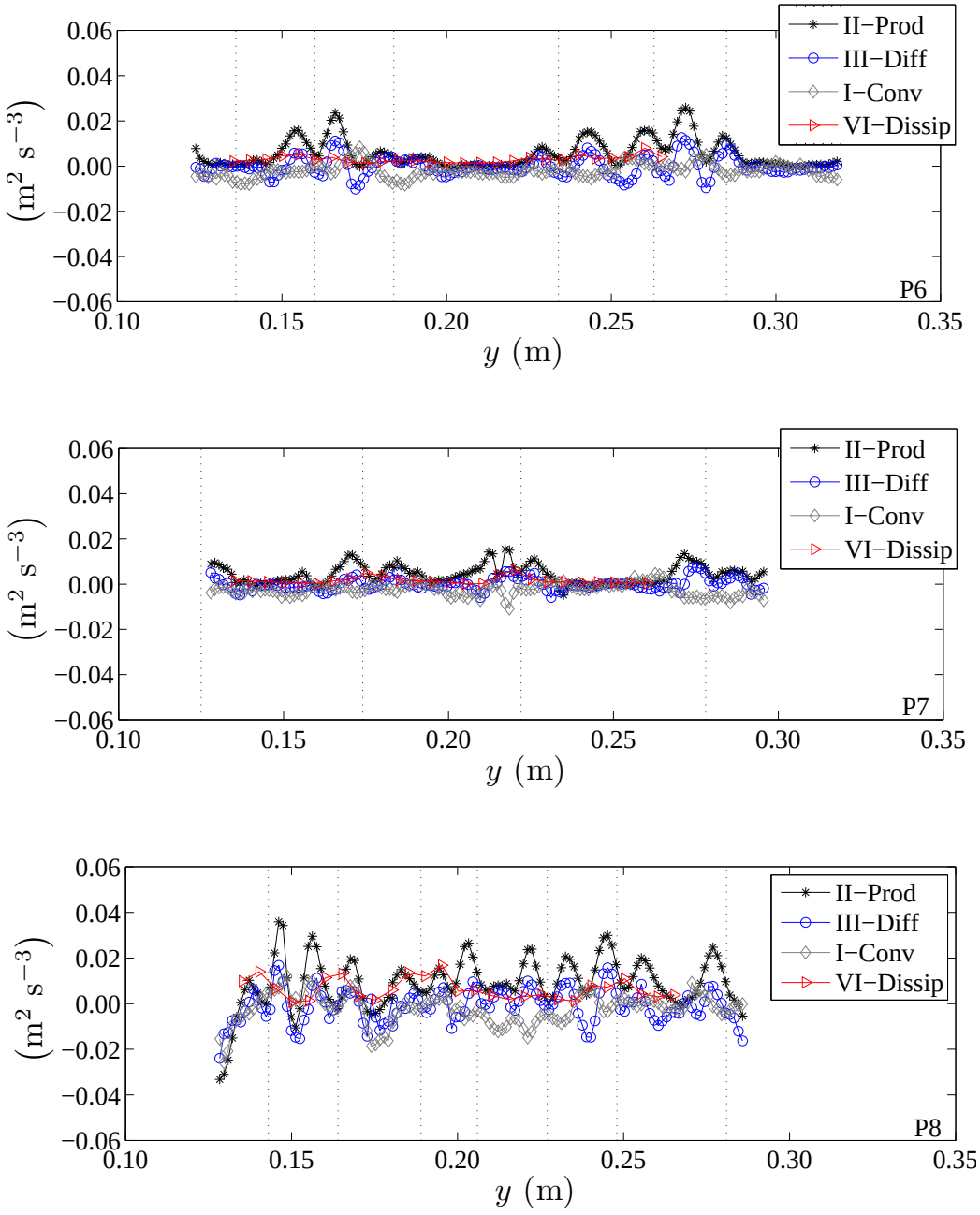

Figure C.10: Lateral profiles of the terms of TKE budget equation for measuring gaps P6 to P8.

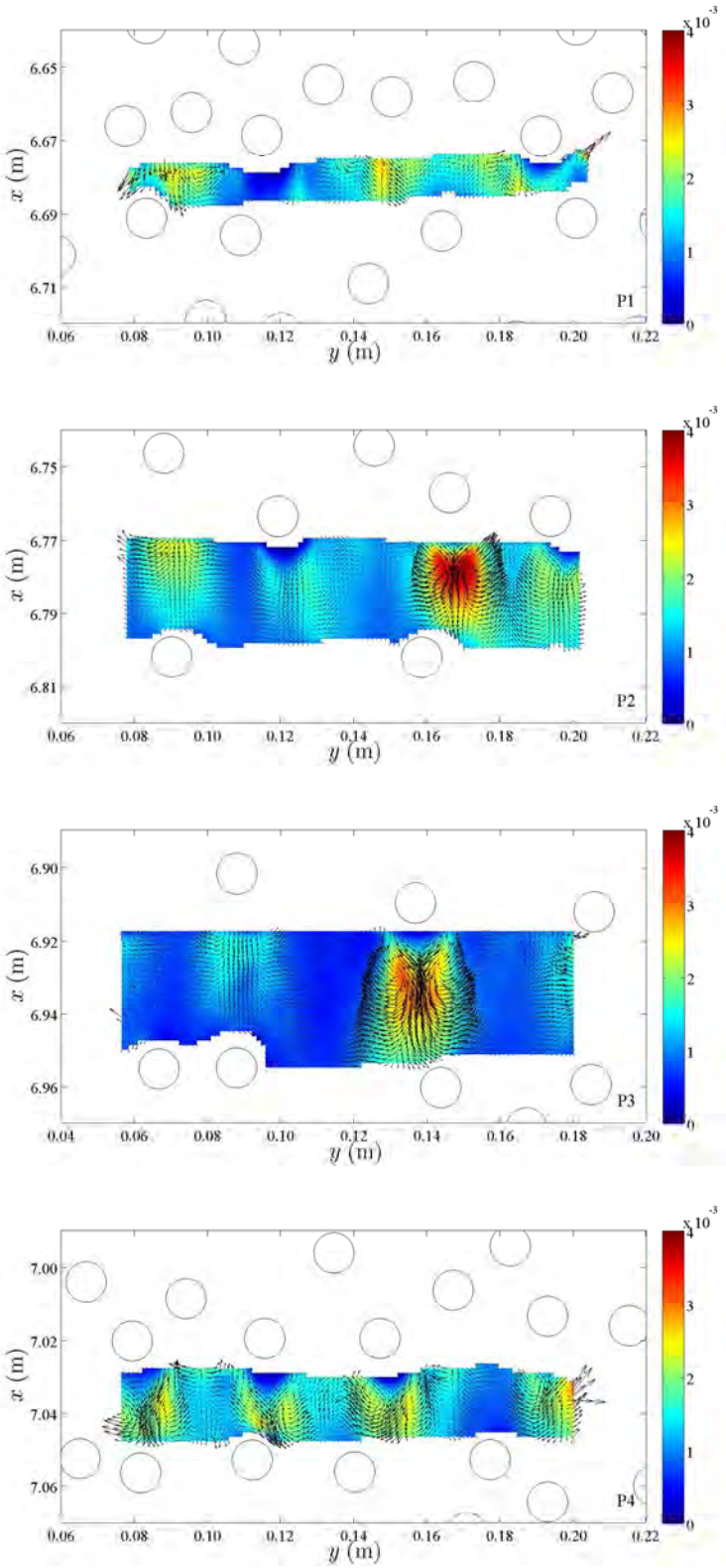

Figure C.11: Two-dimensional maps of $1/2\left(\overline{u'u'}+\overline{v'v'}\right)$ overlapped by a vector plot of the flux of TKE, for measuring gaps P1 to P4. The colorbar units are m^2s^{-2}.

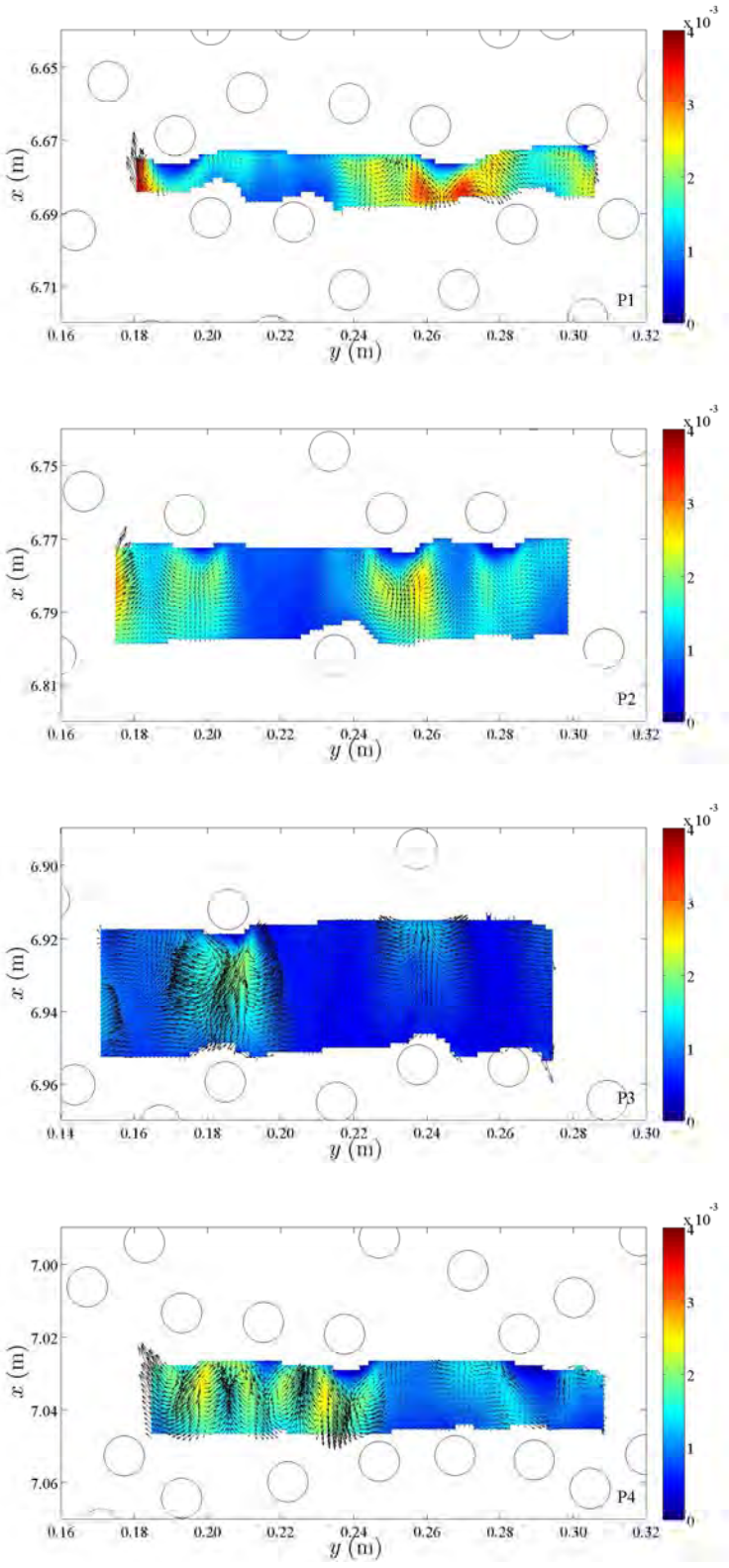

Figure C.12: Two-dimensional maps of $1/2\left(\overline{u'u'}+\overline{v'v'}\right)$ overlapped by a vector plot of the flux of TKE, for measuring gaps P1 to P4. The colorbar units are m^2s^{-2}.

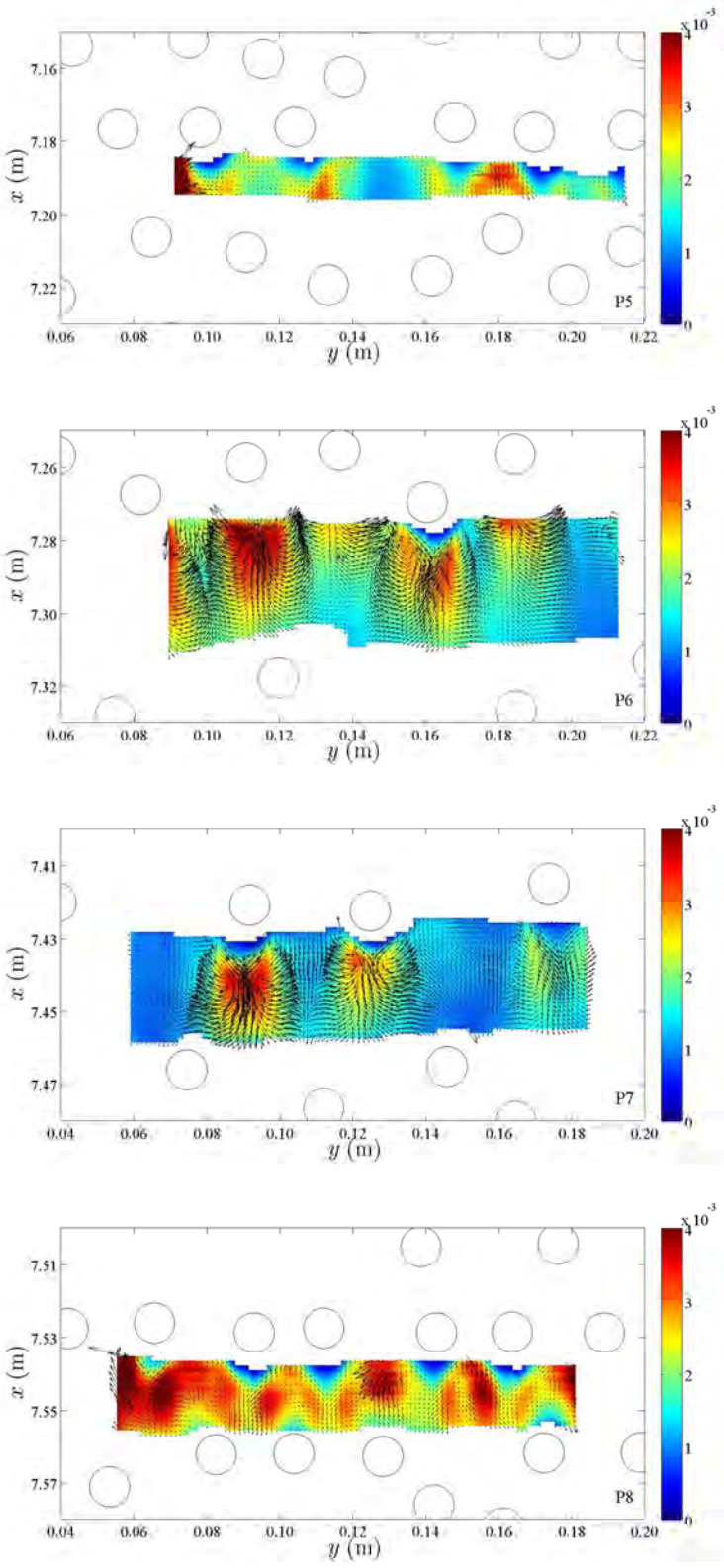

Figure C.13: Two-dimensional maps of $1/2\left(\overline{u'u'}+\overline{v'v'}\right)$ overlapped by a vector plot of the flux of TKE, for measuring gaps P5 to P8. The colorbar units are m^2s^{-2}.

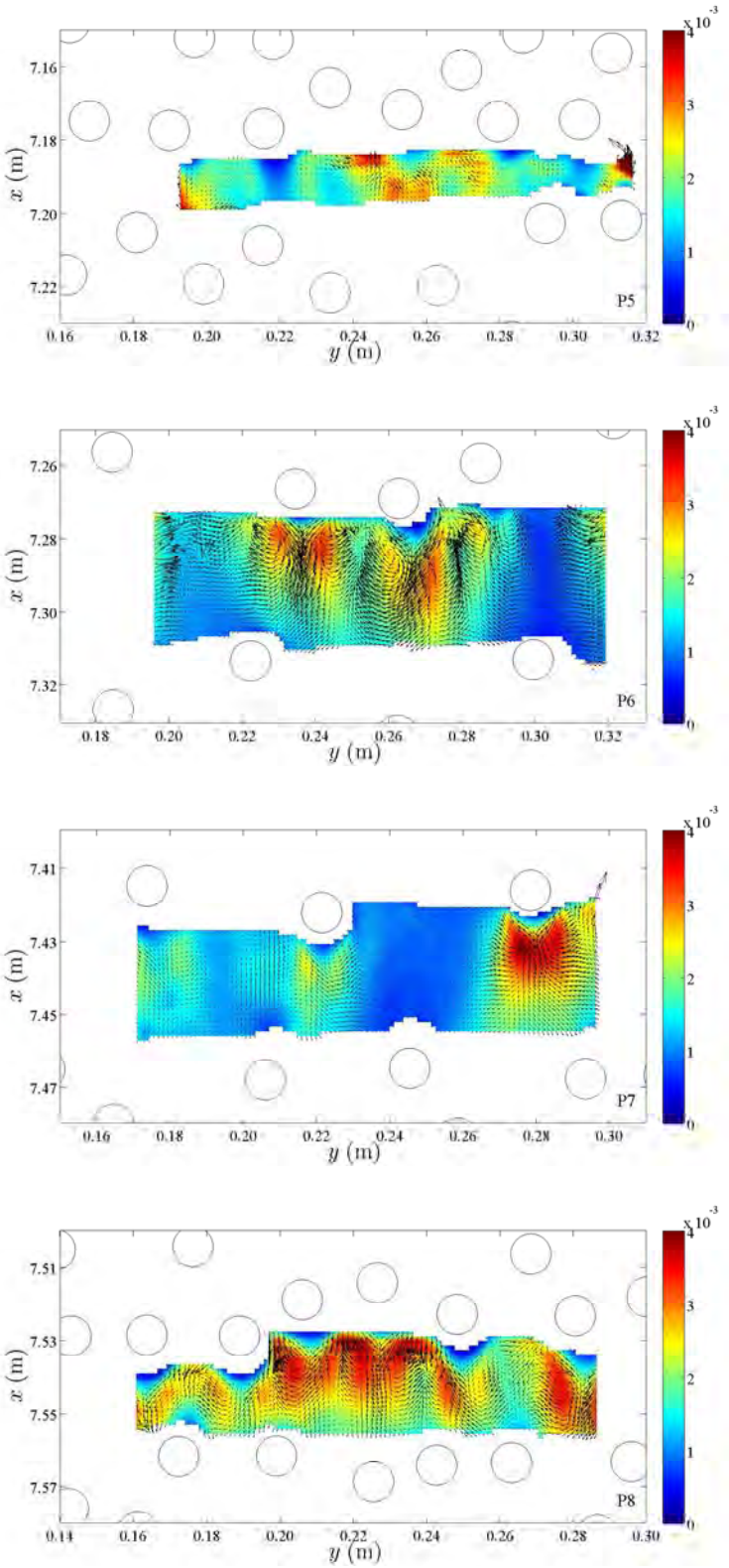

Figure C.14: Two-dimensional maps of $1/2\left(\overline{u'u'}+\overline{v'v'}\right)$ overlapped by a vector plot of the flux of TKE, for measuring gaps P5 to P8. The colorbar units are m^2s^{-2}.

Communications du Laboratoire de Constructions Hydrauliques ISSN 1661-1179
Ecole Polytechnique Fédérale de Lausanne
Editeur: Prof. Dr A. Schleiss

N° 43	2010	Master of Advanced Studies (MAS) in Hydraulic Engineering, édition 2007-2009 - Collection des articles des travaux de diplôme
N° 44	2010	J.-L. Boillat, M. Bieri, P. Sirvent, J. Dubois TURBEAU – Turbinage des eaux potables
N° 45	2011	J. Jenzer Althaus Sediment evacuation from reservoirs through intakes by jet induced flow
N° 46	2011	M. Leite Ribeiro Influence of tributary widening on confluence morphodynamics
N° 47	2011	M. Federspiel Response of an embedded block impacted by high-velocity jets
N° 48	2011	J. García Hernández Flood management in a complex river basin with a real-time decision support system based on hydrological forecasts
N° 49	2011	F. Hachem Monitoring of steel-lined pressure shafts considering water-hammer wave signals and fluid-structure interaction
N° 50	2011	J.-M. Ribi Etude expérimentale de refuges à poissons aménagés dans les berges de rivières soumises aux éclusées hydroélectriques
N° 51	2012	W. Gostner The Hydro-Morphological Index of Diversity: a planning tool for river restoration projects
N° 52	2012	M. Bieri Operation of complex hydropower schemes and its impact on the flow regime in the downstream river system under changing scenarios
N° 53	2012	M. Müller Influence of in- and outflow sequences on flow patterns and suspended sediment behavior in reservoirs
N° 54	2013	V. Dugué Influencing river morphodynamics by means of a bubble screen: application to open-channel bends
N° 55	2013	E. Person Impact of hydropeaking on fish and their habitat
N° 56	2013	T. Cohen Liechti Influence of dam operation on water resources management under different scenarios in the Zambezi River Basin considering environmental objectives and hydropower
N° 57	2014	A. M. da Costa Ricardo Hydrodynamics of turbulent flows within arrays of circular cylinders

ISSN 1661-1179

Prof. Dr A. Schleiss
Laboratoire de constructions hydrauliques - LCH
EPFL, Bât. GC, Station 18, CH-1015 Lausanne
http://lch.epfl.ch
e-mail: secretariat.lch@epfl.ch